UNIVERSITÉ DE LORRAINE

École Doctorale IAEM Lorraine

Quantification of Electrical Properties of Organs by Magnetic Resonance Imaging

Quantification des Propriétés Électriques des Organes par Imagerie par Résonance Magnétique

Thèse

Présentée et soutenue publiquement pour l'obtention du titre de

DOCTEUR DE l'UNIVERSITE DE LORRAINE

Mention : « Automatique, Traitement du Signal et des Images, Génie Informatique »

par **Zhongzheng HE**

Soutenue le 17 octobre 2024

Membres du jury :

Président de jury :	**Dr. Olivier BEUF**	**Directeur de Recherche CNRS, CREATIS, INSA – Université Claude Bernard, Lyon**
Rapporteurs :	**Pr. Marie POIRIER-QUINOT**	**Professeur, BioMaps, Université Paris-Saclay, Orsay**
	Dr. Ulrich KATSCHER	**Senior Scientist, Philips Research, Hamburg, Germany**
Directeurs de thèse :	**Dr. Freddy ODILLE**	**Directeur de Recherche INSERM, IADI, Université de Lorraine, Nancy**
	Dr. Pauline LEFEBVRE	**Maître de Conférences, IADI, Université de Lorraine, Nancy**
Membres invités :	**Dr. Paulo LOUREIRO DE SOUSA**	**Ingénieur de Recherche CNRS, HDR, ICUBE, Université de Strasbourg**
	Dr. Paul SOULLIÉ	**PhD, IADI, Université de Lorraine, Nancy**

Laboratoire d'Imagerie Adaptative Diagnostique et Interventionnelle, INSERM U1254

CHRU de Nancy Brabois, Rue du Morvan, 54511 Vandœuvre-lès-Nancy

UNIVERSITÉ DE LORRAINE

École Doctorale IAEM Lorraine

Quantification of Electrical Properties of Organs by Magnetic Resonance Imaging

Quantification des Propriétés Électriques des Organes par Imagerie par Résonance Magnétique

Thèse

Présentée et soutenue publiquement pour l'obtention du titre de

DOCTEUR DE l'UNIVERSITE DE LORRAINE

Mention : « Automatique, Traitement du Signal et des Images, Génie Informatique »

par **Zhongzheng HE**

Soutenue le 17 octobre 2024

Membres du jury :

Président de jury :	**Dr. Olivier BEUF**	**Directeur de Recherche CNRS, CREATIS, INSA – Université Claude Bernard, Lyon**
Rapporteurs :	**Pr. Marie POIRIER-QUINOT**	**Professeur, BioMaps, Université Paris-Saclay, Orsay**
	Dr. Ulrich KATSCHER	**Senior Scientist, Philips Research, Hamburg, Germany**
Directeurs de thèse :	**Dr. Freddy ODILLE**	**Directeur de Recherche INSERM, IADI, Université de Lorraine, Nancy**
	Dr. Pauline LEFEBVRE	**Maître de Conférences, IADI, Université de Lorraine, Nancy**
Membres invités :	**Dr. Paulo LOUREIRO DE SOUSA**	**Ingénieur de Recherche CNRS, HDR, ICUBE, Université de Strasbourg**
	Dr. Paul SOULLIÉ	**PhD, IADI, Université de Lorraine, Nancy**

Laboratoire d'Imagerie Adaptative Diagnostique et Interventionnelle, INSERM U1254

CHRU de Nancy Brabois, Rue du Morvan, 54511 Vandœuvre-lès-Nancy

Acknowledgements

I extend my deepest gratitude to Freddy Odille and Pauline Lefebvre for their exceptional guidance, steadfast support, and relentless encouragement throughout my doctoral journey. Their invaluable expertise, remarkable patience, and unwavering dedication have profoundly influenced my research direction and scholarly development. Additionally, their encouragement to engage in teaching activities and supervise an M2 internship student has enriched my professional experience. I feel incredibly fortunate to have had the privilege of working under their mentorship and am deeply indebted to them for their exceptional contributions to this thesis. Without their resources and support, advancing my thesis work would have been exceedingly challenging.

I also wish to express my heartfelt appreciation to my friends and colleagues, Paul Soullié and Bailiang Chen, for their invaluable help in my research. Our frequent discussions and their insightful ideas often inspired me to think more deeply and clearly about the problems at hand. They were great teachers and colleagues in the lab. I also thank Martin Doguet for his assistance, especially at the beginning of my thesis projects, and Guillaume Paillart for his support on the local SAR project. Additionally, I am grateful to Jacques Felblinger, Pierre-André Vuissoz, and Julien Oster for their encouragement, valuable discussions, and research spirit that have inspired me to explore the world of MRI.

My sincere thanks go to Dr. Paulo Loureiro de Sousa and Dr. Julien Lamy for their warm reception during my visit to Strasbourg and for their inspiring and stimulating discussions and collaborative spirit. Moreover, I am immensely grateful to Paulo for his meticulous review of this thesis.

I am deeply grateful to the administrative staff, engineers, and clinical study staff at IADI and CIC-IT (including Frédérique Chabourel, Céline Fournier, Stéphanie Magniere, Fabienne Antoine, Agnès Basile, Gabriela Hossu, Guillaume Drouot, Claire Dessale, Marine Beaumont, Damien Husson, Emilien Micard, Nicolas Weber, Marc Fauvel, and others) for their exceptional assistance, prompt responses, and efficient services. Their unwavering efforts have facilitated my access to essential resources, invaluable data, and crucial infrastructure, enabling me to conduct my research effectively and efficiently.

To my friends and family, your unwavering belief in me and constant encouragement have been the pillars of strength that have sustained me throughout the challenges of this academic journey. Your boundless love, unwavering support, and profound understanding have made this journey possible.

I would like to acknowledge the invaluable contributions and insightful feedback provided by my monitoring committee, Paul and Xavier Maître, and the members of my thesis committee, Olivier Beuf, Ulrich Katscher, Marie Poirier-Quinot, Paulo, and Paul. Their expertise, constructive criticism, and

expert suggestions have significantly enhanced the quality and rigor of this research. I am deeply grateful for their commitment and for the diverse perspectives they have brought to this study.

Finally, my deepest appreciation goes to all the participants who generously contributed their time, insights, and expertise to this research. Their willingness to engage and participate has been indispensable to the successful completion of this study, and I am genuinely thankful for their invaluable contributions.

Abstract

Tissue electrical properties (EPs), including electrical conductivity and permittivity, define the pathways through which current flows in the body in response to an electromagnetic (EM) field. These properties are influenced by tissue composition, internal structure, aging, and factors like water content, ion concentration, and the medium in which they reside (intra- or extracellular). EPs vary significantly across different tissues and pathological conditions, making them potential biomarkers for clinical applications such as cancer diagnosis, therapy monitoring, and fundamental etiology research. Additionally, understanding EPs allows for the calculation of EM field distribution within the body, which is crucial for assessing personalized specific absorption rate (SAR) in MRI systems to ensure radiofrequency (RF) safety.

Among the various technologies for imaging EPs, Magnetic Resonance Electrical Properties Tomography (EPT) stands out due to its non-invasive nature and high spatial resolution. EPT reconstructs the quantitative spatial distribution of EPs from the measured B_1 field variations in MRI. The overarching goal of this thesis is to evaluate and optimize EPT methods, and explore the variability of EPs in the population to benefit accurate SAR modeling.

This thesis provides a comprehensive overview of the state-of-the-art in EPT, detailing the analysis and review of EPT reconstruction and data acquisition methods. The performance of various EPT methods was first evaluated using conductivity phantoms in terms of accuracy and resolution limits. Considering the advantages and drawbacks of each technique proposed for MR-EPT, image-based EPT with Ultra-short Echo Time (UTE) sequence was selected as the most promising practical approach. The second part of the study focused on evaluating permittivity reconstruction accuracy in image-based EPT with different flip angles of UTE. An optimal flip angle for permittivity was identified, enhancing the reliability of permittivity measurements. Thirdly, to ensure the validity of homogeneous Helmholtz EPT formulations in large homogeneous regions, an adaptive Savitzky-Golay kernel was proposed for any arbitrary tissue shape with anatomical prior knowledge. Additionally, a numerical method for the surface integral version of EPT was developed, providing reduced noise effects by converting second derivatives to first derivatives in the formulation. The fourth part of the thesis explored in vivo conductivity changes in the brain and torso related to age, fat fraction, and sex. These findings offer insights into accurate SAR modeling with corrected conductivity values, accounting for their variability in the population. Finally, the application of EPT in local SAR calculation was developed and compared with those based on literature EPs values. This comparison validated the reliability of EPT, emphasizing its importance in SAR modeling.

Résumé de la Thèse

Introduction

L'imagerie par tomographie des propriétés électriques (EPT) par résonance magnétique (RM) est une technologie innovante non invasive qui fournit une distribution spatiale quantitative des propriétés électriques (EPs) des tissus à la fréquence de Larmor. Les EPs, comprenant la conductivité électrique et la permittivité, définissent la manière dont le courant circule dans le corps en réponse à un champ électromagnétique (EM). Ces propriétés sont influencées par la composition des tissus, leur structure interne, le vieillissement et des facteurs comme la teneur en eau, la concentration en ions et le milieu dans lequel elles se trouvent (intra- ou extracellulaire). Les EPs varient considérablement selon les différents tissus et les conditions pathologiques, ce qui en fait des biomarqueurs potentiels pour des applications cliniques telles que le diagnostic du cancer, le suivi thérapeutique et la recherche étiologique fondamentale. De plus, comprendre les EPs permet de calculer la distribution des champs EM dans le corps, ce qui est crucial pour évaluer le débit d'absorption spécifique (DAS) personnalisé dans les systèmes d'IRM afin d'assurer la sécurité en radiofréquence (RF).

Ces dernières années, de nombreuses méthodes de reconstruction EPT ont été développées, la plupart reposant sur les équations de Maxwell comme principes fondamentaux. Parmi elles, les méthodes différentielles sont les plus répandues en raison de leur simplicité, de leur facilité de mise en œuvre et de leur efficacité computationnelle. Elles sont basées sur l'équation de Helmholtz avec différentes exigences de données B_1^+. Cependant, comme l'EPT est un domaine relativement nouveau, il existe une variabilité significative entre les EPs reconstruites produites par différentes méthodes, en particulier pour les résultats in vivo. Évaluer la performance et la fiabilité de ces méthodes est essentiel pour faire progresser leurs applications cliniques et garantir des mesures précises et cohérentes.

Objectif de la Thèse

L'objectif principal de cette thèse est d'évaluer et d'optimiser les méthodes EPT afin d'établir un protocole fiable pour estimer les EPs in vivo dans divers organes. Cela implique de comparer les EPs in vivo de populations adultes avec des valeurs de référence ex vivo et d'identifier des tendances liées à des caractéristiques individuelles telles que l'âge, le sexe et la fraction de graisse. En atteignant ces objectifs, cette recherche vise à contribuer de manière significative à l'exactitude de la modélisation du DAS, ce qui est crucial pour garantir la sécurité des patients dans les environnements d'IRM à champ élevé.

Organisation de la Thèse

Cette thèse est structurée comme suit :

- **Chapitre 1 :** Introduction aux propriétés électriques des tissus, leurs applications et méthodes de mesure, fournissant un contexte sur la RM-EPT.
- **Chapitre 2 :** Revue comparative des principales techniques de RM-EPT, discutant de leurs avantages et limitations.
- **Chapitre 3 :** Détails sur l'acquisition des données EPT utilisant différentes séquences RM et les résultats comparatifs entre les méthodes Ultrashort Echo Time (UTE) et phase-cycled balanced Steady-State Free Precession (bSSFP).
- **Chapitre 4 :** Évaluation de la conductivité électrique dans des fantômes comparée aux mesures de référence par un analyseur de réseau vectoriel (VNA).
- **Chapitre 5 :** Évaluation de la permittivité électrique dans des fantômes en utilisant des techniques de comparaison similaires.
- **Chapitre 6 :** Développement et application d'un noyau intégral adaptatif de Savitzky-Golay et de surface en EPT pour améliorer la précision de reconstruction.
- **Chapitre 7 :** Étude in vivo explorant les changements liés à l'âge, la fraction de graisse et le sexe dans la conductivité électrique.
- **Chapitre 8 :** Application des résultats EPT au calcul du DAS local, en soulignant l'importance des mesures EPs in vivo précises pour la sécurité des patients.
- **Chapitre 9 :** Conclusion résumant les principaux résultats et suggérant des orientations pour de futures recherches.

Chapitre 1 : Introduction aux Propriétés Électriques des Tissus

Le premier chapitre de cette thèse introduit les propriétés électriques des tissus (EPs) et leur importance dans le domaine biomédical et la sécurité RF. Les EPs, comprenant la conductivité électrique et la permittivité, jouent un rôle crucial dans la définition des chemins par lesquels le courant électrique circule à travers le corps en réponse à un champ électromagnétique (EM). Ces propriétés varient significativement selon la composition des tissus, la structure interne, l'âge et d'autres facteurs tels que la teneur en eau et la concentration ionique.

Modèle de circuit équivalent des tissus biologiques

Les tissus biologiques peuvent être représentés par un modèle de circuit équivalent RC (résistance-capacité), où les électrolytes intra- et extracellulaires contribuent à la résistance et les membranes cellulaires agissent comme des capacités. Ce modèle aide à comprendre comment les charges électriques se déplacent et se polarisent en réponse à un champ électrique externe, influençant ainsi la conductivité et la permittivité des tissus.

Dépendance à la fréquence

Les EPs des tissus présentent une dépendance en fréquence, appelée "dispersion". À basse fréquence, les membranes cellulaires agissent comme des barrières, conduisant à une haute permittivité et une faible conductivité. À haute fréquence, les membranes deviennent transparentes aux courants électriques, augmentant ainsi la conductivité et réduisant la permittivité. Cette caractéristique permet d'obtenir des informations sur la composition et la microstructure des tissus à différentes fréquences.

Mesure des EPs des tissus

La mesure des EPs peut se faire par des méthodes invasives et non invasives. Les méthodes invasives utilisent des sondes coaxiales connectées à un analyseur de réseau vectoriel (VNA) pour mesurer les coefficients de réflexion complexes et déterminer les EPs. Cependant, ces méthodes sont limitées par leur nature invasive et leur incapacité à caractériser des tissus hétérogènes.

Les méthodes non invasives incluent la tomographie par impédance électrique (EIT), la tomographie par induction magnétique (MIT) et la tomographie par impédance électrique par résonance magnétique (MREIT). Ces techniques utilisent des électrodes ou des bobines pour injecter des courants ou induire des champs électromagnétiques et mesurer les réponses correspondantes. La MR-EPT se distingue par son caractère non invasif et sa capacité à fournir des images à haute résolution spatiale des EPs en utilisant les champs B_1 mesurés en IRM.

En conclusion, ce chapitre fournit une base essentielle pour comprendre les principes de base, les applications et les défis associés à l'EPT, préparant ainsi le terrain pour les discussions plus techniques et les développements méthodologiques présentés dans les chapitres suivants.

Chapitre 2: Revue des méthodes pour la tomographie des propriétés électriques par résonance magnétique (MR-EPT)

Le deuxième chapitre de cette thèse offre une revue complète des différentes méthodes développées pour la tomographie des propriétés électriques par résonance magnétique (MR-EPT). Ces méthodes se sont diversifiées pour aborder divers aspects de la reconstruction des propriétés électriques (EPs), en tirant parti de l'interaction entre les champs électromagnétiques de radiofréquence (RF) B_1 et les EPs des tissus. Les méthodes MR-EPT peuvent être classées en deux grandes catégories selon leur formulation mathématique : les approches basées sur des modèles physiques et celles basées sur des modèles non-physiques.

Approches basées sur des modèles non-physiques : Ces méthodes incluent l'EPT basée sur la teneur en eau et l'EPT basée sur l'apprentissage profond. Ces approches manquent généralement de généralisation et conviennent à des organes spécifiques.

Les méthodes basées sur des modèles physiques reposent sur l'équation centrale de l'EPT dérivée des équations de Maxwell. Elles se divisent en deux sous-catégories : les méthodes intégrales et les méthodes différentielles.

Méthodes intégrales : Des exemples comme l'Inversion de Source de Contraste (CSI) visent à minimiser la différence entre les champs B_1 mesurés et simulés sur la base des EPs supposées. Bien qu'elles évitent la différenciation ou les processus de débruitage, elles nécessitent des simulations électromagnétiques précises et de nombreuses itérations, ce qui entraîne une complexité computationnelle élevée.

Méthodes différentielles : Ces méthodes sont plus rapides et plus faciles à mettre en œuvre. L'équation centrale pour l'EPT différentielle est :

$$\nabla^2 \mathbf{B} + \frac{\nabla \kappa}{\kappa} \times \nabla \times \mathbf{B} = i\omega\mu_0 \kappa \mathbf{B}$$

où $\mu_0$est la perméabilité du vide, ω est la fréquence de Larmor, et $\kappa = \sigma + i\omega\varepsilon_0\varepsilon_r$ est l'admittivité composée de la conductivité σ et de la permittivité relative ε_r. Les approches différentielles peuvent ignorer ou inclure le terme gradient des EPs, se subdivisant ainsi en familles basées sur Helmholtz et sur convection-réaction (cr).

La famille EPT basée sur Helmholtz ignore le gradient des EP, ce qui en facilite la mise en œuvre mais au prix d'artefacts de frontière, la rendant moins adaptée aux structures de petite taille. La famille cr-EPT réécrit l'équation sous forme d'équation aux dérivées partielles de convection-réaction (cr-PDE), en conservant le terme de gradient mais en supposant que $\nabla B_z=0$ en raison de son inaccessibilité en IRM. Cette supposition, ainsi que d'autres utilisées pour les simplifications, peut être invalide pour l'ensemble de l'objet imagé, ce qui donne lieu à une cr-PDE imparfaite où les termes sont seulement approximativement égaux. Pour améliorer la stabilité numérique, des stratégies de régularisation, telles que l'ajout d'un terme de diffusion artificielle dans la cr-PDE ou la régularisation par variation totale, peuvent être utilisées. Cependant, le coefficient de régularisation peut varier dans l'espace et même devenir nul à certains points. Ainsi, les cr-PDE sont généralement difficiles à résoudre et ne sont pas largement utilisées en recherche clinique.

Selon les exigences du champ B_1 en entrée, l'EPT basée sur des méthodes différentielles peut également être catégorisée en EPT standard, basée sur le champ B_1 relatif, basée uniquement sur la phase, et basée sur une image complexe. Celles-ci nécessitent respectivement le champ B_1 absolu, généralement avec l'hypothèse TPA (Transceive Phase Assumption), le champ B_1 relatif utilisant un système de transmission RF multicanaux, la phase d'émission-réception, et l'image complexe MR à faible angle de bascule, avec différentes hypothèses.

De plus, l'opérateur Laplacien amplifie le bruit, entraînant des erreurs numériques significatives dans les cartes EPs reconstruites. Une autre approche consiste à convertir l'équation sous forme de Laplacien en une forme intégrale de surface en utilisant le théorème de divergence, réduisant les dérivées de second ordre à des dérivées de premier ordre du champ B_1 mesuré.

Cette revue vise à fournir un aperçu complet des différentes méthodes MR-EPT différentielles et de leur conversion en formes intégrales de surface, catégorisées selon leurs exigences de mesure du champ B_1.

Chapitre 3 : Acquisition des Données EPT et Séquences EPT

Étant donné l'inaccessibilité de l'amplitude absolue $|B_1^-|$et de la phase $\varphi^{\pm}$ en IRM, l'approche standard consiste à mesurer l'amplitude de transmission $|B_1^+|$ et la phase d'émission-réception φ_{tr}. Ces deux types de séquences d'impulsions — la cartographie $|B_1^+|$ et la mesure de la phase d'émission-réception — sont résumés.

Acquisition de la Phase d'Emission-Réception

1) Spin Echo (SE)
   - Avantages : simple et élimine efficacement les effets de hors-résonance (off-resonance) et les effets de déplacement chimique.
   - Limites : acquisition lente ; sensible aux effets des courants de Foucault et aux mouvements

2) UTE/ZTE (Ultra-Short/Zero Echo Time)
   - Avantages : acquisition rapide ; presque pas d'effets de hors-résonance; convient aux tissus à faible T2*, tels que les os corticaux et les poumons.
   - Limites : sensible aux effets de courant de Foucault.

3) Multi Gradient Echo (MGRE)
   - Avantages : capable de traiter simultanément EPT et QSM.
   - Limites : problèmes de repliement spatial et temporel de la phase.
4) balanced Steady-State Free Precession (bSSFP)
   - Avantages : rapide avec un rapport signal sur bruit (SNR) élevé, capable de traiter simultanément EPT et QSM ; comportement bénin hors-résonance lorsque $\Delta B_0 \approx 0$.
   - Limites : Sensible à l'inhomogénéité de B_0 ; Artefacts de bandes.

Récemment, deux méthodes avancées utilisant une série de séquences bSSFP avec cyclage de phase, PLANET et la transformation de Fourier rapide (FFT), ont été proposées pour éliminer plus efficacement les artefacts de bandes et extraire la phase d'émission-réception pure. Après les avoir comparées avec les séquences standard bSSFP et UTE dans un fantôme de conductivité et dans le

cerveau d'un volontaire sain dans le contexte de l'EPT basée sur la phase, FFT et UTE sont recommandées pour l'acquisition de la phase d'émission-réception.

Méthodes de Cartographie $|B_1^+|$

La cartographie $|B_1^+|$ est cruciale car elle permet de mesurer l'amplitude du champ de transmission, qui est liée à l'angle de bascule en IRM. Les méthodes couramment utilisées incluent :

1) Double Angle Method (DAM)
   - Avantages : simple
   - Limites : temps de répétition long (TR) et acquisition lente ; dépendance au T1
2) Dual Refocusing Echo Acquisition Mode (DREAM)
   - Avantages : rapide et précis ; insensible aux effets hors-résonance, ainsi qu'aux T1, T2, et TR.
   - Limites : problèmes de repliement de phase ; DAS élevé.
3) Bloch-Siegert Shift (BSS)
   - Avantages : une des méthodes les plus rapides, faible DAS.
   - Limites : Précision relative faible, sensible aux effets hors-résonance et aux flux.
4) Actual Flip Angle Imaging (AFI)
   - Avantages : rapide ; acquisition 3D facile ; insensible aux T1 et T2.
   - Limites : inadapté aux régions à faible T1 ; sensible aux effets hors-résonance.
5) Presaturation TurboFLASH (satTFL)
   - Avantages : rapide et efficace en termes de DAS ; insensible aux T1, T2, flux et mouvements.
   - Limites : sensible aux effets hors-résonance et de déplacement chimique ; certaines dépendances en T1.

Chapitre 4 : Évaluation par Fantôme de la Conductivité Électrique par EPT

Le chapitre 4 de la thèse est dédié à l'évaluation de la conductivité électrique par tomographie de propriétés électriques (EPT) à l'aide de fantômes. Cette évaluation se concentre sur deux objectifs principaux : la quantification absolue de la conductivité et l'analyse de la limite de résolution. Dans cette étude, les mesures de conductivité à haute fréquence sont réalisées à l'aide d'un analyseur de réseau vectoriel (VNA), considéré comme vérité terrain (GT).

Deux expériences principales sont menées :

Quantification Absolue : Des fantômes homogènes sont utilisés pour cette analyse. Sept cylindres contenant des mélanges d'eau déionisée, d'agar ou d'éthanol et différentes concentrations de NaCl sont

préparés pour simuler une gamme de conductivités allant de 0 à 3 S/m, couvrant ainsi la gamme typique des EPs du corps humain.

Limite de Résolution : Un fantôme dédié à l'évaluation de la résolution est conçu avec de l'agar et des trous remplis de solution saline. Cette conception permet de simuler des structures de petite taille sans barrière artificielle entre les compartiments, bien que la diffusion du sel dans le gel doive être surveillée.

Résultats

Les résultats montrent une bonne corrélation entre les mesures de conductivité du VNA et celles obtenues par EPT. Les différences en termes de RMSE (erreur quadratique moyenne) entre les différentes méthodes d'EPT sont modérées, les méthodes basées sur la phase et sur l'image complexe montrant des erreurs comparables.

Pour les structures de petite taille, la reconstruction de la conductivité est plus difficile, les artefacts de bord et les effets de volume partiel influençant les résultats. La limite de résolution théorique est déterminée à environ 3 mm, mais en pratique, elle se situe autour de 5 mm en raison du bruit et d'autres facteurs.

Conclusion

Les méthodes d'EPT montrent une bonne capacité à quantifier la conductivité électrique dans des fantômes homogènes et à évaluer la résolution spatiale. Des ajustements tels que la régularisation adaptative peuvent améliorer la précision des reconstructions, mais augmentent également la complexité et le temps de calcul nécessaires. L'amélioration de la résolution des images IRM brutes reste un défi, surtout pour des structures de moins de 5 mm.

Chapitre 5 : Évaluation par Fantôme de la Permittivité Électrique par EPT Basée sur l'Image

Le chapitre 5 de la thèse se concentre sur l'évaluation de la permittivité électrique à l'aide de la tomographie des propriétés électriques (EPT) basée sur l'image. Contrairement à la conductivité, la permittivité est moins souvent considérée dans les études d'EPT en raison de sa sensibilité moindre aux mesures de B_1^+ et de son impact clinique moins connue. Cependant, elle est essentielle pour la modélisation précise du taux d'absorption spécifique (DAS) et les calculs de DAS local.

Méthodologie

Des fantômes liquides de différentes compositions (huile de colza, éthanol, mélanges d'éthanol et d'eau, et eau déionisée) ont été utilisés pour simuler une gamme de permittivités relatives (3 à 76). Les

données ont été acquises avec un scanner IRM de 3T en utilisant une séquence UTE Spiral VIBE à différents angles de bascule (1° à 10°).

Résultats

Les résultats montrent que le SNR augmente avec l'angle de bascule, améliorant la qualité des images. La meilleure corrélation entre la permittivité EPT et les mesures VNA a été observée à un angle de bascule de 1°, avec un coefficient de corrélation de 0,99. Les angles de bascule de 2° et 3° offrent la meilleure précision de reconstruction.

Conclusion

Les méthodes EPT basées sur l'image sont efficaces pour quantifier la permittivité électrique avec des angles de bascule optimaux de 2° à 3°. Des améliorations sont nécessaires pour optimiser le SNR et la qualité de la reconstruction.

Chapitre 6 : Noyau Adaptatif pour la Différentiation et l'Intégration Numériques en EPT

Le chapitre 6 présente l'amélioration des méthodes de différentiation et d'intégration numériques en tomographie des propriétés électriques (EPT) grâce à des noyaux adaptatifs. Les cartes de propriétés électriques reconstruites sont souvent sensibles au bruit en raison de l'utilisation de dérivées secondes. Pour pallier ce problème, des filtres de Savitzky-Golay (SG) sont utilisés pour lisser les données.

Méthodologie

- **Noyau SG Standard :** Utilise un noyau cubique uniforme, susceptible de générer des artefacts de bord.
- **Noyau SG Adaptatif :** Ajuste la taille et la forme du noyau en fonction des formes tissulaires pour réduire les artefacts.
- **Noyau SG Adaptatif KNN :** Sélectionne les K plus proches voisins, évitant les voxels distants et réduisant les artefacts.
- **Noyau des Intégrales de Surface :** Des noyaux similaires sont développés pour l'intégration numérique via l'EPT basée sur les intégrales de surface, transformant les dérivées secondes en dérivées premières pour améliorer la robustesse contre le bruit.

Résultats et Conclusion

Les noyaux adaptatifs et KNN montrent une meilleure précision et une réduction des erreurs par rapport aux noyaux standards, particulièrement les noyaux adaptatifs. L'EPT basée sur les intégrales de surface offre de meilleurs résultats en simulation et dans les études sur fantôme de résolution.

Chapitre 7 : Étude In Vivo - Changements de la Conductivité Électrique en Fonction de l'Âge, de la Fraction de Graisse et du Sexe

Le chapitre 7 explore les variations de la conductivité électrique dans le corps humain en fonction de l'âge, de la fraction de graisse (FVF) et du sexe, en utilisant la tomographie des propriétés électriques par résonance magnétique (MR-EPT).

Le DAS pour la sécurité des examens IRM nécessite des valeurs précises des propriétés électriques (EPs). Cette étude vise à améliorer les bases de données actuelles en estimant les valeurs macroscopiques de la conductivité dans plusieurs organes (cerveau et torse) d'une petite population adulte (17 volontaires) en utilisant des images complexes d'une séquence 3D UTE et une formulation homogène de Helmholtz MR-EPT. Les relations entre ces valeurs et des paramètres biologiques tels que l'âge, la FVF, l'IMC et le sexe sont ensuite explorées pour identifier les corrélations pertinentes.

Résultats

Les valeurs de conductivité in vivo dévient des valeurs ex vivo. Plusieurs corrélations sont trouvées :

Âge : La conductivité augmente avec l'âge dans toutes les régions cérébrales, mais diminue dans le rein droit et le pancréas.

FVF : La conductivité diminue avec l'augmentation de la FVF dans plusieurs organes : rate, rein droit, foie, cœur.

Sexe : Des différences significatives de conductivité entre hommes et femmes dans le foie, l'estomac, le pancréas, le duodénum, le cœur, les poumons, l'aorte.

Conclusion

Cette étude a établi un protocole fiable pour estimer la conductivité in vivo, révélant des écarts par rapport aux valeurs ex vivo et des variations interindividuelles significatives. Ces résultats sont essentiels pour une modélisation précise du DAS et la sécurité des patients lors des examens IRM.

Chapitre 8 : Application des Résultats EPT au Calcul du DAS Local

Ce chapitre discute de l'application des valeurs de conductivité in vivo obtenues par EPT aux calculs de DAS local. Les résultats montrent une meilleure précision par rapport aux méthodes traditionnelles basées sur les valeurs de la littérature, soulignant l'importance de l'EPT pour la modélisation du DAS.

Introduction

Le DAS est un paramètre crucial pour garantir la sécurité des patients lors des procédures IRM. Il représente la quantité d'énergie électromagnétique absorbée par les tissus et doit être maintenu à des niveaux sûrs.

Méthodologie

Les valeurs de conductivité in vivo obtenues par EPT ont été utilisées pour calculer le DAS local. Des expériences ont été réalisées sur des fantômes et in vivo pour valider ces calculs par rapport aux valeurs de la littérature.

Résultats

Les résultats montrent que les valeurs de conductivité in vivo offrent une meilleure précision pour les calculs de DAS, minimisant les risques de surchauffe et de dommages tissulaires.

Conclusion

L'utilisation de valeurs de conductivité in vivo permet de développer des protocoles cliniques optimisés, améliorant ainsi la sécurité des patients lors des procédures IRM à champ élevé.

Chapitre 9 : Conclusion

Le chapitre 9 résume les principaux résultats et contributions de la thèse, mettant en évidence les avancées réalisées dans l'optimisation des méthodes EPT et l'exploration de la variabilité des propriétés électriques (EPs).

Contributions

1. Optimisation des Séquences IRM : La séquence UTE avec un angle de bascule de 3° a été recommandée pour la reconstruction de la conductivité et de la permittivité via l'EPT basée sur l'image.

2. Validations par Fantômes : Des fantômes ont été utilisés pour valider les méthodes EPT par rapport aux mesures VNA, confirmant la précision de ces techniques.

3. Noyau Adaptatif de Savitzky-Golay : Un noyau adaptatif (de SG et pour l’intégrale de surface) a été proposé pour améliorer les reconstructions, réduisant les effets de bruit et les artefacts de bord.

4. Étude des Changements de Conductivité In Vivo : Des corrélations ont été trouvées entre la conductivité et des facteurs tels que l'âge, la fraction de graisse et le sexe, cruciales pour une modélisation précise du DAS.

Travaux Futurs

Les directions futures pour le développement et la recherche en tomographie des propriétés électriques (EPT) incluent :

1. Shim de Phase RF : Améliorer la reconstruction de la permittivité en utilisant le shim de phase RF pour minimiser la variation de phase tout en évitant les zones sans signal et les déviations significatives.

2. Cartographie de la Densité de Protons : Éviter les erreurs de reconstruction en utilisant la cartographie quantitative de la densité de protons, ce qui permettra une estimation plus précise du DAS local.

3. Stratégie de Régularisation dans l'EPT Basée sur la Divergence : Stabiliser la solution des problèmes mal posés en ajoutant des termes de régularisation comme la diffusion ou la variation totale des EPs.

4. EPT Basée sur les Réseaux de Neurones Informés par la Physique (PINNs) : Utiliser les PINNs pour une reconstruction rapide et robuste des EPs, validée en simulation et sur fantômes.

5. Sélection Automatisée des Paramètres de Régularisation et de la Taille du Noyau : Automatiser la sélection des paramètres de régularisation et de la taille du noyau de filtrage pour améliorer la précision et réduire la subjectivité des reconstructions.

6. Études sur des Populations Plus Larges : Valider les résultats et explorer la variabilité des EPs dans des groupes plus larges pour établir une base de données in vivo et développer des modèles de DAS plus précis.

Table of Contents

List of Abbreviations

bSSFP	Balanced Steady-State Free Precession
cr-EPT	convection-reaction EPT
CSI-EPT	Contrast-Source-Inversion-Electrical Properties Tomography
DAM	Double Angle Method
ECG	Electrocardiography
EEG	Electroencephalography
EIT	Electrical Impedance Tomography
EM	Electromagnetic
EPs	Electrical Properties
EPT	Electrical Properties Tomography
FA	Flip Angle
FFT	Fast Fourier Transform
FID	Free Induction Decay
FOV	Field of View
FSE/TSE	Fast Spin Echo/ Turbo Spin Echo
GIB	Generalized-Image-based
GRE	Gradient Echo
IB	Image-based
MAE	Mean Absolute Error
MEG	Magnetoencephalography
MIT	Magnetic Induction Tomography
MR	Magnetic Resonance
MREIT	Magnetic Resonance Electrical Impedance Tomography
MR-EPT	Magnetic Resonance- Electrical Properties Tomography

MRI	Magnetic Resonance Imaging
NEX	Number of Excitation
NRMSE	Normalized Root Mean Square Error
PB	Phase-based
PB-cr	Phase-based-convection-reaction
QSM	Quantitative Susceptibility Mapping
RC	Resistor Capacitor
RF	Radio Frequency
RMSE	Root Mean Square Error
ROI	Region of Interest
rTMS	repetitive Transcranial Magnetic Stimulation
SAR	Specific Absorption Rate
SD	Standard Deviation
SE	Spin Echo
SENSE	SENSitivity Encoding
SNR	Signal-to-Noise-Ratio
SS	Sum of Squares
TE	Echo Time
TPA	Transceive Phase Assumption
TR	Repetition Time
TV	Total Variation
UTE	Ultra-short Echo Time
VIBE	Volumetric interpolated breath-hold examination
VNA	Vector Network Analyzer
ZTE	Zero Echo Time

List of Figures

List of Tables

General Introduction

Motivation

Magnetic Resonance Electrical Properties Tomography (MR-EPT) is a novel non-invasive imaging technology that provides quantitative spatial distribution of tissue electrical properties (EPs) at Larmor frequency. EPs, including electrical conductivity and permittivity, define the pathways through which current flows in the body in response to an electromagnetic (EM) field. These properties are influenced by tissue composition, internal structure, aging, and factors like water content, ion concentration, and the medium in which they reside (intra- or extracellular). EPs vary significantly across different tissues and pathological conditions, making them potential biomarkers for clinical applications such as cancer diagnosis, therapy monitoring, and fundamental etiology research. Additionally, understanding EPs allows for the calculation of EM field distribution within the body, which is crucial for assessing personalized specific absorption rate (SAR) in MRI systems to ensure radiofrequency (RF) safety.

In recent years, numerous EPT reconstruction methods have been developed, with most relying on Maxwell's equations as the foundational principles. Among them, differential methods are the most prevalent because of their simplicity, ease of implementation, and computational efficiency. They are based on the Helmholtz equation with different B_1^+ data requirements.

However, as EPT is a relatively new field, significant variability exists between the reconstructed EPs produced by different methods, particularly for in vivo results. Evaluating the performance and reliability of these methods is essential for advancing their clinical applications and ensuring accurate and consistent measurements.

The primary objective of this thesis is to evaluate and optimize EPT methods to establish a reliable protocol for estimating in vivo electrical properties (EPs) in various organs. This involves comparing the in vivo EPs of adult populations with reference ex vivo values and identifying trends related to individual characteristics such as age, sex, and fat fraction. By achieving these goals, this research aims to contribute significantly to the accuracy of Specific Absorption Rate (SAR) modeling, which is crucial for ensuring patient safety in high-field MRI environments.

Organization of the Thesis

This thesis is structured as follows:

- **Chapter 1:** Introduction to tissue electrical properties, their applications, and measurement methods, providing a background on MR-EPT.
- **Chapter 2:** A comparative review of the main MR-EPT techniques, discussing their advantages and limitations.

- **Chapter 3:** Details on EPT data acquisition using different MR sequences and the comparative results between the Ultrashort Echo Time (UTE) and phase-cycled balanced Steady-State Free Precession (bSSFP) methods.
- **Chapter 4:** Evaluation of electrical conductivity in phantoms compared to ground truth measurements by a Vector Network Analyzer (VNA).
- **Chapter 5:** Assessment of electrical permittivity in phantoms using similar comparison techniques.
- **Chapter 6:** Development and application of an adaptive Savitzky-Golay and surface integral kernel in EPT for improved reconstruction accuracy.
- **Chapter 7:** An in vivo study exploring age-/fat fraction-/sex-related changes in electrical conductivity.
- **Chapter 8:** Application of EPT findings to local SAR calculation, emphasizing the importance of accurate in vivo EP measurements for patient safety.
- **Chapter 9:** Conclusion summarizing the key findings and suggesting future research directions.

List of Publications

Research Articles:

1. **He Z**, Soullié P, Lefebvre PM, Ambarki K, Felblinger J, Odille F. Changes of in vivo electrical conductivity in the brain and torso related to age, fat fraction and sex using MRI. *Sci Rep* **14**, 16109 (2024). https://doi.org/10.1038/s41598-024-67014-9

2. **He Z,** Lefebvre PM, Soullié P, Doguet M, Ambarki K, Chen B, Odille F. Phantom evaluation of electrical conductivity mapping by MRI: Comparison to vector network analyzer measurements and spatial resolution assessment. *Magn Reson Med.* 2024; 1-17. doi: 10.1002/mrm.30009

Conference Proceedings:

1. Paillart G, **He Z**, Soullié P, Romero G, Ferry P, Felblinger J, Odille F. Radiofrequency safety modeling in Magnetic Resonance Imaging (MRI): an experimental study of the impact of electrical properties. In: *Proceedings of European Society for Magnetic Resonance in Medicine and Biology (ESMRMB) 2024 Annual scientific meeting*. Barcelona, Spain; 2024 :397. (Poster)

2. **He Z**, Soullié P, Ambarki K, Lefebvre PM, Odille F. Age-related changes of electrical conductivity in adults: preliminary results with MR-EPT. In: *Proceedings of 32nd Annual Meeting of International Society of Magnetic Resonance in Medicine (ISMRM)*. Singapore; 2024:3686. (Digital Poster)

3. Hattat R, Zambrano M, **He Z**, Bozec E, Ngremmadji MA, Beaumont M, Morel O, Grandjean GA, Chen B. Development of a cross-modality tissue-mimicking and anatomic mimicking Fetal Phantom to improve image based fetus assessment. In: *Proceedings of 32nd Annual Meeting of International Society of Magnetic Resonance in Medicine (ISMRM)*. Singapore; 2024:0816. (Power Pitch)

4. **He Z**, Chen B, Lefebvre PM, Odille F. An Adaptative Savitzky-Golay Kernel for Laplacian Estimation in Magnetic Resonance Electrical Property Tomography. In: 2023 45th Annual International Conference of the IEEE Engineering in Medicine & Biology Society (EMBC). Sydney, Australia; 2023:1-4. doi:10.1109/EMBC40787.2023.10341200. (Full Contributed Paper + Poster)

5. **He Z**, Loureiro de Sousa P, Ambarki K, Lefebvre PM, Odille F. Phantom validation of MR-EPT: comparison to vector network analyzer and resolution assessment. In: *Proceedings of 2022 Joint Workshop on MR phase, magnetic susceptibility and electrical properties mapping (QMR Lucca).* Lucca, Italy; 2022:S04.OR08_EPT.015. (Oral)

6. **He Z**, Doguet M, Soullié P, Loureiro de Sousa P, Lefebvre P, Odille F. Comparison and validation of multiple MR-EPT methods with ground truth vector network analyzer measurements. In: *Proceedings of 30th Annual Meeting of International Society of Magnetic Resonance in Medicine (ISMRM*). London, UK; 2022:2910. (Digital Poster)

7. **He Z**, Barrau N, Barakat CP, Maître X. Lung segmentation with deep learning for 3D MR spirometry. In: *Proceedings of 30th Annual Meeting of International Society of Magnetic Resonance in Medicine (ISMRM*). London, UK; 2022:2223. (Digital Poster)

8. Barrau N, Barakat PC, **He Z**, Emre T, Nemeth A, Afkir A, Cai W, Brulon V, Boucneau T, Fernandez B, Besson F, Lebon V, Maître X. 3D MR spirometry sensitivity to gravity lung dependence in healthy volunteers. In: *Proceedings of 30th Annual Meeting of International Society of Magnetic Resonance in Medicine (ISMRM)*. London, UK; 2022:2064. (Digital Poster)

Chapter 1. Background

1.1. Tissue Electrical Properties (EPs)

Electrical properties (EPs), also known as dielectric properties, comprise conductivity (σ) and permittivity (ε) and are inherent characteristics of tissues. Most materials, including biological tissues, manifest a combination of free electrical charges and bounded charges which behave like orientable dipoles [1]. When subjected to an external electric field, charged particle such as ions move within the medium. Conductivity indicates the capacity for this charge migration. At the same time, electric dipoles, consisting of pairs of two equal and opposite charges, realign themselves in response to the field (with positive and negative charges shifting in the same or opposite direction of the field), a phenomenon termed polarization. This polarization generates an internal electric field, which acts as a counteracting mechanism against the external electric field. Permittivity indicates the capacity for this dipole realignment or for charge/energy storage from the external electric field. Consequently, the electric field experiences attenuation within the material, due to these EPs. This attenuation highlights the effect of EPs on the behavior of electric fields in tissues, with wide-ranging implications for diverse biomedical applications, including medical diagnostics, radio-frequency (RF) hyperthermia and safety.

1.1.1. Biological Tissue Equivalent Circuit Model

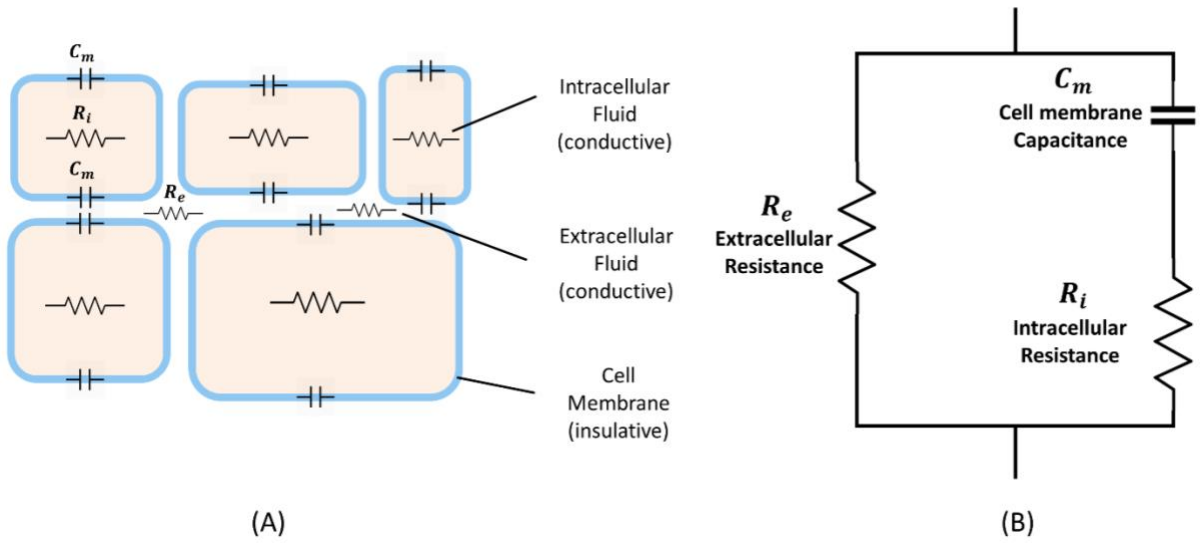

Figure 1. (A) Biological tissue composition. (B) Tissue equivalent circuit model.

As depicted in Figure 1A, tissues consist of both conducting electrolytes (intra/extracellular fluid), which contribute to resistance, and insulating cell membranes, serving as capacitance [1]. While conductivity varies with the volumes of intracellular and extracellular fluids, along with their ionic concentrations and mobilities [2], permittivity is largely influenced by the cell membrane extent in the

tissue [2]. Therefore, a biological tissue can be analogously represented as an equivalent three-element Resistor Capacitor (RC) circuit [3], as shown in Figure 1B. This model illustrates a parallel combination of an extracellular resistance (R_e) and an intracellular resistance (R_i) with a cell membrane electrical capacitance (C_m). This equivalent circuit can represent both a cell and a tissue, with their respective equivalent R_e, R_i and C_m.

The tissue impedance (Z) under the influence of a time-harmonic electric field at an angular frequency ω, can therefore be represented as:

$$Z = \left(\frac{1}{R_e} + \frac{1}{R_i + \frac{1}{i\omega C_m}}\right)^{-1} = \left(\frac{1 + i\omega C_m(R_i + R_e)}{R_e(1 + i\omega C_m R_i)}\right)^{-1}$$
$$= \left(\frac{1 + \omega^2 C_m^2 R_i(R_i + R_e)}{R_e\left(1 + \omega^2 C_m^2 R_i^2\right)} + i\omega\frac{C_m}{1 + \omega^2 C_m^2 R_i^2}\right)^{-1}. \quad (1.1)$$

The tissue EPs can be expressed as the admittivity $\kappa = \sigma + i\omega\varepsilon_0\varepsilon_r$, where σ is conductivity, ε_0 is vacuum permittivity and ε_r is relative permittivity. Assuming that the tissue is a cylinder with a uniform surface area S and length L, and that its EPs are isotropic, we can establish the following equation to relate the tissue impedance Z with EPs:

$$Z = \frac{1}{\kappa}\frac{L}{S} = \frac{1}{\sigma + i\omega\varepsilon_0\varepsilon_r}\frac{L}{S} = \left(\frac{S}{L}(\sigma + i\omega\varepsilon_0\varepsilon_r)\right)^{-1}. \quad (1.2)$$

If $\sigma \gg \omega\varepsilon_0\varepsilon_r$, which is typically the case at low frequencies, then $Z \approx \frac{L}{\sigma S} = R$ and the material is resistive. Conversely, if $\sigma \ll \omega\varepsilon_0\varepsilon_r$, which is typically the case at high frequencies or when σ is small, then $Z \approx \frac{1}{i\omega\varepsilon_0\varepsilon_r\varepsilon}\frac{L}{S} = \frac{1}{i\omega C}$ and the material is capacitive. Most biological tissues exhibit mainly resistive behavior at low frequencies, typically below 10 kHz, where the permittivity term is not significant. However, beyond 10 kHz, the permittivity term becomes non-negligible [4].

Conductivity σ and relative permittivity ε_r can be determined from the real part and imaginary part of Eq.(1.1), respectively:

$$\sigma = \frac{1 + \omega^2 C_m^2 R_i(R_i + R_e)}{R_e\left(1 + \omega^2 C_m^2 R_i^2\right)}\frac{L}{S} \quad (1.3)$$

and

$$\varepsilon_r = \frac{C_m}{1 + \omega^2 C_m^2 {R_i}^2}\frac{L}{\varepsilon_0 S}. \quad (1.4)$$

Both conductivity σ and relative permittivity ε_r depend on the angular frequency ω. The EPs, i.e., admittivity κ, can be specified as a function of frequency:

$$\kappa(\omega) = \sigma(\omega) + i\omega\varepsilon_0\varepsilon_r(\omega). \tag{1.5}$$

1.1.2. Frequency-dependence

From Eq.(1.3), Eq.(1.4) and Eq.(1.5), it is evident that tissue EPs exhibit frequency-dependent behavior, often termed "dispersion", which primarily arises from the characteristics of insulating cell membranes. As frequency increases, conductivity also increases (as the numerator term $\omega^2 C_m^2 R_i(R_i + R_e)$ surpasses the denominator term $\omega^2 C_m^2 R_i^2$ in Eq.(1.3)), but permittivity decreases (as the denominator term $\omega^2 C_m^2 {R_i}^2$ increases in Eq.(1.4)).

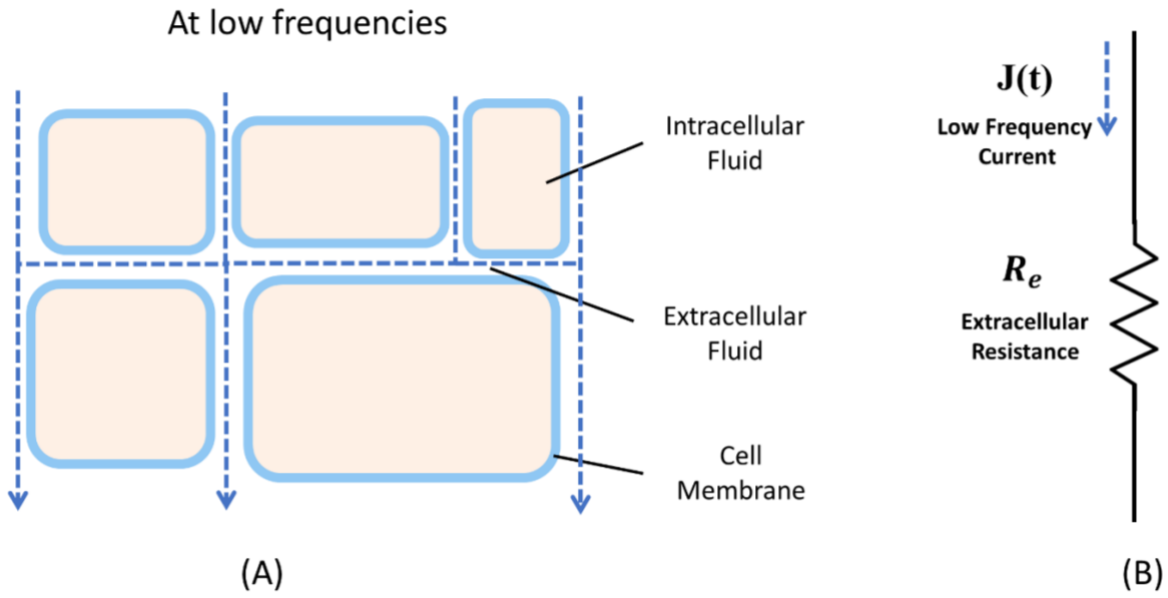

Figure 2. (A) Flow of current at low frequencies. (B) Equivalent circuit at low frequencies.

Low Frequency

At low frequencies (< 10 kHZ), the dipoles in the cell membrane can effectively follow the applied electric field, generating an internal field to counteract it. Since the cell membrane acts as a barrier hindering charge displacement, the current primarily flows through the extracellular fluid (as shown in Figure 2A). Consequently, the equivalent circuit simplifies to include only R_e (as shown in Figure 2B), leading to relatively low conductivity ($\sigma \approx \frac{1}{R_e}\frac{L}{S} \propto \frac{1}{R_e}$) and high permittivity ($\varepsilon_r \approx C_m \frac{L}{\varepsilon_0 S} \propto C_m$).

The conductivity measured in different directions within the same tissue may vary due to changes in the current trajectory, which depends on the distribution and architecture of insulating cell membranes. This phenomenon, referred to as "Electrical Anisotropy", is most pronounced at low frequencies [5]. Therefore, EPs at low frequencies inherently provide insights into the microstructure of the tissue. This

tissue microstructure, reflected in the density and shape of cells and the contents of extra-cellular matrix, affects ionic mobility, thereby influencing conductivity values.

High Frequency

Conversely, at high frequencies (>50 MHz), the dipoles in the cell membrane cannot keep pace with the rapidly changing electric field. In this scenario, the capacitance C_m behaves like a conductor, facilitating current flow through the cell membrane and intracellular fluid, as shown in Figure 3A. The model transitions into a parallel circuit of R_e and R_i, as shown in Figure 3B, where the total resistance is smaller than R_e alone. Consequently, there is an increase in conductivity ($\sigma \approx \frac{\omega^2 C_m^2 R_i (R_i+R_e)}{\omega^2 C_m^2 R_i^2 R_e}\frac{L}{S} = \frac{R_e+R_i}{R_e R_i}\frac{L}{S} \propto \frac{R_e+R_i}{R_e R_i} = \frac{1}{R_i}+\frac{1}{R_e} > \frac{1}{R_e}$) and a decrease in permittivity ($\varepsilon_r \approx \frac{C_m}{1+\omega^2 C_m^2 R_i^2}\frac{L}{\varepsilon_0 S} \propto \frac{C_m}{1+\omega^2 C_m^2 R_i^2} < C_m$) at high frequencies. As frequencies rise, charge trapping effects in cell membranes become less significant. The conductivity at high frequencies reflects total tissue ionic concentration, including both the extra- and intra-cellular spaces.

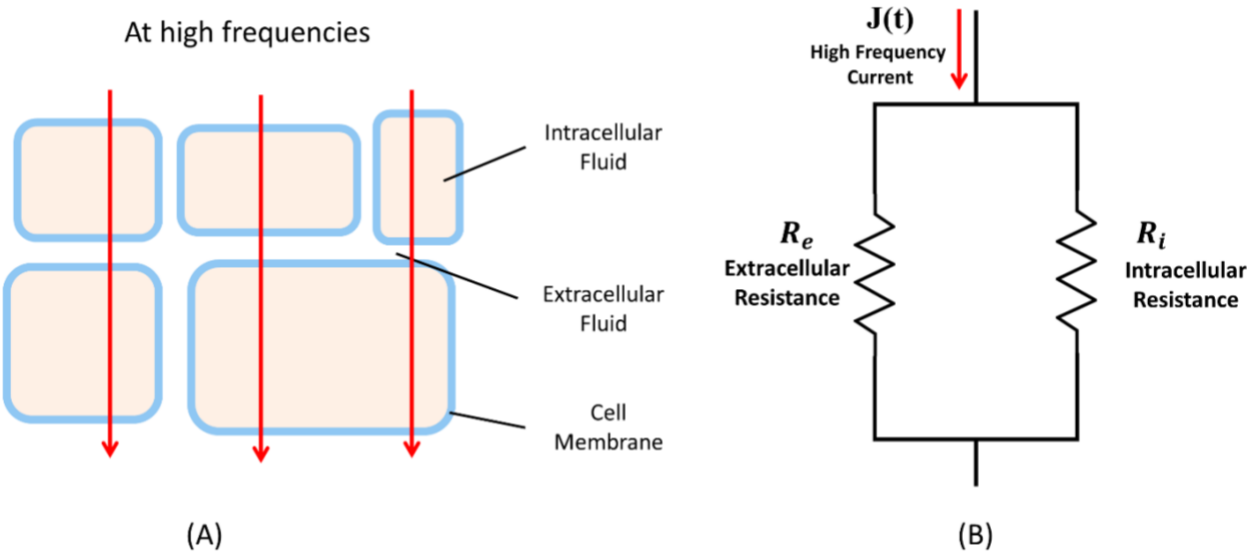

Figure 3. (A) Flow of current at high frequencies. (B) Equivalent circuit at high frequencies.

High Frequency to Low Frequency

Due to the high-frequency current trajectory comprising both extra- and intra-cellular spaces, it is possible to convert high-frequency conductivity σ_{HF} to low-frequency conductivity σ_{LF}, where the current flows only in the extra-cellular space. This technique, which uses water diffusion coefficient to make this conversion, is called Conductivity Tensor Imaging (CTI) [6], [7].

Assuming an isotropic tissue, the high-frequency conductivity σ_{HF} (i.e., total tissue conductivity) of a macroscopic voxel can be expressed as a sum of low-frequency conductivity σ_{LF} and intra-cellular space conductivity σ_i:

$$\sigma_{HF} = \sigma_e + \sigma_i = \sigma_{LF} + \sigma_i \tag{1.6}$$

where $\sigma_e = \sigma_{LF}$ is the extra-cellular space conductivity. Furthermore, σ_{LF} and σ_i can be linked with the volume fraction of extracellular space χ, ion concentration, and mobility:

$$\sigma_{LF} = \chi \bar{c}_e m_e \tag{1.7}$$

$$\sigma_i = (1-\chi)\bar{c}_e m_e \tag{1.8}$$

$$\sigma_{HF} = \chi \bar{c}_e m_e + (1-\chi)\bar{c}_i m_i \tag{1.9}$$

where $\bar{c}_e$ and $\bar{c}_i$ are the ion concentrations in the extra- and intra-cellular spaces, m_e and m_i are the ionic mobilities in the extra- and intra-cellular spaces, respectively. Considering that ions and water molecules exist in the same microscopic environment, the ion mobility is proportional to water diffusion coefficient:

$$m_e = K d_e^w \text{ and } m_i = K d_i^w, \tag{1.10}$$

where K is a constant, and d_e^w and d_i^w are the extra- and intra-cellular water diffusion coefficients. The unknown $\bar{c}_e$ and $\bar{c}_i$ can be further linked with the ion concentration ratio of intra- and extra-cellular spaces β, which is estimated to be about 0.41 in human brain:

$$\bar{c}_i = \beta \bar{c}_e. \tag{1.11}$$

Substituting Eq.(1.10) and Eq.(1.11) into Eq.(1.9), $\bar{c}_e$ can be expressed as:

$$\bar{c}_e = \frac{1}{K} \frac{\sigma_{HF}}{\chi d_e^w + (1-\chi) d_i^w \beta}. \tag{1.12}$$

σ_{LF} can therefore be obtained using Eq.(1.7):

$$\sigma_{LF} = \chi \bar{c}_e m_e = \chi \frac{1}{K} \frac{\sigma_{HF}}{\chi d_e^w + (1-\chi) d_i^w \beta} K d_e^w = \frac{\chi \sigma_{HF}}{\chi d_e^w + (1-\chi) d_i^w \beta} d_e^w. \tag{1.13}$$

For an anisotropic tissue, σ_{LF} can be expressed as a tensor **C**, replacing water diffusion coefficients with tensors **D**:

$$\boldsymbol{C} = \frac{\chi \sigma_{HF}}{\chi \boldsymbol{D}_e^w + (1-\chi) \boldsymbol{D}_i^w \beta} \boldsymbol{D}_e^w. \tag{1.14}$$

σ_{LF} and σ_{HF} can reflect the total and extracellular water contents, ion concentrations and mobilities (fluid viscosity), respectively. Conversely, the difference between them indicates the intracellular information [7].

1.1.3. Applications

The heterogeneous nature of tissue, primarily caused by insulating cell membranes, leads to different current trajectories at low and high frequencies. Consequently, low frequencies (< 100 kHz) enable the detection of both tissue composition and microstructure. However, at high frequencies, where thin cell membranes become transparent, some microstructural information such as cell swelling, vessel walls and nerve fibers becomes undetectable [8], [9].

Tissue composition can be detected at both low and high frequencies. The detailed composition of tissues involves ion concentration and mobility (e.g., Na^+, K^+, Cl^-, Mg^{2+}) and water content (e.g., amounts of intra- and extra-cellular fluids). These properties exhibit dynamic changes with aging [10], [11] and across various pathological conditions [12]. Additionally, as shown in Eq.(1.7) and Eq.(1.9), alterations in the proportion between intra- and extra-cellular space χ, especially in fibrotic tissues where the extracellular space predominates, might impact EPs. Research [13], [14] has demonstrated that the EPs of cancerous tissues exhibit significantly higher values compared to normal tissue. This observed increase in conductivity and permittivity (capacitance) within tumors is attributed to elevated water content and sodium content, a consequence of vascularization. Consequently, the EPs could be used as new biomarkers for cancer detection [15], [16], [17] and play a pivotal role in calculating the optimal thermal doses of RF hyperthermia therapy for cancer treatment [18], [19].

In addition, the understanding of EPs at varying frequencies holds significant implications in medical applications. At low frequencies, EPs provide crucial insights for dose studies (intensity of the applied EM field) in repetitive transcranial magnetic stimulation (rTMS) [20], which is a therapeutic modality employed in treating neurological conditions such as chronic pain, depression, and epilepsy. Furthermore, the high-resolution spatial distribution of low-frequency EPs are required for source localization in EEG/MEG source imaging for the brain [21], or in ECG imaging for the heart [22], aiming to pinpoint the internal electrical activities generated by nerves or muscle. Conversely, at high frequencies, EPs play a key role in calculating the personalized specific absorption rate (SAR) [23], crucial for RF safety in wireless devices (mobile phone, Bluetooth, etc.), high-field MRI environments and implantable devices. In conclusion, this highlights the multifaceted importance of EPs in understanding electromagnetic (EM) field distribution and estimating EM energy within the body across various fields such as medical imaging, diagnostics, and therapy.

1.2. How to Measure Tissue EPs

The key idea is to observe how current flows through tissue under the influence of EPs. In this way, measuring the electrical properties (EPs) of tissues could be linked to measuring the impedance ($Z \propto \frac{1}{\kappa} = \frac{1}{\sigma + i\omega\varepsilon_0\varepsilon_r}$) of an electric RC circuit, as depicted in Figure 1. According to Ohm's law, this requires

knowledge of the current and voltage within a given volume of tissue. In practice, it typically involves introducing a certain type of electromagnetic (EM) energy, such as injected current or induced current, to generate internal current and voltage or electric field within the body, and then measuring the response. However, unlike an electric circuit, installing a voltmeter and an ammeter inside the body for direct measurements of current and voltage is not feasible. Instead, responses are often measured indirectly or externally, such as through complex reflection coefficient with probe and Vector Analyzer Network (VNA), voltage near the skin with surface electrodes, EM signals (e.g., induced magnetic field) with coils, etc... Tissue EPs measurements can be categorized into two main approaches: invasive methods and non-invasive imaging methods. A comparison table outlining these methods is provided in Table 1.

Table 1. Summary of tissue EPs measurement methods.

	Methods	Requirements	Measurements	Advantages	Limitations
Invasive /Contact-based	**VNA** Open-ended coaxial probe connected to a Vector Network Analyzer [24]	• Open-ended coaxial probe • VNA • Calibration	Complex reflection coefficient	• Fast, accurate and reliable • Gold standard	• Invasive • Not suitable for heterogenous tissue • Requires good probe-tissue contact • Limited probe sensing volume
Non-invasive Imaging	**EIT** Electrical Impedance Tomography [25]	• Surface electrodes • Low-frequency current injection (≤1 MHz)	Surface voltage data	• Cost-effective • High temporal resolution	• Current injection (safety concerns) • Poor spatial resolution • ill-posed inverse problem
	MIT Magnetic Induction Tomography [26]	• Excitation and measuring coils	Secondary magnetic field data generated by induced eddy current	• Cost-effective • Contact less • No current injection required	• Low sensitivity • Poor spatial resolution • ill-posed inverse problem

	Methods	Requirements	Measurements	Advantages	Limitations
	MREIT Magnetic Resonance Electrical Impedance Tomography [9]	• MRI • Surface electrodes • Low-frequency current injection (≤1 kHz)	Internal magnetic field $\boldsymbol{B_z}$ data induced by injected current	• High spatial resolution	• Only conductivity • Current injection (safety concerns) • Limited SNR
	MR-EPT Magnetic Resonance-Electrical Properties tomography [27]	• MRI	B_1 field data	• Easy implementation • High spatial resolution • High SNR	• Unmeasurable B_1 component such as $\varphi+/\varphi-$ and B_z • Boundary artifacts • Sensitive to noise

1.2.1. Invasive/Contact-based Method

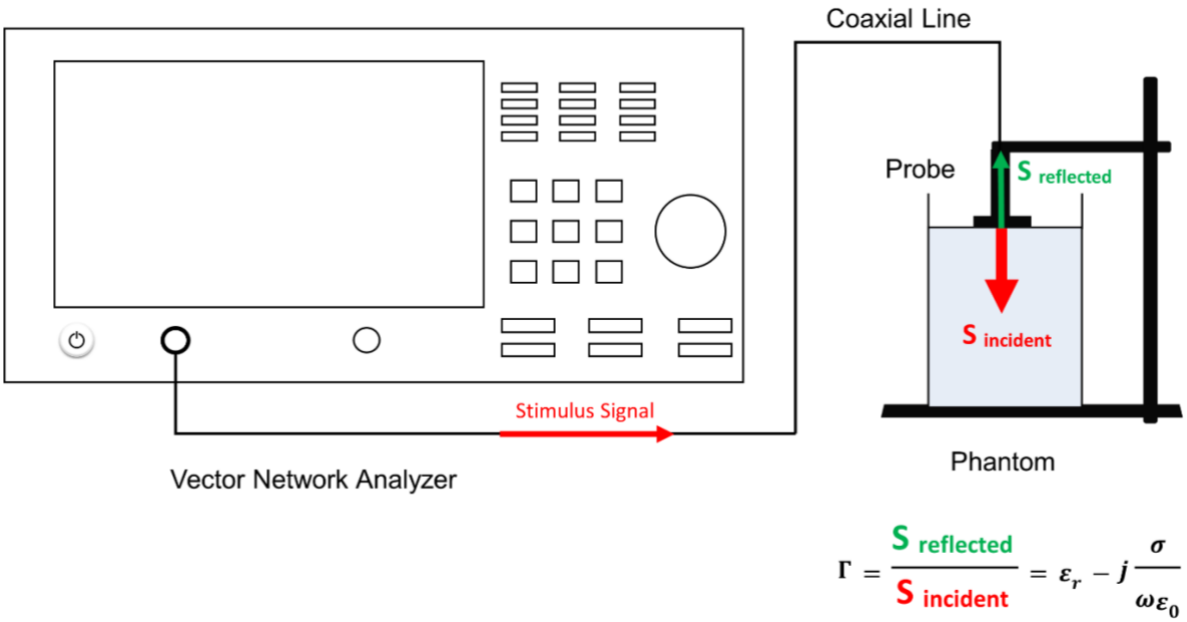

Figure 4. Schematic of Vector network analyzer (VNA) measurement of EPs.

Ex-vivo Database of Human Tissue

The necessity for comprehensive data on the electrical properties (EPs) of biological tissues is widely recognized among scientists and researchers investigating the interactions of electromagnetic (EM) field

distribution inside tissue. In the 1990s, C. Gabriel and colleagues addressed this need by measuring ex-vivo EPs values in post-mortem samples [28], [29], [30]. This ex-vivo database of human tissues (in the frequency range from 10 Hz to 100 GHz) is openly available at https://itis.swiss/virtual-population/tissue-properties/database/database-summary/. About the source of samples, human skin and tongue samples were acquired in vivo, while other human tissue samples were obtained between 24 to 48 hours after death [29]. However, details such as age, sex, body mass index (BMI) and health status of the subjects are not provided in the literature. In a subsequent study in 2007, Peyman et al. [10], [11] found significant age-related variation in EPs in pig brains. Additionally, differences between in vivo and ex vivo measurements, including variations in water content, temperature and physiological parameters (such as blood flow in vessels, ischemia, heart rate, respiration rate, etc.), can lead to differences in the measured EPs [24]. Therefore, while the database serves as a valuable reference, it is important to consider individual variability when applying the data to specific scenarios or studies.

VNA Method

Gabriel's method involved utilizing an open-ended coaxial probe connected to an impedance analyzer or a vector network analyzer (VNA) [24], [31], which is regarded as the gold standard for reliable EPs measurements. As shown in Figure 4, incident signals of a wide range of frequencies generated by a VNA, are partially reflected at the tissue-probe tip interface. By measuring and analyzing the complex reflection coefficient (Γ or S_{11}), which represents the ratio of reflected signal to incident signal, the EPs of tissue at different frequencies can be determined (Figure 4). The dataset generated from these measurements has since become invaluable in various applications, including human specific absorption rate (SAR) modeling in EM field exposure studies. However, this method requires invasive operations to access the tissue, such as immersion into a liquid or contact with a flat surface of a semi-solid or solid material. Additionally, the measured EPs values represent a global assessment of a certain volume of material (dependent on the probe sensing volume), assuming homogeneity within the sample under test. This assumption may introduce limitations in accurately characterizing the electrical properties of heterogeneous tissue and therefore influence their aforementioned applications. The principle and procedure of this VNA method will be further detailed in Section 4.2.

1.2.2. Imaging Methods

In response to the growing need for high-resolution electrical properties (EPs) measurements in living tissues, various EPs imaging techniques have been explored. To understand the distribution of EPs, Ohm's law ($\mathbf{J} = \kappa\mathbf{E}$) serves as a fundamental principle, where κ represents the admittivity ($\sigma + i\omega\varepsilon_0\varepsilon_r$), incorporating both conductivity σ in the real part and relative permittivity ε_r in the imaginary part. Therefore, reconstructing the EPs distribution necessitates knowledge of the 3D distribution of both the current density ($\mathbf{J}$) and the electric field ($\mathbf{E}$) within a given volume of tissue. These internal distributions of $\mathbf{J}$ and $\mathbf{E}$ are generated practically through injecting current using surface electrodes or

inducing current using external coils. In cases where direct and non-invasive methods to measure **E** and/or **J** inside the body are unavailable, it is possible to measure the induced internal magnetic flux density **B** by coils or an MRI scanner [9]. Maxwell's equations, including Ampere's and Faraday's laws, can be employed to relate **B** to **E** and/or **J**, allowing for the interchangeability of **E** or **J** with **B**:

$$\mathbf{J} = \kappa\mathbf{E} = (\sigma + i\omega\varepsilon_0\varepsilon_r)\mathbf{E} = \frac{1}{\mu_0}\nabla \times \mathbf{B}, \tag{1.15}$$

$$\nabla \times \mathbf{E} = -i\omega\mathbf{B}, \tag{1.16}$$

where μ_0 is vacuum permeability. This enables the indirect observation of the distribution of EPs inside the body.

For instance, at low frequencies, Electrical Impedance Tomography (EIT) [25] employs surface electrodes attached on the skin to inject a known low-frequency current (≤ 1 MHz) and records the resulting induced voltage at the surface. Typically, a pair of electrodes functions either as a current source to inject a current, or as a voltmeter to measure the boundary voltage difference ($\mathbf{E} = -\nabla u$). Multiple pairs of electrodes are strategically positioned to acquire boundary current-voltage data surrounding the imaging object. However, direct current injection in the body raises safety concerns and can cause discomfort and even burns, limiting routine clinical use. To mitigate this, Magnetic Induction Tomography (MIT) [26] uses induced current in the body by an oscillating magnetic field and detects the resulting magnetic fields outside the object using external coils. However, both EIT and MIT surfer form limited spatial resolution and accuracy due to their intrinsic ill-posed inverse problem. Magnetic Resonance Electrical Impedance Tomography (MREIT) [9], [32] addresses these challenges by using MRI systems to access deep tissue regions and measuring the magnetic flux density induced (**B**) from MR phases images resulting from external injected current (≤1 kHz) after RF pulses in the patient. However, MREIT faces similar issue as EIT, such as discomfort from current injection and dependence of signal-to-noise ratio (SNR) on injected current amplitude, raising safety concerns [32]. In particular, it remains still a challenge to attenuate the injection current to a level suitable for routine clinical practice while maintaining the SNR and spatial resolution for the resulting EPs images.

In practice, at low frequencies (especially ≤ 10 kHz), the permittivity term or displacement current term in Eq.(1.15), i.e., $i\omega\varepsilon_0\varepsilon_r\mathbf{E}$, is often negligible:

$$\mathbf{J} = \sigma\,\mathbf{E} = \frac{1}{\mu_0}\nabla \times \mathbf{B}, \tag{1.17}$$

due to $\sigma\,\mathbf{E} \gg \omega\varepsilon_0\varepsilon_r\mathbf{E}$. This simplification leads to some low-frequency EPs imaging approaches providing only the conductivity distribution, such as MREIT.

1.3. Magnetic Resonance-Electrical Properties tomography (MR-EPT)

Different from the methods mentioned above, Magnetic Resonance - Electrical Properties Tomography (MR-EPT), also known as Electrical Properties Tomography (EPT) [27], is an advanced technique that aimed at reconstructing tissues EPs from measurements of the complex RF field (also referred to as B_1 field) in MRI. This RF field, used for spin excitation, can easily penetrate most biological tissues and is subsequently modulated/distorted by the tissue EPs at the Larmor frequency of an MRI scanner. Unlike MREIT, EPT does not require any electrodes and does not induce additional external energy into the body. Furthermore, EPT has the capability to provide both conductivity and permittivity. This makes MR-EPT a promising method for imaging in vivo tissue EPs.

The idea of extracting EPs from B_1-weighted MR images was first introduced in 1991 by Haacke et al. [33] and first demonstrated in the phantom and in vivo studies in 2003 by Wen [34]. EPT is a field in active development with the potential to offer quantitative physiological biomarker. Its future applications are still under development, including functional EPT (fEPT, measurements of dynamic changes in conductivity after brain stimulation) [35], [36], sodium concentration estimation [37], water content estimation [38], local SAR measurement [39], real-time temperature measurements (EPs $\propto$ temperature), and more. Furthermore, EPT, which provides high-frequency conductivity, is essential in Conductivity Tensor Imaging (CTI) for converting to low-frequency conductivity with directionality. This capability allows EPT to be extended to low-frequency applications.

The upcoming sections will offer a concise overview of the B_1 field in MRI and its application for imaging electrical properties (EPs). Furthermore, the theoretical foundation and the inevitable technical limitations associated with MR-EPT will be discussed.

1.3.1. B_1 Field in MRI Signal

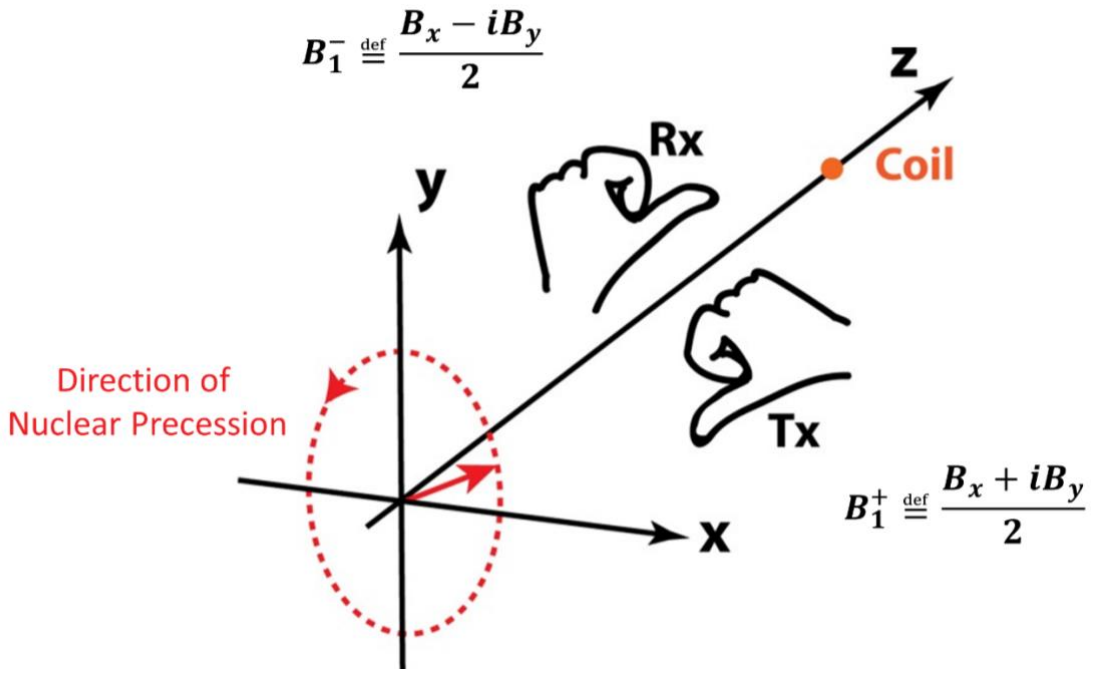

Figure 5. Illustration of the opposite circular polarization of transmit (Tx) and receive (Rx) B1 fields, adapted from Vaidya et al. 2016 [40]. During transmission, the B1 field propagates from the coil (orange) to the spin (red), with fingers curling in the direction of nuclear precession, indicated by the thumb of the right hand. This transmit field, denoted as B_1^+, is defined as the positive (counterclockwise) circularly polarized component of the B_1 fields. Conversely, during reception, the B1 field propagates from the spin to the coil, with fingers curling in the same direction of nuclear precession, as indicated by the thumb of the left hand. This receive field, denoted as B_1^-, is therefore the negative (clockwise) circularly polarized component.

In MR-EPT, the current in tissues is induced by the time-harmonic B_1 field of an RF coil. This field can be represented as a vector with three components: $B_1 = \begin{bmatrix} B_x \\ B_y \\ B_z \end{bmatrix}$ parallel to the x, y, and z axes. Since the B_z component, which is parallel to the main magnetic field B_0, does not affect the MRI signal, it cannot be measured. However, in the RF quadrature volume coils, B_z is much smaller than B_x and B_y, making it negligible. Only the transverse B_{xy} field, which rotates at Larmor frequency and is circularly polarized about the z-axis, is useful. Circular polarization can be achieved by quadrature excitation in a body coil, where using two coils produce linearly polarized fields (B_x and B_y) that are physically orthogonal, with one coil excited with a 90-degree phase lag relative to other [40]. As shown in Figure 5, the combined circularly polarized B_1 field can be further decomposed into two oppositely polarized fields, the positive (counterclockwise) circularly polarized transmit field B_1^+ and the negative (clockwise) circularly polarized receive field B_1^- in the rotating frame, as described by Hoult [41]:

$$B_1^+ \overset{\text{def}}{=} \frac{B_x + iB_y}{2} = |B_1^+|e^{j\varphi^+}$$
$$B_1^- \overset{\text{def}}{=} \frac{B_x - iB_y}{2} = |B_1^-|e^{j\varphi^-}, \tag{1.18}$$

where $\left|B_1^{\pm}\right|$ and $\varphi^{\pm}$ are the amplitude and phase of $B_1^{\pm}$ field, respectively. In this way, if we use the same coil for transmission and reception, the B_1 can be consisted of transmission field B_1^+, reception field B_1^- and B_z component:

$$\mathrm{B}_1 = \begin{bmatrix} B_x \\ B_y \\ B_z \end{bmatrix} = \begin{bmatrix} \frac{B_x + iB_y}{2} + \frac{B_x - iB_y}{2} \\ -i\frac{B_x + iB_y}{2} + i\frac{B_x - iB_y}{2} \\ B_z \end{bmatrix} = \begin{bmatrix} B_1^+ + B_1^- \\ -iB_1^+ + iB_1^- \\ B_z \end{bmatrix} = \begin{bmatrix} B_1^+ + B_1^- \\ -i(B_1^+ - B_1^-) \\ B_z \end{bmatrix} \tag{1.19}$$

The B_1^+ field rotates the same sense of the nuclear precession and thus it can be used in MRI to flip the spin magnetization (M_0) from the z-axis to the transverse xy-plane. The resulting transverse magnetization M_{xy} can be expressed as:

$$M_{xy} = M_0 \sin(\alpha)\, e^{i\varphi^+}, \tag{1.20}$$

where α is the flip angle, which is proportional to the gyromagnetic ratio γ, the amplitude of B_1^+ and the RF pulse duration or flip time τ in hard RF pulses:

$$\alpha = \gamma\tau|B_1^+|. \tag{1.21}$$

Substituting the expression of α into Eq.(1.20), we get:

$$M_{xy} = M_0 \sin(\gamma\tau|B_1^+|)\, e^{i\varphi^+}. \tag{1.22}$$

The B_1^+ field is typically excited by the body coil. Once the B_1^+ field is turned off, the spins begin to return to their equilibrium position along B_0. During this relaxation process, changes in the transverse magnetization (M_{xy}) induce an RF signal in the receive coils, which are placed parallel to B_0. This signal is proportional to the reception field B_1^-, which characterizes the receive coil sensitivity. As such, ignoring T1 and T2 relaxation effects and using RF reciprocity principle, the detected MRI signal can be represented with B_1^+ and B_1^- as [27], [41]:

$$S \approx M_{xy}B_1^- = M_0 \sin(\gamma\tau|B_1^+|)\, e^{i\varphi^+}B_1^- \tag{1.23}$$

Furthermore, since M_0 is directly proportional to the proton density ρ_0, we can obtain:

$$S \propto \rho_0 \sin(\gamma\tau|B_1^+|)\, e^{i\varphi^+}B_1^-. \tag{1.24}$$

When the flip angle is close to 0 ($\sin(\alpha) \approx \alpha$), such as in Ultrashort Echo Time (UTE) or Zero Echo Time (ZTE) sequence, Eq.(1.24) can be further simplified as:

$$S \propto \rho_0 \gamma \tau |B_1^+| e^{j\varphi^+} B_1^- = \rho_0 \gamma \tau B_1^+ B_1^-. \quad (1.25)$$

As such, the received signal for small flip angles (< 10°) is proportional to $B_1^+ B_1^-$.

1.3.2. EPT Central Equation

Since the inverse problem of Electrical Properties Tomography (EPT) is to obtain the admittivity ($\kappa = \sigma + i\omega\varepsilon_0\varepsilon_r$) from the measured magnetic field data **B**, typically used in connection with the $\mathbf{B_1}$ field, we require an equation that directly relates **B** and κ without involving the electrical field (**E**). To achieve this, we can express **E** using in terms of **B** using Ampere-Maxwell's law Eq.(1.15) :

$$\mathbf{E} = \frac{1}{\mu_0 \kappa} \nabla \times \mathbf{B}, \quad (1.26)$$

where μ_0 is vacuum permeability. By substituting this expression into Faraday's law (Eq.(1.16)), we obtain:

$$\nabla \times \mathbf{E} = \nabla \times \left(\frac{1}{\mu_0 \kappa} \nabla \times \mathbf{B}\right) = -i\omega \mathbf{B}$$

$$\frac{1}{\mu_0} \nabla \times \left(\frac{1}{\kappa} \nabla \times \mathbf{B}\right) = -i\omega \mathbf{B}$$

$$\nabla \frac{1}{\kappa} \times \nabla \times \mathbf{B} + \frac{1}{\kappa} (\nabla \times \nabla \times \mathbf{B}) = -i\omega\mu_0 \mathbf{B}$$

$$-\frac{\nabla \kappa}{\kappa} \times \nabla \times \mathbf{B} + \nabla \times \nabla \times \mathbf{B} = -i\omega\mu_0 \kappa \mathbf{B}. \quad (1.27)$$

Given that $\nabla \times \nabla \times \mathbf{B} = \nabla(\nabla \cdot \mathbf{B}) - \nabla^2 \mathbf{B}$ and the Gauss's law ($\nabla \cdot \mathbf{B} = 0$), Eq.(1.27) simplifies to:

$$\nabla^2 \mathbf{B} + \frac{\nabla \kappa}{\kappa} \times \nabla \times \mathbf{B} = i\omega\mu_0 \kappa \mathbf{B}. \quad (1.28)$$

This equation represents the central framework of EPT, also referred to as the Generalized Helmholtz equation, and it serves as the foundation for all EPT methods.

1.3.3. Limitations

The EPT poses two main inherent challenges for practical applications: one is the unmeasurable B_1 components (such as φ^+/φ^- and B_z) in MRI, the other is the complexity of the gradient term ($\frac{\nabla \kappa}{\kappa} \times \nabla \times \mathbf{B}$) in the governing equation (1.28).

Concerning $\mathbf{B_1}$ measurement, the B_z component, aligned with the B_0 direction, cannot be directly measured in MRI. However, the transverse components B_x and B_y, which influence the MRI signal, can be derived from the transmit field B_1^+ or receive field B_1^-. Extracting the precise values of B_1^+ or B_1^- from MRI images remains challenging. Currently, only the magnitude of the transmit field $|B_1^+|$ is measurable based on its relationship with the flip angle, typically using methods involving several MR

scans, known as "$|B_1^+|$ mapping" technique. Moreover, absolute transmit phase φ^+ or receive phase φ^- cannot be measured directly either. Only the combination of these two phases, referred to as the transceive phase ($\varphi_{TR} = \varphi^+ + \varphi^-$), can be measured using specific sequences. As such, a common practice in EPT is to use half of the transceive phase ($\varphi^+ = \varphi^- = \frac{\varphi_{TR}}{2}$), known as the "transceive phase assumption" (TPA). This assumption is valid for field strengths up to 3 T and for specific coil setups [42], which impact applications in personalized SAR evaluation of high-field MRI.

Regarding the gradient term, assuming the local homogeneity of EPs ($\nabla\kappa = 0$) allow us to neglect the gradient term. However, this assumption is invalid at tissues boundaries, leading to boundary artifacts. Conversely, including the gradient term increases computational complexity and requires establishing the relationships of EPs between the target voxel and its neighbors to constrain the solution. This necessitates employing certain regularization strategies to improve the reconstructed EPs image quality [23], [27]. As a result, these approaches achieve less noise effect than those without the gradient term. However, implementing these strategies is also challenging and can introduce instability to the solution.

To make EPT applicable in practice, simplifications and improvements are necessary, leading to the development of various EPT methods. Each method entails different levels of assumptions or B_1 data requirements to simplify the central equation for clinical use. Chapter 2 will provide a comprehensive review of these EPT methods, while Chapter 3 will focus on B_1 field data acquisition techniques.

Chapter 2. Review of Methods for MR-EPT

Magnetic Resonance Electrical Properties Tomography (MR-EPT) has been explored in implementation for nearly 20 years, leading to the development of various methods, each with unique approaches and assumptions to simplify the governing equations and improve reconstruction feasibility. These methods have evolved to address different aspects of electrical properties (EPs) reconstruction, leveraging the interaction between radiofrequency (RF) electromagnetic fields B_1 and the EPs of tissues.

According to their mathematical formulations, EPT methods can be categorized into Physical model-based and Non-Physical model-based approaches. Physical model-based EPT approaches rely on the central EPT equation, derived from Maxwell's equations. Non-physical model-based EPT approaches involve water-content-based EPT [38], which relies on models linking EPs with the water content of tissues measured from T1-weighted images, and data-driven deep learning-based EPT [43], which employs end-to-end neural network models to map B_1 field to EPs using the simulated dataset. However, these non-physical methods lack generalization and are typically suitable only for specific organs.

Physical model-based EPT can be further divided into integral form and differential form methods. Integral form methods, such as Contrast Source Inversion (CSI) EPT [44], [45], aim to minimize the difference between measured and simulated B_1 fields based on assumed EPs. This approach avoids differentiation or denoising processes but requires highly accurate electromagnetic simulations and numerous iteration steps, resulting in high computational complexity.

Conversely, differential form EPT methods [27] are relatively faster and easier to implement. The central equation for differential EPT is:

$$\nabla^2\mathbf{B} + \frac{\nabla\kappa}{\kappa} \times \nabla \times \mathbf{B} = i\omega\mu_0\kappa\mathbf{B}, \tag{2.1}$$

where μ_0 is vacuum permeability, ω is the angular Lamor frequency, $\kappa = \sigma + i\omega\varepsilon_0\varepsilon_r$ is admittivity consisted of conductivity σ and relative permittivity ε_r. Depending on whether or not the gradient EP term ($\frac{\nabla\kappa}{\kappa} \times \nabla \times \mathbf{B}$) is retained, differential form approaches can be further divided into Helmholtz-based and Convection Reaction (cr) EPT families. The Helmholtz-based EPT family ignores the gradient of EPs, resulting in easy implementation but at the cost of boundary artifacts, making it less suitable for small structures. The cr-EPT family rewrites Eq.(2.1) in a convection-reaction partial differential equation (cr-PDE) form, keeping the gradient term but assuming $\nabla B_z = 0$ due to its inaccessibility in MRI. This assumption, along with others used for simplifications, may be invalid for the entire imaging object, resulting in an imperfect cr-PDE where terms are only approximately equal. To improve numerical stability, regularization strategies [46], [47], such as adding an artificial diffusion term into cr-PDE or total variation regularization, can be used. However, the regularization coefficient may vary

in space and can even become zero at certain points [48]. As such, the cr-PDEs are generally difficult to solve and are not widely used in clinical practice.

According to the input B_1 field requirements, differential based EPT [27] can be also categorized into standard, relative B_1 based, Phase-only based and Complex-Image-based EPT, which requires absolute B_1 field usually with the TPA (Transceive Phase Assumption) assumption, relative B_1 using multi-channel RF transmission system, transceive phase and low flip angle MR complex image, respectively, along with different assumptions.

Furthermore, the operator of Laplacian amplifies noise, resulting in significant numerical errors in reconstructed EPs maps. A further approach is to convert the Laplacian form equation to a surface integral form using the divergence theorem, reducing the second-order derivatives to first-order derivatives of the measured B_1 data [49].

This review aims to provide a comprehensive overview of the various differential MR-EPT methods and their conversion to surface integral forms, categorized by their B_1 measurement requirements. Table 2 summarizes their underlying mathematical derivations, measurement requirements, validity conditions, advantages and limitations.

Table 2. Summary of differential EPT methods.

Method (Acronym)	Absolute B_1-based		Relative B_1-based	Phase-only-based		Complex-Image-based	
	STANDARD [34]	CONVECTION-REACTION(CR-EPT) [50]	GRADIENT EPT (GEPT) [51]	PHASE-BASED (PB) [52]	PHASE-BASED CONVECTION-REACTION (PB-CR) [46]	IMAGE-BASED (IB) [53]	GENERALIZED IMAGE-BASED (GIB) [54]
Input	Absolute magnitude $\lvert B_1^+\rvert$ and phase $\varphi^+ \approx \varphi_{tr}/2$		Relative field between p,r channels $B_{1pr}^+ = \lvert B_{1p}^+\rvert\, e^{i(\varphi_{pr}^+)}$	Transceive phase φ_{TR}		Low-flip-angle complex image, such as UTE/ZTE, which is proportional to B_1 ($I_{UTE/ZTE} = I_0 B_1^+ B_1^- \approx B^2$).	
Output	Complex admittivity ($\kappa = \sigma + j\omega\varepsilon_0\varepsilon_r$) i.e. conductivity σ and permittivity ε_r			Conductivity σ		Complex admittivity ($\kappa = \sigma + j\omega\varepsilon_0\varepsilon_r$) i.e. conductivity σ and permittivity ε_r	
Governing Equation	$\kappa = \frac{\nabla^2 B_1^+}{i\omega\mu_0 B_1^+}$	$\beta^+ \cdot \nabla(\kappa^{-1}) + \nabla^2 B_1^+ \kappa^{-1} = i\omega\mu_0 B_1^+$	$\beta_p^+ \cdot \nabla(\kappa^{-1}) + \nabla^2 B_{1p}^+ \kappa^{-1} = i\omega\mu_0 B_{1p}^+$ $with\ B_{1p}^+ = B_{1pr}^+ e^{i(\varphi_r^+)}$	$\sigma \approx \frac{\nabla^2 \varphi_{tr}}{2\omega\mu_0}$	$\nabla^2 \varphi_{TR}\sigma^{-1} + \nabla\varphi_{TR} \cdot \nabla(\sigma^{-1}) = 2\mu_0\omega$	$k = \frac{\nabla^2 B}{i\omega\mu_0 B}$	$\frac{\nabla^2 B}{B}k^{-1} + \frac{\nabla B}{B}\cdot\nabla(k^{-1}) = i\mu_0\omega$
Surface-Integral Form	$\kappa = \frac{\oiint \nabla B_1^+ \, dS}{\iiint i\omega\mu_0 B_1^+ \, dV}$	$\oiint \beta^+\kappa^{-1}\cdot\hat{n}\, dS = \iiint i\omega\mu_0 B_1^+ \, dV$	None	$\sigma = \frac{\oiint \nabla\varphi_{tr}\, dS}{\iiint 2\omega\mu_0\, dV}$	$\oiint \nabla\varphi_{tr}\sigma^{-1}\cdot\hat{n}\, dS = \iiint 2\omega\mu_0\, dV$	$\kappa = \frac{\oiint \nabla B\ dS}{\iiint i\omega\mu_0 B\, dV}$	$\oiint \nabla B\kappa^{-1}\cdot\hat{n}\, dS = \iiint i\omega\mu_0 B\, dV$
Required Assumptions	1) $\varphi^+ = \varphi^- = \varphi_{tr}/2$ 2) $\nabla k = 0$	1) $\varphi^+ = \varphi^- = \varphi_{tr}/2$ 2) $(\nabla B_z)_{x,y,z} = 0$	$(\nabla B_z)_{x,y,z} = 0$	1) $\nabla\lvert B_1^{\pm}\rvert = 0$ 2) $\nabla\sigma = 0$ 3) $\sigma \gg \omega\varepsilon$	1) $\nabla\lvert B_1^{\pm}\rvert = 0$ 2) $\frac{(\nabla B_z)_{x,y,z}}{2B_1^{\pm}} = 0$ 3) $\frac{\partial_{y,x}(\varphi^+ - \varphi^-)}{\partial_{x,y}(\varphi_{TR})} = 0$ 4) $\sigma^2 \gg (\omega\varepsilon)^2$	1) $\nabla I_0 = 0$ 2) $\nabla k = 0$ 3) $\frac{1}{4}\nabla ln\frac{B_1^-}{B_1^+}\cdot\nabla ln\frac{B_1^-}{B_1^+} = 0$	1) $\nabla I_0 = 0$ 2) $\frac{1}{4}\nabla \ln\frac{B_1^-}{B_1^+}\cdot\nabla\ln\frac{B_1^-}{B_1^+} = 0$ 3) $\frac{1}{2}\nabla_{x,y} ln\frac{B_1^-}{B_1^+} = 0$ 4) $\frac{(\nabla B_z)_{x,y,z}}{4B_1^{\pm}} = 0$
Conditions of Validity for Assumptions	1) ≤ 3T. Center of birdcage/TEM coil. Symmetric objects and imaging setup.	1) ≤ 3T. Center of birdcage/TEM coil. Symmetric objects and imaging setup.	Center of birdcage/TEM coil, but errors gradually increase as slices move off-center	1) ≤ 3T or RF shimming. 2) Piecewise homogenous conductivity.	1) ≤ 3T or RF shimming. 2) Center of birdcage/TEM coil. Symmetric objects and imaging setup. 3) True for these two coil configurations:	1) Piecewise homogenous "natural contrast" I_0. 2) Piecewise homogenous EPs. 3) Hold in most cases because of an error of	1) Piecewise homogenous "natural contrast" I_0. 2) Hold in most cases because of an error of second-order effect with respect to $B_1^+ - B_1^-$, then

Method (Acronym)	Absolute B_1-based		Relative B_1-based	Phase-only-based		Complex-Image-based	
	STANDARD [34]	CONVECTION-REACTION(CR-EPT) [50]	GRADIENT EPT (GEPT) [51]	PHASE-BASED (PB) [52]	PHASE-BASED CONVECTION-REACTION (PB-CR) [46]	IMAGE-BASED (IB) [53]	GENERALIZED IMAGE-BASED (GIB) [54]
	2) Piecewise homogenous EPs.	2) Center of birdcage/TEM coil, but errors gradually increase as slices move off-center		4) $\leq$ 3T for most human tissues.	transmission form birdcage and reception from birdcage or phased array coil 4) $\leq$ 3T for most human tissues	second-order effect with respect to $B_1^+ - B_1^-$, then less sensitive to the difference between B_1^+ and B_1^-.	less sensitive to the difference between B_1^+ and B_1^-. 3) An error of first-order effect with respect to $B_1^+ - B_1^-$, also ignorable in most cases. 4) Center of birdcage/TEM coil. Symmetric objects and imaging setup.
Advantages	Relative accurate and fast	LHA-free and generalized version of standard EPT	i) TPA-free ii) LHA-free ii) Suitable for high field MRI at 7T or above	i) Fast and easy implementation ii) TPA-free	i) LHA-free and generalized version of PB ii) TPA-free	i) TPA-free ii) Fast and easy implementation iii) A single acquisition for EPs reconstruction	i) TPA-free ii) LHA-free and generalized version of IB iii) A single acquisition for EPs reconstruction
Limitations	a) Long scan time for $\lvert B_1^+ \rvert$ mapping b) TPA requirement c) Boundary artifacts and not suitable for small structure	a) Long scan time for $\lvert B_1^+ \rvert$ mapping b) TPA requirement c) Difficult to solve	a) $\lvert B_1^+ \rvert$ mapping requirement b) Longer scan time for each transmission channel c) Multi-channel RF transmission system	a) About 10% systematic error with phase-only assumption b) Boundary artifacts and not suitable for small structure c) Only conductivity	a) About 10% systematic error with phase-only assumption b) Difficult to solve c) Only conductivity	a) I_0 problem b) Boundary artifacts and not suitable for small structure	a) I_0 problem b) Difficult to solve

2.1. Standard EPT and Limitations

2.1.1. Standard B_1^+-based EPT

The standard EPT (so-called Helmholtz-based EPT [27], [34]), based on the local homogeneity assumption (LHA), assumes that the variation of EPs is low within the ROI ($\nabla\kappa = 0$). Consequently, the central EPT equation (2.1) can be derived as:

$$\nabla^2\mathbf{B} = i\omega\mu_0\kappa\mathbf{B}. \tag{2.2}$$

In each Cartesian component (x, y, z), we have:

$$\nabla^2 B_{x,y,z} = i\omega\mu_0\kappa B_{x,y,z}. \tag{2.3}$$

By combining x- and y-components of Eq.(2.3), we can reformulate them in terms of the transmit B_1 field ($B_1^+ = \frac{B_x+iB_y}{2}$), which can be measured in MRI:

$$\frac{\nabla^2 B_x + i\nabla^2 B_y}{2} = i\omega\mu_0\kappa\frac{B_x + iBy}{2},$$
$$\nabla^2 B_1^+ = i\omega\mu_0\kappa B_1^+. \tag{2.4}$$

Consequently, taking the normalized Laplacian (second-order derivative) of B_1^+, the admittivity κ can be determined voxel by voxel as:

$$\kappa = \frac{\nabla^2 B_1^+}{i\omega\mu_0 B_1^+}. \tag{2.5}$$

We can derive the conductivity σ and relative permittivity ε_r from the real and imaginary parts in Eq.(2.5), respectively:

$$\sigma = Re\left(\frac{\nabla^2 B_1^+}{i\omega\mu_0 B_1^+}\right) \quad \text{and} \quad \varepsilon_r = \frac{1}{\omega\varepsilon_0} Im\left(\frac{\nabla^2 B_1^+}{i\omega\mu_0 B_1^+}\right). \tag{2.6}$$

While this explicit method is prized for its simplicity, ease of implementation, and computational speed, it faces challenges at tissue boundaries due to the local homogeneity assumption (LHA). Moreover, applying the Laplacian operator (∇^2) to the B_1^+ data amplifies noise [55]. To address noise effects, filtered Laplacians with large kernel size (typically larger than [7×7×7]) can be employed, albeit at the expense of significant numerical boundary error propagation [56]. Additionally, this method necessitates knowledge of the complex B_1^+, including both its amplitude $|B_1^+|$ and absolute transmit phase φ^+. Since φ^+ is typically unavailable, the method often relies on the transceive phase assumption (TPA) in practice. However, combining $|B_1^+|$ and φ^+ obtained from different acquisitions in the same phase poses challenges for image registration in moving organs, such as the heart and lungs.

2.1.2. Standard B_1^--based EPT

Similarly, EPs can be obtained from the receive B_1 field ($B_1^- = \frac{B_x - iB_y}{2}$):

$$\kappa = \frac{\nabla^2 B_1^-}{i\omega\mu_0 B_1^-}. \tag{2.7}$$

However, since absolute B_1^- fields cannot be measured in a straightforward way, Eq.(2.5) using B_1^+ is the prevailing approach, representing the standard EPT method. Alternatively, Marques et al. [57] have proposed using the relative receive coil sensitivities B_{1r}^- to replace the unmeasurable B_1^- field in Eq.(2.7). This involves considering the signal ratio between two coils, which cancels out all non-B_1^--related contributions:

$$B_{1r}^- = \frac{S_{coil\ 2}}{S_{coil\ 1}} = \frac{B_{1\ coil\ 2}^-}{B_{1\ coil\ 1}^-}. \tag{2.8}$$

Here, $S_{coil\ 1}$ is considered as the reference coil sensitivity, which can be a single receive coil or a suitable combination of coils. While this method does not require the transceive phase assumption (TPA), it is more sensitive to input image noise compared to the B_1^+ based method. This is mainly because it implicitly uses the third-order derivatives of the coil sensitivity data [57].

2.2. Convection-reaction EPT

2.2.1. Derivation

The standard EPT described above relies on the homogeneous Helmholtz equation, a common approach in many EPT studies. However, this assumption may not hold true for all biological tissues, particularly those with complex structures that exhibit rapid changes in electrical properties (EPs). To address this limitation and maintain the gradient term, convection-reaction EPT (cr-EPT) [50] formulates the central EPT equation in a linear convection-reaction form.

Following the rule of cross product and curl operation ($\nabla \times \mathbf{B} = \begin{bmatrix} \frac{\partial B_z}{\partial y} - \frac{\partial B_y}{\partial z} \\ \frac{\partial B_x}{\partial z} - \frac{\partial B_z}{\partial x} \\ \frac{\partial B_y}{\partial x} - \frac{\partial B_x}{\partial y} \end{bmatrix}$), we can write the x-, y- and z-components of Eq.(2.1) as:

$$\nabla^2 B_x + \frac{1}{\kappa}\frac{\partial \kappa}{\partial y}\left(\frac{\partial B_y}{\partial x} - \frac{\partial B_x}{\partial y}\right) - \frac{1}{\kappa}\frac{\partial \kappa}{\partial z}\left(\frac{\partial B_x}{\partial z} - \frac{\partial B_z}{\partial x}\right) = i\omega\mu_0\kappa B_x$$
$$\nabla^2 B_y + \frac{1}{\kappa}\frac{\partial \kappa}{\partial z}\left(\frac{\partial B_z}{\partial y} - \frac{\partial B_y}{\partial z}\right) - \frac{1}{\kappa}\frac{\partial \kappa}{\partial x}\left(\frac{\partial B_y}{\partial x} - \frac{\partial B_x}{\partial y}\right) = i\omega\mu_0\kappa B_y. \quad (2.9)$$
$$\nabla^2 B_z + \frac{1}{\kappa}\frac{\partial \kappa}{\partial y}\left(\frac{\partial B_z}{\partial y} - \frac{\partial B_y}{\partial z}\right) - \frac{1}{\kappa}\frac{\partial \kappa}{\partial x}\left(\frac{\partial B_x}{\partial z} - \frac{\partial B_z}{\partial x}\right) = i\omega\mu_0\kappa B_z$$

To express in terms of the transmit B_1 field ($B_1^+ = \frac{B_x + iB_y}{2}$), we can multiply the y-component by "i" and add it to the x-component in Eq.(2.9):

$$\nabla^2 B_x + i\nabla^2 B_y - i\frac{1}{\kappa}\frac{\partial \kappa}{\partial x}\left(\frac{\partial B_y}{\partial x} - \frac{\partial B_x}{\partial y}\right) + \frac{1}{\kappa}\frac{\partial \kappa}{\partial y}\left(\frac{\partial B_y}{\partial x} - \frac{\partial B_x}{\partial y}\right) - \frac{1}{\kappa}\frac{\partial \kappa}{\partial z}\left(\frac{\partial B_x - i\partial B_y}{\partial z} - \frac{\partial B_z}{\partial x} - i\frac{\partial B_z}{\partial y}\right)$$
$$= i\omega\mu_0\kappa\left(B_x + iB_y\right).$$

By replacing $B_x + iB_y$ with $2B_1^+$, we obtain:

$$2\nabla^2 B_1^+ - i\frac{1}{\kappa}\frac{\partial \kappa}{\partial x}\left(\frac{\partial B_y}{\partial x} - \frac{\partial B_x}{\partial y}\right) + \frac{1}{\kappa}\frac{\partial \kappa}{\partial y}\left(\frac{\partial B_y}{\partial x} - \frac{\partial B_x}{\partial y}\right) - \frac{1}{\kappa}\frac{\partial \kappa}{\partial z}\left(2\frac{\partial B_1^+}{\partial z} - \frac{\partial B_z}{\partial x} - i\frac{\partial B_z}{\partial y}\right)$$
$$= 2i\omega\mu_0\kappa B_1^+. \quad (2.10)$$

Using the Gauss's law for magnetism ($\nabla \cdot B = \frac{\partial B_x}{\partial x} + \frac{\partial B_y}{\partial y} + \frac{\partial B_z}{\partial z} = 0$), we can modify the $\frac{\partial B_y}{\partial x} - \frac{\partial B_x}{\partial y}$ term as:

$$\frac{\partial B_y}{\partial x} - \frac{\partial B_x}{\partial y} = \frac{\partial B_y}{\partial x} - \frac{\partial B_x}{\partial y} - i\left(\frac{\partial B_x}{\partial x} + \frac{\partial B_y}{\partial y} + \frac{\partial B_z}{\partial z}\right) = -i\left(\frac{\partial B_x - i\partial B_y}{\partial x} - i\frac{\partial B_x - i\partial B_y}{\partial y} + \frac{\partial B_z}{\partial z}\right)$$

$$\frac{\partial B_y}{\partial x} - \frac{\partial B_x}{\partial y} = -2i\left(\frac{\partial B_1^+}{\partial x} - i\frac{\partial B_1^+}{\partial y} + \frac{1}{2}\frac{\partial B_z}{\partial z}\right). \quad (2.11)$$

Eq.(2.10) can be further simplified using (2.11):

$$\nabla^2 B_1^+ - \frac{1}{\kappa}\frac{\partial \kappa}{\partial x}\left(\frac{\partial B_1^+}{\partial x} - i\frac{\partial B_1^+}{\partial y} + \frac{1}{2}\frac{\partial B_z}{\partial z}\right) - \frac{1}{\kappa}\frac{\partial \kappa}{\partial y}\left(i\frac{\partial B_1^+}{\partial x} + \frac{\partial B_1^+}{\partial y} + i\frac{1}{2}\frac{\partial B_z}{\partial z}\right)$$
$$- \frac{1}{\kappa}\frac{\partial \kappa}{\partial z}\frac{1}{2}\left(-\frac{1}{2}\frac{\partial B_z}{\partial x} - i\frac{1}{2}\frac{\partial B_z}{\partial y} + \frac{\partial B_1^+}{\partial z}\right)$$
$$= i\omega\mu_0\kappa B_1^+. \quad (2.12)$$

By dividing both sides by κ, and substituting the partial derivatives term $-\frac{\nabla\kappa}{\kappa^2}$ with $\nabla(\kappa^{-1})$, the generalized Helmholtz equation can be derived in convection-reaction form without any assumptions:

$$\underbrace{\beta^+ \cdot \nabla(\kappa^{-1})}_{\text{Convection}} + \underbrace{\nabla^2 B_1^+ \kappa^{-1} = i\omega\mu_0 B_1^+}_{\text{Reaction}}, \quad (2.13)$$

where

$$\beta^{+}=\begin{bmatrix}\frac{\partial B_1^{+}}{\partial x}-i\frac{\partial B_1^{+}}{\partial y}+\frac{1}{2}\frac{\partial B_z}{\partial z}\\ i\frac{\partial B_1^{+}}{\partial x}+\frac{\partial B_1^{+}}{\partial y}+i\frac{1}{2}\frac{\partial B_z}{\partial z}\\ -\frac{1}{2}\frac{\partial B_z}{\partial x}-i\frac{1}{2}\frac{\partial B_z}{\partial y}+\frac{\partial B_1^{+}}{\partial z}\end{bmatrix} \tag{2.14}$$

is the convective field. Similarly, B_1^{-} based version can be derived in similar way ($B_1^{-}=\frac{B_x-iB_y}{2}$). For completeness, cr-EPT based on B_1^{+} or B_1^{-} can be written as follows:

$$\beta^{\pm}\cdot\nabla(\kappa^{-1})+\nabla^2 B_1^{\pm}\kappa^{-1}=i\omega\mu_0 B_1^{\pm}, \tag{2.15}$$

where

$$\beta^{\pm}=\begin{bmatrix}\frac{\partial B_1^{\pm}}{\partial x}\mp i\frac{\partial B_1^{\pm}}{\partial y}+\frac{1}{2}\frac{\partial B_z}{\partial z}\\ \pm i\frac{\partial B_1^{\pm}}{\partial x}+\frac{\partial B_1^{\pm}}{\partial y}\pm i\frac{1}{2}\frac{\partial B_z}{\partial z}\\ -\frac{1}{2}\frac{\partial B_z}{\partial x}\mp i\frac{1}{2}\frac{\partial B_z}{\partial y}+\frac{\partial B_1^{\pm}}{\partial z}\end{bmatrix}. \tag{2.16}$$

In practice, due to the fact that B_z is inaccessible in MRI, we assume the contribution of B_z could be neglected compared to $B_1^{\pm}$, i.e., $\frac{\partial B_z}{\partial x,y,z}\approx 0$. Consequently, the convective field $\beta^{\pm}$ is further simplified as:

$$\beta^{\pm}\approx\begin{bmatrix}\frac{\partial B_1^{\pm}}{\partial x}\mp i\frac{\partial B_1^{\pm}}{\partial y}\\ \pm i\frac{\partial B_1^{\pm}}{\partial x}+\frac{\partial B_1^{\pm}}{\partial y}\\ \frac{\partial B_1^{\pm}}{\partial z}\end{bmatrix}. \tag{2.17}$$

This assumption holds true at the center of birdcage/TEM coil, but errors in reconstruction gradually increase as slices move off-center, especially with short birdcage coils like head coils [50]. Eq (2.16) is a linear partial differential equation, which can be considered as:

$$Ax=b, \tag{2.18}$$

where x is the inverse of admittivity κ^{-1}. To solve this equation, we optimize it in the minimum-norm least-squares sense (using MATLAB function backslash operator "\"):

$$\hat{x}=\arg\min_x\|Ax-b\|_2^2. \tag{2.19}$$

If the EPs are piecewise constant, i.e. $\nabla\kappa = 0$, the gradient term in Eq.(2.15) can be neglected and simplifying the equation to standard EPT. As such, cr-EPT can be considered as a generalized version of standard EPT.

2.2.2. Limitations and Regularization Strategy

In Hafalir et al. 2014 [50], this inverse problem is solved within the 2D transverse plane using a finite difference method implemented on a triangular mesh with Dirichlet boundary conditions. However, as B_1 data are acquired in a rectangular grid, this necessitates some transformation at the k-space level [50]. In practice, a uniform cartesian discretization may be more suitable. However, the cr-EPT model is often unstable and struggles to converge because of the limited mesh size for discretization or the discontinuities in $\nabla^2 B_1^{\pm}$, leading to spurious oscillations from the boundary to the interior of the structure. Furthermore, the cr-EPT may not be applicable in regions where the convective field $\beta^{\pm}$ is low, almost at the center, referred to as the Low Convective Field (also called LCF region), which can result in spot-like artifacts [50], [58]. Yildiz and Ider [58] proposed using high dielectric pads surrounding the imaging object to effectively alter the $B_1^{\pm}$ distribution, shifting the LCF region outside the center and thus eliminating the LCF artifacts.

Another approach to address these artifacts involves introducing an artificial diffusion term $-\lambda\nabla^2(\kappa^{-1})$ into the equation [46], [59]:

$$\underbrace{-\lambda\nabla^2(\kappa^{-1})}_{\text{Diffusion}} + \underbrace{\beta^{\pm}\cdot\nabla(\kappa^{-1})}_{\text{Convection}} + \underbrace{\nabla^2 B_1^{\pm}\kappa^{-1} = i\omega\mu_0 B_1^{\pm}}_{\text{Reaction}}. \tag{2.20}$$

Here, λ represents the regularization diffusion coefficient, which is typically chosen empirically, typically to be positive and smaller than 1. This additional diffusion term acts as a low-pass filter and makes the cr-EPT relatively robust to noise. A high value of λ can decrease oscillations and numerical artifacts, resulting in a smoother reconstruction, but at the cost of resolution and contrast loss [60]. Li et al.[59] proposed that λ can be determined as several times or a fraction of the maximum amplitude of the x-convective field $\beta^{\pm}$, i.e., $\lambda = c \times \max(|{\beta_x}^{\pm}|)$.

Indeed, despite its numerical instability problems, cr-EPT represents a significant step forward. By incorporating the gradient of the EPs, it provides a more comprehensive equation, offering valuable insights for the future EPT algorithms. However, like standard EPT, cr-EPT faces similar limitations. It requires the complex $B_1^{\pm}$ field as input, necessitating knowledge of both the magnitude $|B_1^{\pm}|$ and the phase $\varphi^{\pm}$. Typically, estimating the phase $\varphi^{\pm}$ relies on the TPA, which is a common practice in both methods. The upcoming sections will introduce EPT methods that do not require TPA or have fewer MR scan requirements, making them more suitable for clinical use.

2.3. Gradient EPT

The Gradient EPT (gEPT) [51] is derived from the same fundamental equation (2.15) as cr-EPT, which assumes negligible spatial variation in B_z ($\frac{\partial B_z}{\partial x,y,z} \approx 0$). It aims to reformulate the inverse problem in terms of relative $B_1^{\pm}$ fields within a multi-channel transceiver RF coil system. This reformulation transforms the original problem into a different linear system, which is then solved to obtain the intermediate solution, the gradient of EPs, hence the name "gradient EPT". Finally, the local spatial distribution of EPs is obtained by integrating the gradient, with the subjective assignment of integration seed points. Due to this integration process, the reconstructed EPs maps exhibit high robustness against noise contamination. Furthermore, since gEPT is based on the relative $B_1^{\pm}$ fields, it eliminates the need for absolute $B_1^{\pm}$ estimation through the transceive phase assumption (TPA). This formulation makes gEPT particularly suitable for high-field MRI (3T or above) applications [23].

2.3.1. Multi-Channel RF Transceiver Coil System

In a typical multi-channel RF transceiver coil array, there are *P* transmit elements and *Q* receive elements. Relative $B_1^{\pm}$ fields between two transmit/receive channels are defined as follows:

$$B_{1pr}^{+} = \left|B_{1p}^{+}\right| e^{i(\varphi_p^{+} - \varphi_r^{+})} = \left|B_{1p}^{+}\right| e^{i(\varphi_{pr}^{+})} \tag{2.21}$$

$$B_{1qr}^{-} = \left|B_{1q}^{-}\right| e^{i(\varphi_q^{-} - \varphi_r^{-})} = \left|B_{1q}^{-}\right| e^{i(\varphi_{qr}^{-})} \tag{2.22}$$

Here, $\varphi_r^{\pm}$ is the unknown absolute phase of a reference transmit/receive channel. The relative phase $\varphi_{pr}^{+}/\varphi_{qr}^{-}$ can be measured by taking the difference of transceive phase φ_{tr} between two transmit/receive channels p/q and r, assuming they use the same receive/transmit coils where the receive/transmit phase φ^{-}/φ^{+} is the same:

$$\varphi_{pr}^{+} = \varphi_{tr,p} - \varphi_{tr,r} = (\varphi_p^{+} + \varphi^{-}) - (\varphi_r^{+} + \varphi^{-}) = \varphi_p^{+} - \varphi_r^{+} \tag{2.23}$$

$$\varphi_{qr}^{-} = \varphi_{tr,q} - \varphi_{tr,r} = (\varphi^{+} + \varphi_q^{-}) - (\varphi^{+} + \varphi_r^{-}) = \varphi_q^{-} - \varphi_r^{-} \tag{2.24}$$

This method effectively eliminates common phase terms irrelevant to the RF field, including those induced from chemical shift, B_0 heterogeneity, and eddy current effects [61]. The absolute transmit/receive field B_{1p}^{+}/B_{1q}^{-} from a single coil element, as required in the cr-EPT equation, can be therefore expressed in terms of measurable relative $B_1^{\pm}$ and an unknown reference phase $\varphi_r^{\pm}$:

$$B_{1p}^{+} = \left|B_{1p}^{+}\right| e^{i\varphi_p^{+}} = \left|B_{1p}^{+}\right| e^{i(\varphi_p^{+} - \varphi_r^{+} + \varphi_r^{+})} = B_{1pr}^{+} e^{i\varphi_r^{+}} \tag{2.25}$$

$$B_{1q}^{-} = \left|B_{1q}^{-}\right| e^{i\varphi_q^{-}} = \left|B_{1q}^{-}\right| e^{i(\varphi_q^{-} - \varphi_r^{-} + \varphi_r^{-})} = B_{1qr}^{-} e^{i\varphi_r^{-}} \tag{2.26}$$

In practice, B_{1pr}^{+} for each transmit channel is acquired with one channel receiving at a time while all channels receiving together [51]. Conversely, B_{1qr}^{-} for each receive channel is acquired with all channels transmitting together. Although the B_{1qr}^{-}-based method appears time-saving, obtaining its magnitude $|B_{1qr}^{-}|$, which is always weighted by proton density, can be complicated.

In the original version of gEPT by Liu et al. 2015 [51], the gradients of EPs using B_{1pr}^{+} and B_{1qr}^{-} at the same voxel, which are conjugates of each other ($g_{+} \equiv g_x + ig_y$ and $g_{-} \equiv g_x - ig_y$), were both calculated and then combined to obtain pure g_x and g_y for the subsequent 2D integration of EPs. This method required measurements of both transmit B_{1pr}^{+} and receive B_{1qr}^{-}, which prolonged scan time and increased complexity. However, it has been demonstrated that only the B_{1pr}^{+} gradient g_x is sufficient for integrating EPs [62], [63]. Consequently, the relative transmit field B_{1pr}^{+}-based gEPT is now often preferred for practical implementation. This preferred method will be chosen and described in the following sections.

2.3.2. B_{1pr}^{+}-based gEPT

By introducing B_{1p}^{+} into the cr-EPT equation (2.15) with Eq.(2.17), we obtain:

$$-\frac{1}{k^2}\begin{bmatrix} \frac{\partial B_{1p}^{+}}{\partial x} - i\frac{\partial B_{1p}^{+}}{\partial y} \\ i\frac{\partial B_{1p}^{+}}{\partial x} + \frac{\partial B_{1p}^{+}}{\partial y} \\ \frac{\partial B_{1p}^{+}}{\partial z} \end{bmatrix} \cdot \begin{bmatrix} \frac{\partial k}{\partial x} \\ \frac{\partial k}{\partial y} \\ \frac{\partial k}{\partial z} \end{bmatrix} + \nabla^2 B_{1p}^{+}\kappa^{-1} = i\omega\mu_0 B_{1p}^{+}$$

$$-\frac{1}{k^2}\left(\frac{\partial B_{1p}^{+}}{\partial x}\left(\frac{\partial k}{\partial x} + i\frac{\partial k}{\partial y}\right) - i\frac{\partial B_{1p}^{+}}{\partial y}\left(\frac{\partial k}{\partial x} + i\frac{\partial k}{\partial y}\right) + \frac{\partial k}{\partial z}\frac{\partial B_{1p}^{+}}{\partial z}\right) + \nabla^2 B_{1p}^{+}\kappa^{-1} = i\omega\mu_0 B_{1p}^{+}\,. \qquad (2.27)$$

By multiplying k both sides of Eq.(2.27), we have:

$$-g_{+}\left(\frac{\partial B_{1p}^{+}}{\partial x} - i\frac{\partial B_{1p}^{+}}{\partial y}\right) - g_z\frac{\partial B_{1p}^{+}}{\partial z} + \nabla^2 B_{1p}^{+} = i\omega\mu_0 B_{1p}^{+}k, \qquad (2.28)$$

where

$$g_{+} = \frac{1}{\kappa}\left(\frac{\partial k}{\partial x} + i\frac{\partial k}{\partial y}\right) = \frac{\partial lnk}{\partial x} + i\frac{\partial lnk}{\partial y} \qquad (2.29)$$

and

$$g_z = \frac{1}{\kappa}\left(\frac{\partial k}{\partial x} + i\frac{\partial k}{\partial y}\right) = \frac{\partial lnk}{\partial z}. \qquad (2.30)$$

Since B_{1p}^{+} can be expressed by B_{1pr}^{+} using Eq.(2.25), its gradient and Laplacian can be expressed as:

$$\frac{\partial B_{1p}^{+}}{\partial x,y,z} = e^{i\varphi_r^{+}} \frac{\partial B_{1pr}^{+}}{\partial x,y,z} + B_{1pr}^{+} \frac{\partial e^{i\varphi_r^{+}}}{\partial x,y,z} \tag{2.31}$$

$$\nabla^2 B_{1p}^{+} = e^{i\varphi_r^{+}} \nabla^2 B_{1pr}^{+} + 2\nabla e^{i\varphi_r^{+}} \cdot \nabla B_{1pr}^{+} + B_{1pr}^{+} \nabla^2 e^{i\varphi_r^{+}} \tag{2.32}$$

By substituting with Eq.(2.31) and Eq.(2.32) into Eq.(2.28), we have

$$-g_+ \left(e^{i\varphi_r^{+}} \frac{\partial B_{1pr}^{+}}{\partial x} + B_{1pr}^{+} \frac{\partial e^{i\varphi_r^{+}}}{\partial x} - ie^{i\varphi_r^{+}} \frac{\partial B_{1pr}^{+}}{\partial y} - iB_{1pr}^{+} \frac{\partial e^{i\varphi_r^{+}}}{\partial y} \right) - g_z \left(e^{i\varphi_r^{+}} \frac{\partial B_{1pr}^{+}}{\partial z} + B_{1pr}^{+} \frac{\partial e^{i\varphi_r^{+}}}{\partial z} \right)$$
$$+e^{i\varphi_r^{+}} \nabla^2 B_{1pr}^{+} + 2\nabla e^{i\varphi_r^{+}} \cdot \nabla B_{1pr}^{+} + B_{1pr}^{+} \nabla^2 e^{i\varphi_r^{+}} = i\omega\mu_0 k B_{1pr}^{+} e^{i\varphi_r^{+}}. \tag{2.33}$$

Cancelling out $e^{i\varphi_r^{+}}$ from both sides of the equation, we get

$$-g_+ \left(\frac{\partial B_{1pr}^{+}}{\partial x} - i\frac{\partial B_{1pr}^{+}}{\partial y} + iB_{1pr}^{+} \frac{\partial \varphi_r^{+}}{\partial x} + B_{1pr}^{+} \frac{\partial \varphi_r^{+}}{\partial y} \right) - g_z \left(\frac{\partial B_{1pr}^{+}}{\partial z} + iB_{1pr}^{+} \frac{\partial \varphi_r^{+}}{\partial z} \right)$$
$$+\nabla^2 B_{1pr}^{+} + 2i\nabla\varphi_r^{+} \cdot \nabla B_{1pr}^{+} + B_{1pr}^{+} (i\nabla^2 \varphi_r^{+} - \|\nabla\varphi_r^{+}\|^2) = i\omega\mu_0 k B_{1pr}^{+}. \tag{2.34}$$

Extracting B_{1pr}^{+}, we obtain

$$B_{1pr}^{+} \left(-i\omega\mu_0 k + i\nabla^2\varphi_r^{+} - \|\nabla\varphi_r^{+}\|^2 - i\left(\frac{\partial\varphi_r^{+}}{\partial x} - i\frac{\partial\varphi_r^{+}}{\partial y} \right) g_+ - i\frac{\partial\varphi_r^{+}}{\partial z} g_z \right)$$
$$+ \begin{bmatrix} \frac{\partial B_{1pr}^{+}}{\partial x} \\ \frac{\partial B_{1pr}^{+}}{\partial x} \\ \frac{\partial B_{1pr}^{+}}{\partial z} \end{bmatrix} \cdot \begin{bmatrix} 2i\frac{\partial\varphi_r^{+}}{\partial x} - g_+ \\ 2i\frac{\partial\varphi_r^{+}}{\partial y} + ig_+ \\ 2i\frac{\partial\varphi_r^{+}}{\partial z} - g_z \end{bmatrix} = -\nabla^2 B_{1pr}^{+}. \tag{2.35}$$

Eq.(2.35) can be rewritten in the matrix form of $Ax = b$ for each voxel:

$$\begin{bmatrix} B_{1pr}^{+} \\ \frac{\partial B_{1pr}^{+}}{\partial x} \\ \frac{\partial B_{1pr}^{+}}{\partial x} \\ \frac{\partial B_{1pr}^{+}}{\partial z} \end{bmatrix}^T \cdot \begin{bmatrix} -i\omega\mu_0 k + i\nabla^2\varphi_r^{+} - \|\nabla\varphi_r^{+}\|^2 - i\left(\frac{\partial\varphi_r^{+}}{\partial x} - i\frac{\partial\varphi_r^{+}}{\partial y} \right) g_+ - i\frac{\partial\varphi_r^{+}}{\partial z} g_z \\ 2i\frac{\partial\varphi_r^{+}}{\partial x} - g_+ \\ 2i\frac{\partial\varphi_r^{+}}{\partial y} + ig_+ \\ 2i\frac{\partial\varphi_r^{+}}{\partial z} - g_z \end{bmatrix} = -\nabla^2 B_{1pr}^{+}. \tag{2.36}$$

This linear system is solved in a least-squares sense to obtain x. Since there are four unknowns (total elements of x vector), it requires at least four relative transmit field B_{1pr}^{+} measurements (i.e., P > 4) to have an overdetermined system. The gradient of EPs in xy-plane $g_+ = \frac{\partial lnk}{\partial x} + i\frac{\partial lnk}{\partial y}$ can be derived from the real part of the second and third elements of x:

$$g_+ = -Re(x_2) - i \cdot Re(x_3) = -Re\left(2i\frac{\partial \varphi_r^+}{\partial x} - g_+\right) - i \cdot Re(ig_+) = Re(g_+) + i \cdot Im(g_+). \quad (2.37)$$

Once the gradient of EPs g_+ and g_z are obtained, an additional least-squares minimization process [64] is required to integrate the EPs $\hat{k}$ using a small number of seed points k_0 to provide initial values:

$$\hat{k} = \arg\min_{\hat{k}}(\left\|g_+(\hat{k}) - g_+\right\|_2^2 + \left\|g_z(\hat{k}) - g_z\right\|_2^2 + \underbrace{\lambda\left\|\hat{k} - k_0\right\|_2^2}_{\text{optional}}). \quad (2.38)$$

The regularization term of $\lambda\left\|\hat{k} - k_0\right\|_2^2$ can be optionally added to the minimization process. This term with $\lambda > 0$, helps to stabilize the solution by forcing the estimated distribution $\hat{k}$ to be similar to the seed points k_0. The seed points (or Dirichlet boundary condition) can be derived by surrounding the object or skin with a gel with known EPs [63] or estimated by standard EPT in a local homogeneous region [61]. Alternatively, a technique that does not require seed points involves directly solving Eq.(2.28) with joint L1 and L2 norm regularization of g_+, as described in Wang et al. [62].

2.3.3. Limitations

gEPT relies on multi-channel transmission to acquire B_{1pr}^+ for each transmit channel for eliminating the TPA. However, these multi-channel RF transmit coil elements (P > 4) are not yet widely available in clinical settings [27]. Moreover, this method requires multiple scans to switch transmit channels, resulting in longer acquisition times compared to standard B_1 field acquisition protocol, and increased sensitivity to motion, making it potentially unsuitable for imaging moving organs. Additionally, similar to cr-EPT, gEPT also requires both $|B_1^+|$ mapping and transceive phase acquisition, which is time-consuming. The complexity and duration of the MR scans may also pose challenges in patient compliance and comfort, especially for those unable to remain still for extended periods. As a result, while gEPT offers significant advancements in high-field MRI applications, these limitations must be addressed to facilitate broader clinical adoption.

2.4. Magnitude and Phase-based EPT

The methods mentioned above rely on measurements of the complex B_1^+ field, requiring both $|B_1^+|$ mapping and transceive phase φ_{tr} acquisition, and typically using the TPA. This dual requirement has hindered the progress of implementing these methods in clinical settings due to the lengthy acquisition times. Additionally, combining $|B_1^+|$ and φ_{tr} from different scans poses challenges for image registration, especially for moving organs. To address these limitations, it is crucial to separate the magnitude and phase expressions [65], thereby simplifying the acquisition process and improving clinical applicability.

2.4.1. Derivation

Using the definition of $B_1^+ = |B_1^+|e^{i\varphi^+}$ in the governing equation of Standard EPT (2.5), we obtain:

$$\kappa = \frac{\nabla^2\left(|B_1^+|e^{i\varphi^+}\right)}{i\omega\mu_0|B_1^+|e^{i\varphi^+}}. \tag{2.39}$$

Expanding this with the identity of $\nabla^2(ab) = a\nabla^2 b + 2\nabla a \cdot \nabla b + b\nabla^2 a$, we get:

$$\kappa = \frac{|B_1^+|\nabla^2 e^{i\varphi^+} + 2\nabla|B_1^+| \cdot \nabla e^{i\varphi^+} + e^{\varphi^+}\nabla^2|B_1^+|}{i\omega\mu_0|B_1^+|e^{i\varphi^+}} \tag{2.40}$$

$$\kappa = \frac{|B_1^+|e^{i\varphi^+}(-|\nabla\varphi^+|^2 + i\nabla^2\varphi^+) + ie^{i\varphi^+}(2\nabla|B_1^+| \cdot \nabla\varphi^+) + e^{i\varphi^+}\nabla^2|B_1^+|}{i\omega\mu_0|B_1^+|e^{i\varphi^+}}. \tag{2.41}$$

Factorizing out the common term $e^{i\varphi^+}$, we get:

$$\begin{aligned}\kappa &= \frac{\nabla^2|B_1^+| - |B_1^+||\nabla\varphi^+|^2 + i(|B_1^+|\nabla^2\varphi^+ + 2\nabla|B_1^+| \cdot \nabla\varphi^+)}{i\omega\mu_0|B_1^+|} \\ &= \frac{|B_1^+|\nabla^2\varphi^+ + 2\nabla|B_1^+| \cdot \nabla\varphi^+ + i(-\nabla^2|B_1^+| + |B_1^+||\nabla\varphi^+|^2)}{\omega\mu_0|B_1^+|}.\end{aligned} \tag{2.42}$$

Separating real and imaginary part of Eq. (2.42) with the definition of $\kappa = \sigma + i\omega\varepsilon_0\varepsilon_r$, we can obtain conductivity σ and relative permittivity ε_r:

$$\sigma = \frac{1}{\omega\mu_0}\left(\nabla^2\varphi^+ + \frac{2\nabla|B_1^+| \cdot \nabla\varphi^+}{|B_1^+|}\right) \tag{2.43}$$

$$\varepsilon_r = \frac{1}{\omega^2\mu_0\varepsilon_0}\left(-\frac{\nabla^2|B_1^+|}{|B_1^+|} + |\nabla\varphi^+|^2\right). \tag{2.44}$$

Assuming that $\nabla^2\varphi^+ \gg \frac{2\nabla|B_1^+| \cdot \nabla\varphi^+}{|B_1^+|}$ and $-\frac{\nabla^2|B_1^+|}{|B_1^+|} \gg |\nabla\varphi^+|^2$, we obtain the Phase and Magnitude-based EPT to reconstruct conductivity σ and relative permittivity ε_r, respectively:

$$\sigma \approx \frac{\nabla^2\varphi^+}{\omega\mu_0} \tag{2.45}$$

$$\varepsilon_r \approx \frac{-\nabla^2|B_1^+|}{\omega^2\mu_0\varepsilon_0|B_1^+|}. \tag{2.46}$$

Similarly, conductivity σ can be obtained using φ^-:

$$\sigma \approx \frac{\nabla^2\varphi^-}{\omega\mu_0}. \tag{2.47}$$

By summing Eq.(2.45) and Eq.(2.47), Phased-based (PB) EPT can be further expressed in terms of φ_{tr}:

$$2\sigma \approx \frac{\nabla^2\varphi^- + \nabla^2\varphi^+}{\omega\mu_0}$$

$$\sigma \approx \frac{\nabla^2\varphi_{tr}}{2\omega\mu_0}. \tag{2.48}$$

Specifically, since conductivity does not change between transmission and reception, this formula can be applied with any combination of transmit (φ^+) and receive (φ^-) coils, highlighting that the TPA is no longer necessary. Moreover, compared to standard EPT for conductivity measurements, Phase-based EPT skips the $|B_1^+|$ mapping which requires lengthy scan times. Thanks to its ease of implementation, Phase-based EPT is the most popular EPT method and has already been developed in clinical studies [66], [67], [68]. This advancement facilitates faster and more efficient conductivity measurements, making Phase-based EPT a valuable tool in medical imaging.

2.4.2. Limitations

Magnitude and Phase-based EPT are based on the local homogeneity assumption (LHA), which can produce boundary artifacts, resulting in inaccurate estimation near the boundaries. This makes it unsuitable for small tissue structures. However, tissue segmentation can be used to apply reconstruction only in homogenous regions, thereby maintaining the LHA and improving boundary reconstruction. This method will be described in Chapter 6.

The use of magnitude- and phase-only assumptions ($\nabla^2\varphi^+ \gg \frac{2\nabla|B_1^+|\cdot\nabla\varphi^+}{|B_1^+|}$ and $-\frac{\nabla^2|B_1^+|}{|B_1^+|} \gg |\nabla\varphi^+|^2$) results in systematic errors in reconstructed EPs maps (overestimation in conductivity but underestimation in permittivity). In Voigt et al. 2011 [52], the highest errors in reconstructed conductivity were found for $\omega\varepsilon_0\varepsilon_r \gg \sigma$. This indicates that the inaccuracy of Phase-based EPT increases with higher Larmor frequency or field strengths. The study by Van Lier et al. 2014 [42] demonstrated significant errors in phase-only reconstruction at 7T, both in simulation and measurements, despite low noise level. Therefore, Phase-based EPT is not suitable for high field MRI. Fortunately, at 1.5 or 3T, the conductivity reconstruction errors are within acceptable limits, up to 10% [42], [52].

Conversely, the highest errors in reconstructed permittivity are found for $\sigma \gg \omega\varepsilon_0\varepsilon_r$ [52]. This suggests that the accuracy of Magnitude-based EPT decreases as the Larmor frequency or field strength decreases. It is recommended to apply Magnitude-based EPT at high field MRI for better accuracy. For most tissues, except for highly conductive body fluids like blood and CSF, the error is approximately 20% at 1.5T [52].

2.4.3. RF Shimming Effects

MRI systems with field strengths of 3T or higher are usually equipped with multiple independent RF transmit channels [27]. For instance, at 3T, there may be two independent transmit channels that can

produce different degrees of elliptically polarized fields. At 7T, there can be up to eight transmit channels with independent magnitude and phase control. In these cases, RF shimming is used to ensure B_1 homogeneity, i.e., $\nabla|B_1^+| \approx 0$.

RF shimming can be performed by adjusting the channel weights using complex B_1 maps measured from each channel, i.e., coil combinations. However, this process affects the accuracy of Magnitude- and Phase-based EPT due to their underlying assumptions [69]. Specifically, the assumptions used in these methods ($\nabla^2\varphi^+ \gg \frac{2\nabla|B_1^+|\cdot\nabla\varphi^+}{|B_1^+|}$ and $-\frac{\nabla^2|B_1^+|}{|B_1^+|} \gg |\nabla\varphi^+|^2$) can be compromised by the phase variations introduced through RF shimming.

Phase-based EPT assumes that $\frac{2\nabla|B_1^+|\cdot\nabla\varphi^+}{|B_1^+|} \approx 0$, implying $\nabla|B_1^+| \approx 0$, an assumption that can be supported by RF shimming [69]. However, RF shimming can adversely affect Magnitude-based EPT, which relies on the spatial variation of $|B_1^+|$. Magnitude-based EPT could benefit from RF phase shimming ($\nabla\varphi^+ \approx 0$), provided that the resulting "inhomogeneous" $|B_1^+|$ does not create signal voids or significant deviations from constancy, i.e. $\nabla|B_1^+| \neq 0$.

2.5. Phase-based Convection Reaction EPT (PB-cr)

Due to the benefits of phase-only approximation, cr-EPT [46] has been proposed based on using only the measurable transceive phase φ_{tr} in MRI for conductivity imaging. Compared to standard Phase-based EPT, PB-cr maintains the gradient term of conductivity, which reduces boundary artifacts and enhances noise robustness.

2.5.1. Derivation

Similar to standard Phase-based (PB) EPT, using the definition of $B_1^\pm = \left|B_1^\pm\right|e^{i\varphi^\pm}$and assuming $\nabla\left|B_1^\pm\right| = 0$ and $\nabla \mathrm{B_z} = 0$, Eq.(2.15) can be expressed as

$$\begin{bmatrix} \left|B_1^\pm\right|e^{i\varphi^\pm}\left(i\frac{\partial\varphi^\pm}{\partial x} \pm \frac{\partial\varphi^\pm}{\partial y}\right) \\ \left|B_1^\pm\right|e^{i\varphi^\pm}\left(\mp\frac{\partial\varphi^\pm}{\partial x} + i\frac{\partial\varphi^\pm}{\partial y}\right) \\ \left|B_1^\pm\right|e^{i\varphi^\pm}i\frac{\partial\varphi^\pm}{\partial z} \end{bmatrix} \cdot \nabla(\kappa^{-1}) + \left|B_1^\pm\right|e^{i\varphi^\pm}\left(-\left|\nabla\varphi^\pm\right|^2 + i\nabla^2\varphi^\pm\right)\kappa^{-1} = i\omega\mu_0\left|B_1^\pm\right|e^{i\varphi^\pm}. \quad (2.49)$$

Cancelling out the common term $\left|B_1^\pm\right|e^{i\varphi^\pm}$, and adding the φ^+ and φ^- based version of Eq.(2.49) to write the equation in terms of φ_{tr}, we have:

$$\begin{bmatrix} i\frac{\partial \varphi_{tr}}{\partial x} + \frac{\partial}{\partial y}(\varphi^+ - \varphi^-) \\ i\frac{\partial \varphi_{tr}}{\partial y} - \frac{\partial}{\partial x}(\varphi^+ - \varphi^-) \\ i\frac{\partial \varphi_{tr}}{\partial z} \end{bmatrix} \cdot \nabla(\kappa^{-1}) + (-|\nabla \varphi_{tr}|^2 - 2\nabla\varphi^+ \cdot \nabla\varphi^- + i\nabla^2\varphi_{tr})\kappa^{-1} = 2i\omega\mu_0. \quad (2.50)$$

Assuming that $\frac{\partial}{\partial x,y}(\varphi^+ - \varphi^-) \approx 0$, and $\sigma^2 \gg (\omega\varepsilon_0\omega\varepsilon_r)^2$ so that $Re(\kappa^{-1}) = \frac{\sigma}{\sigma^2 + (\omega\varepsilon_0\omega\varepsilon_r)^2} \approx \sigma^{-1}$, the imaginary part of this equation can be written in terms of σ^{-1} as:

$$\nabla\varphi_{tr} \cdot \nabla(\sigma^{-1}) + \nabla^2\varphi_{tr}\sigma^{-1} = 2\omega\mu_0. \quad (2.51)$$

Eq.(2.51) can be rewritten into a linear system form Ax=b, where x is a vector for each σ^{-1} and can be solved using the finite-difference method on a Cartesian grid. If the conductivity is piecewise constant, i.e., $\nabla\sigma = 0$, the gradient term in Eq.(2.51) can be neglected and simplifying the equation to PB EPT. As such, PB-cr can be considered as a generalized version of PB EPT.

For stabilizing this linear system, it is recommended to add an artificial diffusion term $\lambda\nabla^2(\sigma^{-1})$ and a weight of convection ν in Eq.(2.51):

$$-\lambda\nabla^2(\sigma^{-1}) + \nu\nabla\varphi_{tr} \cdot \nabla(\sigma^{-1}) + \nabla^2\varphi_{tr}\sigma^{-1} = 2\omega\mu_0, \quad (2.52)$$

where λ is an empirically determined diffusion coefficient, typically ranging from 0.005 to 0.05 [46] and ν is a convection coefficient [70]. A high value of λ can decrease oscillations and numerical artifacts, resulting in a smoother reconstruction, but at the cost of resolution and contrast loss [46], [58], [60]. The closer the value of ν is to 0, the closer PB-cr is to its simplified version, Phase-based EPT. The choices of λ and ν are both empirical for the whole ROI. However, they could also be further chosen in a pixelwise manner, with values that vary with the geometric structure of EPs. An optimization for local coefficient maps λ and ν with physics-coupled neural networks was recently published [48]. Moreover, it has been demonstrated that Dirichlet boundary conditions are not necessary to specify [70].

2.5.2. Limitations

PB-cr can be considered as a generalized version of standard Phase-based EPT, allowing for large spatial variations in tissue conductivity ($\nabla\sigma \neq 0$). To uphold the phase-only approximation $\nabla\left|B_1^{\pm}\right| = 0$ and $\sigma^2 \gg (\omega\varepsilon_0\omega\varepsilon_r)^2$, PB-cr is not suitable for MRI above 3T.

PB-cr can also be considered as a phase version of cr-EPT. To maintain the gradient term, we have to assume $\nabla B_z = 0$. However, this assumption is only valid in the central region of the birdcage/TEM coil, and for tissue with slow EPs variations along the z-axis. Similar to cr-EPT, PB-cr can also exhibit low LCF artifacts, especially in regions where $\nabla\varphi_{tr}$ and $\nabla^2\varphi_{tr} \approx 0$. This spot-like artifact can be mitigated by adding the diffusion term. However, selecting optimal regularization coefficients λ and ν

remains challenging. Additionally, the method's computational complexity and processing time, and challenges in implementing it for a whole 3D volume, present significant obstacles, making it not ready for clinical use.

2.6. Complex-Image-based EPT

Although phase-only methods (PB and PB-cr) skip $|B_1^+|$ mapping to effectively reduce scan time, these methods do not allow for the permittivity reconstruction and introduce an additional systematic error of about 10% in conductivity estimation below 3T [52]. Another method, called Complex-Image-based EPT ([53], [54]) utilizes both the magnitude and phase information from acquired images using low flip-angle GRE sequences, particularly Zero Echo Time (ZTE) and Ultra-short Echo Time (UTE) sequences. This approach enables the reconstruction of both conductivity and permittivity in a single acquisition.

From Eq.(1.25), the complex image for any low-flip-angle GRE sequence is roughly proportional to the complex RF field ($B = \sqrt{B_1^+ B_1^-}$) and can be essentially expressed as:

$$I = \rho_0 \gamma \tau B_1^+ B_1^- = I_0 B_1^+ B_1^- \overset{\text{def}}{=} I_0 B^2 \tag{2.53}$$

where ρ_0 is the proton density, γ is the gyromagnetic ration and τ is the RF pulse duration. Here, $I_0 = \rho_0 \gamma \tau$ is a natural contrast term involving all non-RF related contribution (principally proton density and relaxation contrasts). Complex-Image-based EPT aims to establish an equation based on the square root of the product transmit and receive fields $B = \sqrt{B_1^+ B_1^-}$, which is proportional to the low-flip angle MR signal. This method can be categorized into Image-based [53] and Generalized-based EPT [54], with the former assuming EPs are piecewise constant and the latter including the gradient term of EPs.

2.6.1. Image-based EPT

2.6.1.1. Derivation

The key idea is to rewrite standard EPT, which assumes $\nabla\kappa = 0$, in terms of $B_1^+ B_1^-$. By multiplying Eq.(2.5) with B_1^- and Eq.(2.7) with $B_1^+$and adding them together, we obtain:

$$2\kappa = \frac{B_1^- \nabla^2 B_1^+ + B_1^+ \nabla^2 B_1^-}{i\omega\mu_0 B_1^+ B_1^-}$$

$$\nabla^2 (B_1^+ B_1^-) - 2i\omega\mu_0 k B_1^+ B_1^- - 2\nabla B_1^+ \cdot \nabla B_1^- = 0. \tag{2.54}$$

By taking $B_1^+ B_1^- = \left(\sqrt{B_1^+ B_1^-}\right)^2$ and defining $a = \sqrt{B_1^+ B_1^-}$ and $b = \sqrt{\frac{B_1^-}{B_1^+}}$, Eq.(2.54) can be rewritten as:

$$2a\nabla^2 a^2 - 2i\omega\mu_0 k a^2 - 2\nabla\frac{a}{b} \cdot \nabla(ab) = 0. \tag{2.55}$$

Using the identity $\nabla^2 a^2 = 2a\nabla^2 a + 2\nabla a + 2\nabla a \cdot \nabla a$ and dividing by $2a^2$, we get:

$$\frac{\nabla^2 a}{a} - i\omega\mu_0 k + \underbrace{\frac{1}{a^2}\left(\nabla a \cdot \nabla a - \nabla\frac{a}{b}\cdot\nabla(ab)\right)}_{\mathrm{k_{error}}} = 0. \tag{2.56}$$

Here, $\mathrm{k_{error}}$ is an error term that can be further simplified to $\frac{1}{4}\nabla\ln\frac{B_1^-}{B_1^+}\cdot\nabla\ln\frac{B_1^-}{B_1^+}$ and can be neglected when $B_1^+ = B_1^-$. Neglecting $\mathrm{k_{error}}$ and simplifying (2.56), we can obtain the governing equation based on $B_1^+B_1^-$:

$$k = \frac{\nabla^2\sqrt{B_1^+B_1^-}}{i\omega\mu_0\sqrt{B_1^+B_1^-}}. \tag{2.57}$$

Replacing $\sqrt{B_1^+B_1^-}$ with B, we get the Image-based (IB) EPT:

$$k = \frac{\nabla^2 B}{i\omega\mu_0 B}, \tag{2.58}$$

where $B = \sqrt{B_1^+B_1^-} = \frac{\sqrt{I}}{\sqrt{I_0}} \propto \sqrt{I}$. If we assume that I_0 is piecewise constant or varies slowly compared to $B_1^+B_1^-$, it can be factored out in the Laplacian, rendering it without impact on the reconstruction. In this way, B can be directly equal to the square root of the complex MR image in implementation ($B = \sqrt{I}$). Finally, we can derive the conductivity σ and relative permittivity ε_r from the real and imaginary parts in Eq.(2.58), respectively:

$$\sigma = Re\left(\frac{\nabla^2 B}{i\omega\mu_0 B}\right) \quad \text{and} \quad \varepsilon_r = \frac{1}{\omega\varepsilon_0} Im\left(\frac{\nabla^2 B}{i\omega\mu_0 B}\right). \tag{2.59}$$

2.6.1.2. Limitations

The governing equation in IB EPT (2.59) is similar to that in standard EPT (2.6), but replaces B_1^+ by the square root of the low-flip angle MR signal $\sqrt{I}$. The LHA assumption still remains, resulting in boundary artifacts. Specifically, the $|B_1^+|$ map is replaced by $\sqrt{|I|}$, leading to poorer quality in permittivity reconstruction [53], as permittivity is more sensitive to image magnitude than phase. Additionally, the magnitude exhibits significant discontinuities at tissue boundaries compared to typical $|B_1^+|$ map. Furthermore, the magnitude is affected by other non-RF related contrast I_0, and magnitude artifacts can be translated to EPs artifacts. To address these issues, the tissue can be segmented and reconstruction can be applied in homogenous regions, improving the accuracy of EPs.

The error term, $\mathrm{k_{error}} = \frac{1}{4}\nabla\ln\frac{B_1^-}{B_1^+}\cdot\nabla\ln\frac{B_1^-}{B_1^+}$, resulting from B_1^+ and B_1^- differences, is reduced to a second-order effect compared to standard EPT [53], which relies on the TPA. This means that Image-based EPT is less sensitive to differences between B_1^+ and B_1^-. However, this approach remains may be

invalid for high field MRI at 7T and above, where the differences between B_1^+ and B_1^- are more pronounced.

2.6.2. Generalized-Image-based EPT

2.6.2.1. Derivation

The key idea is to rewrite cr-EPT, which assumes $\nabla B_z = 0$, in terms of $B_1^+ B_1^-$. By multiplying the transmit version of cr-EPT Eq.(2.15) with B_1^- and its receive version with B_1^+ and adding them together, we obtain:

$$(B_1^+\beta^- + B_1^-\beta^+)\cdot\nabla(\kappa^{-1}) + \kappa^{-1}(B_1^+\nabla^2 B_1^- + B_1^-\nabla^2 B_1^+) = 2i\omega\mu_0 B_1^+ B_1^- \tag{2.60}$$

Using the Laplacian identity $\nabla^2(B_1^+B_1^-) = B_1^+\nabla^2 B_1^- + B_1^-\nabla^2 B_1^+ + 2\nabla B_1^+\cdot\nabla B_1^-$, we can rewrite Eq.(2.60) as:

$$\nabla^2(B_1^+B_1^-)\kappa^{-1} + (B_1^+\beta^- + B_1^-\beta^+)\cdot\nabla(\kappa^{-1}) - 2\nabla B_1^+\cdot\nabla B_1^-\kappa^{-1} = 2i\omega\mu_0 B_1^+B_1^- \tag{2.61}$$

Dividing both side by $2B_1^+B_1^-$, we get:

$$\left(\frac{\nabla^2(B_1^+B_1^-)}{2B_1^+B_1^-} - \frac{\nabla B_1^+\cdot\nabla B_1^-}{B_1^+B_1^-}\right)\kappa^{-1} + \frac{B_1^+\beta^- + B_1^-\beta^+}{2B_1^+B_1^-}\cdot\nabla(\kappa^{-1}) = i\omega\mu_0 \tag{2.62}$$

Defining $B^2 = B_1^+B_1^-$, the first term can be expressed as:

$$\frac{\nabla^2(B_1^+B_1^-) - 2\nabla B_1^+\cdot\nabla B_1^-}{2B_1^+B_1^-} = \frac{2B\nabla^2 B + 2\nabla B\cdot\nabla B - 2\nabla B_1^+\cdot\nabla B_1^-}{2B^2} = \frac{\nabla^2 B}{B} + \frac{\nabla B\cdot\nabla B - \nabla B_1^+\cdot\nabla B_1^-}{B^2} \tag{2.63}$$

And the second term $\frac{B_1^+\beta^- + B_1^-\beta^+}{2B_1^+B_1^-}$ can be expressed as:

$$\frac{B_1^+\beta^- + B_1^-\beta^+}{2B_1^+B_1^-} = \begin{bmatrix} \frac{\partial lnB}{\partial x} + \frac{i}{2}\frac{\partial ln\frac{B_1^-}{B_1^+}}{\partial y} \\ \frac{\partial lnB}{\partial y} - \frac{i}{2}\frac{\partial ln\frac{B_1^-}{B_1^+}}{\partial y} \\ \frac{\partial lnB}{\partial z} \end{bmatrix} \approx \begin{bmatrix} \frac{\partial lnB}{\partial x} \\ \frac{\partial lnB}{\partial y} \\ \frac{\partial lnB}{\partial z} \end{bmatrix} = \frac{\nabla B}{B} \tag{2.64}$$

Keeping only the first term in each row and assuming $\frac{1}{2}\partial_{x,y} ln\frac{B_1^-}{B_1^+} = 0$ (which is a first-order effect with respect to the differences between B_1^+ and B_1^-), the second term can be simplified to $\frac{\nabla B}{B}$. Substituting Eq.(2.64) and Eq.(2.63) into Eq.(2.62), we get:

$$\frac{\nabla^2 B}{B}\kappa^{-1} + \frac{\nabla B}{B}\cdot\nabla(\kappa^{-1}) + \underbrace{\frac{\nabla B\cdot\nabla B - \nabla B_1^+\cdot\nabla B_1^-}{B^2}}_{\mathrm{k_{error}}}\kappa^{-1} = i\omega\mu_0 \tag{2.65}$$

If we define $a = B = \sqrt{B_1^+ B_1^-}$ and $b = \sqrt{\frac{B_1^-}{B_1^+}}$, the error term $\mathrm{k_{error}}$ can be expressed as:

$$\mathrm{K_{error}} = \frac{1}{a^2}\left(\nabla a \cdot \nabla a - \nabla \frac{a}{b} \cdot \nabla(ab)\right) \tag{2.66}$$

This is the same error term as in IB EPT and can be simplified [53]to:

$$\mathrm{K_{error}} = \frac{1}{4}\nabla \ln \frac{B_1^-}{B_1^+} \cdot \nabla \ln \frac{B_1^-}{B_1^+} \tag{2.67}$$

This error term, which is a second-order effect with respect to the differences between B_1^+ and B_1^-, can be neglected when $B_1^+ = B_1^-$. In this way, we get the Generalized-Image-based (GIB) EPT:

$$\frac{\nabla^2 B}{B}\kappa^{-1} + \frac{\nabla B}{B} \cdot \nabla(\kappa^{-1}) = i\omega\mu_0 \tag{2.68}$$

Eq.(2.68) can be rewritten into a linear system form Ax=b, where x is a vector for each κ^{-1} and can be solved using the finite-difference method on a Cartesian grid. Assuming $\nabla I_0 = 0$, taking $B = \sqrt{I/I_0}$, the impacts of I_0 can be cancelled out of the differential term. Therefore, we calculate EPs by replacing B in Eq.(2.68) with the square root of a complex low-flip angle MR image in implementation. If the EPs are piecewise constant, i.e., $\nabla\kappa = 0$, the gradient term in Eq.(2.68) can be neglected and simplifying the equation to standard EPT. As such, GIB EPT can be considered as a generalized version of IB EPT.

The same as PB-cr, for stabilizing this linear system, it is recommended to add an artificial diffusion term $\lambda\nabla^2(\kappa^{-1})$ and a weight of convection ν in Eq.(2.51) for stabilizing the linear system:

$$-\lambda\nabla^2(\kappa^{-1}) + \frac{\nabla^2 B}{B}\kappa^{-1} + \nu\frac{\nabla B}{B} \cdot \nabla(\kappa^{-1}) = i\omega\mu_0, \tag{2.69}$$

where λ is an complex empirically determined diffusion coefficient, typically ranging from 0.005i to 0.05i [54] and ν is a convection coefficient [70].

2.6.2.2. Limitations

Compared to IB, GIB maintains the gradient term of EPs, resulting in fewer boundary artifacts and increased noise robustness. However, it retains the same assumptions, including $\nabla I_0 = 0$ and $B_1^+ \approx B_1^-$. The former can affect the accuracy at I_0 boundaries, and the latter should be verified at high field MRI (7T or above).

GIB is also part of the cr-EPT family and inherits the assumption $\nabla B_z = 0$, which is valid in the central region of the birdcage/TEM coil, and for tissue with slow EPs variations along the z-axis. Moreover, the complexity of computation and optimization of the regularization coefficients (λ and ν) present significant challenges.

2.7. Conversion to Surface Integral Form

To mitigate the noise amplification inherent in methods that rely on the Laplacian term, it is possible to convert their governing equations into a surface integral form using the divergence theorem [49], [52]. This conversion transforms the second-order derivatives into a form that integrates the normal first order derivates over the surface of a volume. By doing so, the need for direct computation of the Laplacian of B_1 at each grid point is eliminated, potentially improving the robustness against noise in B_1 measurements. This approach is applicable to all types of Laplacian-based EPT. The numerical differentiation and integration methods for surface-integral-based EPT will be described in Chapter 6.

2.7.1. Standard and cr-EPT

We can start with the governing equation of cr-EPT which is:

$$\beta^{\pm} \cdot \nabla(\kappa^{-1}) + \nabla^2 B_1^{\pm} \kappa^{-1} = i\omega\mu_0 B_1^{\pm}, \tag{2.70}$$

with

$$\beta^{\pm} = \begin{bmatrix} \frac{\partial B_1^{\pm}}{\partial x} \mp i\frac{\partial B_1^{\pm}}{\partial y} \\ \pm i\frac{\partial B_1^{\pm}}{\partial x} + \frac{\partial B_1^{\pm}}{\partial y} \\ \frac{\partial B_1^{\pm}}{\partial z} \end{bmatrix}. \tag{2.71}$$

Taking the divergence of $\beta^{\pm}$, it can be shown that:

$$\nabla \cdot \beta^{\pm} = \frac{\partial^2 B_1^{\pm}}{\partial x^2} + \frac{\partial^2 B_1^{\pm}}{\partial y^2} + \frac{\partial^2 B_1^{\pm}}{\partial z^2} = \nabla^2 B_1^{\pm} \tag{2.72}$$

Substituting Eq.(2.72) into Eq.(2.70), we obtain:

$$\beta^{\pm} \cdot \nabla(\kappa^{-1}) + \nabla \cdot \beta^{\pm} \kappa^{-1} = i\omega\mu_0 B_1^{\pm} \tag{2.73}$$

Using the product rule of divergence $\nabla \cdot (ab) = (\nabla a) \cdot b + a(\nabla \cdot b)$, we get:

$$\nabla \cdot (\beta^{\pm} \kappa^{-1}) = i\omega\mu_0 B_1^{\pm} \tag{2.74}$$

We take the volume integral on both sides of Eq.(2.74):

$$\iiint \nabla \cdot (\beta^{\pm} \kappa^{-1})\, dV = \iiint i\omega\mu_0 B_1^{\pm}\, dV \tag{2.75}$$

Applying the divergence theorem $\iiint \nabla \cdot \mathrm{F}\, dV = \oiint \mathrm{F} \cdot \hat{n}\ dS$ to the left side of (2.75), we get:

$$\oiint \beta^{\pm} \kappa^{-1} \cdot \hat{n}\ dS = \iiint i\omega\mu_0 B_1^{\pm}\, dV \tag{2.76}$$

where V is a volume in 3D space, S is the boundary surface, and $\hat{n}$ is the outward unit normal vector of the boundary S. For a volume of a 3×3×3 isotropic cube, the surface integral can be further calculated by the sum of its corresponding six surfaces and the volume integral can be calculated by the sum of these 27 voxel volumes.

Eq. (2.76) is the surface-integral form of cr-EPT, which does not include the Laplacian term and is also called Divergence-based EPT [49]. In Liu et al. 2021 [49], Eq. (2.76) was expressed as in the form of Ax=b via a Yee-Cell like mesh, where A is a coefficient matrix of the surface integral of $\beta^{\pm}$ (first derivatives of $B_1^{\pm}$), b is the volume integral of $B_1^{\pm}$, and x is the unknown vector of κ^{-1}. However, boundary conditions are required during the construction of A to avoid singularity.

If EPs are piecewise constant ($\nabla\kappa = 0$), we can take κ^{-1} out of the surface integral, yielding the surface integral form of Standard EPT [52]:

$$\kappa = \frac{\oiint \beta^{\pm} \cdot \hat{n}\ dS}{\iiint i\omega\mu_0 B_1^{\pm}\, dV} = \frac{\oiint \nabla B_1^{\pm}\ dS}{\iiint i\omega\mu_0 B_1^{\pm}\, dV} \tag{2.77}$$

2.7.2. PB and PB-cr EPT

Similarly, we can start with the governing equation of PB-cr EPT which is:

$$\nabla\varphi_{tr} \cdot \nabla(\sigma^{-1}) + \nabla^2\varphi_{tr}\sigma^{-1} = 2\omega\mu_0. \tag{2.78}$$

Using the product rule of divergence $\nabla \cdot (ab) = (\nabla a) \cdot b + a(\nabla \cdot b)$, we get:

$$\nabla \cdot (\nabla\varphi_{tr}\sigma^{-1}) = 2\omega\mu_0. \tag{2.79}$$

Eq.(2.79) can be transformed into a linear system Ax=b by the central difference method, however, A is easy to be singular. In Sun et al. 2020 [47], this issue was solved using second-order total generalized variation regularization.

We take the volume integral on both sides of Eq.(2.79):

$$\iiint \nabla \cdot (\nabla\varphi_{tr}\sigma^{-1})\, dV = \iiint 2\omega\mu_0\, dV \tag{2.80}$$

Applying the divergence theorem $\iiint \nabla \cdot \mathrm{F}\, dV = \oiint \mathrm{F} \cdot \hat{n}\ dS$ to the left side of (2.80), we get the surface integral form of PB-cr:

$$\oiint \nabla\varphi_{tr}\sigma^{-1} \cdot \hat{n}\ dS = \iiint 2\omega\mu_0\, dV \tag{2.81}$$

If conductivity is piecewise constant ($\nabla\sigma = 0$), we can take σ^{-1} out of the surface integral, yielding the surface integral form of PB [52]:

$$\sigma = \frac{\oiint \nabla \varphi_{tr} \; dS}{\iiint 2\omega\mu_0 \, dV} \tag{2.82}$$

2.7.3. IB and GIB EPT

Similarly, we can start with the governing equation of GIB EPT which is:

$$\frac{\nabla^2 B}{B}\kappa^{-1} + \frac{\nabla B}{B} \cdot \nabla(\kappa^{-1}) = i\omega\mu_0. \tag{2.83}$$

Multiplying B on both sides of the equation and using the product rule of divergence $\nabla \cdot (ab) = (\nabla a) \cdot b + a(\nabla \cdot b)$, we get:

$$\nabla \cdot (\nabla B \kappa^{-1}) = i\omega\mu_0 B. \tag{2.84}$$

We take the volume integral on both sides of Eq.(2.84):

$$\iiint \nabla \cdot (\nabla B \kappa^{-1}) \, dV = \iiint i\omega\mu_0 B \, dV \tag{2.85}$$

Applying the divergence theorem $\iiint \nabla \cdot \mathrm{F} \, dV = \oiint \mathrm{F} \cdot \hat{n} \; dS$ to the left side of Eq.(2.85), we get the surface integral form of GIB:

$$\oiint \nabla B \kappa^{-1} \cdot \hat{n} \; dS = \iiint i\omega\mu_0 B \, dV \tag{2.86}$$

If EPs are piecewise constant ($\nabla\kappa = 0$), we can take κ^{-1} out of the surface integral, yielding the surface integral form of IB:

$$\kappa = \frac{\oiint \nabla B \; dS}{\iiint i\omega\mu_0 B \, dV} \tag{2.87}$$

2.7.4. Limitations

Firstly, the surface-integral-based EPT, which requires volume integral calculation, is not suitable for 2D applications. This necessitates 3D acquisitions or more slices in 2D acquisitions, which may not be suitable for 2D spin echo sequences due to well-known random phase offsets between slices [71].

Additionally, the surface integral form of the cr-EPT family (cr-EPT, PB-cr, GIB) is often ill-conditioned even with boundary conditions. Improving numerical stability can be achieved by adding an artificial diffusion term or other regularization methods.

Due to the high computational complexity and numerical stability issues, only their simplified versions (standard EPT, PB, and IB) are more feasible for implementation. Numerically, the minimal surface integral kernel size is larger than the minimal Laplacian kernel size, finding a better trade-off between SNR and boundary artifacts [69]. Recently, it has been demonstrated [72], [73] that the surface

integral form surpasses its Laplacian form in terms of accuracy and edge preservation, making it a promising direction for future research and development in MR-EPT methods.

Chapter 3. EPT Data Acquisition Methods

The EPT reconstruction relies on the knowledge of the complex RF transmit/receive field $B_1^{\pm} = \left|B_1^{\pm}\right| e^{i\varphi^{\pm}}$, which requires two different sequences to measure magnitude $\left|B_1^{\pm}\right|$ and phase $\varphi^{\pm}$ separately. Extracting the precise values of B_1^{+} or B_1^{-} from MRI images remains challenging. Currently, only the magnitude of the transmit field $|B_1^{+}|$ is measurable, based on its relationship with the flip angle, typically using methods involving several MR scans, known as "$|B_1^{+}|$ mapping" technique. Moreover, absolute transmit phase φ^{+} or receive phase φ^{-} cannot be measured directly either. Only the combination of these two phases, referred to as the transceive phase ($\varphi_{TR} = \varphi^{+} + \varphi^{-}$), can be measured using specific sequences. Therefore, a common practice in EPT is to use half of the transceive phase ($\varphi^{+} = \varphi^{-} = \frac{\varphi_{TR}}{2}$), known as the "transceive phase assumption" (TPA).

Given the inaccessibility of absolute $|B_1^{-}|$ and phase $\varphi^{\pm}$ in MRI, the standard approach is to measure the transmit magnitude $|B_1^{+}|$ and the transceive phase φ_{tr}. These two types of pulse sequences—$|B_1^{+}|$ mapping and transceive phase measurement—will be summarized in the following sections. The common sequences are summarized in Table 3, highlighting their advantages and limitations.

Table 3. Summary of transceive phase (φ_{tr}) measurement and $|B_1^{+}|$ mapping methods.

	Sequences	Advantages	Limitations
φ_{tr} Measurement Methods	**SE** Spin Echo [65]	• Simple • Without off-resonance and chemical shift effects	• Slow • Sensitive to eddy current and motion effects
	MGRE Multi Gradient Echo [74]	• Able to simultaneously address EPT and QSM	• Spatial and temporal phase unwrapping issues • Sensitive to the measurement at the first TE
	UTE/ZTE Ultrashort/Zero Echo Time [53], [54]	• Fast • TE≈0, almost no off-resonance effects • Suitable for both Phase/Complex-Image-based EPT • Suitable for short T2* tissues, such as cortical bone and lung	• Eddy current effects
	bSSFP balanced Steady-State Free Precession [75]	• Fast and high SNR • Benign off-resonance behavior when $\Delta B_0 \approx 0$ • Insensitive to eddy current and flow or motion effects	• Sensitive to B_0 inhomogeneity • Banding artifacts

	Sequences	Advantages	Limitations
$\lvert B_1^+ \rvert$ Mapping Methods	**DAM** Double Angle Method [76]	• Simple	• Long TR and slow • T1 dependence
	DREAM Dual Refocusing Echo Acquisition Mode [77]	• One of the fastest B1 mapping methods • Low SAR	• Relative low accuracy • Sensitive to off-resonance and flow • Some T1, T2 dependences
	BSS Bloch-Siegert shift [78]	• Fast and accurate • Insensitive to off-resonance, T1, T2 and TR.	• Phase unwrapping issues • High SAR
	AFI Actual Flip Angle Imaging [79]	• Fast • Easy 3D acquisition • Insensitive to T1, T2	• Not suitable for low T1 regions • Sensitive to off-resonance
	satTFL Presaturation TurboFLASH [80], [81]	• Fast and SAR efficient • Insensitive to T1, T2, flow and motion	• Sensitive to off-resonance and chemical shift • Some T1 dependences

3.1. Transceive Phase Measurements

Neglecting phase wraps and chemical shifts, the phase measured with an RF coil in a gradient echo (GRE) and a spin echo (SE) sequence can be expressed as:

$$\varphi_{GRE} = \varphi_{tr} + \underbrace{2\pi\gamma\Delta B_0 \cdot TE}_{\varphi_{off}} + \varphi_{eddy} + \varphi_m \tag{3.1}$$

and

$$\varphi_{SE} = \varphi_{tr} + \varphi_{eddy} + \varphi_m. \tag{3.2}$$

Here, φ_{tr}, φ_{off}, φ_{eddy} and φ_m represent the phase contributions from RF transceive phase, off-resonance or B_0 inhomogeneity effects (cancelling out by 180° RF pulse in SE), eddy currents induced by gradient switching and patient or flow motion, respectively. Specially, φ_{off} in GRE is the term of interest for Quantitative Susceptibility mapping (QSM), which represents the phase shift caused by the derivation ΔB_0 of the magnetic field from the uniform main magnetic field B_0 and is linearly dependent on the echo time TE.

For EPT, the goal is to exclude all non-RF effects terms (φ_{off}, φ_m and φ_{eddy}) as much as possible, retaining only the transceive phase φ_{tr}. Four types of sequences are commonly discussed for measuring the transceive phase: Spin Echo (SE), balanced Steady-State Free Precession (bSSFP), Multi Gradient Echo (MGRE) and Ultrashort/Zero Echo Time (UTE/ZTE) sequences. A comparison of these sequences in conductivity phantoms will be discussed in Chapter 4. Additionally, my contributions to the implementation of phase-cycled bSSFP methods for removing banding artefacts, in comparison with UTE sequence, are presented in Section 3.1.5.

3.1.1. Spin Echo (SE)

Spin echo based sequences are the most straightforward method for transceive phase acquisitions due to their effective elimination of unwanted B_0-related contributions (φ_{off}) [5], [65] and their availability in all clinical MR scanners. The refocusing RF pulse not only rephases spins but also cancels out the phase shifts caused by B_0 field inhomogeneities, static tissue susceptibility gradients and chemical shifts, thereby automatically removing these phase artifacts, as expressed in Eq.(3.2). However, for a perfect measurement of φ_{tr}, the phase error effects of eddy currents (φ_{eddy}) and motion (φ_m) also need to be minimized.

Mitigating Eddy Currents

Eddy currents (φ_{eddy}) induced by gradient switching can distort the measured phase, leading to inaccuracies in the final images. A practical solution to this problem is to repeat the measurement with inverted gradient polarity. By averaging the results from these repeated measurements (either before or after EPT reconstruction), the distortions caused by eddy currents can be effectively canceled out [65], [82].

Addressing Flow Motion

Flow motion during scans can introduce additional phase errors (φ_m), complicating the accurate reconstruction of images. Since the flow motion from both vessel and capillaries is coherent, phase cancellation occurs at even echoes due to spin rephasing. As such, double spin echo sequences can be employed. These sequences use two refocusing pulses with a relatively long TE to correct motion-induced phase shifts, thereby enhancing the robustness of the imaging process against flow motion [83].

Improving SNR

Moreover, for high-quality imaging, multi-spin multi-echo (MSME) sequences can be utilized [84]. These sequences collect multiple echoes after each excitation pulse, providing a higher SNR by averaging the signals from different echoes.

Limitations

However, a significant drawback of standard spin echo (SE) sequences is their often-lengthy acquisition times (long TR), especially when volumetric datasets are required. This lengthy acquisition time can be impractical for clinical applications and patient comfort. Furthermore, multi-slice 2D spin echo sequences often exhibit well-known random phase offsets between slices [71], making them unsuitable for 3D Laplacian calculations, and thereby influencing EP reconstruction accuracy [85].

To address the issue of extended acquisition times and to facilitate 3D imaging, various 3D accelerated ("turbo/fast") sequence versions have been developed. These turbo/fast spin echo (TSE/FSE) sequences significantly reduce data acquisition time by rapidly cycling through multiple refocusing pulses with multiple phase-encoding lines after a single 90°-pulse. This approach not only speeds up the data collection process but also maintains the phase correction benefits inherent in SE sequences.

3.1.2. Multi Gradient Echo (MGRE)

Due to φ_{off} being negligible at TE=0, an alternative method for measuring φ_{tr} is to use a Multi Gradient Echo (MGRE) sequence and extrapolate the phase to TE=0 s. This phase extrapolation can be accomplished by fitting a simple linear model as a function of TE ($\varphi = \varphi_{tr} + 2\pi\gamma\Delta B_0 \cdot TE$) at each voxel. However, since phase values range from -π to π, phase unwrapping methods must be applied temporally and spatially before fitting. Techniques such as Laplacian unwrapping [86], region growing [87] and ROMEO [88] have been developed for this purpose.

As TE increases, phase artefacts caused by φ_m and φ_{eddy}, along with phase unwrapping errors, tend to accumulate, causing later echo points to deviate from a linear relationship [89]. If the echo train used for fitting is far from TE=0 s, accurately retrieving φ_{tr} at TE=0 s becomes challenging. Therefore, it is crucial to ensure that the echo times are sufficiently close to 0 s to minimize these errors and achieve a reliable phase extrapolation.

In this context, it may be preferable to directly use ultrashort/zero echo time (UTE/ZTE) sequences, which inherently minimize TE and thus reduce the associated phase errors. However, a significant advantage of MGRE sequences is their ability to simultaneously address EPT and Quantitative Susceptibility Mapping (QSM) in a single acquisition [74]. Recently, another kind of MGRE, Multi Gradient-Echo Echo-Planar Imaging (MGRE-EPI) sequence has been demonstrated to simultaneously handle functional MRI (fMRI), QSM, and EPT in a single acquisition [90]. This multi-functional capability makes MGRE sequences particularly valuable for comprehensive imaging studies, despite the challenges associated with phase unwrapping and extrapolation.

3.1.3. Ultrashort/Zero Echo Time (UTE/ZTE)

Due to the imaging encoding starting immediately (TE=0 s) after a non-selective short hard RF pulse with a low flip angle, UTE/ZTE sequences leave negligible time to induce phase changes because of external causes, such as B_0 inhomogeneity φ_{off}, chemical shift and flow motion φ_m [91]. This

characteristic makes UTE/ZTE highly effective in minimizing phase artefacts from these sources, thereby enhancing the accuracy of the pure transceive phase φ_{tr} measurement.

In my thesis, we used the UTE Spiral Volumetric Interpolated Breath-hold Examination (VIBE) sequence [92], [93], illustrated in Figure 6. In this sequence, spiral sampling is employed in the transverse k-xy plane, while Cartesian sampling is used along the kz direction. This stack-of-spirals trajectory as shown in Figure 6B can effectively reduce the minimum time required to cover k-space compared to a 3D radial trajectory. After the RF excitation, the duration of the slice-encoding gradient (Gz) varies with encoding step (kz), and each spiral readout starts immediately after the 3D phase encoding gradient (Gx and Gy). Hence, as depicted in Figure 6B, the TE varies with different slice-encoding steps. The minimum TE is achieved for the central slice where the slice-encoding gradient is not applied (kz = 0). As the slice-encoding gradient increases towards the outer slices, the TE also increases, reaching a maximum for the outermost slice (kz = ± max). Since the central slice primarily determines the overall contrast of the image, this approach ensures a minimum TE ($\approx 50\mu s$) for the overall 3D acquisition. Furthermore, if the variation of the imaged object in the z-direction is minimal or remains roughly uniform (e.g., a homogeneous cylindrical phantom), the off-resonance effects resulting from deviations in minimum TE can be considered negligible.

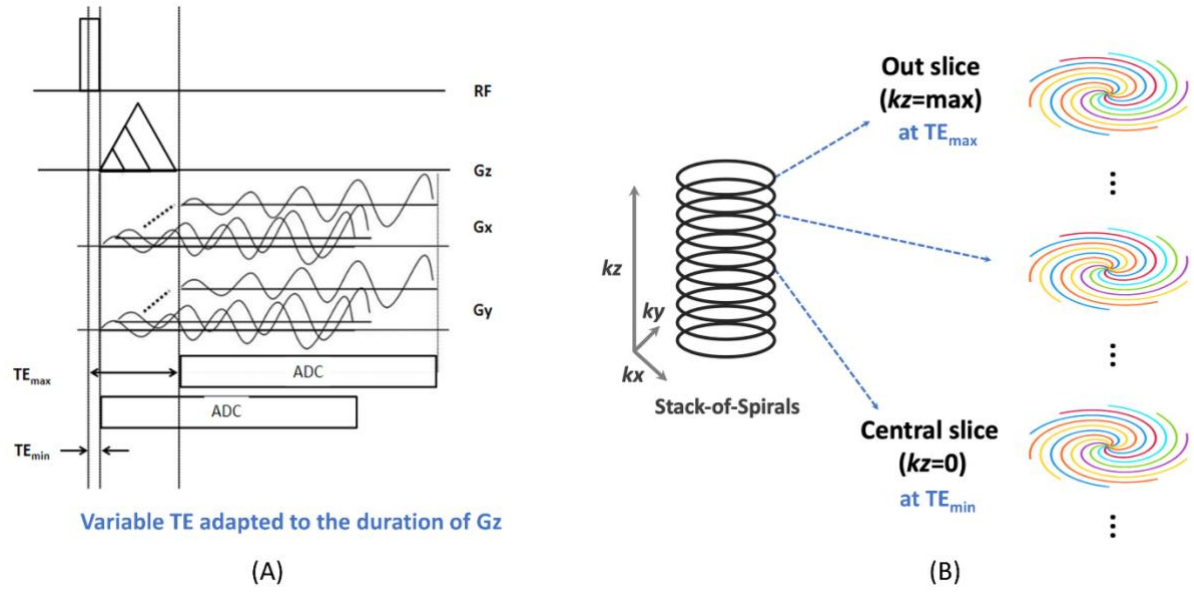

Figure 6. (A) Sequence diagram of the UTE Spiral VIBE acquisition. (B) Stack-of-spirals trajectory, adapted from Valentin et al., 2024 [94]. The stack-of-spirals are acquired in the transverse plane (k-xy) with Cartesian sampling along the kz direction. The variable TE is adapted to the duration of the slice-encoding gradient (Gz) for different image slices, ranging from minimum TE at kz=0 to maximum TE at kz=±max, with center-out sampling during data acquisition.

Additionally, UTE/ZTE enables visualization of short T2* tissues with high SNR, providing valuable quantification assessments of EPs for these tissues, such as cortical bone or lung. Moreover, the inherent

property of a low flip angle makes UTE/ZTE suitable for complex-Image-based EPT, allowing conductivity and permittivity reconstruction in a single acquisition.

However, despite these advantages, UTE/ZTE requires rapid gradient switching, resulting not only in acoustic noise but also in eddy-current-induced errors φ_{eddy}. Eddy currents are transient currents generated in conductive materials (including the human body, which acts like a large bag of saline) when exposed to changing magnetic fields, such as those used in MRI gradient switching. These currents can distort the magnetic field and introduce phase errors (φ_{eddy}) in the acquired images. To address this issue, several strategies can be employed in the design of phase-encoding (Gx and Gy) gradients. One approach is to lock the gradient polarity for each repeated update [53], reducing the abrupt transitions that can induce eddy currents. Another effective strategy is to add an opposite gradient field to balance the gradients. As shown in 6B, sinusoidal gradients of Gx and Gy partially compensate for the eddy current effects [54]. By incorporating these strategies, it has been demonstrated in phantoms that φ_{eddy} can be neglected in conductivity reconstruction [53], [54].

3.1.4. balanced Steady-State Free Precession (bSSFP)

As shown in Eq.(3.1), besides imaging at TE=0 s to eliminate φ_{off}, another method is to measure φ_{off} and exclude it from measured phase image:

$$\varphi_{off} = 2\pi\gamma\Delta B_0 \cdot TE = 2\pi\Delta f_0 \cdot TE. \tag{3.3}$$

Here, B_0 field inhomogeneity (ΔB_0) and off-resonance frequency (Δf_0) can be interchanged, introducing the gyromagnetic ratio $\gamma = 42.58$ MHz/T, using the definition $\Delta f_0 = \gamma\Delta B_0$. ΔB_0 can be measured from any kind of B_0 mapping. One particular sequence, which is very sensitive to ΔB_0 and exhibits the well-known banding artifacts, is called balanced Steady-State Free Precession (bSSFP) sequence. The bSSFP image phase is inherently insensitive to phase shifts such as φ_{eddy} and φ_m, due to its balanced gradients and short TR. Consequently, wherever there are no banding artifacts, it can be assumed that $\Delta B_0 \approx 0$, indicating benign off-resonance behavior [65], [75]. In this case, its phase is almost equal to φ_{tr}.

Advantages of Balanced Gradients

In a steady-state condition (TR << T2), tissue spins cannot fully relax after one TR. Spin dephasings occur due to gradient pulses and B_0 inhomogeneities. The extent of this dephasing within TR depends on the spatial position and the gradient's strength and duration. bSSFP sequences are designed so that the gradient-induced dephasing within TR is exactly zero [95]. This is achieved by counterbalancing the dephasing gradient lobe with an opposing rephasing gradient lobe in all three gradient axes (Gz, Gy, and Gx). This balance results in a single magnetization vector at the end of each TR.

Balanced gradients in bSSFP not only manage dephasing but also compensate for eddy current effects (φ_{eddy}) [65]. If the gradient is fully balanced at TE=TR/2, eddy current effects are inherently compensated. However, while the phase encoding gradients (Gy) are balanced in each TR, they may not balance at TE, inducing eddy current dephasing (φ_{eddy}). This φ_{eddy} can be compensated by alternating RF scheme of bSSFP ($+\alpha° \rightarrow -\alpha° \rightarrow +\alpha°$), a common version in bSSFP, which incorporates two identical phase encoding steps, called the "pairing strategy" [96]. In this approach an arbitrary line in k-space linked with one of its neighboring lines, intrinsically canceling the preceding dephasing by simply reproducing the same phase error but with an opposite sign in the succeeding step:

$$\varphi_{eddy}^{n+1} - \varphi_{eddy}^{n} \approx 0. \tag{3.4}$$

This ensures the phase is practically balanced before the next excitation, preventing long-standing residual eddy currents. If not sufficient, these effects can be eliminated by averaging two measurements with opposing gradient polarities [97].

Motion Robustness

In general, bSSFP shows robustness to flow or motion. Due to the short TR, the flow sensitivity of the bSSFP signal at TE is relatively small, adding only a minor phase shift (φ_m) to the corresponding k-space line and does not perturb steady state. For low flow velocities (below 0.5-1m/s), the "pairing strategy" using the alternating RF scheme can effectively compensate the flow dephasing [98]:

$$\varphi_{m}^{n+1} - \varphi_{m}^{n} \approx 0. \tag{3.5}$$

However, uncompensated first-order gradient moments can induce significant spin phase variations at high velocities. This can be addressed by nulling first-order gradient moments with a motion-compensated bSSFP scheme, though this comes at the cost of a 50% longer TR [98].

Off-resonance effects and Banding Artifacts

Despite the balanced gradient design and the alternating RF scheme, strong B_0 inhomogeneities can still cause additional dephasing, which modifies the resulting steady state and can lead to signal loss near dephasing angles of 180°, resulting in the well-known banding artifacts [95]. Neglecting chemical shift, motion and eddy current effects, the complex signal of bSSFP at TE using alternating RF pulses with a flip angle α can be expressed as [97], [99]:

$$S = KMe^{-\frac{TE}{T_2}} \frac{1 - ae^{-i(\theta_0+\pi)}}{1 - bcos(\theta_0 + \pi)} e^{i(2\pi\Delta f_0 \cdot TE + \varphi_{tr})} \tag{3.6}$$

where K is a scaling constant which includes the magnitude of the receive coil sensitivity, and θ_0 is a dephasing angle which is proportional to the off-resonance frequency Δf_0 and TR:

$$\theta_0 = 2\pi\Delta f_0 TR. \tag{3.7}$$

The definition of M, a and b are as follows:

$$a = E_2 = e^{-\frac{TR}{T_2}} \tag{3.8}$$

$$M = \frac{M_0(1 - E_1)\sin(\alpha)}{1 - E_1\cos(\alpha) - E_2^2(E_1 - \cos(\alpha))} \tag{3.9}$$

$$b = \frac{E_2(1 - E_1)(1 + \cos(\alpha))}{1 - E_1\cos(\alpha) - E_2^2(E_1 - \cos(\alpha))} \tag{3.10}$$

with $E_{1,2} = e^{-\frac{TR}{T_{1,2}}}$.

Specifically, when the dephasing angle θ_0 is near to 180° (i.e., $\Delta f_0 = \frac{1}{2TR}$), the middle component of numerator in Eq.(3.6) becomes:

$$1 - ae^{-i(\theta_0+\pi)} = 1 - a \approx 0 \tag{3.11}$$

due to $a = e^{-\frac{TR}{T_2}} \approx 1$ for the case of bSSFP where $TR \ll T_2$. Consequently, $S \approx 0$, resulting in a void signal, i.e., banding artifacts in both magnitude and phase images. To mitigate these artifacts, a shorter TR (3~5ms) allows a wider range of off-resonance frequencies ($\Delta f_0 = \frac{1}{2TR}$), making bSSFP less sensitive to B_0 inhomogeneities. Additionally, other strategies to reduce dephasing include local B_0 shimming ($\Delta B_0 \approx 0$) to minimize Δf_0 or choosing an optimal resonance frequency in a pre-scan to set the RF frequency before scanning.

The measured phase of bSSFP can be obtained by taking the angle of Eq.(3.6):

$$\varphi_{bSSFP} = \angle\left(1 - ae^{-i(\theta_0+\pi)}\right) + 2\pi\Delta f_0 \cdot TE + \varphi_{tr}. \tag{3.12}$$

Here, $a = e^{-\frac{TR}{T_2}} \approx 1$ due to $TR \ll T_2$. If the B_0 inhomogeneities are negligible ($\Delta f_0 \approx 0$), the dephasing angle can be therefore neglected ($\theta_0 = 2\pi\Delta f_0 TR \approx 0$), resulting in the phase of bSSFP being equal to φ_{tr}:

$$\varphi_{bSSFP} = \angle\left(1 - e^{-i\pi}\right) + \varphi_{tr} = \varphi_{tr}. \tag{3.13}$$

It has been demonstrated that if Δf_0 lies in the range $[-\frac{1}{3TR}, \frac{1}{3TR}]$ (around ±100 Hz at 3T), φ_{tr} is generally approximated by φ_{bSSFP}[97].

In summary, bSSFP is highly favorable for transceive phase measurement due to its high SNR and fast scan speed, achieved through the formation of multiple echoes and short TR. Although B_0 inhomogeneities must be carefully managed to avoid banding artifacts, the use of balanced gradients and the pairing strategy ensures phase stability and minimizes the effects of eddy currents. Additionally,

bSSFP demonstrates robustness against flow and motion artifacts, making it an interesting choice for accurate EPT reconstruction in cardiology [100].

3.1.5. Phase-Cycled bSSFP

It has been suggested that the optimal field for EPT is at 3T [42]. At this field strength, Δf_0 is twice as large at 3T compared to 1.5T, leading to more banding artifacts, especially when the ROI is large and patient susceptibility is high. To understand the impact, let's convert the Δf_0 range for banding artifacts-free imaging (around ±100 Hz at 3T) to a relative unit compared to Larmor frequency:

$$\frac{\Delta f_0}{f_{Larmor}} = \frac{100\ Hz}{128\ MHz} = 0.78\ ppm.$$

However, maintaining this level of homogeneity is challenging due to patient tissue susceptibility or implants. For example, the average B_0 homogeneity values are approximately 0.8 ppm for the brain and 1.6-3.2 ppm for the body with active B_0 shimming [101]. These values can range from 0 ppm in homogeneous tissues to 9 ppm at air/tissue boundaries, and as high as 10^4-10^{11} ppm near metal objects. Given these susceptibility variations, it is crucial to address Δf_0 effects to avoid banding artifacts for accurate φ_{tr} measurement.

The most common method to mitigate the banding artifacts is called phase-cycled bSSFP. In this method, multiple bSSFP acquisitions of the same anatomy are collected for a range of different RF phase-cycling increments ($\Delta\theta_n$) between [0 2π], yielding multiple images in which banding artifacts are spatially shifted with respect to each other. The phase-cycled signal can be expressed as [97]:

$$S_n = KMe^{-\frac{TE}{T_2}}\frac{1-ae^{-i(\theta_0-\Delta\theta_n)}}{1-bcos(\theta_0-\Delta\theta_n)}e^{i(2\pi\Delta f_0\cdot TE+\varphi_{tr})} \tag{3.14}$$

where $\Delta\theta_n = \frac{2\pi n}{N} - \pi$ with $n \in [1\ N]$ is the nth RF phase increment. Specially, when n=0, $\Delta\theta_0 = -\pi$, Eq.(3.14) returns the standard bSSFP signal equation (3.6). After these scans, combining or averaging the signals across phase cycles using methods such as complex-sum, maximum intensity projection or sum-of-squares reduces the severity of artifacts [99]. The reduction of banding artifacts improves as the number of RF phase cycles (N) increases, and the SNR can also benefit from these combinations. However, it is important to note that none of these techniques can completely remove banding artifacts when only a finite number of phase cycles are combined.

Recently, two advanced methods, PLANET [97] and fast Fourier transform (FFT) [102], have been proposed to more effectively remove banding artifacts and extract the pure transceive phase. In this section, we will discuss the implementation of these methods and compare them with the standard bSSFP and UTE sequences in a conductivity phantom and in a healthy volunteer brain within the context of phase-based EPT.

3.1.5.1. PLANET

Xiang and Hoff [103] demonstrated that Eq.(3.14) can be described by an ellipse model. Each measured complex value of the bSSFP signal acquired with a specific phase-cycling increment (Δθ) corresponds to a point in the complex plane on the ellipse, as shown in Figure 7. In fact, at TE=0 s, i.e., right after the RF excitation, the orange ellipse lies on the positive Mx-axis. This vertical-orientation ellipse is linked directly to M, a and b. The measured data points at TE form a rotated version of the ellipse (shown in blue), with an angle Ω that includes φ_{tr}:

$$\Omega = 2\pi\Delta f_0 \cdot TE + \varphi_{tr}. \tag{3.15}$$

PLANET proposes a geometric solution by fitting the ellipse constituted by phase-cycled bSSFP signals for a given voxel to estimate T1, T2, Ω, Δf_0, and thus φ_{tr}.

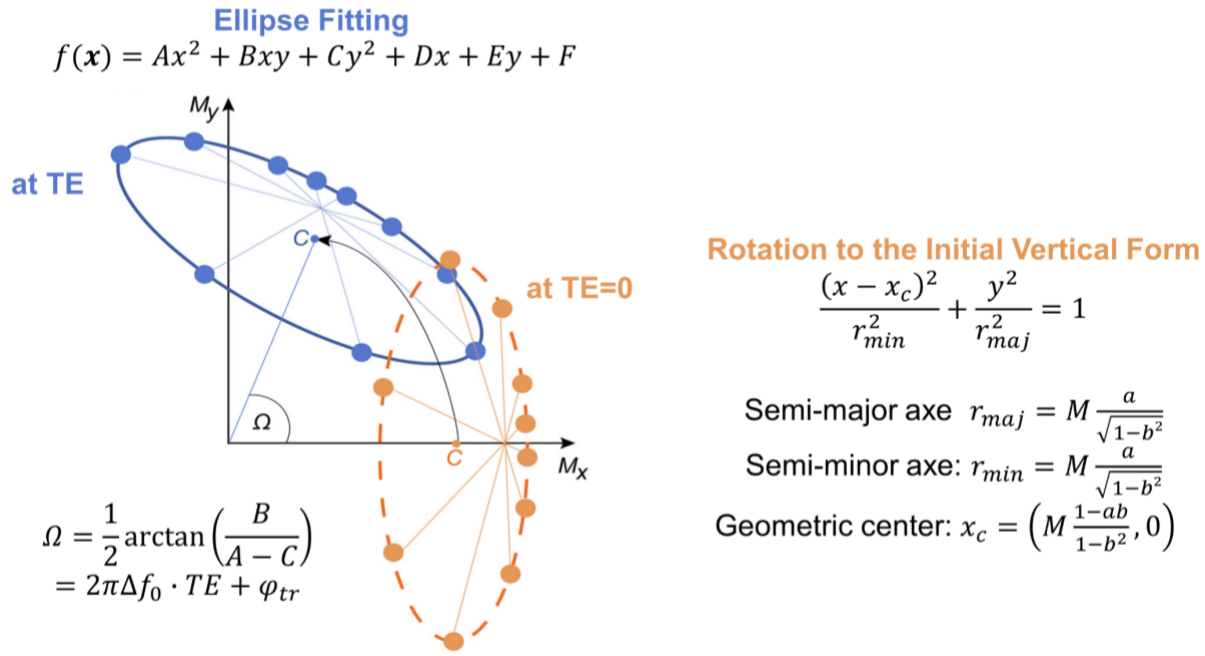

Figure 7. Adapted from Gavazzi et al. 2020 [97]. The complex bSSFP signal right after the RF excitation (at TE=0 s) defines a vertically-orientated ellipse (in orange). At TE, the ellipse rotates by an angle Ω to form the blue ellipse. The measured phase-cycled bSSFP data points are depicted as colored dots. The geometry of the orange ellipse is linked to the three parameters of bSSFP signal (M, a and b), establishing three equations with three unknowns that can be solved.

An ellipse can be described in a canonical form:

$$f(\boldsymbol{x}) = Ax^2 + Bxy + Cy^2 + Dx + Ey + F \tag{3.16}$$

where x and y are real and imaginary components of data points $\boldsymbol{x}$ and A through F are coefficients needed to fit. This can be considered as a second-order polynomial fitting problem, which can be solved by least-squares with at least six data points $\boldsymbol{x}$. The rotation angle Ω can be obtained by [104]:

$$\Omega = \frac{1}{2}\arctan\left(\frac{B}{A-C}\right). \tag{3.17}$$

After back-rotation by Ω, the coefficients are updated as follows:

$$\begin{cases} A' = Acos^2(\Omega) + Bsin(\Omega)\cos(\Omega) + Csin^2(\Omega) \\ B' = 0 \\ C' = A\,sin^2(\Omega) - Bcos(\Omega)\sin(\Omega) + Ccos^{2(\Omega)} \\ D' = Dcos(\Omega) + Esin(\Omega) \\ E' = Ecos(\Omega) - Dsin(\Omega) \\ F' = F - \left(\frac{D'^2}{4A'} + \frac{E'^2}{4C'}\right) \end{cases}. \tag{3.18}$$

The semi-major/minor axe (r_{maj}/r_{min}) and the geometric center (x_c, y_c) of the vertical-orientated ellipse, which link to bSSFP signal, can be obtained using theses updated coefficients:

$$\begin{cases} r_{maj} = \sqrt{\frac{-F'}{C'}} \\ r_{min} = \sqrt{\frac{-F'}{A'}} \\ x_c = \frac{-D'}{2A'} \\ y_c = \frac{-E'}{2C'} = 0 \end{cases}. \tag{3.19}$$

However, y_c may not strictly be zero due to noise, which can indicate a failed ellipse fitting. Additionally, as shown in Eq.(3.17), since Ω is defined within $[-\frac{\pi}{4}, +\frac{\pi}{4}]$ due to the arctan function's range of $[-\frac{\pi}{2}, +\frac{\pi}{2}]$, Ω may not ensure a vertical-orientated ellipse. Adjustments should be made when the following conditions occur:

1. If the ellipse is vertical but $x_c < 0$, $\Omega = \Omega - sign(\Omega) \cdot \pi$
2. If the ellipse is horizontal with $y_c > 0$, $\Omega = \Omega + \frac{\pi}{2}$
3. If the ellipse is horizontal with $y_c < 0$, $\Omega = \Omega - \frac{\pi}{2}$

Once the center x_c and semi-axes r_{min} and r_{maj} are known, we can calculate a, b and M in Eq.(3.14) using relationships illustrated in Figure 7 as follows [104]:

$$\begin{cases} b = \dfrac{-r_{min}x_c + r_{maj}\sqrt{x_c^2 - r_{min}^2 + r_{maj}^2}}{x_c^2 + r_{maj}^2} \\ a = \dfrac{r_{maj}}{x_c\sqrt{1-b^2} + r_{maj}b} \\ M = \dfrac{x_c(1-b^2)}{1-ab} \end{cases}. \tag{3.20}$$

Here, M corresponds to the banding-free magnitude image of bSSFP without any off-resonance dependency. Additionally, T1 and T2 values can be derived analytically with a and b [104]:

$$T_1 = -\frac{TR}{\ln\frac{a(1+\cos\alpha - ab\cos\alpha)-b}{a(1+\cos\alpha-ab)-b\cos\alpha}}, T_2 = -\frac{TR}{\ln a} \tag{3.21}$$

where α is the flip angle. Normally, α is set by the nominal flip angle user-controlled before the bSSFP scans. However, for better accuracy in T1 and T2 mapping, α should be replaced by the actual flip angle for each voxel by B_1 mapping techniques [105].

For transceive phase measurement, the dephasing angle θ_0, which is proportional to off-resonance frequency Δf_0, should also be derived. Using the expression of $\theta_N = \theta_0 - \Delta\theta_N$ and taking the cosine function on both sides $\cos(\theta_N) = \cos(\theta_0)\cos(\Delta\theta_N) + \sin(\theta_0)\sin(\Delta\theta_N) = K_1\cos(\Delta\theta_N) + K_2\sin(\Delta\theta_N)$, we can establish the following system of equations that can be solved by linear least-squares fitting approach with x_c, b, r_{min} and $\Delta\theta_N$:

$$\begin{bmatrix}\cos(\Delta\theta_1) & \sin(\Delta\theta_1)\\ \vdots & \vdots \\ \cos(\Delta\theta_N) & \sin(\Delta\theta_N)\end{bmatrix}\begin{bmatrix}K_1\\K_2\end{bmatrix} = \begin{bmatrix}\cos(\theta_1)\\ \vdots \\ \cos(\theta_N)\end{bmatrix} \tag{3.22}$$

where

$$\cos(\theta_n) = \frac{\cos\left(\frac{x_n - x_c}{r_{min}}\right) - b}{\cos\left(\frac{x_n - x_c}{r_{min}}\right)b - 1} \tag{3.23}$$

Then, the dephasing angle θ_0 and the off-resonance frequency Δf_0 can be obtained with K_1 and K_2 as follows:

$$\begin{aligned}\theta_0 &= \arctan\frac{K_2}{K_1} = 2\pi\Delta f_0 TR\\ \Delta f_0 &= \frac{\theta_0}{2\pi TR}.\end{aligned} \tag{3.24}$$

Here, Δf_0 can be converted to $\Delta B_0 = \gamma\Delta f_0$ in units of Tesla to estimate the B_0 homogeneity. Finally, substituting Eq.(3.24) into Eq.(3.15), we can obtain φ_{tr}

$$\varphi_{tr} = \Omega - 2\pi\Delta f_0 TE = \Omega - \frac{TE}{TR}\theta_0. \tag{3.25}$$

In summary, PLANET relies on an ellipse fitting to map T_1, T2 and banding free magnitude image M, along with an additional linear fitting to determine Δf_0 and φ_{tr}. The performance of these fittings and the SNR of reconstructed images improve as the number of phase increments or scans (N) increases, but this comes at the cost of longer acquisition times. Recently, N has been minimized to 4 using

constrained ellipse fitting combined with dictionary-based ellipse identification [105], significantly reducing the acquisition time while maintaining accuracy.

3.1.5.2. Fast Fourier Transform Method

The Fast Fourier Transform (FFT) method [102] provides direct access to the transceive phase from the set of phase-cycled bSSFP scans without the need for complex fitting procedures, unlike PLANET. This method exploits the periodic nature of the complex magnetization in bSSFP with respect to the RF phase increment ($\Delta\theta_N$), as shown in Eq.(3.14). This periodicity allows the representation of the magnetization in a Fourier (configuration) space, thereby linking the off-resonance frequency Δf_0 and the transceive phase φ_{tr} with the configuration modes. These parameters can be directly retrieved using FFT as follows:

$$\theta_0 = 2\pi\Delta f_0 TR = \pi + \angle\left(\frac{S^{(0)}}{S^{(-1)}}\right) \tag{3.26}$$

$$\varphi_{tr} = \frac{1}{2}\cdot\angle\left(S^{(0)}\cdot S^{(-1)}\right) \tag{3.27}$$

where $S^{(0)}$ and $S^{(-1)}$, which are two lowest-order components of FFT of N phase-cycled bSSFP signals S_N for a given voxel, correspond to the two middle elements of the result of the "ifft" (inverse fast Fourier transform) function after shifting to center in MATLAB. Additionally, the banding-free magnitude image of bSSFP can be also obtained using $S^{(0)}$ and $S^{(-1)}$ as follows:

$$M = \sqrt{\left|S^{(0)}\cdot S^{(-1)}\right|} \tag{3.28}$$

Similar to PLANET, the performance of the FFT method is also dependent on the number of phase cycles N. The off-resonance related phase error in the estimated φ_{tr} by FFT is modulated with a period of $2\pi/N$, indicating that its accuracy can benefit from more phase-cycled data. However, validation experiments have demonstrated [102] that the FFT method showed a lower noise propagation in most settings, making it a preferable choice for transceive phase estimation in practical applications.

3.1.5.3. Experimental Comparisons with Standard bSSFP and UTE

Objective

The objective is to evaluate the performance of PLANET and FFT methods for phase-based EPT, in comparison to a single scan of standard bSSFP and UTE. This study was conducted using a conductivity phantom and the brain of a healthy adult.

MRI data acquisitions

MRI measurements were performed on a 3T MAGNETOM Prisma MRI scanner (Siemens Healthineers, Erlangen, Germany), using a standard quadrature birdcage coil for transmission. A 20-

channel and 18+20-channel phased array coils were respectively used in receive mode for brain and phantom mapping, respectively.

Phantom scans: The phantom consisted of 1 liter of deionized water, 17 g agar and 2.5% mass concentrations of NaCl. Its EPs at Larmor frequency of our scanner 123 MHz were measured using an open-ended coaxial probe DAK12 (SPEAG, Zürich, Switzerland) connected to VNA [85] : $\sigma = 3.58$ S/m and $\varepsilon_r = 76$. For PLANET and FFT analysis, eight phase-cycled 3D bSSFP scans were acquired with RF phase increments of 0°, 45°, 90°, 135°, 180°, 225°, 270°, and 315°. For the phantom scans, a TE/TR of 2.2/4.4 ms was used, and the voxel size was set to 1 × 1 × 1 mm³ for an imaging matrix of 256 × 256 × 144. A single bSSFP scan took 1 minute 28 seconds, and scanning was completed in about 11 minutes 44 seconds. Additionally, UTE images with the same voxel and matrix sizes were acquired for comparison using a UTE Spiral VIBE sequence [92] (TE/TR = 50 µs/4.4 ms, FA = 2.5°, acquisition time = 5 min 40 s).

In vivo scans: This study was approved by an ethics committee (Comité de Protection des Personnes Sud Est III) and informed written consent was obtained (ClinicalTrials.gov identifier: NCT04645628, first trial registration 27/11/2020). A shorter TE/TR of 2.06/4.11 ms was used, and the voxel size was set to 1.3 × 1.3 × 1.3 mm³ for an imaging matrix o 192 × 192 × 144. A single bSSFP scan took 36 seconds, and scanning was completed in about 5 minutes. Additionally, UTE images were acquired with a voxel size of 0.675 × 0.675 × 1.3 mm³ for an imaging matrix of 384 × 384 × 144. A reference anatomical volume was also acquired using a conventional MPRAGE sequence. The UTE and MPRAGE images were resampled and re-aligned to the bSSFP images. The gray matter (GM), white matter (WM) and cerebrospinal fluid (CSF) were segmented from registered MPRAGE images using SPM's segmentation tool (SPM12, London, UK) for ROI analysis.

Transceive phase estimation

The 5th phase-cycled bSSFP image with a phase increment of 180° is considered to be the standard bSSFP images. The phase images of standard bSSFP and UTE directly represent the transceive phase. PLANET and FFT methods were performed on these eight phase-cycled bSSFP data to obtain banding-free magnitude and transceive phase images. All transcieve phase images were unwrapped into $[-\pi, +\pi]$ using the Laplacian method [86].

Conductivity reconstruction

The local conductivity was reconstructed by Phase-based EPT [65] assuming $\nabla\sigma \approx 0$ and $\nabla\left|B_1^{\pm}\right| = 0$, as follows:

$$\sigma \approx \frac{\nabla^2 \varphi_{tr}}{2\omega\mu_0}. \tag{3.29}$$

Due to Eq.(3.29) being valid in a homogenous region, the Laplacian was estimated by an adaptative Savitzky-Golay kernel. This kernel has a restricted shape determined by a reference image, which could be a mask or magnitude image, and is designed to fit the tissue size and shape for each kernel domain. For the phantom, a threshold segmentation was used as a reference image for Laplacian estimation, with a kernel size of [11 11 11]. For the brain, the MPRAGE images were used as a reference image for Laplacian estimation, with a kernel size of [21 21 21].

Phantom Result

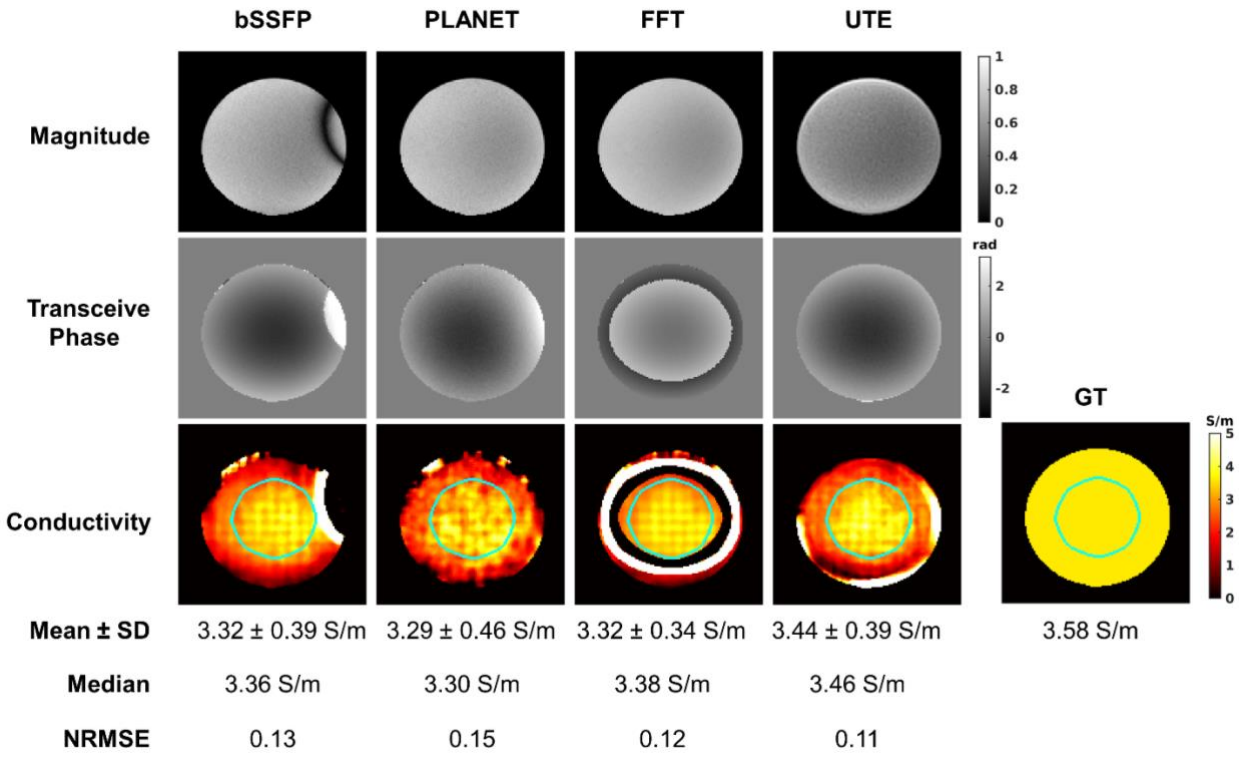

Figure 8. Middle slices of magnitude, transceive phase and conductivity maps obtained using different transceive phase measurements methods on a conductivity gel phantom (2.5% NaCl): standard bSSFP, PLANET, FFT and UTE. The ground-truth (GT) conductivity map, measured by VNA, is also provided in the bottom-right corner. The ROIs depicted in cyan, used for quantification, were eroded by a disk-shaped structure element with a radius of 20 pixels. The mean, standard deviation (SD), median and normalized root mean square error (NRMSE) calculated within the ROI are shown below the conductivity maps.

The magnitude, transceive phase and reconstructed conductivity maps, along with the mean, standard deviation (SD), median as well as normalized root mean square error (NRMSE) are shown in Figure 8 for each transceive phase measurement method. The standard bSSFP images exhibit typical banding artifacts in both magnitude and transceive phase images, and its reconstructed conductivity map is also affected by these effects. Both PLANET and FFT provide banding-free magnitude and transceive phase images. However, their signal-to-noise ratio (SNR) levels of transceive phase differ, affecting the homogeneity of reconstructed conductivity maps and the standard deviation (SD) values of reconstructed conductivity. Specifically, PLANET has the lowest SNR, followed by standard bSSFP,

with FFT having the highest SNR. This discrepancy may be attributed to inaccurate parameter estimations including the ellipse fitting in the PLANET method. However, FFT transceive phase images exhibit phase wrappings, which cannot be eliminated by Laplacian unwrapping method, resulting in inaccurate conductivity reconstruction near the boundaries. In contrast, the transceive phase images of PLANET, which use the same data, are free of phase wrapping. Moreover, the transceive phase images of bSSFP, FFT and UTE are similar.

For a fair comparison on conductivity, an eroded ROI depicted in cyan in Figure 8 was chosen on the wrapping-free region of conductivity maps for quantification. For conductivity reconstruction, all methods show typical boundary artifacts. UTE has the lowest NRMSE (0.11) and its mean (3.44 S/m) and median (3.46 S/m) values are the closest to the ground truth (3.58 S/m). However, FFT has the smallest standard deviation (0.34 S/m) and the second lowest NRMSE (0.12).

In vivo Result

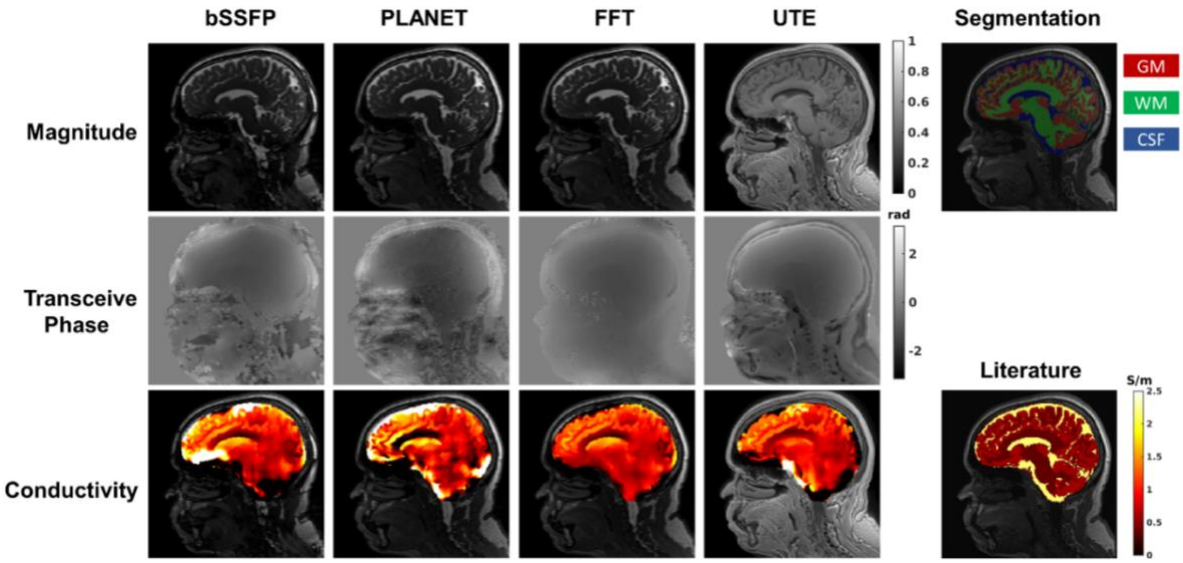

Figure 9. Middle slices of magnitude, transceive phase, and conductivity maps obtained using different transceive phase measurement methods on a healthy adult brain: standard bSSFP, PLANET, FFT, and UTE. Additionally, the MPRAGE image fused with segmentation labels (gray matter in red, white matter in green, and CSF in blue) and the literature conductivity map (from Gabriel et al. 1996 [28], [29], [30]) are provided.

The magnitude, transceive phase and reconstructed conductivity maps, along with the segmentation labels and the literature ex vivo conductivity map (from Gabriel et al. 1996 [28], [29], [30]), are shown in Figure 9. Compared to the standard bSSFP images, PLANET and FFT effectively remove banding artifacts from both magnitude and transceive phase images, resulting in cleaner conductivity images. While their magnitude images appear almost identical, the transceive phase image of PLANET provides more structure information but it is the noisiest. Visually, the UTE transceive phase appears the cleanest of all.

For conductivity reconstruction, all methods show typical boundary artifacts. The conductivity map of PLANET is particularly sensitive to the CSF, representing the highest values of CSF compared to FFT and UTE. In contrast, UTE is relative insensitive to the CSF, with some CSF values near the boundaries being underestimated or even missing.

Table 4. Mean reconstructed conductivity values (S/m) and standard deviations along with median values via each transceive phase measurement methods (bSSFP, PLANET, FFT and UTE) with two-voxels boundary erosions. The literature values from (from Gabriel et al. 1996 [28], [29], [30]) at 123 MHz are also provided.

	Literature	**bSSFP**		**PLANET**		**FFT**		**UTE**	
	at 123MHz	Mean ± SD	Median	Mean ± SD	Median	Mean ± SD	Median	Mean ± SD	Median
GM	0.58	0.23 ± 1.36	0.51	1.03 ± 1.12	0.98	0.75 ± 0.33	0.74	0.47 ± 0.96	0.74
WM	0.34	0.66 ± 0.70	0.64	0.74 ± 0.34	0.70	0.68 ± 0.16	0.66	0.81 ± 0.27	0.77
CSF	2.14	1.18 ± 1.28	1.35	1.92 ± 1.45	1.58	0.95 ± 0.68	1.07	0.81 ± 1.84	1.07

Table 4 presents the mean conductivity values, standard deviations, and median values in the WM, GM, and CSF tissue segmentations with 2-voxel boundary erosions to minimize boundary artifacts. Except for CSF and the case of GM in bSSFP, all conductivity values are overestimated by approximately 0.3-0.4 S/m compared to the literature values.

PLANET provides the closest CSF conductivity values to the literature, in terms of both mean and median. The median values of FFT and UTE are consistent, though their mean values differ. Notably, PLANET and FFT methods yield higher conductivity in GM compared to WM, which aligns with the literature, whereas UTE shows comparable or even inversely related conductivity values for GM and WM. This inverse can also be observed in bSSFP. Regarding standard deviations, FFT has the lowest standard deviations, followed by UTE, PLANET, and bSSFP. This variation in standard deviations reflects the differing SNR levels of the transceive phase measurements for each method.

Discussions and Conclusions

The standard bSSFP phase images with banding artifacts are unsuitable for conductivity reconstruction. PLANET and FFT methods can effectively and successfully remove these banding artifacts in both magnitude and phase images, providing cleaner conductivity reconstruction. While PLANET and FFT methods generate almost the same banding-free magnitude images, the reconstructed images of FFT exhibit less noise than those from PLANET, i.e., indicating a higher SNR. PLANET method requires several parameter estimations, and the cumulative errors during this process affect the resulting transceive phase quality, potentially degrading the SNR level compared to a single bSSFP scan. Additionally, the median values of FFT reconstructed conductivity, both in phantom and in vivo (GM

and WM), align better with those from PLANET. Therefore, it is recommended to use the FFT method for transceive phase mapping.

In general, phantom conductivities are in good agreement with the VNA measurement. However, almost all in vivo values, except for CSF, are overestimated compared to the literature values. This discrepancy may be due to differences between the physiological environment in vivo and ex vivo [24] or the inherent systematic error of phase-based EPT [42], which assumes that the B_1 magnitude is spatially constant. Additionally, CSF pulsation can induce motion phase errors in transceive phase measurements [106].

UTE provides clean transceive phase, with minimal phase wrapping issues, likely due to its ultra-short TE. Additionally, UTE acquisition time is shorter than that of phase-cycled bSSFP sequences. However, bSSFP sequences demonstrate better motion insensitivity than the UTE sequence, yielding CSF conductivity values closer to the literature values. Among the methods, PLANET is robust for CSF conductivity estimation despite having high standard deviations, indicating its potential for heart or flow conductivity estimation.

3.2. $|B_1^+|$ Mapping methods

Unlike transceive phase mapping, the $|B_1^+|$ information cannot be directly acquired from MR sequences. It must be derived from a model describing the sequence-specific B_1^+ encoding mechanism. This requires at least two acquisitions in a given voxel to exclude all non-$|B_1^+|$ related contributions (such as relaxation parameters T1 and T2 and coil sensitivity B_1^-). As a result, $|B_1^+|$ mapping methods often involve longer acquisition time and limited spatial resolution. Additionally, the two images acquired at different times should be registered to avoid motion effects, which is particularly challenging for moving organs.

The $|B_1^+|$ field in MRI serves to flip the initial magnetization (M_0) to the transverse xy-plane with a flip angle α. The relation between $|B_1^+|$ and flip angle α in a hard pulse is defined as follows:

$$\alpha = \gamma\tau|B_1^+| \tag{3.30}$$

where $\gamma = 42.58$ MHz/T is the gyromagnetic ratio and τ is the RF pulse duration. As such, $|B_1^+|$ map can be obtained by extracting the flip angle component from the MRI signal. Generally, τ in MR sequences is not disclosed to operators, so $|B_1^+|$ is often obtained in units of degrees or radians rather than in T, i.e., also known as "actual flip angle" map. However, the knowledge of absolute value of $|B_1^+|$ is not required for EPT because the differential terms $\frac{\nabla|B_1^+|}{|B_1^+|}$ or $\frac{\nabla^2|B_1^+|}{|B_1^+|}$ in the central equations factors out the scaling factor ($\gamma\tau$) in the denominator.

$|B_1^+|$ mapping methods are generally divided into two categories: magnitude-based methods and phase-based methods.

Magnitude-based Methods: These methods encode $|B_1^+|$ variations into the magnitude of the MR signal. They typically acquire two magnitude images, each with different sensitivity to $|B_1^+|$ variations but with the same sensitivity to other effects such as T1, T2 and B_1^-. For example, double angle method (DAM) acquires two images with different flip angles, where the second angle is twice the first ($\alpha_2 = 2\alpha_1$); actual flip angle imaging (AFI) [79] acquires two images with two identical RF pulses followed by two different repetition times ($TR_2 > TR_1 \gg$ T1). By taking the ratio of the magnitudes of these two images, any non-$|B_1^+|$ related variations are factorized out. However, these methods require a relatively long TR to eliminate T1 effects, resulting in long acquisition times. In practice, they often have limited spatial resolution or use 2D acquisition to reduce acquisition time. This insufficient sampling discretization leads to inaccuracies in EPs reconstruction. To reduce the acquisition time, the dual refocusing echo acquisition mode (DREAM) [77] technique measures these two magnitude images (the stimulated echo and the FID signals quasi-simultaneously) in a single acquisition, resulting in a short TR of 3.2 ms, making it one of the fastest B_1 mapping methods.

Phase-based methods: These methods encode $|B_1^+|$ variations into the phase of MR signal. They acquire two phase images with different phase sensitivities to $|B_1^+|$ variations while maintaining the same sensitivity to other sources. For example, Bloch-Siegert shift (BSS) method [78] acquires two phase images with opposite offset RF frequencies far from resonance. These off-resonance frequencies impart a phase shift in MRI images, which is proportional to $|B_1^+|^2$. Taking the phase difference between the images extracts the signal dependence on B_1 while canceling out sensitivities to other sources. Phase images are generally insensitive to relaxation effects (T1 and T2), making phase-based methods less sensitive to relaxation effects and offering greater accuracy compared to magnitude-based methods.

In Gavazzi et al., 2019 [107], three B_1 mapping methods— AFI, BSS and DREAM—are compared for permittivity reconstruction in simulations, phantoms and in vivo measurement at 3T. It has been demonstrated that although DREAM provides the fastest acquisition, AFI and BSS are recommended for permittivity estimation due to their accuracy. However, these advanced methods may not be available on all clinical MR scanners for commercial or technical reasons. The most common method remains DAM due to its ease of implementation, which can be achieved with two acquisitions of gradient echo or spin echo based-sequences. Along with AFI, DAM is often considered as a gold standard when validating the new $|B_1^+|$ mapping methods. Unfortunately, AFI is not available on our version of Siemens Prisma MR scanner. However, another magnitude-based $|B_1^+|$ mapping sequence faster than DAM, call pre-saturation TurboFlash (presatTFL), is available on Siemens systems. Consequently, the following sections will focus on the details of DAM, AFI and presatTFL [80], [81].

3.2.1. Double Angle Method

The Double Angle Method (DAM) [76] is one of the simplest $|B_1^+|$ mapping techniques available. It involves acquiring two magnitude images with different flip angles, where $\alpha_2 = 2\alpha_1$. Neglecting the T1, T2 relaxation effects, the acquired MRI signal can be approximated by:

$$S \approx M_{xy}B_1^- = M_0 \sin(\alpha)\, e^{i\varphi^+} B_1^- \tag{3.31}$$

where M_0 is the initial magnetization, α is flip angle, φ^+ is the RF transmit phase, and B_1^- is the complex reception field or coil sensitivity. By taking the ratio of the magnitude images acquired with flip angles α and 2α, we get:

$$r = \frac{|S_2|}{|S_1|} = \frac{\sin(2\alpha)}{\sin(\alpha)} = \frac{2\sin(\alpha)\cos(\alpha)}{\sin(\alpha)} = 2\cos(\alpha) \tag{3.32}$$

The ratio eliminates M_0 and B_1^- from the equation, allowing us to derive the flip angle α:

$$\alpha = \arccos\left(\frac{r}{2}\right). \tag{3.33}$$

Once α is known, $|B_1^+|$ can be directly mapped using the relationship described in Eq.(3.30):

$$|B_1^+| = \frac{1}{\gamma\tau}\alpha = \frac{1}{\gamma\tau}\arccos\left(\frac{r}{2}\right). \tag{3.34}$$

DAM is suitable for both standard gradient echo and spin echo-based sequences, provided that all sequence parameters except the flip angle are identical in both acquisitions. This includes ensuring that the refocusing pulse in the spin echo sequence is the same for both acquisitions [76]. While the transverse relaxation (T2) effects are cancelled out in the ratio, the longitudinal relaxation (T1) effects which depend on the last longitudinal magnetization (M_z), may not be fully canceled in a short TR. If M_z just before the next RF pulse (i.e., at TR) does not return to the initial maximum magnetization M_0 due to the recovery process governed by T1 relaxation, M_z is weighted by the flip angle, and cannot be completely canceled in the ratio:

$$M_z = M_0\left(\frac{1 - e^{-TR/T1}}{1 - \cos(\alpha)e^{-TR/T1}}\right). \tag{3.35}$$

Consequently, to eliminate these T1 dependences, a long TR ($TR \geq 5T1$) should be chosen to ensure $1 - e^{-\frac{TR}{T1}} \approx 0$. This leads to a long acquisition time. Additionally, since DAM requires double angle acquisitions, the total acquisition time can reach up to 20 min for a 3D volume. To avoid long TR and reduce acquisition time, T1 mapping techniques could be used to correct the T1 dependences before or during the ratio process [108].

3.2.2. Actual Flip Angle Imaging

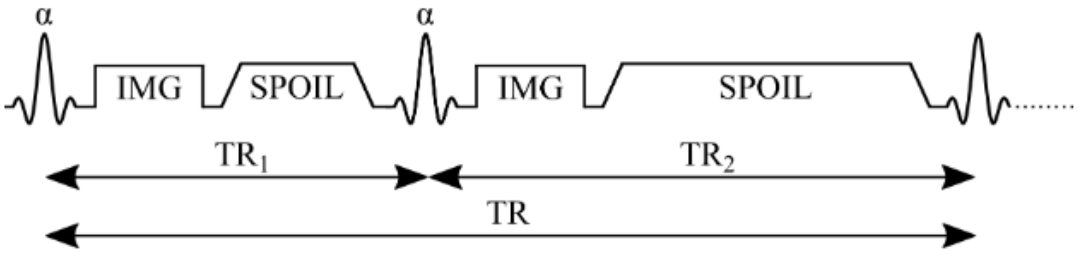

Figure 10. Simplified AFI sequence diagram, taken from qmrlab.org. The AFI method pulse sequence uses a steady-state spoiled gradient-echo acquisitions with two different repetition times TR_1 and TR_2 after two identical RF pulses with flip angle α.

Unlike DAM, which uses different flip angles, the actual flip angle imaging (AFI) methods [79] uses two different TRs to encode $|B_1^+|$ variations into the signal magnitude. As shown in Eq.(3.35), the term $\cos(\alpha)$ which involves $|B_1^+|$ information, will remain in the ratio of the two magnitude images acquired with different TRs. This allows for a much freer choice of TRs, allowing the use of short TRs while minimizing T1 effects ($TR_1 < TR_2 \ll T_1$).

Figure 10 shows the simplified AFI sequence diagram. The AFI technique is a steady-state spoiled gradient-echo sequence with two interleaved repetition times TR_1 and TR_2 after two identical RF pulses with a flip angle α. Two images are acquired in each TR interval. Additionally, the sequence is spoiled at the end of each TR to eliminate all transverse magnetization and T2 relaxation before the next RF pulse. Under the assumption that $TR_1 < TR_2 \ll T_1$, the T1 relaxation effects can be ignored. The ratio of these two magnitude images is then related to the flip angle as follow:

$$r = \frac{|S_2|}{|S_1|} \approx \frac{1 + n\cos\alpha}{n + \cos\alpha} \tag{3.36}$$

where $n = \frac{TR_2}{TR_1}$. Finally, the actual flip angle can be calculated as follow:

$$\alpha = \arccos\left(\frac{rn - 1}{n - r}\right). \tag{3.37}$$

In practice, it is recommended to set a nominal flip angle range of 20°~70° for accurate $|B_1^+|$ mapping. Additionally, using a n ranged between 4 to 6 (e.g. $TR_1/TR_2 = 20/100$ ms) provides a sufficient signal ratio r and sensitivity to $|B_1^+|$ variations. These short TRs make the AFI method suitable for fast 3D $|B_1^+|$ mapping. The acquisition time can benefit from the shortest possible TR_1 value, although it is limited by sequence design and hardware. However, the accuracy of the method decreases for very short T_1 values (<200 ms), in regions with flow, and in off-resonance areas [79].

3.2.3. Presaturation TurboFLASH (satTFL)

According to the rotation matrix, the longitudinal residual magnetization (M_z) can be expressed with a flip angle α and the initial maximum magnetization (M_0):

$$M_z = M_0 \cos \alpha \,. \tag{3.38}$$

The flip angle α can therefore be solved as:

$$\alpha = \arccos\left(\frac{M_z}{M_0}\right). \tag{3.39}$$

Chung et al., 2009 [80] proposed replacing the ratio of $\frac{M_z}{M_0}$ by the ratio of two magnitude images acquired with and without a preconditioning (also called presaturation) RF pulse using the prestaturation TurboFLASH (satTFL) sequence:

$$\alpha_{sat} = \arccos\left(\frac{|S_{sat}|}{|S_{no\ sat}|}\right) \tag{3.40}$$

where α_{sat} is the nominal saturation RF pulse angle (typically of order 60°-120°). Here, $|S_{sat}|$ is the magnitude images captured immediately after the presaturation RF pulse using the TurboFLASH readout sequence. $|S_{no\ sat}|$, acquired without the presaturation pulse, is considered as a reference image, also called proton density image.

The satTFL method requires a significant delay (typically 5T1) between the reference image $S_{no\ sat}$ and the preconditionned image S_{sat} to enable full relaxation to avoid T1 dependences, similar to DAM. Despite this delay, the satTFL sequence is faster than DAM, which requires two separate acquisitions with a total TR that is effectively double that of 5T1. Additionally, the use of small excitation flip angles in the TurboFLASH readout makes the satTFL method more SAR efficient. However, the satTFL method is sensitive to off-resonance effects and chemical shift artifacts. Additionally, achieving uniform saturation across the whole subject is difficult in practice, and may raise SAR concerns at 7T. Recent advancements, such as those demonstrated by Kent et al., 2023 [81], have shown that by reducing the delay to zero, the T1 contrast in $S_{no\ sat}$ can be matched in S_{sat}. This innovation allows for the implementation of fast 3D acquisition with reduced T1 bias, further enhancing the speed and efficiency of $|B_1^+|$ mapping.

Chapter 4. Phantom Evaluation of Electrical Conductivity by EPT

4.1. Introduction

In previous chapters, numerous MR-EPT reconstruction methods and EPT data acquisitions techniques were introduced. Evaluating the performance of MR-EPT is crucial for developing the aforementioned applications. However, there is a lack of systematic studies that would allow answering the following two key questions: what is the accuracy of MR-EPT in terms of absolute quantification? And what is the spatial resolution limit of MR-EPT?

Absolute quantification refers to the accuracy and precision of the reconstructed EP values compared to a gold standard, while the spatial resolution limit refers to the ability of EPT to detect and quantify EP changes in small structures. Documenting and improving these performances are necessary for EPT to become a clinical standard. Reconstruction algorithms have been evaluated previously using synthetic B_1 field data. However, these simulations generally use the same birdcage coil model for RF transmission (B_1^+ field) and reception (B_1^- field) so they do not include the use of receive coil arrays and coil combination methods [46], [49], [54], [109]. In terms of absolute quantification, some studies compared EPT [46], [102], [109] to EP values estimated from salt concentration [110] in phantoms, but few studies used an open-ended coaxial probe, connected to a vector network analyzer (VNA), to measure EPs at Larmor frequency. The latter method is considered as the gold standard for EP measurements. It was used to build the databases of EP values in biological tissues [24], [28], [29], [30] - created mainly from *ex vivo* human samples and animal studies - that are widely used for human SAR modelling for instance.

Spatial resolution is also a concern because EPT quantifies small modulations of the RF waves, which are intrinsically changing slowly in space. As differential methods in EPT rely on the estimation of spatial derivatives, the slow spatial changes result in a low signal-to-noise ratio for tissue structures in the mm range, which makes their reconstruction difficult [56]. Moreover, certain methods referred to as simplified versions in this paper (PB and IB) explicitly assume that EPs are piecewise constant, allowing the reconstruction of large homogeneous regions but this may not hold in regions with small tissue structures, and usually results in boundary artifacts [55], [111]. Overall, to our knowledge, few studies have specifically addressed on the object resolution limit of EPT.

In this chapter, we investigated four widely used MR-EPT reconstruction methods described previously in Chapter 2: Phase-based Helmholtz (PB), Phase-based convection-reaction (PB-cr), Image-based (IB) and Generalized-Image-based (GIB). We evaluated the performance of these differential

MR-EPT methods through phantom experiments, in terms of absolute quantification and resolution limit. Bobowski and Johnson's [31] VNA measurement method was used as a reference. We focused on conductivity σ which has given the most promising results and which has more direct applications, such as SAR calculation, diagnostic value in oncology, etc. The objectives of the study are twofold: 1) to design dedicated phantoms and an experimental protocol for evaluating the performance of MR-EPT; 2) to compare the four differential EPT reconstruction methods, and various sequences for transceive phase acquisition.

This study resulted in three conference presentations:

- **He Z**, Loureiro de Sousa P, Ambarki K, Lefebvre PM, Odille F. Validation sur fantômes et évaluation de la résolution des méthodes MR-EPT : Comparaison avec les mesures VNA. In: *Proceedings of 6th Congrès scientifique de la Société Française de Résonance Magnétique en Biologie et Médecine (SFRMBM)*. Paris, France; 2023:079. (Power Pitch + Poster)
- **He Z**, Loureiro de Sousa P, Ambarki K, Lefebvre PM, Odille F. Phantom validation of MR-EPT: comparison to vector network analyzer and resolution assessment. In: Proceedings of 2022 Joint Workshop on MR phase, magnetic susceptibility and electrical properties mapping (*QMR Lucca).* Lucca, Italy; 2022:S04.OR08_EPT.015. (Oral)
- **He Z**, Doguet M, Soullié P, Loureiro de Sousa P, Lefebvre P, Odille F. Comparison and validation of multiple MR-EPT methods with ground truth vector network analyzer measurements. In: *Proceedings of 30th Annual Meeting of International Society of Magnetic Resonance in Medicine (ISMRM*). London, UK; 2022:2910. (Digital Poster)

And one published article:

- **He Z,** Lefebvre PM, Soullié P, Doguet M, Ambarki K, Chen B, Odille F. Phantom evaluation of electrical conductivity mapping by MRI: Comparison to vector network analyzer measurements and spatial resolution assessment. *Magn Reson Med.* 2024; 1-17. doi: 10.1002/mrm.30009

4.2. High Frequency EP Measurements by Vector Network Analyzer (VNA)

The EPs of a dielectric material can be measured by means of an open-ended coaxial probe connected to a VNA (Figure 11A). The VNA allows the measurement of reflection coefficient denoted as ρ_m for a material under test (MUT). The reflection coefficient is defined as the ratio between the reflected signal and incident signal, and it is related to the load impedance and characteristic impedance of the line (Z_0). When the probe is in contact with the MUT, this is equivalent to the probe impedance being in parallel with the MUT's impedance. In this way, the impedance of the transmission line and the probe need to be considered at high frequencies using a calibration procedure described hereafter, in order to

relate measured reflection coefficient (ρ_m, at the VNA test port) to the desired reflection coefficient at the probe tip (Γ), which is directly related to the MUT's relative permittivity (ε_r) and conductivity (σ) [31] by:

$$\Gamma = \varepsilon_r - j\frac{\sigma}{\omega\varepsilon_0}. \tag{4.1}$$

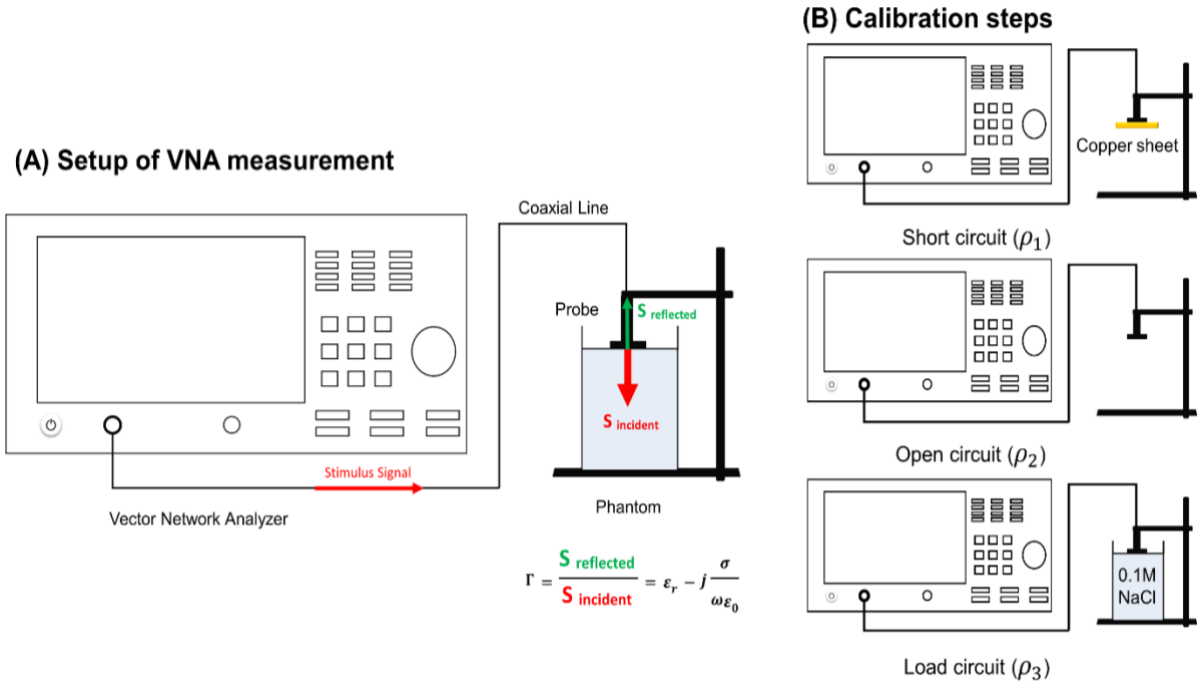

Figure 11. Setup of VNA measurement (A) and Calibration steps (B).

Using a two-port network model between the VNA test port and the probe tip, the calibration consists of measuring the reflection coefficients with three standard terminations of the probe: short-circuit (ρ_1), open-circuit (ρ_2), and loaded-circuit with the probe immersed into a standard load (ρ_3). The calibration method proposed by Bobowski [31] (Figure 11B) consists of calculating three parameters A_1, A_2, A_3 as follows :

$$A_1 = \frac{(\rho_2 - \rho_1) + (\rho_1 - \rho_3)(\varepsilon_r^s - j\frac{\sigma^s}{w\varepsilon_0})}{\rho_3 - \rho_2} \tag{4.2}$$

$$A_2 = \frac{\rho_3(\rho_2 - \rho_1) + \rho_2(\rho_1 - \rho_3)(\varepsilon_r^s - j\frac{\sigma^s}{w\varepsilon_0})}{\rho_3 - \rho_2} \tag{4.3}$$

$$A_3 = \rho_1 \tag{4.4}$$

where ε_r^s and σ^s are the relative permittivity and conductivity of the standard load with known EP values. The reflection coefficient Γ at the probe tip is then calculated from the VNA measurement ρ_m for any material under test:

$$\Gamma = \frac{A_2 - \rho_m A_1}{\rho_m - A_3} \tag{4.5}$$

from which we can derive the permittivity ε_r and conductivity σ from the real and imaginary parts in Eq.(4.1):

$$\varepsilon_r = Re(\Gamma) \tag{4.6}$$

$$\sigma = -\omega\varepsilon_0 \times Im(\Gamma) \tag{4.7}$$

4.3. Methods

4.3.1. Phantom Experimental Protocol

Two experiments were conducted: one with homogeneous phantoms for the absolute quantification and one with a dedicated resolution phantom for spatial resolution assessment. For both phantoms, mixtures of water, agar, and NaCl were used to mimic the EPs of tissues, which are both aqueous and concentrated in ions.

Homogeneous phantom experiments

We made seven cylindrical phantoms (diameter = 6.2 cm, height = 7 cm) composed of 120 ml deionized water, 1.8 g agar (Agarose D5, EUROMEDEX) and different mass concentrations of NaCl (99.5% Sodium chloride, Sigma-Aldrich) at levels of 0%, 0.25%, 0.5%, 0.75%, 1%, 1.5%, and 2%, respectively. This resulted in a diverse range of conductivities spanning from 0 to 3 S/m (at 123 MHz), thus encompassing the conductivity range of a human body [28], [29], [30]. Furthermore, the permittivity was kept relatively constant (ε_r = 72~78). To evaluate the reconstruction robustness against permittivity variations, we prepared two additional 100 mL ethanol phantoms (diameter = 5 cm, height = 5 cm), with 0.5% of NaCl each. The first contained 75% ethanol and 25% deionized water (σ = 0.23 S/m and ε_r = 35), while the other contained 50% ethanol and 50% deionized water (σ = 0.38 S/m and ε_r = 52). All VNA measurements were performed immediately after MR scanning to minimize temperature effects.

Resolution phantom experiment

To design the resolution phantom, we chose to use agar and holes filled in with a saline solution. This way, small holes (of a few mm) can be made easily, and there are no artificial barriers between compartments. The drawback is that diffusion of the saline into the gel has to be monitored to correctly assess changes in conductivities.

To make the resolution phantom, four cylinders of different diameters (5 mm, 10 mm, 15 mm and 20 mm) and a cross-shaped rod (width of 2.5 mm) were glued to the bottom of a container and the gel

was poured and solidified around. The resulting holes were overfilled right before the imaging pipeline (Figure 12) with a 2.5% saline solution of 3.66 S/m dyed with a few drops of blue colorant (allowing us to visualize the speed at which diffusion occurred during the experiments).

MR measurements were repeated 6 times with VNA measurements taken before and after each MR measurements (overall time 12 min 28 s for each scan). All VNA measurements were done in the preparation room next to the MR unit by gathering all the dyed saline solution used to fill the resolution phantom into the same container as it was prepared. The whole experiment took 100 min. The accumulated diffusion time of saline in the phantom (diffusion occurring during MRI scanning) was recorded to compare the conductivity dynamics of EPT to VNA. The diffusion time of each MRI scan was considered to be the center time of the sequence (i.e. 6 min 14 s after the sequence start).

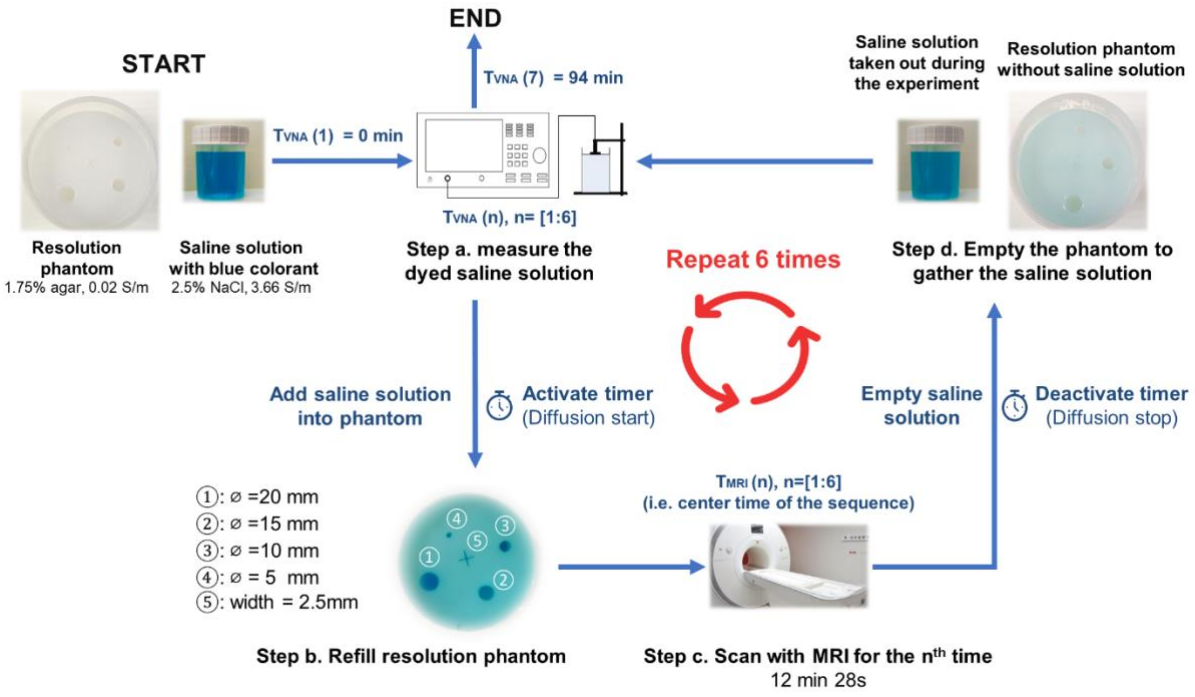

Figure 12. Workflow of the resolution phantom experiments (where T_{VNA}/T_{MRI} is the accumulated diffusion time when the VNA measurements/MRI scans are performed, and ⌀ is the hole diameter).

4.3.2. Image Acquisition Protocol

Prior to the beginning of imaging procedure, all phantoms were reset to the room temperature. All phantom data were acquired using a 3T clinical MRI scanner (MAGNETOM Prisma, Siemens Healthcare, Erlangen, Germany). Homogeneous phantoms were imaged with a UTE Spiral VIBE sequence [112], a multiple gradient echo (MGRE) sequence, a balanced steady-state free precession (bSSFP) sequence, a 2D spin echo (SE) sequence and a turbo spin echo (TSE) sequence. All acquisitions had an isotropic resolution of 1 mm and were acquired within the same FOV. For the bSSFP sequence, B_0 shimming was applied to each phantom sequentially (9 scans in total) to minimize banding artifacts. Sequence parameters are shown in Table 5. Resolution phantom data were exclusively obtained using

the UTE sequence with a larger matrix acquisition size (288×288×134 voxels) and a doubled number of excitations (NEX =2) to improve SNR (≈ 30 dB). This modification extended the total acquisition time to 12 min 28 s. RF excitation was performed by the volume body coil (in quadrature), and reception by a combination of surface coils (an 18-channel body matrix coil and a 32-channel posterior spine coil), using the vendor's adaptive coil combination [54], [113].

Table 5. Information on transceive phase acquisition sequences used in homogeneous phantoms.

Sequences	Dimension	Matrix Size	Resolution (mm)	Acquisition Time	TE (ms)	TR (ms)	Flip Angle (°)	Pixel Bandwidth (Hz)
UTE	3D	224×224×72	1×1×1	3 min 07s	0.05	4.3	5	2350
MGRE[a]	3D	224×224×72		2 min 35s	2.75, 6.25, 9.75, 13.25, 16.75	21	20	390
bSSFP	3D	256×256×72		1 min 30s	2.49	5	45	558
SE (2D)	2D	256×256×72		7 min 20s	13	1740	90, 180	391
TSE[b]	3D	224×224×72		6 min 23s	10	149	180	392

[a] with an acceleration factor of 2 by GRAPPA; [b] with a turbo factor of 7.

4.3.3. VNA Measurements

We used the dedicated flange probe (diameter of 48 mm) from a commercial dielectric assessment kit (DAK 12, from SPEAG, Zurich, Switzerland), connected to a VNA (VNA ZNB 4, Rhodes & Schwartz), to measure the reflection coefficient at the Larmor frequency of our scanner, i.e. 123.25 MHz. For the standard load, we used a 0.1M NaCl liquid with known EP values [114]. Using a tissue simulating liquid (TSL-HU16) as a test material (which has known EPs values), we validated our VNA calibration method to ensure that the measurement error was below 2.5%.

4.3.4. Conductivity Reconstruction

The transceive phase φ_{TR} was defined as the raw phase image for all sequences, without the need for spatial unwrapping, except in the case of bSSFP where Laplacian unwrapping [86] was applied, and for MGRE, where φ_{TR} was extrapolated linearly back to TE = 0 s after being unwrapped both temporally and spatially using ROMEO [88]. All sequences were used for Phase-only-based EPT. However, for Complex-Image-based EPT, only UTE was applied.

To mitigate noise amplification induced by the differentiation operator, we computed the derivatives of φ_{TR} and B using a 3D second-order Savitzky-Golay filter [56], [115]. We employed a filter size of

[9 9 9]/[7 7 7] for homogeneous phantoms/resolution phantom. In addition, the different kernel size effects on resolution phantom were also analyzed. We also applied two steps of median filtering [3 3 3], both after differentiation and reconstruction. This approach was effective in reducing boundary effects, and also mitigating the presence of I_0 for Complex-Image-based methods [54]. The strategy was kept constant for all calculations. The partial differential equations of PB-cr and GIB (Eq.(2.52) and Eq.(2.69)) were solved using a 3D finite-difference scheme without any specific boundary conditions [116].

In the literature, the diffusion coefficients $\lambda_{GB}/\lambda_{GIB}$ were selected empirically with v=1 in whole ROI [54], [60]. A high value of λ is favorable in large homogeneous ROIs to eliminate artifacts (including low convective field artifact [58]) and results in a smoother reconstruction; nevertheless, the smoothing should not be excessive for depicting small structures. Consequently, a trade-off combination of a small λ (to preserve the details) and a v smaller than 1 (to mitigate the artifacts caused by this small λ) was applied to small structures. Compared to the pure imaginary version of λ_{GIB} described in the literature [54], we found that adding a real part further removed boundary artifacts in ~mm structures. As such, v=1 and $\lambda_{GB}/\lambda_{GIB}$=0.02/0.02i were selected for homogeneous phantoms based on visual assessment, while v=0.5 and $\lambda_{GB}/\lambda_{GIB}$ = 0.005/0.005×(1+i) were selected for the resolution phantom.

4.3.5. Comparison of Reconstruction Methods

ROIs were derived from magnitude images for both phantom experiments. For homogeneous phantoms, thresholding was employed, while for the resolution phantom, Canny edge detection was utilized after enhancing contrast. To ensure a fair comparison of different reconstruction methods, precautions were taken to mitigate the influence of boundary artifacts. This was achieved by using disk-shaped erosion (radius: 10px) for homogeneous phantoms and square-shaped erosion (width: 1px) for the resolution phantom.

In the absolute quantification analysis, comparisons were carried out to assess the correlation between the measured VNA and MR-EPT conductivities. Additionally, voxel-wise differences between σ_{EPT} and σ_{VNA} were also analyzed by monitoring the root-mean-square errors (RMSE) in S/m.

For the resolution phantom, we compared the dynamics of σ_{VNA} and σ_{EPT}. To monitor the shift in accumulated diffusion time between VNA and MRI measurements, a linear fit of the 7 VNA measurements was applied to estimate the ground truth conductivity at the center time of each MRI scan. In order to determine the resolution limit, both root-mean-square error (RMSE, S/m) and normalized root-mean-square error (NRMSE) w.r.t σ_{VNA} – representing the percentage difference for each hole size over the whole dynamics – were calculated.

4.4. Results

4.4.1. Absolute Quantification Analysis (with homogeneous phantoms)

Figure 13 displays the magnitude and transceive phase of various MR sequences on homogeneous phantoms. Notably, banding artifacts are apparent in the bSSFP magnitude images, with observed phase wrapping at the phantom boundary in its phase images. Persistent phase wrapping, especially noticeable in the two ethanol phantoms, is challenging to eliminate in the MGRE transceive phase and deserves attention.

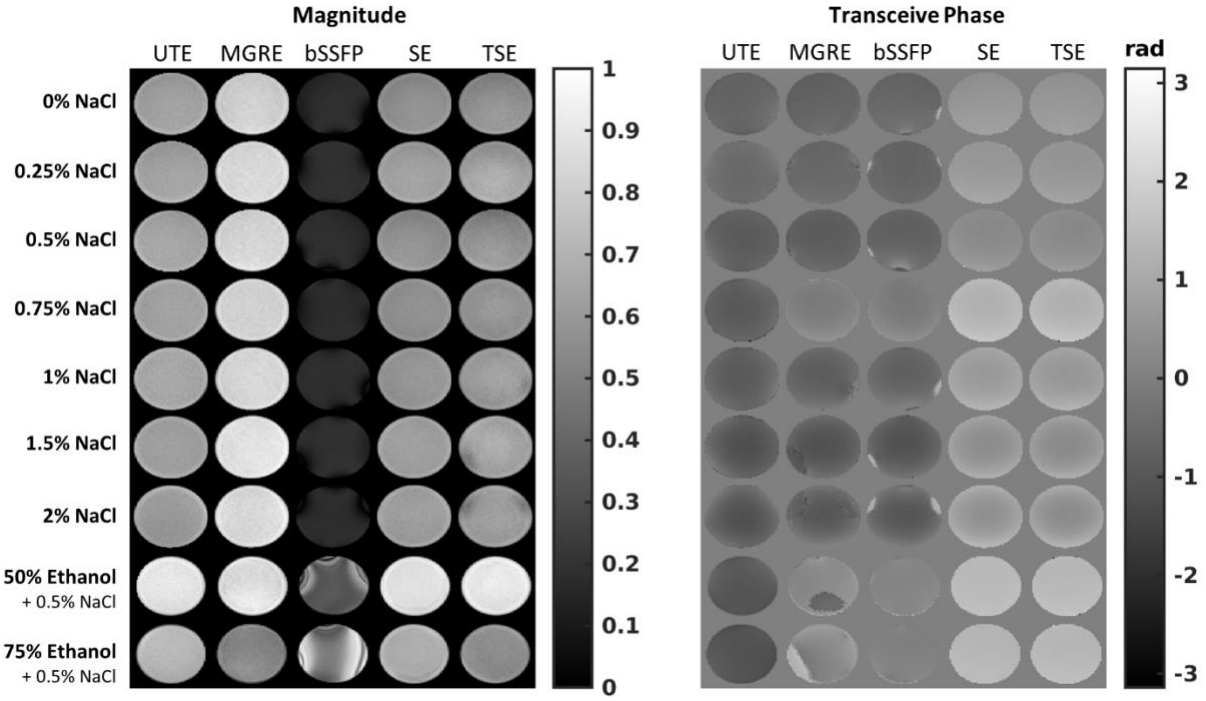

Figure 13. Magnitude (left) and transceive phase (right) of different transceive phase acquisition sequences on homogenous phantoms. The magnitude of MGRE shown here corresponds to the first echo time (TE = 2.75 ms), its transceive phase is linearly extrapolated back to TE = 0 s using phases measured at five different echo times (TE = 2.75 ms, 6.25 ms, 9.75 ms, 13.25 ms, 16.75 ms). The transceive phase images for other sequences are simply their respective phase image. Typical banding artifacts are evident in the bSSFP magnitude. This effect is also noticeable in its phase image. It's important to highlight that persistent phase wrappings, challenging to eliminate (particularly pronounced in the two ethanol phantoms), are observed in the MGRE transceive phase. This may be due to the fact that the initial echo time (TE = 2.75 ms) is considerably distant from TE = 0 s, resulting in an inadequate fit.

Conductivity maps reconstructed using PB (Figure 14A) and PB-cr methods (Figure 14B), along with the overall RMSE across all phantoms (Figure 14C), are presented for each transceive phase acquisition sequence. The PB-cr method outperformed PB, demonstrating advantages such as reduced boundary artifacts, improved uniformity, enhanced noise robustness, and lower RMSE in the reconstructed conductivity results. Regarding sequences, MGRE reconstruction for ethanol phantoms was only partially successful, indicating its relatively lower robustness compared to other sequences.

The UTE sequence exhibits the smallest RMSE in both PB-cr and PB methods (0.14 S/m and 0.25 S/m), followed closely by bSSFP (0.15 S/m and 0.26 S/m) and SE (0.14 S/m and 0.53 S/m).

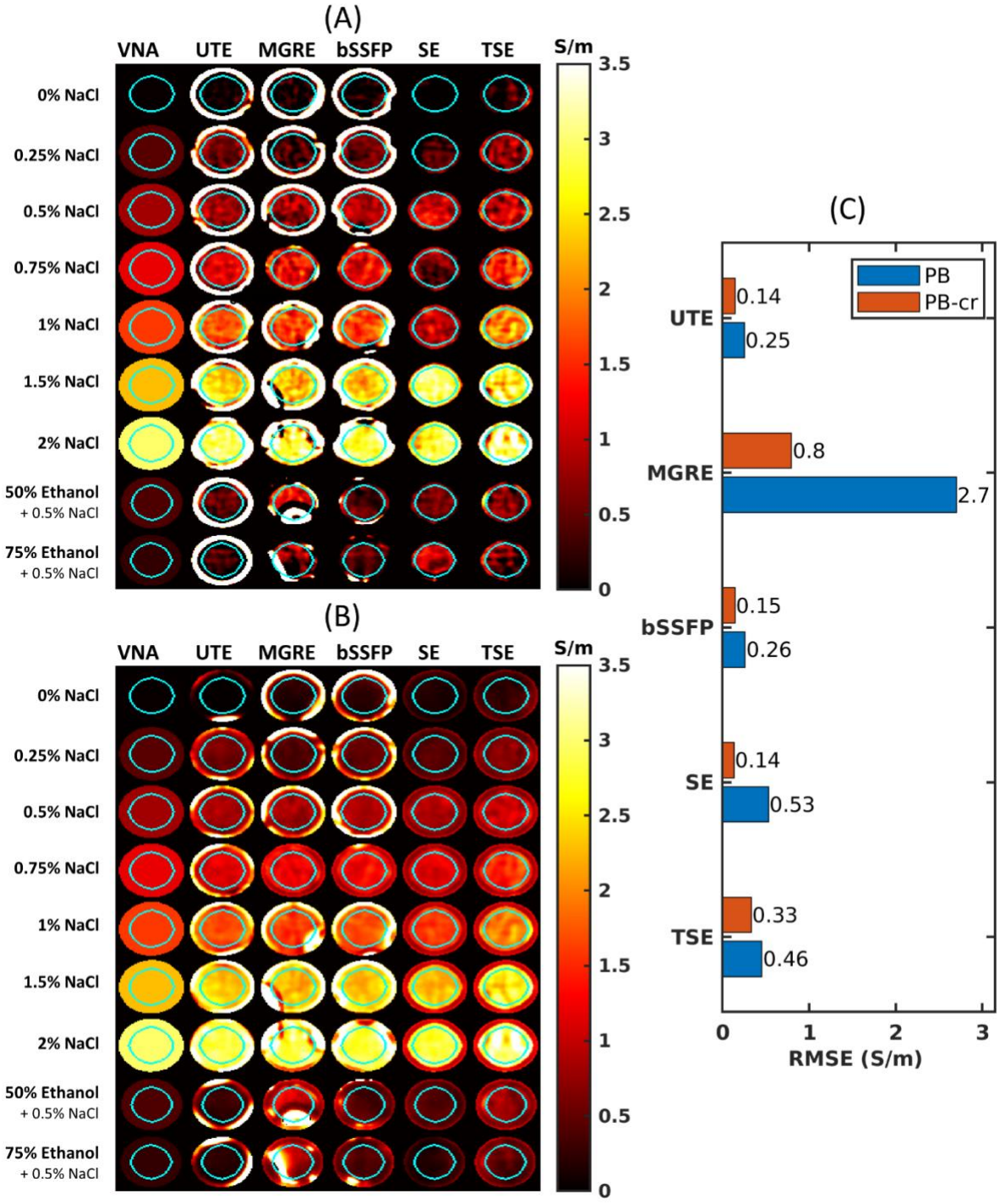

Figure 14. The middle slice of Phase-only-based EPT reconstruction with different transceive phase acquisition sequences on homogeneous phantoms, compared to VNA measurements. (A) VNA measurements and reconstructed conductivity maps with PB method. (B) VNA measurements and reconstructed conductivity maps with PB-cr method (v = 1, λ = 0.02). The ROIs depicted in cyan, utilized for quantification, were eroded by a disk-shaped structure element with a radius of 10 pixels. These eroded are also visible in both (A) and (B). (C) RMSE of different sequences to VNA

measurements on all homogeneous phantoms. The RMSE is calculated within the vicinity of the middle slice, encompassing 8 neighboring slices (totaling 9 slices), all situated with the defined ROI.

The reconstructed conductivity maps with the UTE sequence (Figure 15A) and the overall RMSE in all phantoms (Figure 15B) are shown across each EPT method. Similarly, the generalized methods (PB-cr and GIB) outperformed the simplified methods (PB and IB) in terms of boundary artifacts, uniformity, noise robustness and RMSE in the reconstructed conductivity results.

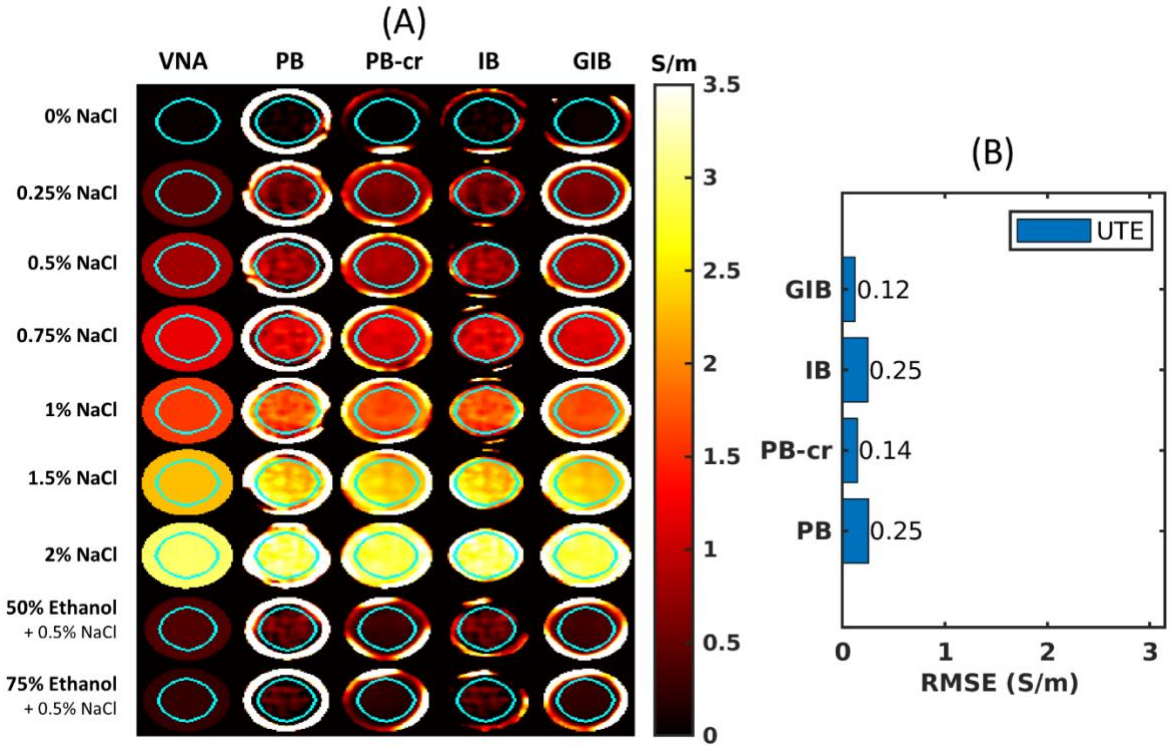

Figure 15. The middle slice of different EPT reconstructions with UTE sequence on homogeneous phantoms, compared to VNA measurements. (A) VNA measurements and reconstructed conductivity maps with PB, PB-cr (v = 1, λ = 0.02), IB and GIB (v = 1, λ = 0.02i) method. The ROIs depicted in cyan, utilized for quantification, were eroded by a disk-shaped structure element with a radius of 10 pixels. These eroded are also visible in (A). (B) RMSE of different reconstruction methods to VNA measurements on all homogeneous phantoms. The RMSE is calculated within the vicinity of the middle slice, encompassing 8 neighboring slices (totaling 9 slices), all situated with the defined ROI.

Figure 16 illustrates the correlations between σ_{VNA} and σ_{EPT} with different EPT methods and different sequences. The MGRE study (Figure 16C) excluded the reconstructions of the two ethanol phantoms due to their significant deviation from the reference line. All EPT methods demonstrated high correlations with VNA measurements (r > 0.99). The correlation lines of UTE (Figure 16A and B) closely align with the reference, featuring the smallest y-intercept. However, the σ_{EPT} obtained with the TSE sequence resulted in an overestimation of about 0.2 S/m compared to σ_{VNA}.

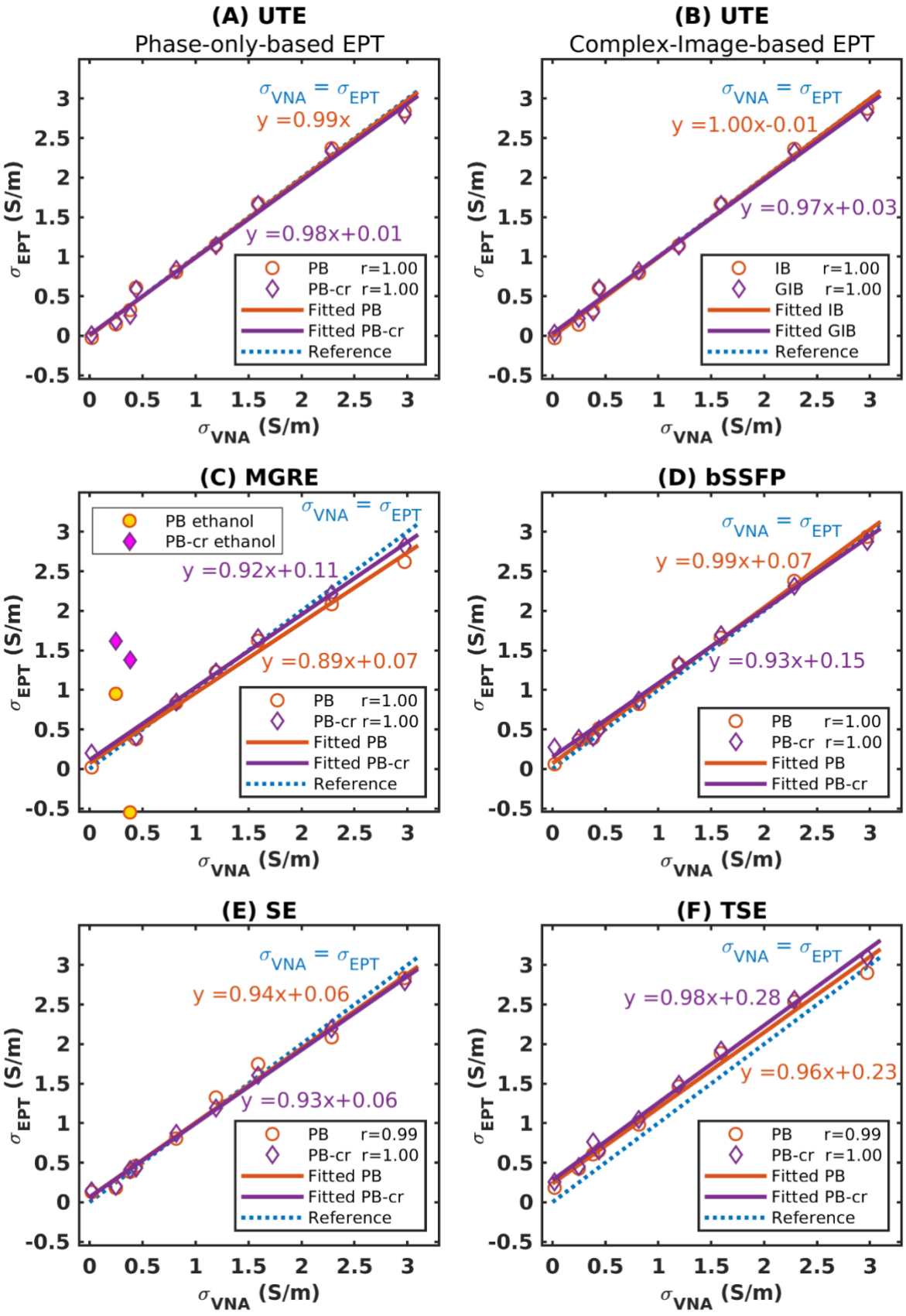

Figure 16. Correlations between the VNA measurements (σ_{VNA}) and the reconstructed conductivity means (σ_{EPT}) with different methods and different sequences. Their corresponding correlation coefficient r is also presented in the legend. In MGRE (C), the values of the two ethanol phantoms

deviate from the reference. This deviation is attributed to the phase wrapping observed in Figure 13. Therefore, these values have been excluded from the correlation study in C. The fitted lines of UTE (A and B) exhibit the closest alignment with the reference, featuring the smallest y-intercept. However, the reconstructed conductivity by TSE (F) overestimates by about 0.2 S/m with both PB and PB-cr methods. This may be due to the heating effect induced by the multiple 180°-RF pulses within the TSE sequence.

4.4.2. Resolution Limit Analysis (with the resolution phantom)

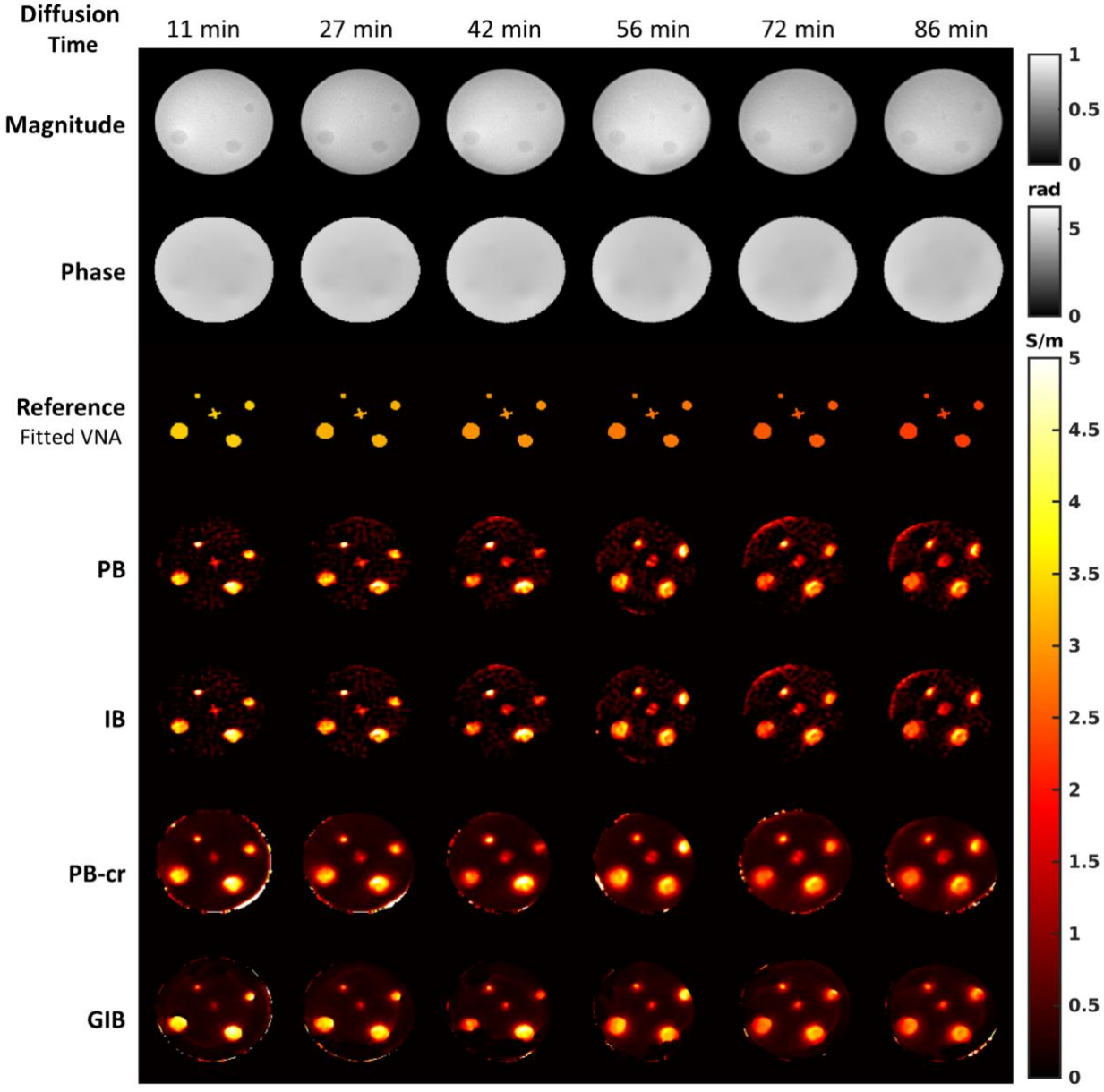

Figure 17. Raw UTE images, fitted VNA measurements and reconstructed conductivity maps with PB, IB, PB-cr (v = 0.5, λ = 0.005) and GIB (v = 0.5, λ = 0.005 + 0.005i) in the resolution phantom with 6 diffusion times.

Figure 17 presents the raw UTE images, fitted VNA measurements (adjusted with the MR sequence center time) and reconstructed conductivity maps at 6 different times, illustrating the evolution of

conductivity with the accumulated diffusion time of the solution in the gel for the resolution phantom. Over time, the conductivity in holes decreased, with the cross-shaped hole gradually blurring and enlarging to form a point. Despite the greater blurring in PB-cr and GIB compared to PB and IB, PB-cr and GIB exhibit less noise due to smoother gel backgrounds. In Figure 18, conductivity profiles across the entire dynamics are depicted for each hole size. For hole sizes $\geq$ 5 mm, a trend of decreasing profiles over time can be observed; however, detecting this decrease is challenging at a hole size of 5 mm. Conversely, for a hole size of 2.5 mm, an increase over time is noticeable, progressively approaching the VNA (reference).

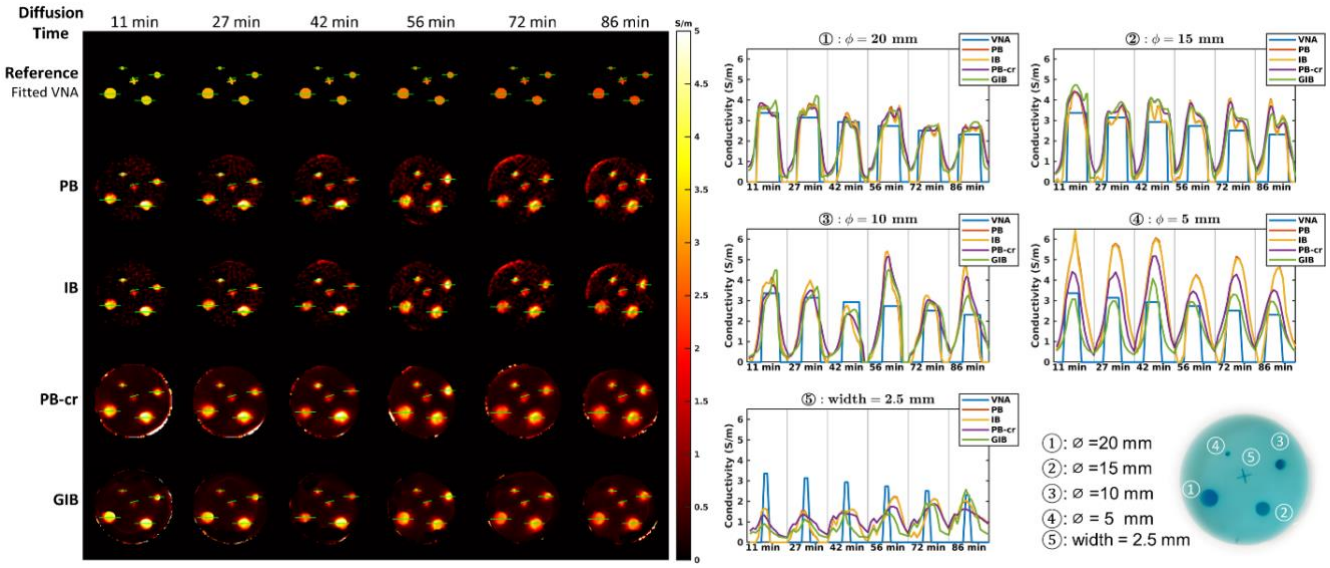

Figure 18. Conductivity profiles over the whole dynamics in each hole size. For each case, conductivity profiles along the green line shown in left are also given. Figure on the right shows combined profiles of each hole in chronological order. For hole sizes > 5 mm, a trend of decreasing profiles over time can be observed; conversely, for hole sizes <= 5 mm, observing this decrease is challenging. Specifically, for a hole size = 2.5 mm, an increase over time is noticeable, progressively approaching the VNA (reference). This phenomenon might be attributed to the gradual enlargement of the "hole size" caused by the diffusion of the saline solution.

The reconstructed conductivity means in each hole and VNA measurements are plotted against measurement time in Figure 19. Their RMSE and their NRMSE are shown in Table 6 and Figure 20. Table 6 also includes the fitted VNA measurement, mean, and standard deviation for the first MRI measurement. Visually, most RMSE (Figure 20A) decreased when the hole size was larger. The NRMSE (Figure 20B) of all EPT methods on the resolution phantom increased as the hole size became smaller. When the hole size was less than 10 mm/5 mm, the NRMSE of the simplified version EPT (PB and IB)/ the generalized version EPT (PB-cr and GIB) increased rapidly and exceeded 0.40. The similar rapid decrease is observed in their RMSE (Figure 20A). Therefore, the resolution limit, where absolute quantification was achieved, was considered to be 5 mm for PB-cr and GIB, and 10 mm for PB and IB. Below this resolution threshold, small structures were still able to be detected on the map but the conductivity values became significantly inaccurate.

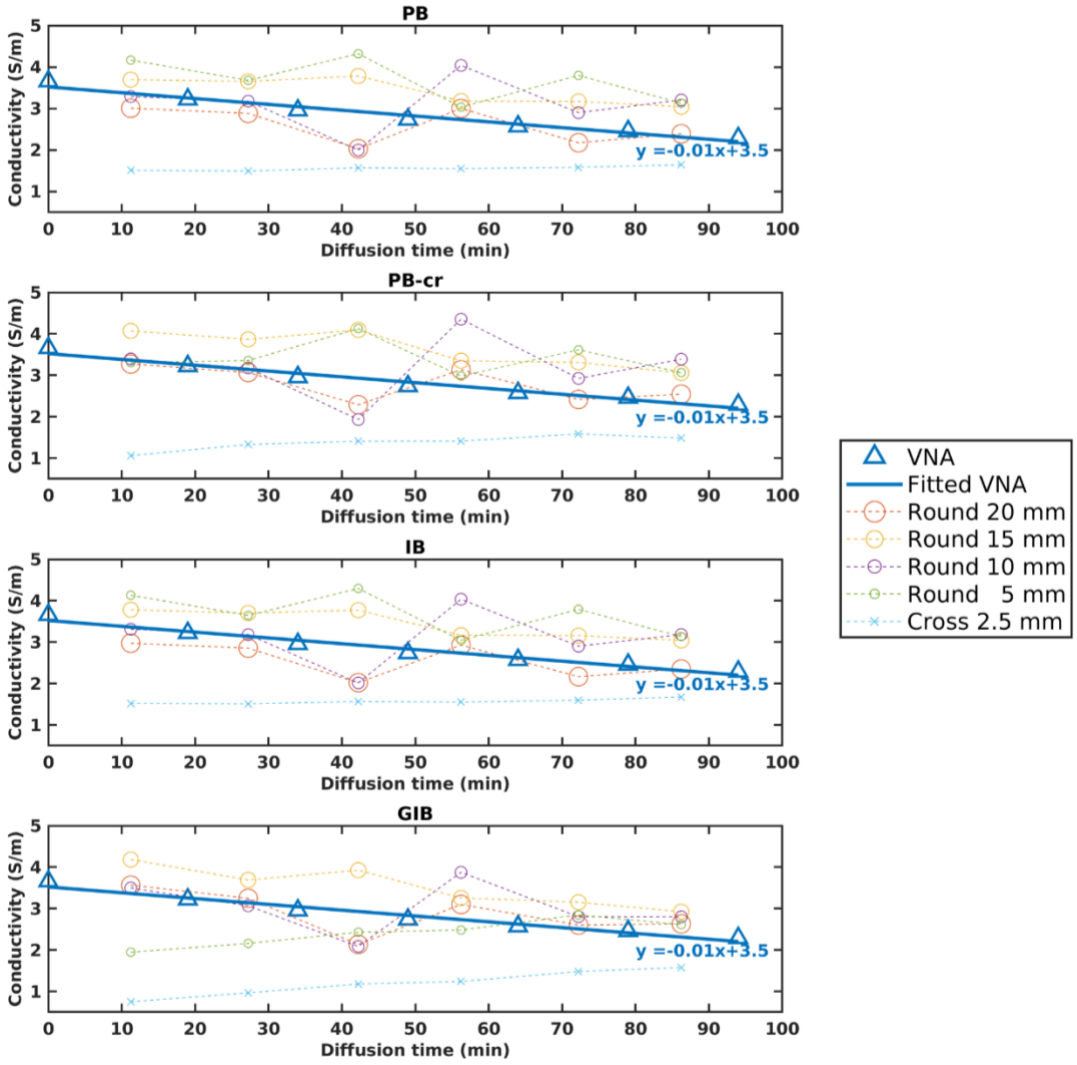

Figure 19. Reconstructed conductivity mean dynamics and fitted VNA measurements in each hole for PB, IB, PB-cr and GIB.

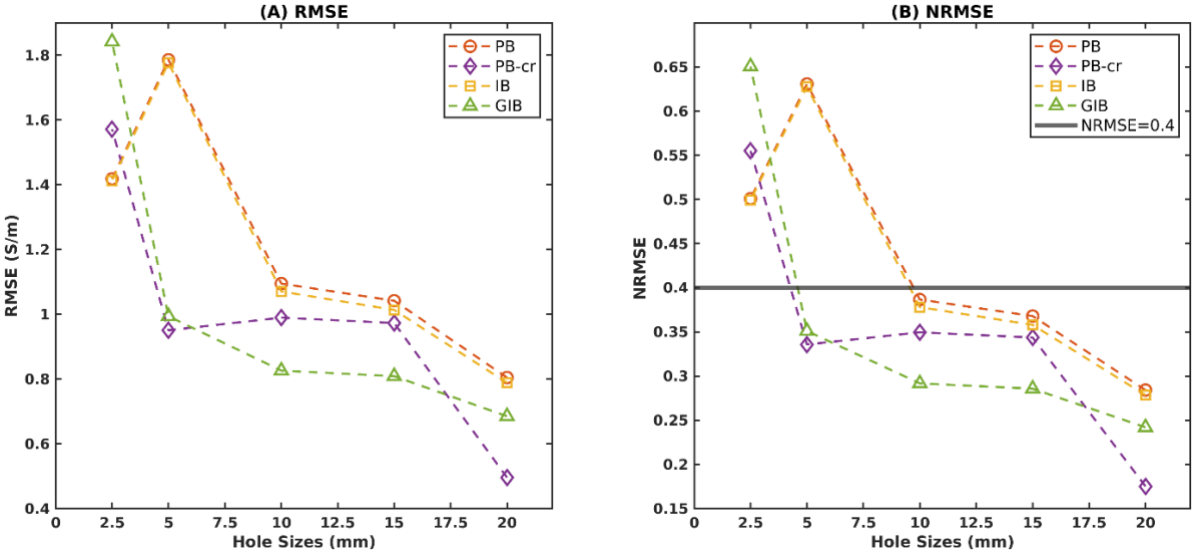

Figure 20. (A) RMSE and (B) NRMSE over the whole dynamics in each hole size. NRMSE is calculated as the RMSE normalized by the fitted VNA measurements.

Table 6. VNA measurements (fitted to MRI scan time) and MRI measurements in the resolution phantom, expressed as mean and standard deviation (SD) for the first MRI measurement, as well as RMSE and NRMSE over the whole dynamics.

Hole Size (mm)	σ_{VNA}* (S/m)	Phase-only-based						Complex-Image-based					
		σ_{PB}			σ_{PB-cr}			σ_{IB}			σ_{GIB}		
		mean ± SD* (S/m)	RMSE (S/m)	NRMSE	mean ± SD* (S/m)	RMSE (S/m)	NRMSE	mean ± SD* (S/m)	RMSE (S/m)	NRMSE	mean ± SD* (S/m)	RMSE (S/m)	NRMSE
2.5	3.36	1.51 ± 0.47	1.41	0.50	1.05 ± 0.35	1.57	0.55	1.51 ± 0.48	1.41	0.50	0.75 ± 0.29	1.84	0.65
5		4.16 ± 1.70	1.78	0.63	3.30 ± 0.86	0.95	0.33	4.13 ± 1.73	1.77	0.62	1.94 ± 0.66	0.99	0.35
10		3.28 ± 0.71	1.09	0.38	3.39 ± 0.31	0.98	0.35	3.31 ± 0.66	1.07	0.37	3.49 ± 0.86	0.82	0.29
15		3.69 ± 1.08	1.04	0.36	4.07 ± 0.61	0.97	0.34	3.78 ± 1.00	1.01	0.35	4.18 ± 0.43	0.80	0.28
20		3.00 ± 0.72	0.80	0.28	3.27 ± 0.42	0.49	0.17	2.97 ± 0.69	0.79	0.27	3.56 ± 0.78	0.68	0.24

*for the first MRI measurement only

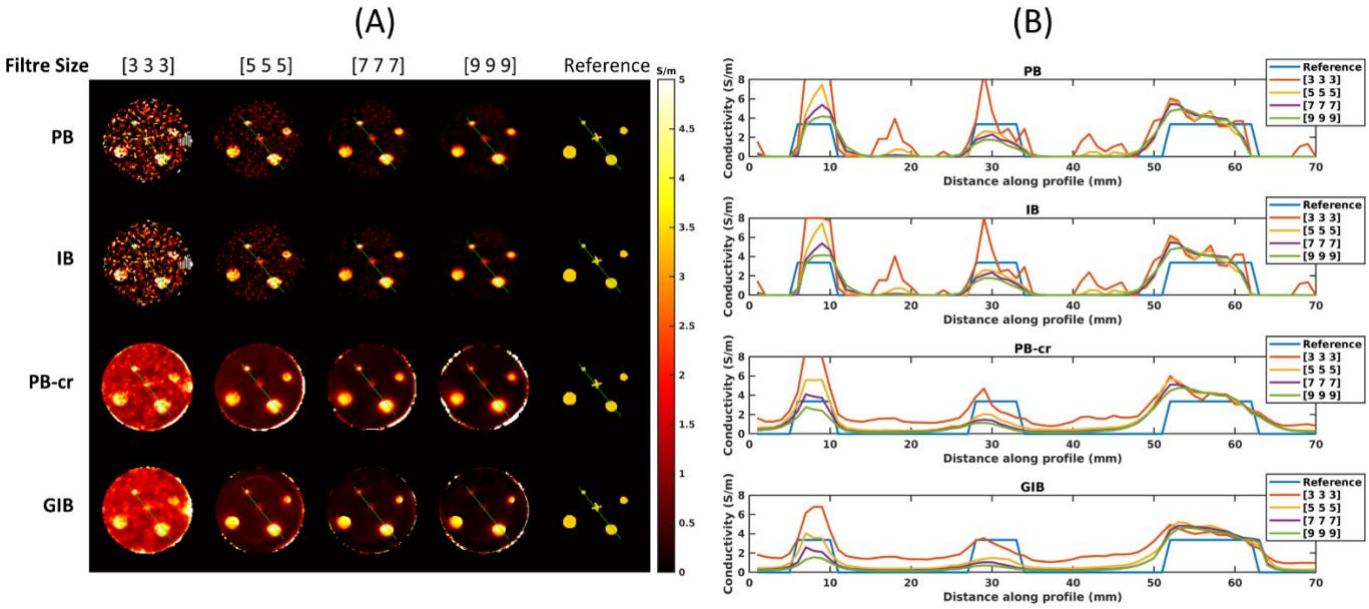

Figure 21. Conductivity reconstruction for the first MR acquisition (at 11 min) with different (second order) Savitzky-Golay filter sizes and (B) conductivity profiles for each EPT methods. For each case, conductivity profiles along the green line shown in (A) are also given. The noise in the background diminishes with increasing size, nonetheless, the sharpness of the smallest cross-shaped hole diminishes as the size increases. The profiles obtained with the generalized methods (PB-cr and GIB) exhibit a lower height compared to their simplified methods (PB and IB) when using the same filter size, especially noticeable at a filter size of [3 3 3]. It's advisable to select the filter size adaptively based on the ROI size. For instance, in the GIB reconstruction of (B), the profile with a filter size of [3 3 3] in the cross-shaped hole aligns closest to the reference; similarly, the profile with a filter size of [5 5

5] in the round hole (ø = 5 mm) closely resembles the reference; to ensure accurate reconstruction in the broader background region, a larger filter size, such as [9 9 9], should be utilized.

Moreover, Figure 21 shows reconstructed conductivity at the first MR acquisition (11 min) using different Savitky-Golay filter sizes from [3 3 3] to [9 9 9] along with their profiles for each EPT methods. As the filter size increases, the noise in the background diminishes; however, the sharpness of the smallest cross-shaped hole decreases. Profiles obtained with the generalized methods (PB-cr and GIB) exhibit a lower height compared to their simplified methods (PB and IB) when using the same filter size, especially noticeable at a filter size of [3 3 3]. This observation supports the notation that PB-cr and GIB methods effectively eliminate oscillations, providing a low-pass filter effect, as previously mentioned by Ozdemir et Ider [60]. The optimal filter size varies depending on the hole size. For instance, in the GIB reconstruction (Figure 21B), the profile with a filter size of [3 3 3] in the cross-shaped hole aligns closest to the reference; similarly, the profile with a filter size of [5 5 5] in the round hole (ø = 5 mm) closely resembles the reference; the profile of the broader background region with a larger filter size, such as [9 9 9], aligns well to the reference.

4.5. Discussion

Few MR-EPT studies have evaluated the accuracy of the reconstructed conductivity maps by comparison to a ground truth, using VNA measurements. While MR-EPT validation commonly involves demonstrating correlations between MR-EPT conductivities and NaCl concentrations in phantoms, this study ensured strong correlations with VNA measurements ($r > 0.99$). Nevertheless, absolute quantification of conductivity shows variations in the accuracy among different methods employing distinct MR sequences.

In this work, we initially investigated the performance of current φ_{TR} acquisition sequences in Phase-only-based EPT for absolute quantification. In the MGRE sequence, the presence of phase wrapping significantly impacts conductivity reconstruction. This issue may be attributed to the initial echo time (TE = 2.75 ms), which is distant from TE = 0 s, resulting in an inadequate fit. Furthermore, phase wrapping becomes more pronounced with a lengthening echo time, adding challenges for unwrapping in both temporal and spatial domains. Notably, this issue is particularly evident in the case of the two ethanol-saline mixture phantoms (Figure 13, Figure 14, and Figure 16C). The observed phenomena are likely due to the significant precession frequency differences of ethanol and water, i.e., chemical shift, therefore challenging the assumption of a linear accumulation of phase over TE. To resolve this issue, it might be beneficial to consider selecting a fixed TE interval when all protons are “in-phase” for all echo times. This indicates that the MGRE sequence may not be suitable for all tissue types. Reconstruction accuracy with the bSSFP sequence, as indicated by the RMSE values (Figure 13), is very promising. However, the process of eliminating banding artifacts in phase is often time-consuming and intricate. For example, advanced methods [60] make use of T_2 and B_0 maps as well as two bSSFP

scans. Additionally, faster techniques such as the fast Fourier transform [102] or PLANET [97], [104] methods rely on phase-cycled bSSFP scans. In the 2D spin echo sequence, “phase jumps”, i.e., random phase offsets [71] between slices consequently lead to “conductivity jumps” when a 3D derivative kernel is applied. This explains why there is a higher RMSE (0.53 S/m) with PB. However, these “conductivity jumps” can be corrected using the PB-cr method, resulting in a significantly reduced RMSE (0.14 S/m). In the TSE sequence, an overestimation of about 0.2 S/m (Figure 16F) is observed. This may be due to the heating effect induced by multiple 180°-RF pulses. Compared to the φ_{TR} acquisition sequences mentioned above, UTE clearly stands out as the most favorable option in terms of acquisition time and complexity, as well as accuracy.

Secondly, we evaluated the absolute quantification using different MR-EPT methods with the UTE sequence. The generalized methods exhibited lower RMSE values than their simplified versions, experienced fewer boundary artifacts, and demonstrated superior noise robustness. This improvement can be attributed to the preservation of the gradient term in Eq.(2.52) and Eq.(2.69). The difference in RMSE between the Phase-only-based and Complex-Image-based EPT is moderate: both PB and IB having the same RMSE of 0.25 S/m, GIB exhibits only a slightly smaller RMSE, with a difference of 0.02 S/m when compared to PB-cr. This further demonstrates that the error resulting from the phase-only approximation ($\nabla|B_1^{\pm}| = 0$) is relatively small, which agrees with the previous research findings [69], [117].

The proposed design for our resolution phantom has numerous advantages. First, it allows ion exchange, which is consistent with biological tissue. Second, the absence of barriers in the phantom alleviates susceptibility issues. These susceptibility gaps may distort the magnetic field distribution and affect the accuracy of EPT reconstructions by making the systems of equations ill-posed.

Designing an MR-EPT resolution phantom makes it harder to measure the ground truth conductivity in small structures (in the range of mm), considering the probe’s size. With the proposed design, by overfilling the resolution phantom with a liquid saline solution, we ensured that all compartments were filled with the same solution, whose EPs can be measured separately. Moreover, according to Fick's law of diffusion, the flow is mostly determined by the concentration gradient, fluid viscosity, and temperature, which remain constant. Therefore, we assume that the conductivity dynamics in each hole are identical over time. As observed on Figure 19, the fitted dynamics of VNA measurements were linear, with very good approximation, and correlated very well with MRI measurements. The decreasing trend in reconstructed conductivity was comparable across all methods, except for the smallest hole (2.5 mm).

The cross-shaped hole can be distinguished in reconstructions for all methods, but without a precise value. The reason might be that at least three voxels in one direction are required to calculate the Laplacian. Therefore, the theoretical EPT resolution limit for MR images with 1 mm isotropic resolution

would be 3 mm, which is greater than the cross-shaped hole's width. Also considering the influence of noise, the actual resolution limit could be at 5 mm, similar to the experimental limit found with PB-cr and GIB. Additionally, the reconstruction of small structures might be affected by partial volume effects. One mm is a typical resolution limit for clinical MRI at 3T, and in light of our results, accurate mapping of electrical conductivity with a resolution below 5 mm is still challenging. It might be possible to improve the spatial resolution of raw images further, but it would result in prohibitive scan time (e.g. 0.5 mm isotropic would cost an 8-fold increase in scan time), and diffusion effects would become more significant.

As shown in Figure 17, reconstructed cross-shaped holes were easier to distinguish for PB and IB, so that these methods seem to provide a higher effective resolution than their generalized versions. It is also noticeable in Figure 20 that their NRMSEs for the cross-shaped hole were lower than those of PB-cr and GIB. This demonstrates that the correction terms result in numerical artifacts and resolution loss. To address this issue, adaptative regularization, e.g., assigning a reduced weight to the convection-reaction term in small ROIs, and/or adaptative filters for Laplacian estimation [65], [118] (Figure 21) might be used to help balance the trade-off between resolution and SNR throughout the reconstruction process. In this study, the choices of λ and ν were both empirical for the whole ROI. However, they could also be further chosen in a pixelwise manner [48], [119], namely with values that vary with the geometric structure of EPs. An optimization for local coefficient maps λ and ν with physics-informed neural networks was recently shown [48]. However, these modifications also increase complexity and computational time required for the reconstruction.

In terms of reconstruction speed, the simplified methods, which involve only convolutional computation, can be completed in less than 1 second with a GPU. In contrast, the generalized method requires solving for the global minimum and takes about 3-5 minutes without GPU or parallel computation. Reducing the reconstruction time remains a challenge for real-time applications in clinical settings.

4.6. Conclusion

The UTE sequence is recommended for φ_{TR} acquisition as it offers the most accurate absolute quantification and robustness to off-resonance effects. All MR-EPT methods tested in this work were highly correlated with ground-truth VNA measurements ($r > 0.99$). The generalized methods, PB-cr and GIB provide greater accuracy than their simplified methods. Additionally, the difference between the Phase-only-based and Complex-Image-based EPT is quite minimal, with the GIB method achieving a minimal RMSE of 0.12 S/m. In terms of spatial resolution, accurate conductivity values were able to be reconstructed for structures down to 10 mm, with simplified reconstruction methods (PB, IB), or down to 5 mm, with generalized methods (PB-cr, GIB). Below 5 mm, conductivity variations were still

detected, but conductivity values were significantly less reliable. Still, generalized reconstruction methods must be improved, since current reconstruction methods are limited by the trade-off between accuracy of the signal model, numerical stability of the reconstruction, and spatial resolution.

Chapter 5. Phantom Evaluation of Electrical Permittivity by Image-based EPT

5.1. Introduction

Currently, permittivity is less frequently considered in EPT studies compared to conductivity, and no study has yet exploited permittivity mapping in clinical scenarios. This is partly due to its lesser-known clinical significance and because the underlying physics makes it less sensitive to B_1^+ measurements [5]. Permittivity mapping requires B_1^+ amplitude, which is measured independently and differently from the B_1^+ phase needed for conductivity. The $|B_1^+|$ encoding mechanism and the limited spatial resolution of $|B_1^+|$ mapping result in even lower signal-to-noise ratios (SNR) for permittivity than for conductivity. Moreover, RF shimming, which homogenizes $|B_1^+|$ by a combination of transmit coils, is unfavorable for permittivity reconstruction that relies on $|B_1^+|$ spatial variations [69]. Consequently, phase-based EPT methods, which bypass the lengthy $|B_1^+|$ mapping acquisitions and focus directly on conductivity reconstruction, have become the most popular in clinical applications [67], [68], [100]. However, permittivity is essential for accurate SAR modeling and local SAR calculations.

Studies suggest that the accuracy of permittivity reconstruction using standard EPT is not as promising as that for conductivity, especially in vivo at field strengths below 7T [42]. Additionally, Gavazzi et al. (2019) [107] reported that the standard deviations of permittivity in phantom experiments at 3T, even with advanced $|B_1^+|$ mapping techniques (AFI, BSS and DREAM), were as high as their mean values. Despite this, there is a lack of studies reporting the permittivity reconstruction performance of Image-based EPT [53], which requires only a single scan of the UTE/ZTE sequence with a low flip angle.

Hence, in this study, we investigate the accuracy of Image-based EPT for permittivity mapping in a single UTE scan. For this aim, four homogeneous phantoms with different relative permittivity ranging from 3 to 76 but the same conductivity (eliminating the effects from conductivity), were made. Given that Image-based EPT requires a low flip angle assumption and that SNR is also flip angle dependent, we evaluated the accuracy across a range of low flip angles (1°-10°) to find an optimal flip angle that provides the lowest error compared to the ground truth VNA measurements.

This work was conducted with Mr Youssef Abdedaim, an M2 intern for 5 months from university of Rouen, under my supervision.

5.2. Theory

The complex image from a spoiled UTE/ZTE scan can be expressed as

$$I = \rho_0 \sin(\alpha\,) e^{i\varphi^+} B_1^- = \rho_0 \sin(\gamma\tau |B_1^+|\,)\, e^{i\varphi^+} B_1^- \tag{5.1}$$

where ρ_0 is the proton density. At a low flip angle ($\sin(\alpha) \approx \alpha$), this equation can be simplified to

$$I \approx \rho_0 \gamma\tau B_1^+ B_1^- = I_0 B_1^+ B_1^- \tag{5.2}$$

where $I_0 = \rho_0\gamma\tau$ is the natural MR images contrast determined by the proton density. The root square of (5.2) is used as the input for image-based EPT (see section 2.6.1). The phase images at any flip angle (both in Eq.(5.1) and Eq.(5.2)) always represent the transceive phase ($\varphi_{tr} = \varphi^+ + \varphi^-$), making conductivity reconstruction therefore less dependent on the flip angle. However, the magnitude images and thus the permittivity reconstruction are more flip angle dependent.

Theoretically, the closer the flip angle is to zero, the more valid the low flip angle simplification is, but this also results in a lower SNR for the acquired MR images. For example, at low flip angles, the signal intensity with a flip angle of 1° is half of that at 2°, meaning their SNR ratio is proportional to the flip angle ratio, assuming the noise level remains constant. Balancing the trade-off between the low flip angle assumption validity and SNR is crucial for optimizing permittivity accuracy and overall reconstruction quality.

5.3. Methods

5.3.1. Phantom Recipes

We prepared four cylindrical liquid phantoms (diameter = 6.2 cm, height = 7 cm) containing different compositions: rapeseed oil, 100% ethanol (Sigma-Aldrich), 50% ethanol and 50% deionized water, and 0% ethanol (i.e., 100% deionized water), respectively. This resulted in a diverse range of relative permittivity spanning from 3 to 76 (at 123 MHz), thus encompassing the majority of the permittivity range found in a human body [28], [29], [30]. The conductivity was kept relatively constant (σ = 0 ~ 0.06 S/m). All VNA measurements were performed immediately after MR scanning to minimize temperature effects.

5.3.2. Image Acquisition Protocol

Prior to imaging, all phantoms were reset to the room temperature. All phantom data were acquired using a 3T clinical MRI scanner (MAGNETOM Prisma, Siemens Healthcare, Erlangen, Germany). 3D images were acquired using a UTE Spiral VIBE sequence [112] (TE/TR = 50 μs/4.2 ms, voxel size = 1×1×1 mm^3, matrix size = 256×256×80, number of excitations = 2). The 3D acquisitions were repeated seven times with different flip angles: FA = [1°, 2°, 3°, 4°, 5°, 7°, 10°]. Each scan took 6 min

43 s. RF excitation was performed by the volume body coil (in quadrature), and reception by a combination of surface coils (an 18-channel body matrix coil and a 32-channel posterior spine coil), using the vendor's adaptive coil combination [54], [113].

5.3.3. Permittivity Reconstruction

The relative permittivity was reconstructed using Image-based EPT [53]:

$$\varepsilon_r = \frac{1}{\omega\varepsilon_0} Im\left(\frac{\nabla^2\left(\sqrt{I_{UTE}}\right)}{i\omega\mu_0\sqrt{I_{UTE}}}\right) \tag{5.3}$$

where I_{UTE} is the UTE complex image, ε_0 is the vacuum permittivity and μ_0 is the vacuum permeability. To mitigate noise amplification induced by the Laplacian operator, we computed the second derivatives of $\sqrt{I_{UTE}}$ using a 3D second-order Savitzky-Golay filter [56], [115]. We employed a filter size of [13 13 13] for all flip angle acquisitions. Additionally, median filtering with size [3 3 3] was applied at the end of reconstruction.

5.3.4. Comparison of Reconstruction Methods

ROIs were derived from magnitude images using thresholding. To ensure a fair comparison and mitigate the influence of boundary artifacts, disk-shaped erosion with a radius of 13 pixels was applied.

The mean and standard deviation (SD) values for each phantom at different flip angles were calculated. Accuracy at each flip angle was assessed by evaluating the correlation between the measured VNA and EPT permittivity. Additionally, the total voxel-wise differences between $\varepsilon_{r\ EPT}$ and $\varepsilon_{r\ VNA}$ at each flip angle were analyzed by monitoring the normalized-root-mean-square errors (NRMSE).

5.4. Results

Figure 22 displays the raw UTE magnitude and transceive phase along with their reconstructed relative permittivity maps at different flip angles. It can be observed that the SNR increases with increasing flip angle, resulting in progressively more uniform images. However, the noise effects are less evident in the transceive phase images compared to the magnitude images. This may be due to the inherent noise robustness of the transceive phase, which is stronger than that of its magnitude. The reconstructed relative maps exhibit the typical boundary artifacts; however, these artifacts will not affect the subsequent quantification process due to the use of erosion. The relative permittivity maps of the rapeseed oil (left-top) and 0% ethanol (right-bottom) phantoms at all flip angles were consistent with the VNA measurements. However, two others phantoms, the 100% and 50% ethanol phantoms displayed inconsistencies at different flip angles. Specifically, the relative permittivity of 50% ethanol phantom (left-bottom) decreases with increasing flip angle, while that of 100% ethanol phantom (right-

top) increases with increasing flip angle. The reconstructed relative maps at flip angle of 2° or 3° were visually the most consistent with the VNA measurements.

Table 7 presents the mean and standard deviation of the reconstructed relative permittivity along with the total NRMSE compared to VNA measurement at each flip angle. In general, the standard deviations were first decreased from a flip angle of 1° to 5°, but increased again at flip angles greater than 5°. This increase may be due to the invalid low flip angle assumption rather than noise effects. Consistent with Figure 22, except for 100% and 50% ethanol phantoms, the mean values of rapeseed oil and 0% ethanol phantoms at all flip angles are consistent with $\varepsilon_{r\,VNA}$. Although the highest standard deviations occur at FA=1°, its mean values are the closest to $\varepsilon_{r\,VNA}$.

Figure 23A-G illustrates the correlation between $\varepsilon_{r\,EPT}$ and $\varepsilon_{r\,VNA}$ with different flip angles. From FA=1° to 10°, the fitted line in red progressively deviates from the reference dotted line in blue where $\varepsilon_{r\,EPT} = \varepsilon_{r\,VNA}$. This deviation is also demonstrated by the slope variation, which progressively diverges from 1. Moreover, the correlation coefficients (r), shown in the legends, decrease with increasing flip angle. The closest fitted line is observed at FA=1° with the highest correlation coefficient r=0.99.

In terms of the total NRMSE compared to $\varepsilon_{r\,VNA}$, illustrated in Figure 23H and Table 7, it initially decreases, reaching a minimum of 0.33 at FA=2° and 3°, then increases. This trend suggests that the errors caused by the low flip angle assumption become significantly larger than the errors from noise when FA $\geq$ 3°. In this case, increasing the flip angle does not benefit permittivity reconstruction. Consequently, there is a substantial decrease in accuracy, with the NRMSE reaching 0.93 at FA=10°. If we consider a limit of NRMSE of 0.35, FA=2° or 3° would be the optimal flip angle for the accurate permittivity reconstruction.

Table 7. Mean and standard deviation (SD) values of the reconstructed relative permittivity ($\varepsilon_{r\,EPT}$) along with NRMSE compared to VNA measurements ($\varepsilon_{r\,VNA}$) at each flip angle. The boundary artifacts were eliminated by applying a disk-shaped erosion with a radius of 13 pixels to the ROIs.

	RAPESEED OIL	**100% ETHANOL**	**50% ETHANOL**	**0% ETHANOL**	**NRMSE**
	$\varepsilon_{r\,EPT}$ mean ± SD				
FA = 1°	5.40 ± 22.45	37.59 ± 22.35	58.33 ± 22.80	76.54 ± 22.88	0.50
FA = 2°	9.69 ± 10.82	44.21 ± 14.32	47.44 ± 8.41	72.43 ± 11.54	0.33
FA = 3°	8.68 ± 8.77	43.36 ± 11.12	37.98 ± 10.14	70.64 ± 6.87	0.33
FA = 4°	6.46 ± 8.85	43.59 ± 10.79	29.06 ± 9.48	71.29 ± 8.68	0.39
FA = 5°	7.64 ± 8.56	45.52 ± 9.84	17.70 ± 10.50	66.96 ± 5.99	0.48
FA = 7°	7.60 ± 8.07	51.81 ± 12.70	-1.78 ± 13.34	67.72 ± 5.69	0.68
FA = 10°	5.74 ± 8.63	66.03 ± 21.66	-20.08 ± 16.72	75.70 ± 5.74	0.93
$\boldsymbol{\varepsilon_{r\,VNA}}$	3.69	25.04	54.61	75.51	

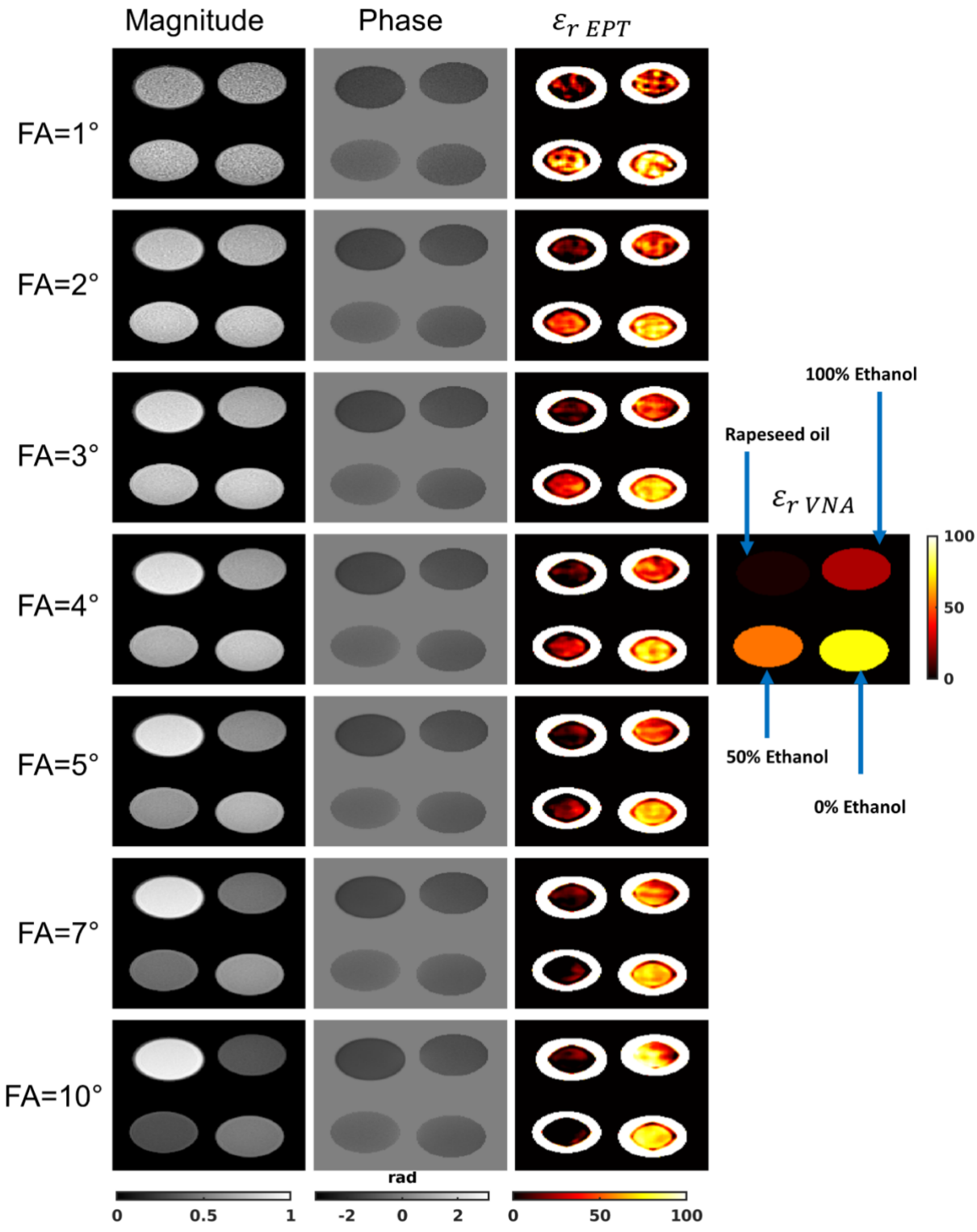

Figure 22. The middle slice of raw UTE magnitude and phase images, along with reconstructed relative permittivity maps at different flip angles from 0° to 10°, compared to the VNA measurements (right).

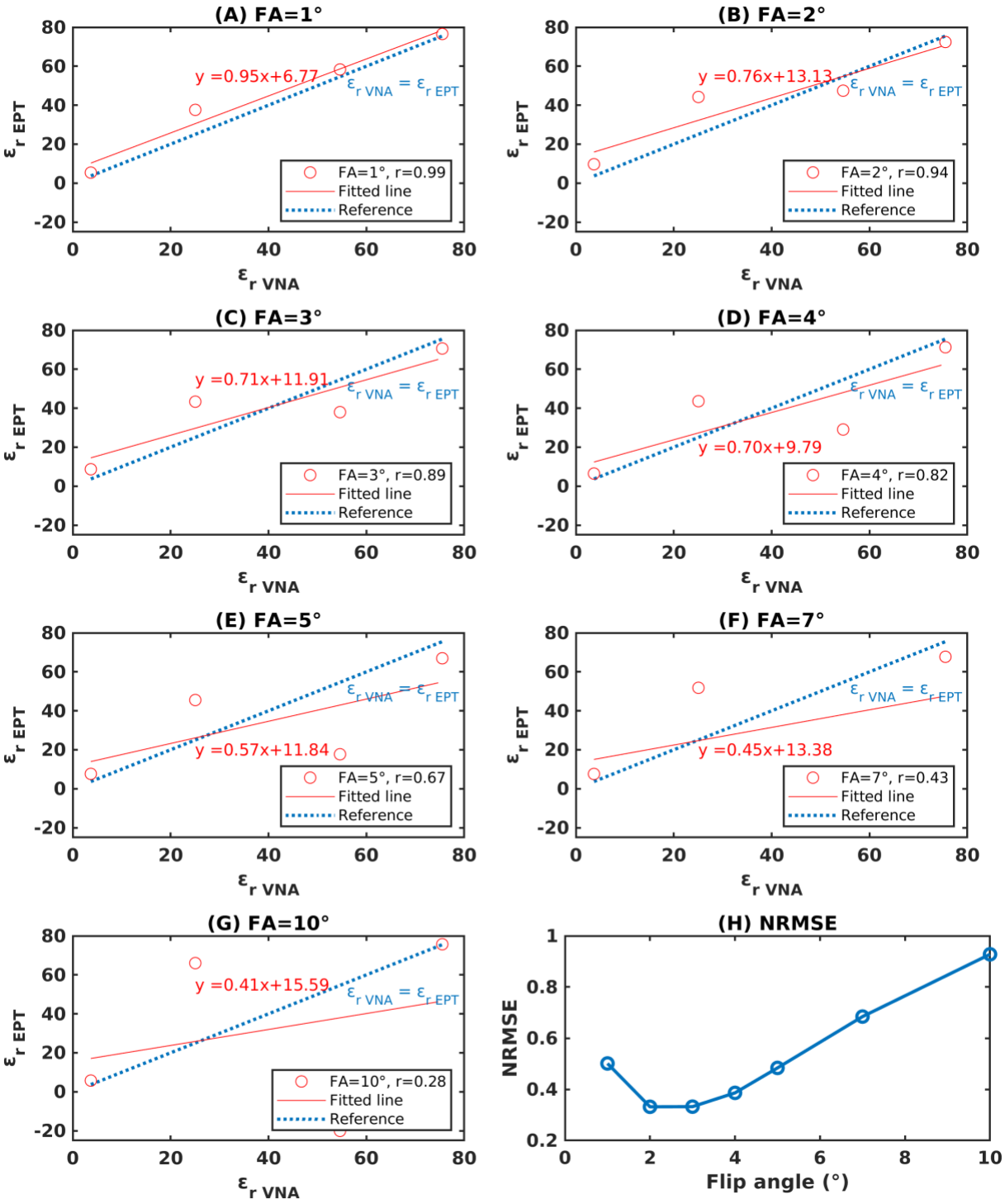

Figure 23. Correlations at different flip angles (A-G) and NRMSE (H) between the VNA measurements ($\varepsilon_{r\ VNA}$) and the reconstructed relative permittivity means ($\varepsilon_{r\ EPT}$). Their corresponding correlation coefficient r is also presented in the legend.

5.5. Discussion and Conclusion

In this study, we evaluated the permittivity reconstruction accuracy of Image-based EPT on homogenous liquid phantoms with different flip angles ranging from 0° to 10°. We demonstrated that the permittivity reconstruction is sensitive to the flip angle in Image-based EPT. Despite the noise effects at very low flip angles, the lower the flip angle, the higher consistence of mean value and correlation to the VNA measurements. This consistence may be attributed to the perfect validity of the low flip angle assumption. However, considering the noise effects, the optimal flip angle would be 2° or 3°, with the lowest NRMSE of 0.33.

To benefit from the accuracy at very low flip angle (for instance at 1°), the noise effects can be mitigated by increasing the number of excitations, using advanced coil combination methods to maximize image intensity and minimize RF phase variation [69], and employing denoising techniques such as larger filter size or deep learning-based denoising methods [120], [121]. Alternatively, it might be possible to extrapolate at FA=1° with high SNR using sinusoidal fitting with multiple points at different flip angles.

Chapter 6. Adaptive Kernel for Numerical Differentiation and Integration in EPT

6.1. Introduction

Due to the use of the second derivative calculations on measured B_1 data in EPT, i.e., the Laplacian operator (∇^2), the reconstructed EP maps are highly susceptible to noise. This increases the difficulty in achieving high resolution, better accuracy, and removing boundary artifacts. To address this issue, strategies have been proposed that use large finite difference (FD) derivative smoothing kernels [55] combined with Gaussian filtering [51] or Savitzky-Golay (SG) filter [115], [122] to mitigate noise amplification. Among these, as shown in [56], the Savitzky-Golay filter (also called quadratic least-squares fitting or parabola fitting) achieves the lowest noise amplification among all linear Laplacian kernels. However, large kernels result in extended numerical boundary propagation [55], [69], which severely hampers the accuracy and resolution of reconstructions for small tissue structures, while small kernels are insufficient for effective denoising. The selection of kernel size is a trade-off between resolution and SNR in reconstructed EPs maps.

In recent years, a more advanced method has been proposed that applies an adaptive SG kernel to force the Laplacian calculation in a local homogeneous region [65], [72], [118], [122]. Its size can adapt to the shape of the tissue using prior anatomical knowledge from MR magnitude images. In other words, the kernel contains only voxels which belong to the same tissue type as the target voxel. This concept effectively boundary artifacts when a large kernel spans two tissue types and maintains the validity of the local homogenous assumption (LHA). However, the effective voxel number in the kernel domain is confined to tissue size. This means large tissues benefit more from filtering than small tissues, where the smoothing effect is impaired. Additionally, Karsa et al., 2021 [123] demonstrated that an oversized adaptive SG kernel also induces reconstruction inaccuracies. To address this, we proposed a novel K-nearest neighbor (KNN) SG kernel based on the adaptive kernel concept, fixing K voxels in the kernel domain for each convolution calculation across all tissues [124], thereby maintaining consistent smoothing effects in ROIs.

Alternatively, it is possible to reduce noise amplification by converting the Laplacian to first derivative using the divergence theorem, i.e., surface integral form EPT [49], [52]. In this formulation, the first derivatives can also be obtained using the SG kernel, and the integral kernel could also be developed into adaptive [72] and KNN forms. However, due to the complex implementation of surface-integral form EPT, this method is less popular than Laplacian-based EPT. A detailed numerical integration method will be described in this chapter.

In this chapter, we will describe the standard, adaptive, and KNN forms of numerical differentiation using the SG filter, as well as numerical integration in surface-integral based EPT. We will compare their standard and adaptive forms to our proposed KNN kernel scheme through simulations and in vivo experiments. Additionally, we proposed a protocol for choosing the optimal kernel size based on a given SNR level in simulation.

This study resulted in a conference communication:

- **He Z**, Chen B, Lefebvre PM, Odille F. An Adaptative Savitzky-Golay Kernel for Laplacian Estimation in Magnetic Resonance Electrical Property Tomography. In: 2023 45th Annual International Conference of the IEEE Engineering in Medicine & Biology Society (EMBC). Sydney, Australia; 2023:1-4. doi:10.1109/EMBC40787.2023.10341200. (Full Contributed Paper + Poster)

6.2. Numerical Differentiation by Savitzky-Golay Filter

The principle of a Savitzky-Golay (SG) filter [115] is to fit a polynomial of chosen order to a subsection of the image by linear least squares. The innovative aspect of derivative calculation at a given voxel by the SG filter is that it computes the derivative of the fitted polynomial. This approach makes numerical differentiation straightforward and provides a closed analytical formula solution for any order of derivatives. Another property of the SG kernel is that its coefficients depend only on the relative coordinates of voxels in the kernel domain rather than the intensity of voxels. This simplifies the kernel calculation, ensuring consistency across any image contrast, as long as the kernel shape remain unchanged.

For EPT, it is common to use a second-order polynomial, as adding higher-order terms to the Laplacian calculation decreases the stability of the fit and its noise robustness [56]. Additionally, the profile of $|B_1^+|$ and transceive phase images in a homogenous region resembles the concave and convex parabola, which corresponds to a second-order polynomial. Consequently, it is also referred to as second-order polynomial fitting or parabola fitting in EPT-related literature [122].

6.2.1. Standard Savitzky-Golay Kernel

The volume around a voxel (x_0, y_0, z_0) is fitted by the second-order polynomial $P_{x_0,y_0,z_0}(x, y, z)$: $\mathbb{R}^3 \longmapsto \mathbb{R}$ with coefficient $a_{i,j,k}$:

$$P_{x_0,y_0,z_0}(x, y, z) = a_{0,0,0} + a_{1,0,0}x_r + a_{0,1,0}y_r + a_{0,0,1}z_r + a_{1,1,0}x_r y_r + a_{1,0,1}x_r z_r + a_{0,1,1}y_r z_r + a_{2,0,0}x_r^2 + a_{0,2,0}y_r^2 + a_{0,0,2}z_r^2 \quad (6.1)$$

where $x_r = x - x_0$, $y_r = y - y_0$ and $z_r = z - z_0$ are the relative coordinates in the x-, y- and z-axis compared to the coordinates of the target voxel (x_0, y_0, z_0).

We can solve for the polynomial coefficients $a_{i,j,k}$ using least squares:

$$\vec{a}\boldsymbol{X} = \vec{d} \tag{6.2}$$

$$\vec{a} = (\boldsymbol{X}^T\boldsymbol{X})^{-1}\boldsymbol{X}^T\vec{d} = \boldsymbol{C}\vec{d} \tag{6.3}$$

where $\vec{a} = [a_{0,0,0}, a_{1,0,0}, a_{0,1,0}, \dots, a_{0,0,2}]$ with dimension 10 and $\vec{d}$ is the image intensity vector with dimension $1 \times N_{voxels}$. Here, $\boldsymbol{X}$ is the relative coordinate matrix of each voxel in the volume with dimension $10 \times N_{voxels}$ defined as $[\mathbf{1}\ \boldsymbol{x_r}\ \boldsymbol{y_r}\ \boldsymbol{z_r}\ \boldsymbol{x_r y_r}\ \boldsymbol{x_r z_r}\ \boldsymbol{y_r z_r}\ \boldsymbol{x_r^2}\ \boldsymbol{y_r^2}\ \boldsymbol{z_r^2}]^T$, and $\boldsymbol{C} = (\boldsymbol{X}^T\boldsymbol{X})^{-1}\boldsymbol{X}^T$ is the pseudo-inverse of $\boldsymbol{X}$ and can be solved using the "pinv" function in MATLAB. The Laplacian L_{SG} of the fitted polynomial at the target voxel (x_0, y_0, z_0) is therefore analytically obtained by:

$$L_{SG}(x_0, y_0, z_0) = 2\big(a_{2,0,0} + a_{0,2,0} + a_{0,0,2}\big) = 2(C_8 + C_9 + C_{10})\vec{d} \tag{6.4}$$

where C_8, C_9, C_{10} are the last three rows of $\boldsymbol{C}$ corresponding to the coefficients of the terms $\boldsymbol{x_r^2}$, $\boldsymbol{y_r^2}$ and $\boldsymbol{z_r^2}$, respectively. They can be reshaped to a 3D convolution kernel, namely the SG Laplacian kernel K_{LSG}:

$$K_{LSG} = 2(C_8 + C_9 + C_{10}). \tag{6.5}$$

Similarly, the first derivatives (i.e., gradient) in x-, y-, z-direction G_x, G_y, G_z at the target voxel (x_0, y_0, z_0) can be obtained by:

$$G_x(x_0, y_0, z_0) = a_{1,0,0} = C_2\vec{d} \tag{6.6}$$

$$G_y(x_0, y_0, z_0) = a_{0,1,0} = C_3\vec{d} \tag{6.7}$$

$$G_z(x_0, y_0, z_0) = a_{0,0,1} = C_4\vec{d} \tag{6.8}$$

Note that the gradient terms with relative coordinates are canceled out because the relative coordinates are zero for the target voxel (x_0, y_0, z_0). Their corresponding SG gradient (GSG) kernel are therefore:

$$K_{Gx} = C_2 \tag{6.9}$$

$$K_{Gy} = C_3 \tag{6.10}$$

$$K_{Gz} = C_4 \tag{6.11}$$

Limitations

The reconstructed EPs images using the SG kernel exhibit grid-like artifacts, due to poor noise suppression at frequencies above the cutoff [125]. However, these artifacts can be easily removed with median filtering, which also helps to reduce boundary errors [100], [126].

According to the kernel domain definition, the kernel can have different shapes. An example of standard cube-shaped kernel is illustrated in Figure 24A. When the kernel domain crosses organ boundaries, the convolution will involve voxels from outside the target organ, leading to boundary artifacts. Arduino et al. 2023 compared [127] three different kernel shapes — cross, sphere and cube — on a homogenous phantom. With the same kernel radii, the cube shape, containing the most voxels, provided the smallest relative deviation from the expected value. The cross shape, containing the fewest voxels, resulted in the least boundary artifacts. However, the median value of all shapes was almost the same. In summary, a larger number of involved voxels in the kernel provides more accurate values but also introduces more boundary effects.

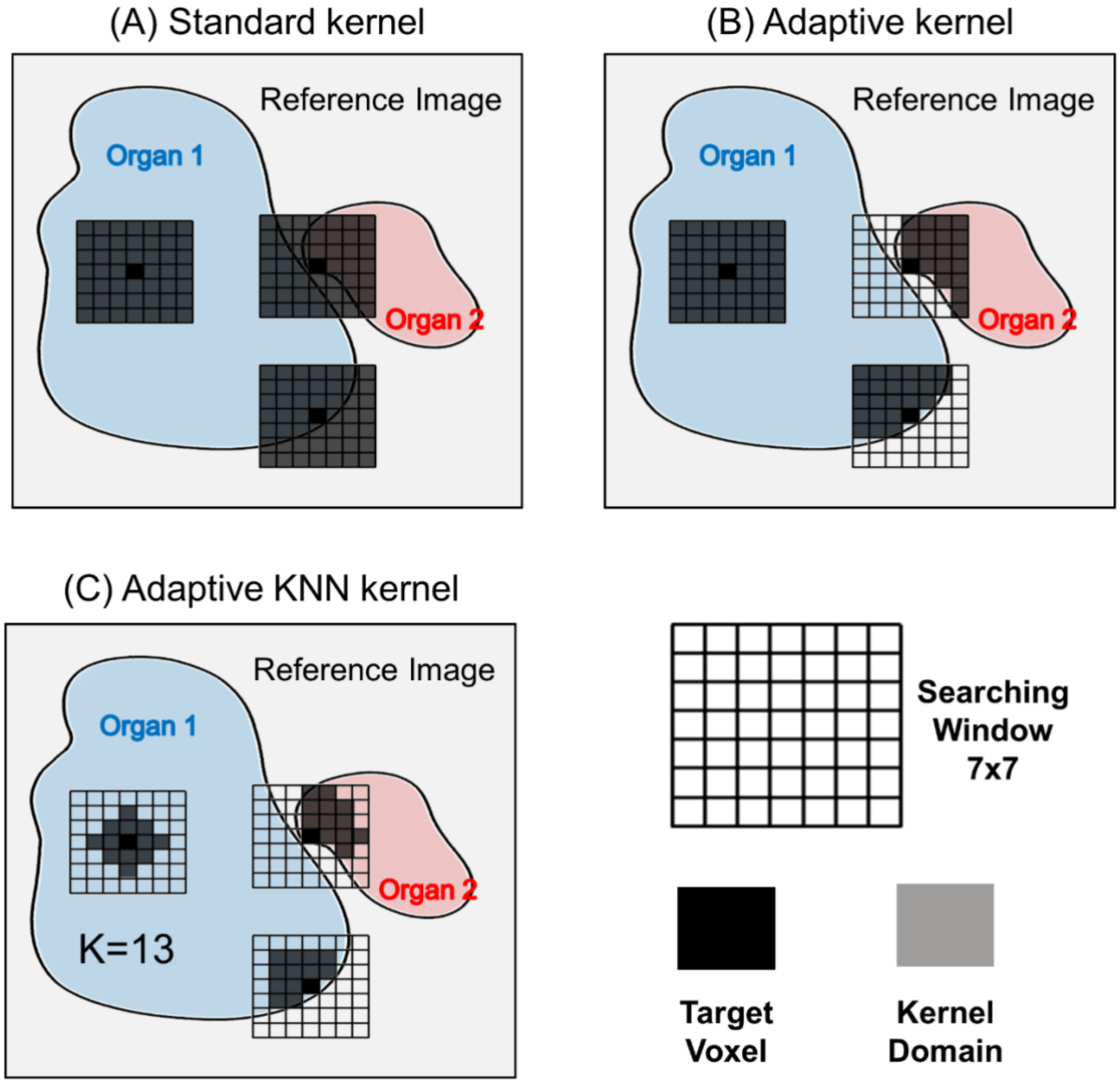

Figure 24. Standard(A), adaptive (B) and adaptive K-nearest neighbor's (C) kernel schemes within a searching window (i.e., maximum of kernel radii) of 7x7. (A) The standard kernel maintains the same cube shape for each target voxel. (B) Based on the standard kernel, the adaptive kernel removes

voxels from outside the target organ. (C) Based on the adaptive kernel, the KNN kernel selects the K (here K=13) nearest neighbors to the target voxel and removes the farther voxels.

6.2.2. Adaptive Savitzky-Golay kernel

To avoid the issue of kernel domain crossing tissue boundaries as shown in Figure 24A and to maintain the validity of the LHA assumption, we need a strategy to restrict the kernel so that it fits the tissue size and shape for each kernel domain.

As illustrated in Figure 24B, when the searching window of the left target voxel is entirely within the homogeneous organ 1, so it remains its original shape for optimal smoothing quality. However, for the two right target voxels, some voxels must be removed to adapt to the edge of the tissue and to prevent the artifact caused by including another tissue.

The identification of tissue type masks and corresponding boundaries can be obtained by segmenting the magnitude image, or another image, acquired with a different MR contrast (e.g. T_1-weighted, T_2-weighted image etc.) [65]. In each kernel domain, the voxels with greatest intensity similarity to the voxel in the center can be identified by an intensity difference threshold h after normalization or windowing on the denoised reference magnitude data:

$$Shape = (|S(x,y,z) - S(x_0,y_0,z_0)| < h) \tag{6.12}$$

where $Shape$ is a logical local mask, $S(x,y,z)$ is the intensity of a local image confined by a searching window, $S(x_0,y_0,z_0)$ is the intensity of the target voxel or the central voxel in the searching window. Using the local mask $Shape$, the relative coordinates matrix $\boldsymbol{X}$ can be rebuild, allowing for the calculation of the adaptive kernel coefficients. Considering that disconnected tissue intensities may be similar and segmented into $Shape$, any non-connected components (under the 26-connectivity rule in 3D) to the target voxel are removed.

It is also possible to add different weights according to the intensity differences of each voxel during the least-squares process:

$$\boldsymbol{C} = (\boldsymbol{X}^T\boldsymbol{W}\boldsymbol{X})^{-1}\boldsymbol{X}^T\boldsymbol{W} \tag{6.13}$$

where $\boldsymbol{W} = diag(w_1, w_2, \dots, w_n)$ is a diagonal weighting matrix. The weights can be assigned using a Gaussian function based on the intensity differences to the target voxel, as shown in [128]. However, if the segmentation is well done or the threshold value h is well defined, this weighting scheme does not significantly alter the result [72].

Since the number of unknown coefficients in Eq.(6.1) is 10, the number of voxels (N_{voxels}) in $Shape$ should be at least 10 to achieve an adaptive SG kernel. When $N_{voxels} < 10$, the relative coordinate matrix $\boldsymbol{X}$ become low rank, resulting in infinitely many solutions. However, the use of the pseudoinverse ("pinv" in MATLAB) provides a unique solution in the sense of the minimum norm least-squares.

6.2.3. Adaptive K-nearest neighbors' kernel

The left target voxel in Figure 24B benefits more filtering with more involved voxels compared to those target voxels at the boundaries. This results in impaired smoothing effects from the organ center to its boundary. To address this, we proposed a novel K-nearest neighbor (KNN) SG kernel based on the adaptive kernel concept. This method selects the fixed K nearest neighbors to the target voxels within the searching window, as shown in Figure 24C.

Once the local logical mask $Shape$ is determined, the index of each "True" voxel can be transformed into its 3D location (x, y, z). Then, we can perform the KNN search using the "knnsearch" function in MATLAB, with the metric being the 3D Euclidean distance ($D_{x,y,z}$) to the central voxel (x_0, y_0, z_0):

$$D_{x,y,z}^2 = (x - x_0)^2 + (y - y_0)^2 + (z - z_0)^2 \tag{6.14}$$

Only the voxels with the K smallest $D_{x,y,z}^2$ values remain in the local mask $Shape$. If the number of "True" voxels in $Shape$ is below K, it will include the maximum number of voxels possible for $Shape$.

Another advantage of this approach is that it ensures the selection of nearby voxels, which have higher contributions and avoids distant adjacent voxels that could introduce significant changes in EPs reconstruction. The more distant a voxel is, the more challenging it becomes to align its corresponding EPs with those of the target voxel, i.e. $\nabla\kappa \neq 0$.

6.3. Numerical Integration in Surface Integral based EPT

The surface integral based EPT (see Section 2.7) converts the second order (Laplacian) to the first order derivatives (gradient) of B_1, thereby improving the robustness against noise. Additionally, the optimal SG kernel size for gradient calculation is much smaller than that for the Laplacian [123]. This significantly shortens the adaptive kernel calculation time.

For example, the standard EPT in surface integral form is:

$$\kappa = \frac{\oiint \nabla B_1^{\pm}\, dS}{\iiint i\omega\mu_0 B_1^{\pm}\, dV} = \frac{\iint \frac{\partial B_1^{\pm}}{\partial x} dydz + \iint \frac{\partial B_1^{\pm}}{\partial y} dxdz + \iint \frac{\partial B_1^{\pm}}{\partial z} dxdy}{i\omega\mu_0 \iiint B_1^{\pm} dxdydz} \tag{6.15}$$

where dx, dy and dz are the spacings of the measured $B_1^{\pm}$ image in the x, y and z directions, respectively. This involves three surface integrals of the gradient of $B_1^{\pm}$ on the x, y and z-plane along with the volume integral of $B_1^{\pm}$ that is enclosed by these surfaces. The gradient terms $\frac{\partial B_1^{\pm}}{\partial x}$, $\frac{\partial B_1^{\pm}}{\partial y}$ and $\frac{\partial B_1^{\pm}}{\partial z}$ can be calculated using the SG gradient kernel. The discretization of the surface or volume integral can be achieved through a convolution kernel.

6.3.1. Standard and Adaptive Surface Integral Kernel

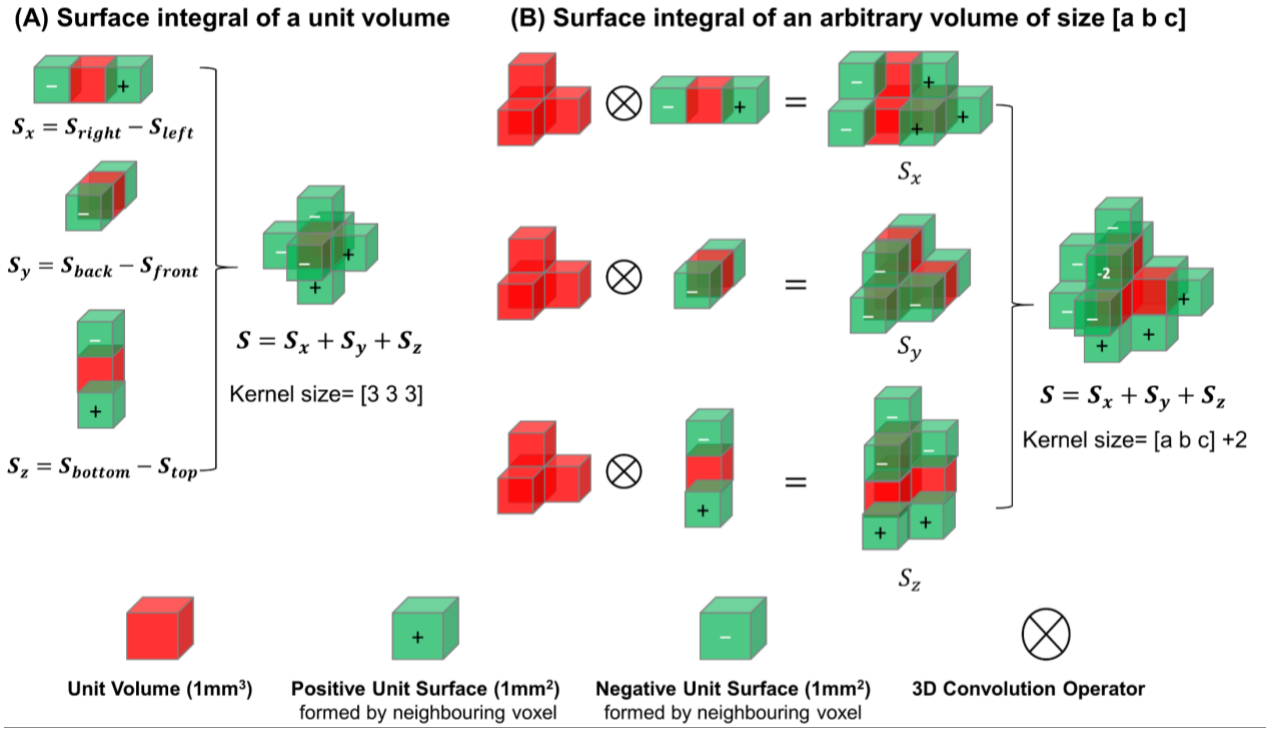

Figure 25. Surface integral kernel schemes for a unit volume (A) and an arbitrary volume (B).

As illustrated in Figure 25A, the surface integral of a volume (S) can be defined as the sum of the surface integrals over the x-, y- and z-planes (i.e., six surrounding surfaces), each with the corresponding outward pointing unit normal vector $\overrightarrow{n_{x,y,z}}$:

$$S = S_x \cdot \overrightarrow{n_x} + S_y \cdot \overrightarrow{n_y} + S_z \cdot \overrightarrow{n_z} = \left(S_{right} - S_{left}\right) + \left(S_{back} - S_{front}\right) + \left(S_{bottom} - S_{top}\right) \quad (6.16)$$

The surface integral kernels on x-, y- and z-planes for a unit volume can be defined as follows:

$$K_{Sx} = [-1\ 0\ 1] \quad (6.17)$$

$$K_{Sy} = \begin{bmatrix} -1 \\ 0 \\ 1 \end{bmatrix} \quad (6.18)$$

$$K_{Sz}(:,:,1) = [-1]\,, K_{Sz}(:,:,2) = [0] \text{ and } K_{Sz}(:,:,3) = [1] \quad (6.19)$$

The total surface integral of $\nabla B_1^{\pm}$ can be calculated as:

$$\oiint \nabla B_1^{\pm}\ dS = \left(\frac{\partial B_1^{\pm}}{\partial x} * K_{Sx}\right) dydz + \left(\frac{\partial B_1^{\pm}}{\partial y} * K_{Sy}\right) dxdz + \left(\frac{\partial B_1^{\pm}}{\partial z} * K_{Sz}\right) dxdy. \quad (6.20)$$

where $*$ is the 3D convolution operator.

In this scenario, the total surface integral kernel size is [3 3 3], with the center being the target voxel. This size may be insufficient for noise suppression. As shown in Figure 25B, the kernel can be expanded to a larger or arbitrary volume using convolution with the unit volume surface kernels mentioned above:

$$K_{Sx}^{adap} = Shape * K_{Sx} \tag{6.21}$$

$$K_{Sy}^{adap} = Shape * K_{Sy} \tag{6.22}$$

$$K_{Sz}^{adap} = Shape * K_{Sz} \tag{6.23}$$

where $Shape$ is the desired volume shape, which can be determined by an adaptative process or a KNN method.

6.3.2. Standard and Adaptive Volume Integral Kernel

Previously, a voxel was considered as a surface within the grid. In this way, six surrounding surfaces form a cuboid volume, with each of the six surrounding voxels contributing equally to the volume, i.e., one-sixth of the total volume. Therefore, the volume integral kernel for a unit volume (Figure 25A) enclosed by its six surrounding surfaces is defined as:

$$K_V(:,:,1) = \begin{bmatrix} 0 & 0 & 0 \\ 0 & \frac{1}{6} & 0 \\ 0 & 0 & 0 \end{bmatrix}, K_V(:,:,2) = \begin{bmatrix} 0 & \frac{1}{6} & 0 \\ \frac{1}{6} & 0 & \frac{1}{6} \\ 0 & \frac{1}{6} & 0 \end{bmatrix} \text{ and } K_V(:,:,3) = \begin{bmatrix} 0 & 0 & 0 \\ 0 & \frac{1}{6} & 0 \\ 0 & 0 & 0 \end{bmatrix}. \tag{6.24}$$

The volume integral of $B_1^{\pm}$ can be calculated as:

$$\iiint i\omega\mu_0 B_1^{\pm}\, dV = i\omega\mu_0 dxdydz \left(B_1^{\pm} * K_V\right). \tag{6.25}$$

Similarly, the volume integral kernel can be expanded to an arbitrary volume with $Shape$:

$$K_V^{adap} = Shape * K_V. \tag{6.26}$$

Notably, since the volume is defined by the enclosing surfaces, the logical local mask $Shape$ must be the same for both K_V^{adap} and $K_{Sx,Sy,Sz}^{adap}$.

This approach can also be considered as an average filtering of the surrounding voxels, enhancing noise robustness. Additionally, for voxels at boundaries that lack 6-connectivity to calculate the surface integral, resulting in partial or incomplete volumes, this kernel can provide a correction.

6.4. Methods

Firstly, we determined the optimal kernel size using in-silico brain data for standard, adaptive, and KNN kernels. Subsequently, these optimized kernels were applied and compared in simulations, on a resolution phantom, and in vivo brain data, with Laplacian-based and Surface Integral-based EPT methods.

6.4.1. Finding the Optimal Kernel Size

The goal is to determine the optimal kernel size for a given SNR level using an in-silico brain data. The in-silico brain data (using Sim4Life) which includes complex B_1^+, ground-truth EPs maps, and segmentations of white matter, gray matter and CSF). These data were extracted from the first MR EPT reconstruction challenge (Phase 2) [129]. Noisy B_1^+ data were obtained by adding Gaussian noise with an SNR of 30 dB (corresponding to our UTE sequence case for in vivo brain) to the real and imaginary components. The label image of segmentation was considered as the reference image during the adaptive process.

For the Laplacian calculation, the optimal kernel size corresponds to the minimum NRMSE between the reconstructed conductivity via standard Laplacian based EPT (Eq.(2.6)) and the GT conductivity. For the gradient calculation, the optimal kernel size corresponds to the minimum of mean absolute error (MAE) [123], defined as follows:

$$MAE_{grad} = \frac{1}{3}\frac{1}{N}\sum_{i=1}^{N}\left|\hat{G}_{xi} - G_{xi}\right| + \left|\hat{G}_{yi} - G_{yi}\right| + \left|\hat{G}_{zi} - G_{zi}\right| \tag{6.27}$$

where $\hat{G}_{xi}$, $\hat{G}_{yi}$ and $\hat{G}_{zi}$ are the gradient of the noisy B_1^+ using the SG kernel, K_{Gx}, K_{Gy}, K_{Gz}, respectively. The GT gradients (G_{xi}, G_{yi}, and G_{zi}) were obtained in the noiseless cases using the central FD kernel, i.e., $\left[-\frac{1}{2}, 0, \frac{1}{2}\right]$. For the surface integral calculation, the optimal kernel size corresponds to the minimum NRMSE between the reconstructed conductivity via standard surface integral based EPT (Eq.(6.15), after applying the optimal GSG kernel) and the GT conductivity. Before these error calculations, two voxels at boundaries were removed in ROIs to avoid the boundary artifacts.

A wide range of kernel sizes from [3 3 3] to [31 31 31] was tested for the optimal standard and adaptive kernel size study. For the KNN kernel, the searching window was fixed at [31 31 31], but the number of neighbors (K-number) ranged from 3^3 to 27^3.

6.4.2. Kernel Comparison Experiments

In silico: The same noisy B_1^+ data (SNR=30 dB) data was used for kernel comparisons via the NRMSE between the reconstructed and GT conductivity.

Resolution Phantom: The first MRI measurement of UTE (at 11 min) on the resolution phantom mentioned in Section 4.3.1 was used for testing. Kernel comparisons were conducted via the NRMSE between the reconstructed and fitted VNA conductivity. The segmentation was considered as the reference image during the adaptive process.

In vivo: The same UTE brain data mentioned in Section 3.1.5.3 was used for testing. Kernel comparisons were conducted via the quantification of conductivity in ROIs including mean, standard deviation and median, compared to ex vivo literature value. The MPRAGE image was considered as the reference image during the adaptive process.

Notably, due to the lack of $|B_1^+|$ data, the conductivity in the resolution phantom and in vivo, was reconstructed using the Image-based EPT formulations, specifically in Laplacian (Eq.(2.59)) and surface integral (Eq.(2.87)) forms.

6.5. Results

6.5.1. Optimal Kernel Size

Figure 26 shows NRMSE and MAE plotted as a function of the kernel size or K-number at SNR=30 dB. In general, except for the gradient kernel, the NRMESE decreases as kernel size and K-number increases. Additionally, the optimal gradient kernel is much smaller than Laplacian kernel (Figure 26C and D). The adaptive kernel consistently provides lower NRMSE or MAE compared to its standard form (Figure 26A, C and E). The NRMSE curves for the Laplacian and surface integral (SI) kernels (Figure 26A, B, E and F) exhibit an exponential-like decline, falling rapidly at first and then leveling off at a kernel size of [25 25 25] or K-number of 23^3. Beyond this point, further increases in kernel size have negligible effects.

The optimal kernel sizes or K-number corresponding to the minimum error are:

- [31 31 31] for LSG, adaptive LSG, SI and adaptive SI
- [5 5 5] for GSG
- [11 11 11] for adaptive GSG
- K=11^3 for KNN GSG
- K=23^3 for KNN LSG and KNN SI.

The above kernel sizes or K-number were fixed for the following studies.

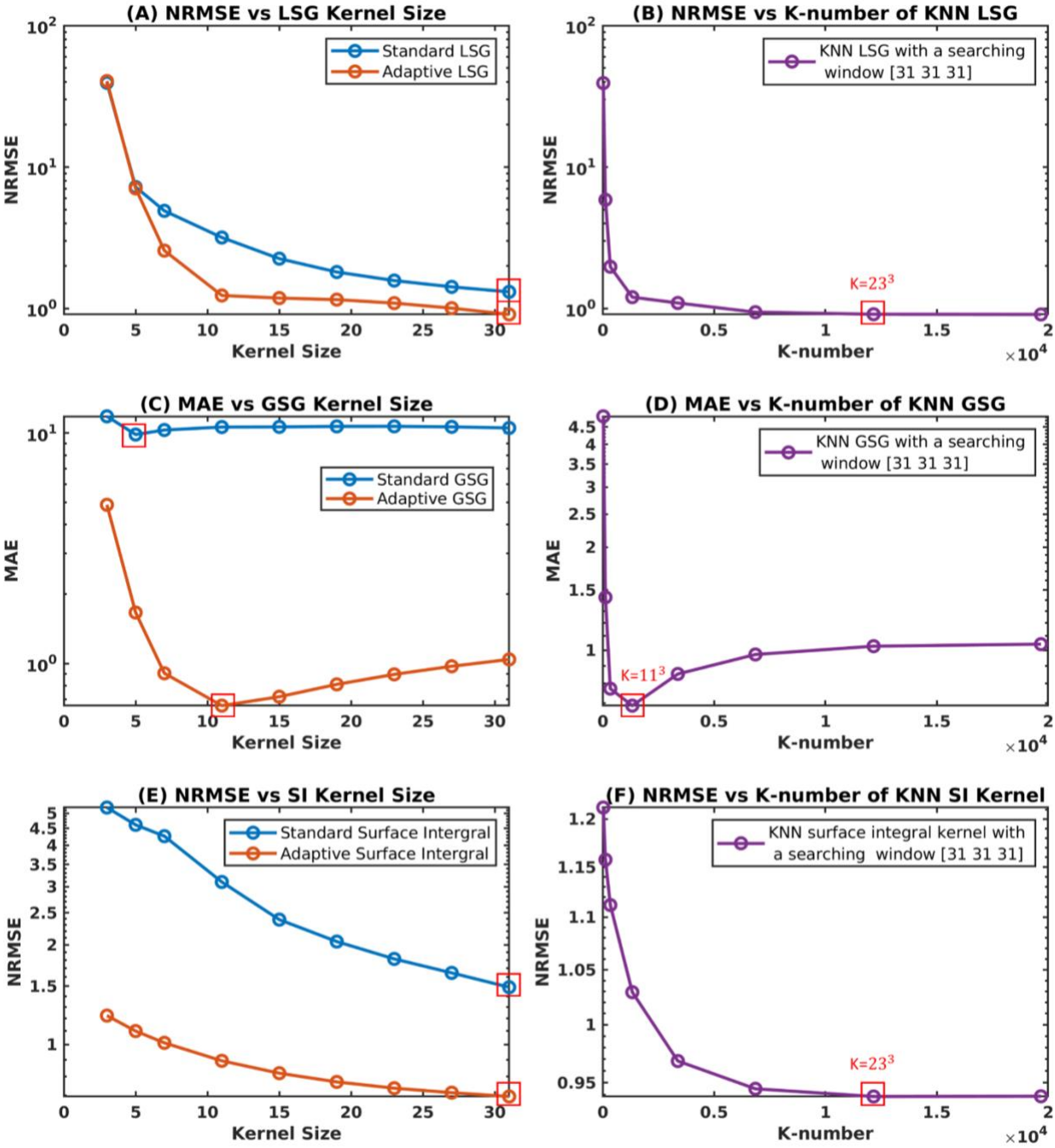

Figure 26. Optimizing the kernel size and K-number for conductivity reconstruction in simulation with SNR= 30 dB. The optimal size or K-number for each kernel is indicated by a red square. (LSG: Laplacian Savitzky-Golay kernel, GSG: Gradient Savitzky-Golay kernel, SI: Surface Integral)

6.5.2. In Silico

Figure 27 displays the reconstructed conductivity maps for different kernel in noisy silico data along with the NRMSE values are displayed. The standard LSG and SI kernels are too large to clearly show the brain structure. However, the adaptive and KNN kernels successfully preserve the edges, with the edges of surface integral (SI) kernels being more evident than those of Laplacian kernels. While the KNN and adaptive Laplacian kernels yield the same conductivity maps and NRMSE values, their

surface integral forms differ in CSF. Specifically, the central CSF values of the adaptive SI kernel are closer to the ground truth (GT), whereas the CSF peripheries are more uniform in the KNN SI kernel. This may be due to the fixed K-number and limited smoothing effects in CSF. The adaptive SI kernel provides a conductivity map closest to the GT with the lowest NRMSE of 0.70.

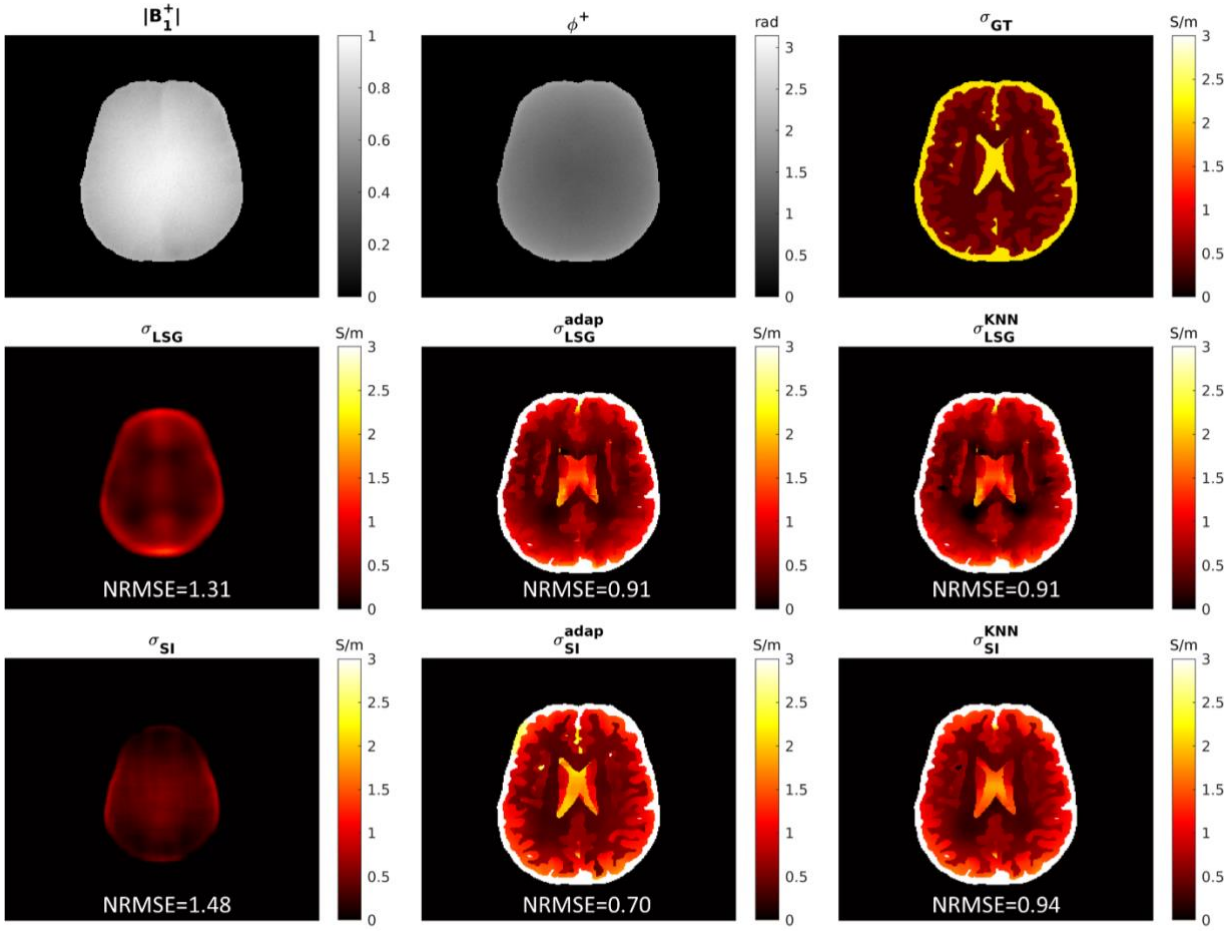

Figure 27. Magnitude and phase of noisy B_1^+ (axial) in silico brain data (SNR=30 dB), along with the ground truth (GT) and reconstructed conductivity maps. The second row corresponds to the Laplacian based EPT using LSG, adaptive LSG and KNN LSG kernel. The third line corresponds to the surface-integral based EPT using surface integral (SI), adaptive SI and KNN SI kernel. The NRMSE values compared to GT are also displayed.

6.5.3. Resolution Phantom

Figure 28 displays the reconstructed conductivity maps for different kernel on the resolution phantom along with the NRMSE values are displayed. Similar, the standard LSG and SI kernel size are too large and unsuitable for achieving resolution. A red halo is present next to the holes in all reconstructed images, possibly due to diffusion effects between the saline in the holes and the surrounding agar gel. Among the kernels, the KNN SI provides the least halo effect and the most uniform background. None of the kernels can accurately resolve the conductivity values of the smallest round hole (d = 5 mm) or the cross hole (width = 2.5 mm), indicating the resolution limit for the homogeneous EPT formulation. The

adaptive SI kernel provides more accurate conductivity values in the second largest round hole (d = 15 mm, indicated by a blue arrow in Figure 28) compared to others, resulting in the lowest NRMSE of 0.55.

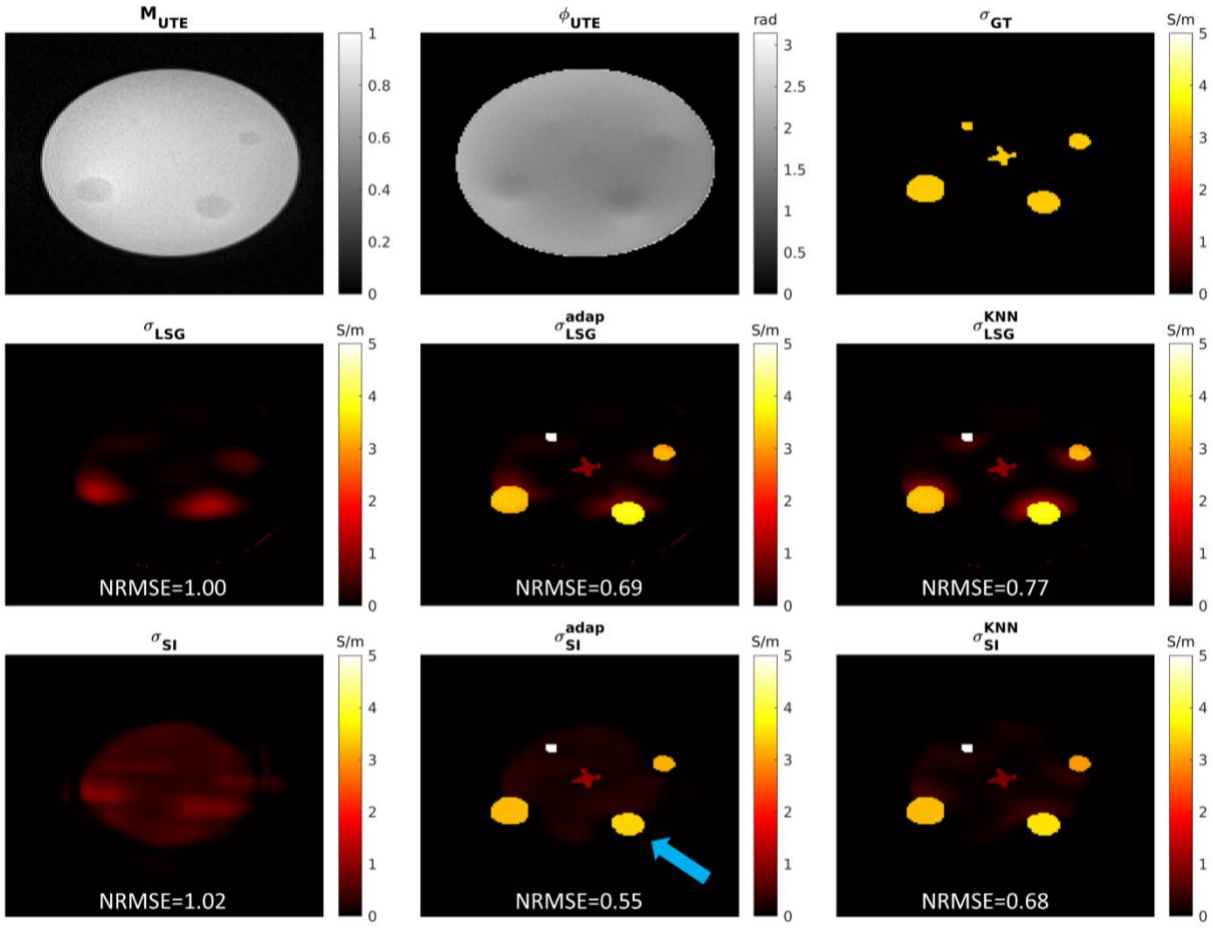

Figure 28. Magnitude and phase of UTE images on resolution phantom (SNR ≈ 30 dB), along with the ground truth (GT) and reconstructed conductivity maps. The second row corresponds to the Laplacian based EPT using LSG, adaptive LSG and KNN LSG kernel. The third line corresponds to the surface-integral based EPT using surface integral (SI), adaptive SI and KNN SI kernel. The NRMSE values compared to GT are also displayed.

6.5.4. In Vivo

Figure 29 displays the reconstructed conductivity maps using different kernels on a healthy volunteer brain, acquired with the UTE sequence. The Laplacian kernels provide more structural information than the surface integral kernels, although the CSF values at the peripheries are missing. The surface integral kernels fail to reconstruct the CSF accurately, and the reconstructed conductivity values are generally lower than those produced by the Laplacian kernels. This discrepancy may be due to the surface integral EPT being more sensitive to segmentation. Comparing the adaptive and KNN kernels, the adaptive LSG and KNN LSG provide almost identical reconstructions, whereas the reconstructions using adaptive SI and KNN SI differ. Notably, the KNN SI provides a more uniform conductivity map.

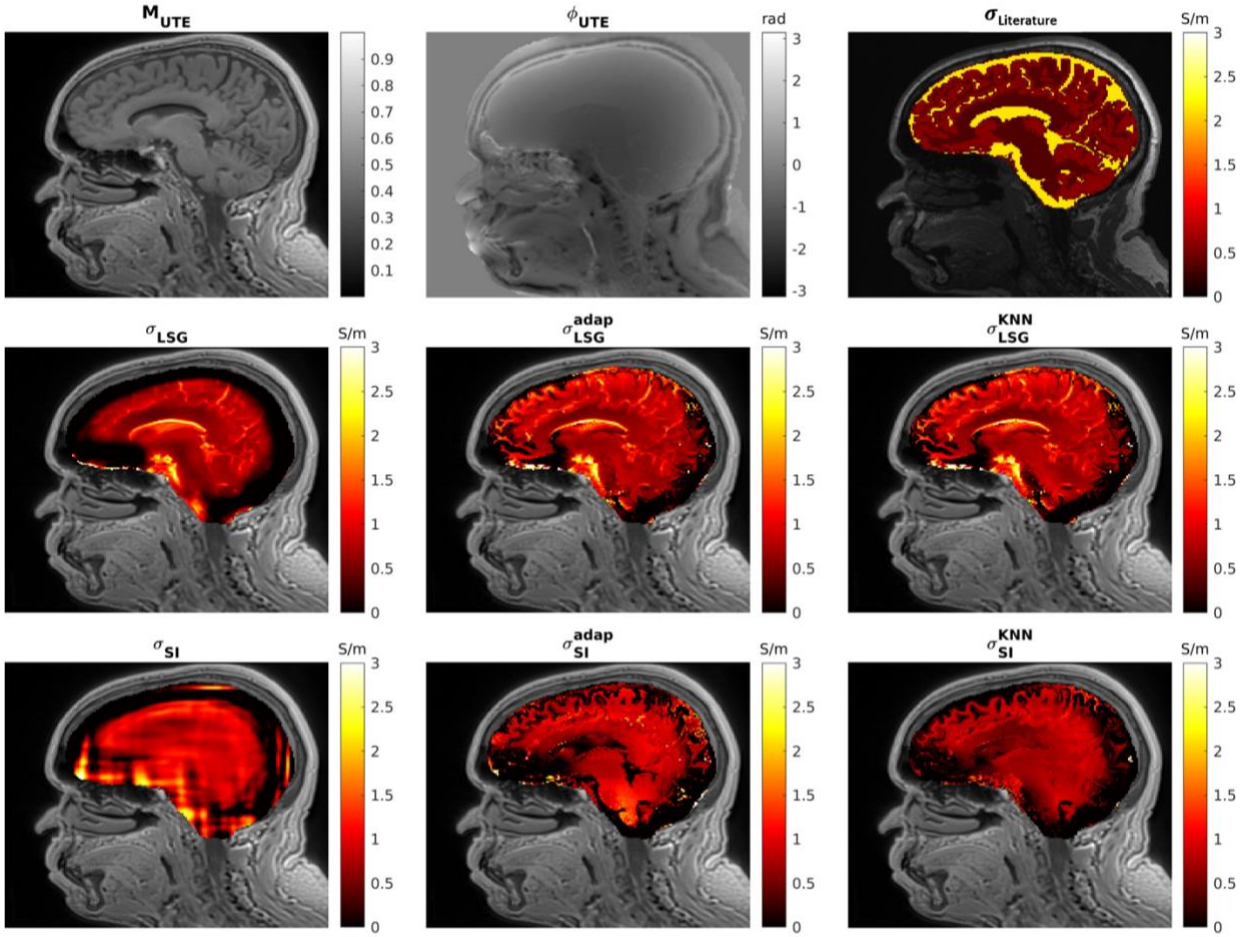

Figure 29. Magnitude and phase of UTE images (sagittal) on a healthy volunteer's brain (SNR ≈ 30 dB), along with the ground truth (GT) and reconstructed conductivity maps. The second row corresponds to the Laplacian based EPT using LSG, adaptive LSG and KNN LSG kernel. The third line corresponds to the surface integral based EPT using surface integral (SI), adaptive SI and KNN SI kernel.

Figure 30 shows the boxplots of reconstructed conductivity using different kernels. For GM, the median values of LSG, adaptive LSG, KNN LSG, and SI are nearly identical and align well with the literature values. For WM, all reconstructed conductivity values are overestimated by about 0.2-0.4 S/m compared to the literature values. Conversely, CSF conductivity is underestimated for all kernels. The boxplots for the Laplacian kernels are generally at the same level and closer to the literature line (in green), with the adaptive LSG and KNN LSG being almost identical. However, the boxplots for the surface integral kernels differ, with adaptive SI showing the greatest deviation from the literature line, followed by KNN SI and SI.

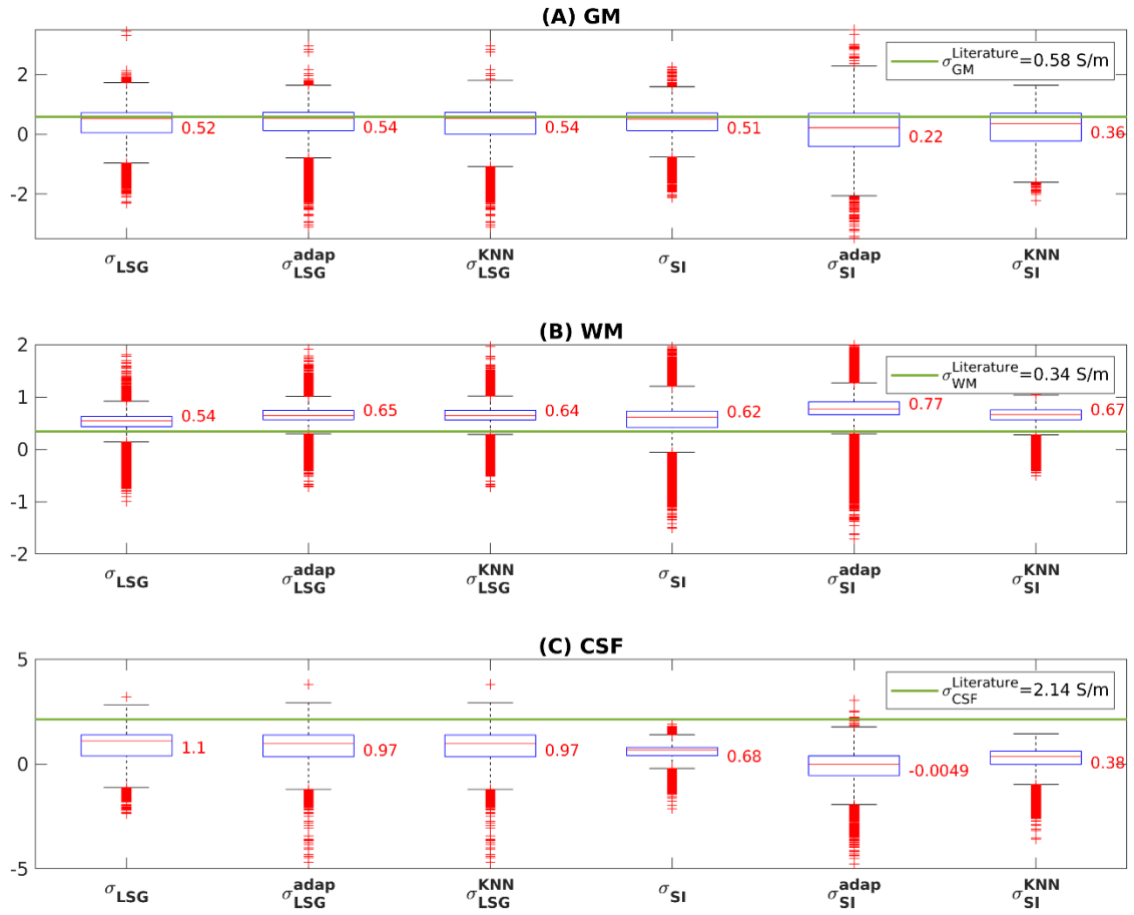

Figure 30. Boxplots of the reconstructed conductivity using different kernels in (A) gray matter (GM), (B) white matter (WM) and (C) cerebrospinal fluid (CSF). The median values are displayed at the right of box. The literature values are also displayed (from Gabriel et al. 1996 [28], [29], [30]).

6.6. Discussion and Conclusion

In this chapter, the implementation of homogeneous Laplacian-based and surface-integral-based EPT using standard, adaptive, and KNN kernel schemes is successfully realized. Optimal kernel sizes were determined by minimizing error in simulated brain data. Generally, the NRMSE decreases as the number of involved voxels increases, except in the case of gradient calculation. Kernel size optimization was primarily based on NRMSE or MAE, focusing on value errors but less on structural information. Consequently, an oversized kernel was chosen for the standard scheme. This could be improved by using a joint metric that includes the Structural Similarity Index Measure (SSIM), shape index, or mutual information.

In terms of kernel schemes, the adaptive scheme appears to be the best in terms of NRMSE, even though KNN provides more uniform reconstruction (i.e., less conductivity dispersion in homogeneous regions). This is because the number of involved voxels in the adaptive scheme is greater than in KNN, resulting in better noise suppression. However, the KNN scheme may benefit more at higher SNR levels.

Among all kernels, the surface-integral-based EPT with the adaptive GSG ([11, 11, 11]) and SI ([31, 31, 31]) kernels achieves the best conductivity reconstruction in simulations and on a resolution phantom at SNR = 30 dB. However, this surface integral formulation seems sensitive to local segmentation or local volume homogeneity, as the adaptive and KNN forms differ, while they are almost the same in the Laplacian method. This leads to poorer quality than the Laplacian method in in-vivo conductivity brain imaging, especially at CSF boundaries. Conversely, the Laplacian method exhibits higher robustness in these ambiguous regions.

Chapter 7. In Vivo Study: Electrical Conductivity Changes Related to Age, Fat Fraction and Sex

7.1. Introduction

The RF pulse during MR scans induces heating in tissue. For safety concerns, it is crucial to estimate the specific absorption rate (SAR), which requires reliable electrical properties (EPs) values. Typically, these values are obtained from ex vivo databases, such as the one compiled by Gabriel in the 1990s from post-mortem samples [28], [29], [30], [130].

However, existing in vivo studies using EPT [37], [71], [131] show significant deviations from these ex vivo reference EPs values. A recent review of the literature on variations in brain tissue conductivity [132] highlights the uncertainties in this regard, noting that correlations with individual conditions – such as pathologies – are evident. Additionally, EP values may be age-dependent [11]. For example, research by Peyman [10] in animal studies demonstrated that conductivity and permittivity of white matter decrease from childhood to adulthood in pigs. This implies that SAR might differ between infants and adults. For instance, Malik et al. (2022) [133] assumed that children have conductivity 0.94 times that of adults for SAR modeling at 7T, due to the lower water content in children compared to adults. This results in different SAR distributions and impacts the guideline limits for children. While these findings offer insight, the exact age-related changes in human conductivity and the resulting SAR variations remain unclear.

Consequently, obtaining reliable in vivo EP values and understanding their variability within the population is especially important for the use of standard electromagnetic models in SAR estimation. Better modeling might reduce safety margins and, ultimately, examination times. Additionally, understanding the evolution of conductivity in relation to patient characteristics may provide new insights into certain physiological mechanisms, such as aging.

In this study, we aimed to improve current databases since personalized SAR estimation would benefit from better EPs estimation. We sought to estimate macroscopic values of conductivity in several organs (brain and torso) within a small adult population of 17 volunteers. This was achieved using complex images from a 3D UTE sequence with a flip angle of 3°, which was identified as the optimal sequence in prior phantom studies. The Generalized-Image-based (GIB) EPT method, which was previously considered optimal in the phantom study, was not selected due to difficulties in optimizing the regularization parameters for the entire ROI, particularly concerning diffusion and convection coefficients. Instead, we opted for its simplified homogeneous version, Image-based (IB) [53] EPT in conjunction with an adaptive Savitzky-Golay KNN kernel for reconstruction. We then explored the

relationship of these values with biological parameters such as age, Fat Volume Fraction (FVF), BMI (Body Mass Index), and sex, identifying relevant correlations.

This study resulted in a conference communication:

He Z, Soullié P, Ambarki K, Lefebvre PM, Odille F. Age-related changes of electrical conductivity in adults: preliminary results with MR-EPT. In: *Proceedings of 32nd Annual Meeting of International Society of Magnetic Resonance in Medicine (ISMRM)*. Singapore; 2024:3686. (Digital Poster)

And one published article:

He Z, Soullié P, Lefebvre PM, Ambarki K, Felblinger J, Odille F. Changes of in vivo electrical conductivity in the brain and torso related to age, fat fraction and sex using MRI. *Sci Rep* **14**, 16109 (2024). https://doi.org/10.1038/s41598-024-67014-9

7.2. Materials and Methods

This study was approved by an ethics committee (Comité de Protection des Personnes Sud Est III) and informed written consent was obtained (ClinicalTrials.gov identifier: NCT04645628, first trial registration 27/11/2020). The study was supported by CIC-IT Nancy, sponsored by CHRU Nancy (Département Méthodologie, Promotion, Investigation), and carried out in accordance with the relevant guidelines and regulations.

7.2.1. Simulation

The proof of concept of this study was performed using a simple EM simulation with the commercial software CST Studio Suite 2023 (V6R2023x.FP.CFA.2419, https://software.3ds.com, Computer Simulation Technology, Dassault Systemes, France). A two-port quadrature birdcage coil and a multi-compartment cylindrical conductive volume were modeled and used to simulate both RF transmit and receive fields at 123 MHz. The outer diameter of the cylindrical volume is 30 cm, comparable to the dimensions of a human body, and the concentric sections are between 3 and 4 cm. The conductivity range has been chosen to be representative of most tissues. The composite RF field data were then exported to MATLAB, where we added artificial Gaussian noise to obtain an SNR comparable to our experimental images. Reconstructed conductivity values were compared with the reference values in both noiseless and noisy models.

7.2.2. Study Population

The average conductivity standard deviation of previous studies [37], [82] can be approximated at 0.3 S/m for the best results. The sample size required to provide a 95% confidence interval with a 0.16 S/m margin of error is fourteen [126]. Assuming a dropout rate of 15%, the MR-EPT study was performed on seventeen volunteers (10 males & 7 females) aged between 25 and 73 years old (mean =

43.5, SD = 16.9), with body mass index range from 19.6 to 32.6 kg/m² (mean = 24.5, SD = 2.6). Besides, this number of volunteers allows us to test a maximum of two predictors.

7.2.3. MRI Measurements

	BRAIN		TORSO	
Sequence	MPRAGE	UTE SpiralVIBE	VIBE DIXON	UTE SpiralVIBE
TE (ms)	2.45	0.05	1.03 - 2.13	0.05
TR (ms)	2300	7.56	4.06	2.73
TI (ms)	900	/	/	/
Flip Angle (°)	9	3	11	3
FoV (mm)	270	270	479	500
Reconstruction Matrix	256 x 256 x 176	224 x 224 x 160	224 x 224 x 110	256 x 256 x 96
Bandwidth (Hz/pixel)	250	2232	1063	2170
Pixel Spacing (mm)	1.06	1.21	2.14	1.95
Slice Thickness (mm)	1	1.2	2	2.5
Echo Train Length	1	3	2	1
Parallel Acceleration Factor	3 (in-plane)	2	3 (out-of-plane)	2 (out-of-plane)
Acquisition Time	4 min 9 s	9 min 1 s	16.8 s	17.3 s

Table 8. MR sequences parameters. TE, echo time; TR, repetition time; TI, inversion time; FoV, field-of-view. Note that Dixon sequence needs two TE for water and fat imaging.

Imaging studies were performed on a 3T MAGNETOM Prisma MRI scanner (Siemens Healthineers, Forchheim, Germany), with standard quadrature birdcage coil for transmission. A 20-channel and 18+20-channel phased array coils were respectively used in receive mode for brain and torso mapping.

For the brain study, a reference anatomical volume was acquired using a conventional MPRAGE sequence while complex images from a UTE SpiralVIBE prototype [93], [112] were used for assessing conductivity. It consists in a stack-of-spirals trajectory with adaptive TE and variable-duration slice encoding to minimize T_2^* decay. The relevance of this type of sequence has been demonstrated in the literature for its significant RF weighting [53], [134] and robustness to off-resonance effect and eddy currents.

Regarding torso imaging, UTE images were acquired during a breath-hold period, optimizing resolution, k-space acquisition scheme and slice direction. Reference Water/Fat images were obtained using a standard VIBE DIXON sequence in coronal view. FVF maps were generated from the ratio F/(W+F) applied to each organ. We should point out that we used a dual-echo acquisition to reduce breath-hold time, and this could also lead to a bias in the exact estimation of fat fraction [135]. If this bias is consistent across all organs, however, the trends measured should be similar.

In each case, an optimal 2-port transmission technique was used [136], and receive coil combination was achieved for UTE imaging using the vendor's reference-based adaptive approach [137] which

mimics the data from a complete body coil scan. Phase unwrapping was applied when needed as a simple constant shift since the range of phase variations for our applications lies into $[-\pi, \pi]$. Moreover, an acceleration factor of 2 was also used with the SPIRiT [138] method to reduce acquisition time, without compromising the reconstruction accuracy [139].

For both tissue classes, the specific sequence parameters are reported in Table 8.

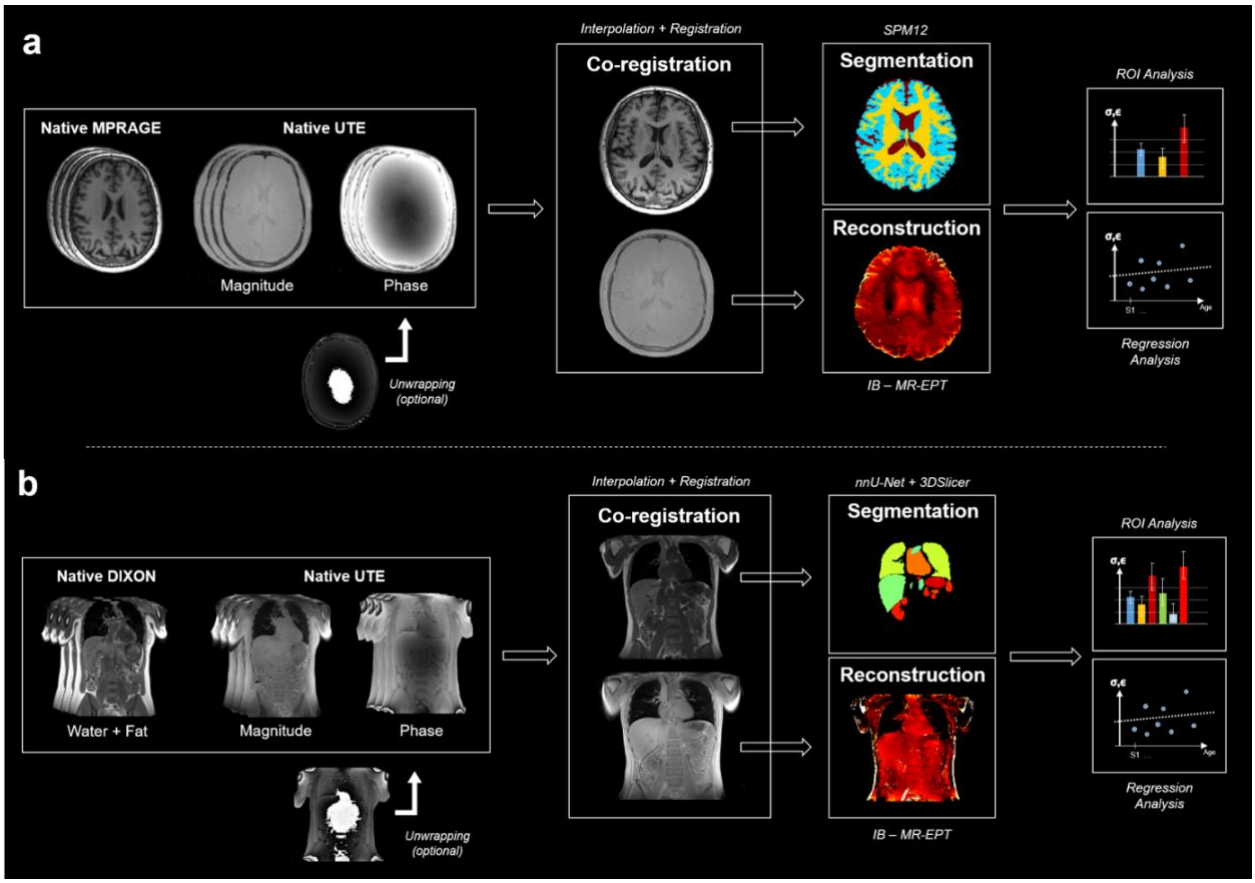

Figure 31. Representation of the reconstruction pipeline for brain (**a**) and torso (**b**) images. Native MPRAGE or VIBE DIXON images are first re-aligned to their respective UTE volumes, then segmented using SPM12 or a combination of nnU-Net and manual delineation. The registered segmentation masks provide both a contrast prior (for constrained estimation of the Laplacian), and the ROIs for subsequent statistical analysis.

7.2.4. Registration and Segmentation

Firstly, in each case, the reference images (i.e., MPRAGE and VIBE DIXON images) were resampled and re-aligned to the UTE magnitude images using spline interpolation and a total-variation-regularized non-rigid registration algorithm [140], respectively (Figure 31). Then for organ-specific region-of-interest (ROI) analysis, we used SPM's segmentation tool (SPM12, London, UK) to post-process the brain MPRAGE registered volume to segment gray matter (GM), white matter (WM) and cerebrospinal fluid (CSF). For torso organ segmentation, we used a semantic nnU-Net pipeline [141] applied to the AMOS22 [142] dataset. This specific database contains images labelled with fifteen

different tissue classes and was the basis of the recent Multi-Modality Abdominal Multi-Organ Segmentation Challenge (MICCAI 2022). The network was implemented with PyTorch [143] and trained in about 8 hours on a GPU (NVIDIA Quadro RTX 5000). After training, we applied it to our registered VIBE DIXON data and segmentations took about one minute per 3D volume. In addition to the tissues labeled in the AMOS database, visceral abdominal fat (VAT), heart and lungs were added semi-automatically from 3DSlicer [144].

7.2.5. Conductivity Reconstruction

After acquisition, the images were transferred to a workstation and processed using MATLAB (The MathWorks, Natick, MA, USA). The choice of a UTE sequence makes it possible to reconstruct conductivity maps directly from complex images, i.e. the combination of magnitude and phase, according to the following relationship [53], [54]:

$$\sigma = \mathrm{Re}(\kappa) = \mathrm{Re}\left(\frac{1}{i\mu\omega}\frac{\Delta\sqrt{B_1^+B_1^-}}{\sqrt{B_1^+B_1^-}}\right) \approx \mathrm{Re}\left(\frac{1}{i\mu\omega}\frac{\Delta\sqrt{S_{UTE}}}{\sqrt{S_{UTE}}}\right)$$

where $\kappa \stackrel{\text{def}}{=} \sigma + i\omega\varepsilon$ is known as complex admittivity, μ is the local magnetic permeability, assumed to be equal to that of the vacuum μ_0 in the RF range, $\omega = \gamma B_0$ is the Larmor frequency, Δ is the Laplacian operator and $B_1^+B_1^-$ is the RF fields product. From a theoretical point of view, this relationship is obtained from a combination of two homogeneous Helmholtz equations applied to B_1^+ and B_1^-, multiplied by B_1^- and B_1^+ respectively, to yield the Laplacian of the product $B_1^+B_1^-$. The square root appears after the neglected terms have been omitted. The magnitude and phase of $\sqrt{B_1^+B_1^-}$ are defined straightforwardly as the magnitude of the product root and half of its phase, assuming proper unwrapping beforehand. Suitability of the UTE sequence here depends on the use of a small flip angle, allowing the product $B_1^+B_1^-$ to appear directly in the signal [41] as $S_{UTE} = I_0 B_1^+B_1^-$ (I_0 = density and relaxation contrasts). This formulation is more general than those involving only the RF phase component [46] and more accurate when the correct assumptions are satisfied [53], essentially that EPs and I_0 contrasts are piecewise constant i.e. $\nabla\kappa = 0$ and $\nabla I_0 = 0$. In this study, the Laplacian was calculated for each target voxel using a bi-adaptive strategy with a constrained Savitzky-Golay kernel. First, a large selection kernel size ([31 31 31]) was used to identify voxels with signal intensity close to the central target voxel. This was done by selecting voxels that belonged to the same segmentation class as the central target voxel, using the segmentation masks obtained from the reference MPRAGE/DIXON images. Once this first mask was obtained, we kept the n nearest neighbors in the sense of the Euclidean distance [124] for the actual fitting process. This bi-adaptive strategy allowed to: (i) limit the bias at the boundaries between tissues; (ii) keep the number of voxels sufficiently large for the Savitzky-Golay fit, thereby preventing noise amplification (Figure 32). The size of the calculation kernel was adapted for each component of this study (brain: N = 15^3 and torso: N = 23^3) as the image resolutions were slightly different. This appeared to be the best compromise for preserving final resolution (brain: 1.2x1.2x1.2

mm^3, torso: 1.95x1.95x2.5 mm^3) and mitigating the effect of noise. Note that no pre- or post-filtering was used to avoid undesired smoothing effects. Conductivity values were finally estimated within the organ-specific ROIs as mean, median and standard deviation. These ROIs are built from individual segmentations where each organ is uniquely labeled, and on which we perform a single-voxel erosion to reduce edge effects.

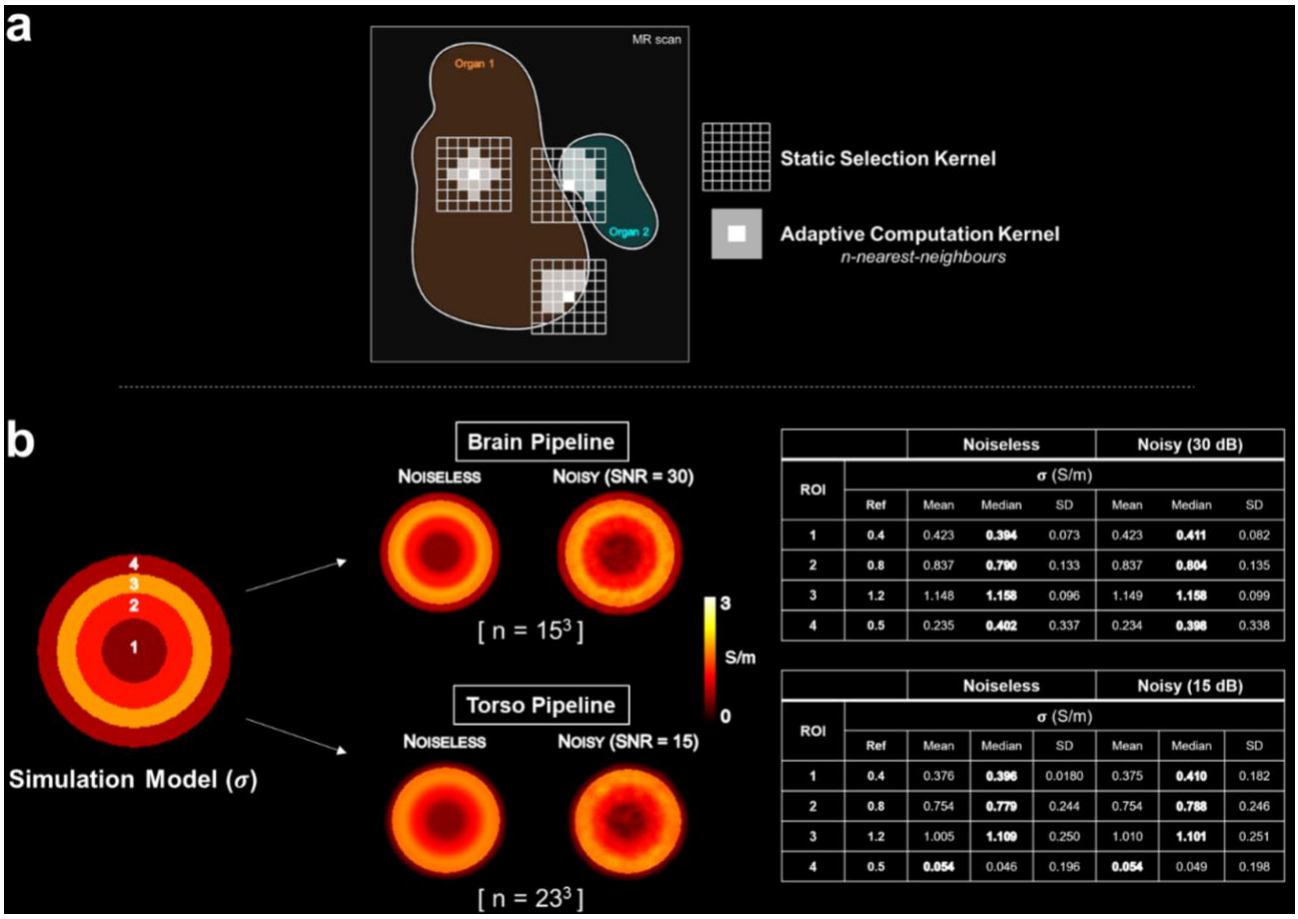

ROI	Noiseless				Noisy (30 dB)		
	σ (S/m)						
	Ref	Mean	Median	SD	Mean	Median	SD
1	0.4	0.423	**0.394**	0.073	0.423	**0.411**	0.082
2	0.8	0.837	**0.790**	0.133	0.837	**0.804**	0.135
3	1.2	1.148	**1.158**	0.096	1.149	**1.158**	0.099
4	0.5	0.235	**0.402**	0.337	0.234	**0.398**	0.338

ROI	Noiseless				Noisy (15 dB)		
	σ (S/m)						
	Ref	Mean	Median	SD	Mean	Median	SD
1	0.4	0.376	**0.396**	0.0180	0.375	**0.410**	0.182
2	0.8	0.754	**0.779**	0.244	0.754	**0.788**	0.246
3	1.2	1.005	**1.109**	0.250	1.010	**1.101**	0.251
4	0.5	**0.054**	0.046	0.196	**0.054**	0.049	0.198

Figure 32. Simulation study as proof of concept. The bi-adaptive kernel (a) optimizes the fitting area and constrains the homogeneity of the Laplacian estimate, based on both contrast proximity and a fixed number of voxels. Both reconstruction pipelines are simulated (b) and the reconstruction results compared with the conductivity model in each case, with and without noise. The respective SNRs are defined according to the values obtained in our in vivo images. The associated tables show the results for each ROI, noting the closest proximity of the median to the reference values.

7.2.6. Statistical Analysis

For this analysis, we included the three types of brain tissue (WM/GM/CSF), as well as fourteen classes of torso tissues from the segmentation step: [Spleen, Right and Left Kidneys, Gallbladder, Esophagus, Liver, Stomach, Aorta, Postcava, Pancreas, Duodenum] from nnU-Net [141] and [Heart, Lungs, Visceral Fat (VAT)] from manual segmentation.

Data were pooled and grouped according to tissue types, in order to determine (i) an estimate of mean/median/SD conductivity for each tissue, (ii) which significant independent variables account for

differences in conductivity, and (iii) any extended relationship between conductivity and reported significant variables.

Boxplot diagrams, presenting the ROIs medians, means and standard deviations of conductivity measurements in our cohort were generated to display variations in conductivity within different tissue classes. We also provide metrics on the number of voxels associated with each ROI, as well as Fat Volume Fraction (FVF) statistics for torso organs only. Note that these numbers of voxels are an important reliability criterion: the higher they are, the more effective the compensation for reconstruction errors.

We aimed to test the independent influence of sex, age, BMI or FVF on tissues conductivity (Two-tailed Pearson's correlation) with a linear model using the MATLAB fit linear model function. Pearson correlation coefficient r and p values for all estimators were given, and p values below 0.05 were considered to indicate statistical significance. Once the univariate regressions have been obtained, and if two predictors are significant, we use multivariate models (glmfit) to test for weighted dependence. The correlation between predictors is also estimated using regression. Linear regression curves were generated for univariate models.

7.3. Results

Brain data from all volunteers (n=17) were used for the analyses whereas only fifteen torso data were usable. One of the volunteers had a known intestinal pathology, and an incidental finding was made in another one. They were excluded from the subsequent statistical analyses, but we do provide reconstruction data for illustrative purposes in Figure 33.

7.3.1. Simulation Study

The use of a bi-adaptive computation kernel optimizes the role of the prior in the reconstruction process as it allows a voxel selection that matches the piecewise constant model equation. A simple illustration is provided in Figure 32. As the typical SNR of our brain images was ~30 dB, and that of our torso images was ~15 dB, we mimicked both reconstruction pipelines and adapted the size of the computation kernel accordingly. While it maintains a very good accuracy in each ROI without excessive smoothing, it is also robust to noise (Figure 32). There are however some visible deviations due to the lack of signal at the edge of the calculation area, as well as visible inconsistencies due to inherent noise amplification. SD values reflect both the effect of smoothing and noise. It is also worth noting here that the median is a better absolute estimator than the mean for central compartments.

7.3.2. Conductivity Maps

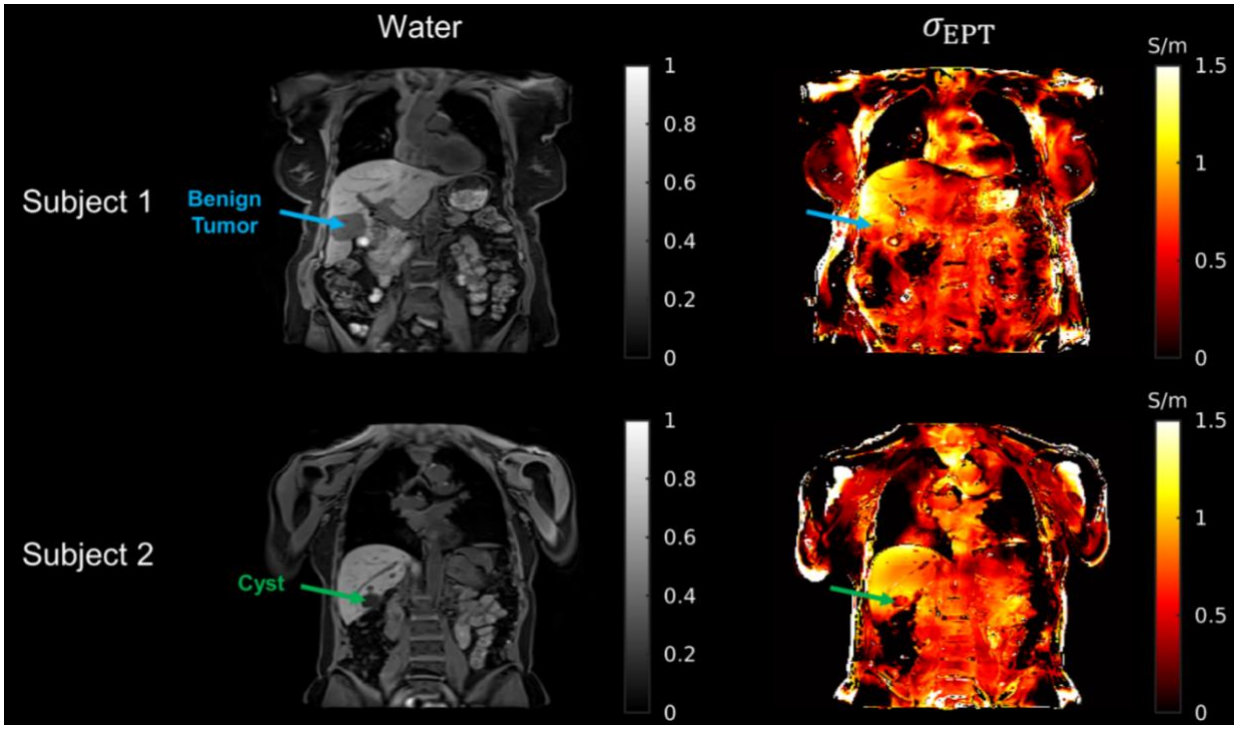

Figure 33. Dixon water images and reconstructed conductivity σ_{EPT} maps on two abnormal subjects: one with a benign liver tumor (Subject 1) and another with liver cysts (Subject 2). These images exhibit distinctive contrasts compared to normal tissue in both water and σ_{EPT} images.

Examples of reconstructed maps are shown in Figure 34 with associated ROIs. The visible segmentations were subsequently eroded for statistical analysis, as the decrease in quality of conductivity maps at the periphery or in certain transition zones, such as the CSF or the heart, quickly became apparent. We also note that the proposed technique resulted in non-physical (negative) conductivity values in the lung. Reconstructed images of subjects with known or incidentally discovered conditions are shown in Figure 33 for information purposes only.

7.3.3. Population Values

Means, medians, and SD of conductivity for all selected organs are shown in Figure 35a. We also provide reference conductivity values from the ex vivo literature for comparison when available. The obtained EP values are close yet not equal to the reported literature values. Significant deviations are observed in some ROIs but no obvious pattern seems to emerge, in particular we do not observe a consistent bias between in vivo and ex vivo values. The example of a histogram associated with the estimation of conductivity in the WM in two different subjects is also shown (Figure 35b), which suggests the near-normality of the data, and the validity of the analysis in terms of mean/median. As suggested earlier, we noticed that the median tends to be more stable over organs, likely due to the weight of certain outliers in the calculation of the means. Therefore, the median values were used for

the statistical analyses (Figure 35c). A focus on standard deviations and the average number of voxels helps identify the most reliable regions (e.g. GM, WM, Spleen, Liver, and Pancreas).

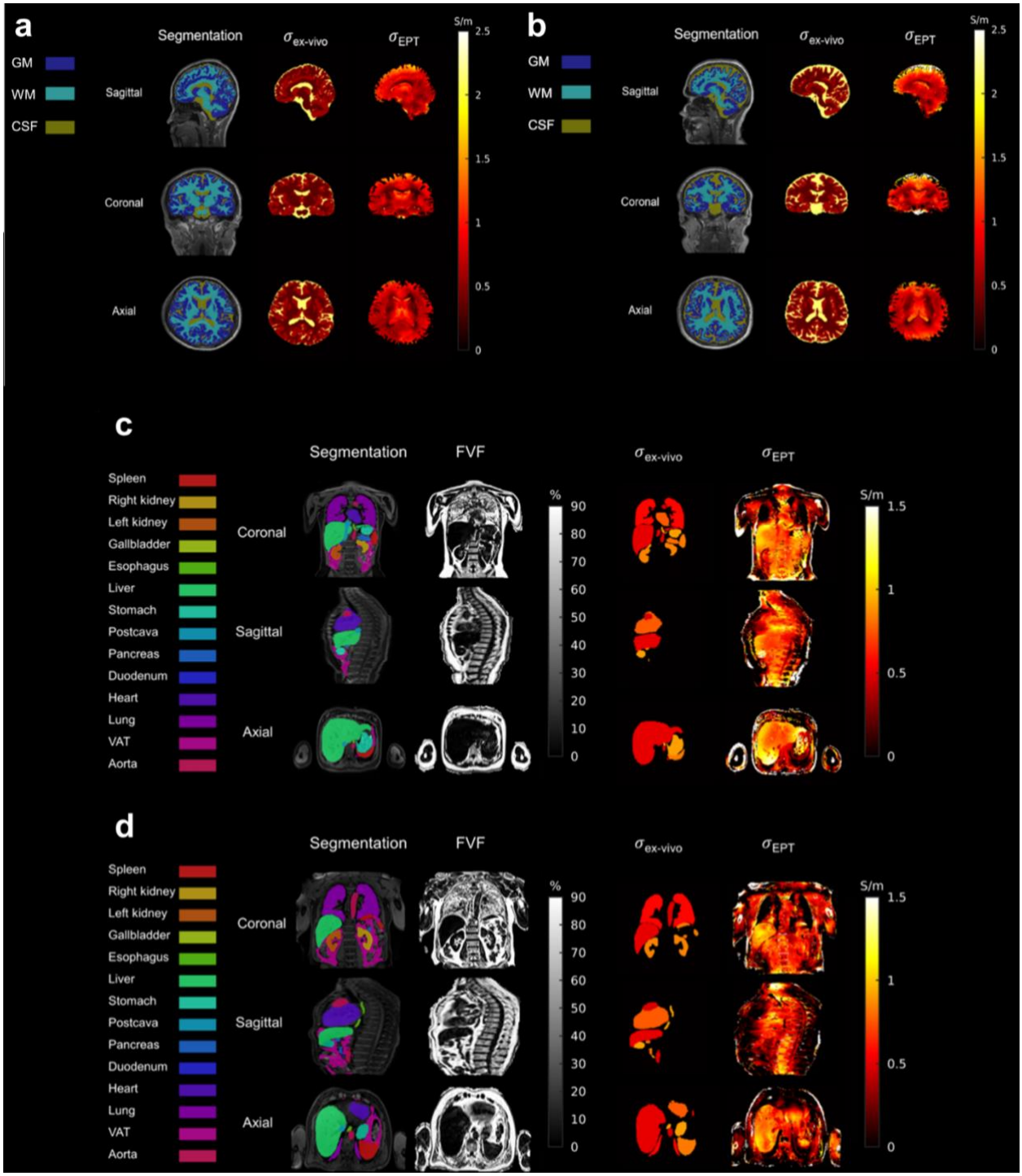

Figure 34. Reconstruction of brain conductivity for two different volunteers (a, b) with their correspondent segmentation and reference maps. Note here the lack of conductivity matching in the ventricles (CSF) due to the insufficient signal in the UTE magnitude map. Similarly, torso conductivity

maps (c, d) for another two volunteers, segmentation and reference maps, as well as estimates of fat fraction. Boundary artefacts at the periphery of the two volumes are clearly visible.

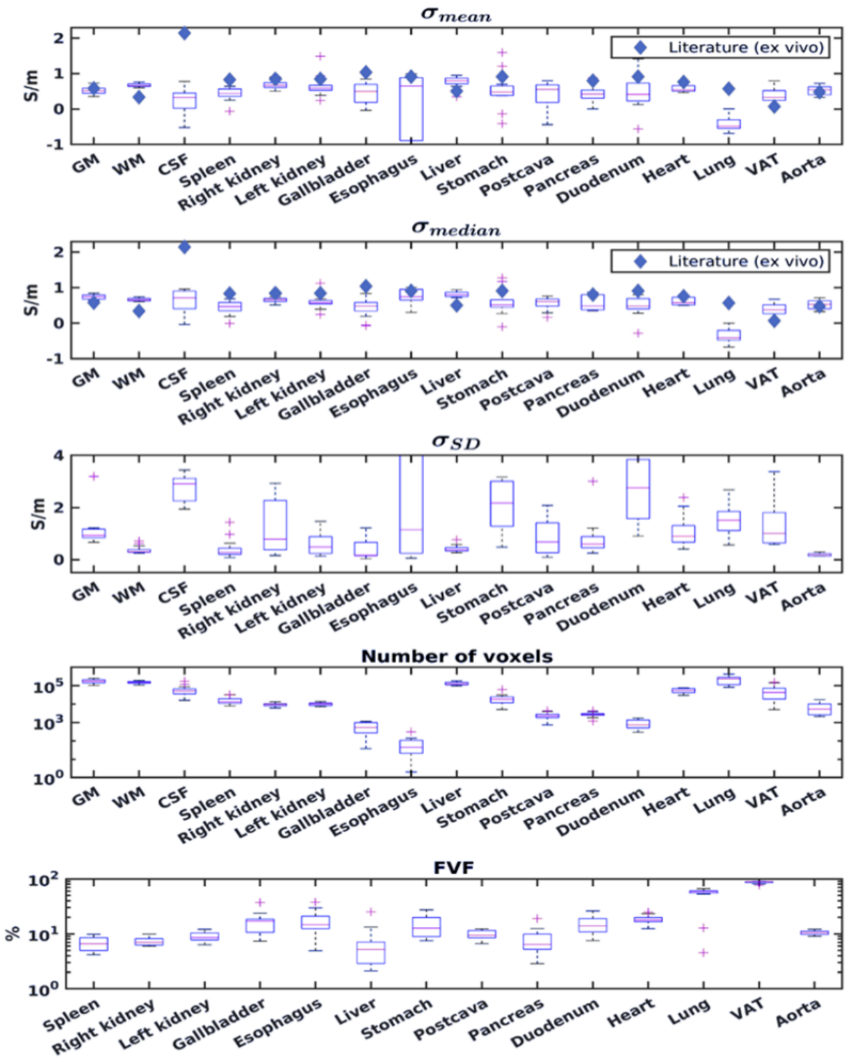

b

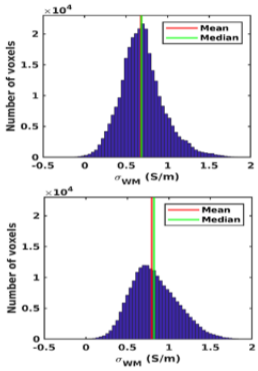

c

Organs	σ_{median} + SD	Ex-vivo(S/m)
GM	0.74 ± 0.06	0.58
WM	0.66 ± 0.04	0.34
CSF	0.61 ± 0.32	2.14
Spleen	0.44 ± 0.18	0.83
Right Kidney	0.65 ± 0.07	0.85
Left Kidney	0.59 ± 0.19	0.85
Gallbladder	0.45 ± 0.27	1.04
Esophagus	0.74 ± 0.22	0.91
Liver	0.80 ± 0.11	0.51
Stomach	0.59 ± 0.36	0.91
Postcava	0.56 ± 0.17	/
Pancreas	0.38 ± 0.77	0.80
Duodenum	0.49 ± 0.28	0.91
Heart	0.62 ± 0.10	0.76
Lung	-0.36 ± 0.20	0.57
VAT	0.38 ± 0.16	0.07
Aorta	0.53 ± 0.13	0.48

d

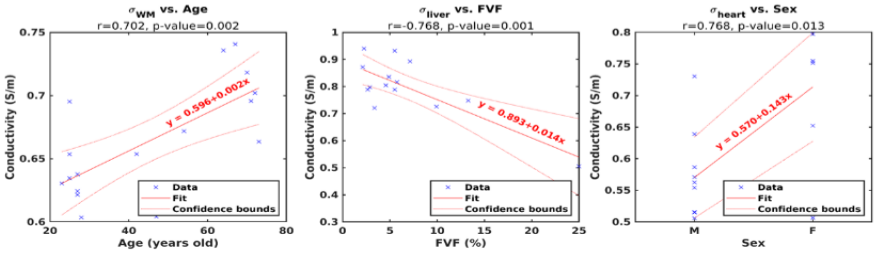

Figure 35. Population statistics. Boxplot representations (a) of the population distribution of mean conductivity in each organ, median conductivity, standard deviation as well as the associated mean number of voxels and volume fat fraction. Colored diamonds represent ex vivo reference conductivity values. Example histograms (b) for a given ROI (WM) in two different volunteers show limited deviation from a Gaussian distribution. Summary table (c) of the population average of the median conductivity values in each organ compared with the corresponding reference value on which linear regressions are performed (d). The regression equations are shown in red and 95% confidence bounds are depicted in dotted lines. Each prediction variable is tested for each organ in a similar way.

Excluding outliers, the ranges of ROIs median conductivities were as follows (min-max): Grey Matter, 0.65-0.85 S/m; White Matter, 0.60-0.74 S/m; Cerebrospinal Fluid, -0.03-0.96 S/m; Spleen, 0.19-0.68 S/m; Right Kidney, 0.51-0.74 S/m; Left Kidney, 0.40-0.68 S/m; Gallbladder, 0.20-0.84 S/m; Esophagus, 0.30-1.10 S/m; Liver, 0.50-0.94 S/m; Stomach, 0.27-0.97 S/m; Postcava, 0.29-0.76 S/m; Pancreas, 0.35-0.87 S/m; Duodenum, 0.28-0.80 S/m; Heart, 0.51-0.80 S/m; Lung, -0.67-0.00 S/m, Visceral Adipose Tissue (VAT), 0.10-0.67 S/m; Aorta, 0.33-0.72 S/m. Negative values reflect the limits of the technique when SNR is very low, as in the lungs, or at the edge of the reconstruction domain, as in the CSF.

7.3.4. Regressions and Correlations

Table 9. Statistical results for monovariate regressions. Four different predictors (Age, FVF, BMI, and Sex) are tested for each organ. p-values <0.05 are shown in bold, as are the associated correlation coefficients. Correlations between predictors are shown to illustrate the importance of multivariate analysis when two explanatory variables are significant.

Organs	AGE		FVF		BMI		SEX (M TO F)		PREDICTORS CORRELATION
	r	*p*-value	r	*p*-value	r	*p*-value	r	*p*-value	*p*-value
GM	**0.506**	**0.038**			0.189	0.467	0.244	0.345	
WM	**0.702**	**0.002**			0.257	0.320	-0.164	0.528	
CSF	**0.559**	**0.002**			0.391	0.702	-0.624	0.542	
Spleen	-0.517	0.059	**-0.719**	**0.004**	-0.518	0.058	0.335	0.242	
Right Kidney	**-0.697**	**0.006**	**-0.601**	**0.023**	-0.362	0.203	0.177	0.545	0.640
Left Kidney	-0.507	0.064	-0.172	0.557	-0.413	0.142	0.274	0.342	
Gallbladder	-0.187	0.523	0.285	0.323	-0.420	0.135	0.509	0.063	
Esophagus	-0.213	0.465	-0.391	0.167	0.027	0.927	0.517	0.058	
Liver	-0.353	0.216	**-0.768**	**0.001**	-0.405	0.151	**0.767**	**0.001**	0.603
Stomach	-0.483	0.080	-0.393	0.165	-0.486	0.078	**0.670**	**0.009**	
Postcava	-0.523	0.055	0.120	0.683	-0.425	0.129	0.422	0.133	
Pancreas	**-0.545**	**0.044**	-0.519	0.057	-0.520	0.057	**0.613**	**0.020**	**0.003**
Duodenum	-0.380	0.181	0.300	0.297	**-0.686**	**0.007**	**0.669**	**0.009**	0.954
Heart	-0.250	0.389	**-0.639**	**0.014**	-0.354	0.214	**0.644**	**0.013**	0.322
Lung	-0.219	0.452	**N/A**	**N/A**	-0.129	0.660	**0.832**	**<0.001**	
VAT	-0.245	0.399	-0.442	0.113	-0.317	0.269	0.472	0.088	
Aorta	**-0.651**	**0.012**	-0.282	0.329	-0.360	0.207	**0.705**	**0.005**	**0.003**

Univariate linear regression models allow a quick account of general trends, as shown in Figure 35d. We observe, for example, that conductivity seems to evolve positively with age in the white matter (p = 0.002), negatively with FVF in the liver (p = 0.001, r = 0.70), and positively in the heart (p = 0.013, r = 0.77) for men compared to women (M to F, r = 0.77). All these trends are summarized in Table 9, with the corresponding p-value indicated. Significant correlations are shown in bold and the curves associated are provided as additional information (Figure 36). Results for multivariate models are presented as additional information when more than one predictor was significant (Table 10). These results must also be balanced with the trust placed in population values. FVF values in the lung were excluded due to the SNR of the DIXON images being nearly zero. Interestingly, conductivity of the three major brain areas is positively and significantly correlated with age, while that of other organs is always negatively correlated. For seven of them, the link is significant or close to it; a larger cohort would allow these findings to be refined. We also note a discrepancy between the two kidneys, which could indirectly reflect a functional asymmetry in our population. FVF seems to be a particularly good predictor of liver and spleen conductivity unlike BMI, which relates only to the duodenum. Finally, sex seems to have a discriminating effect on certain organs, notably the liver and pancreas.

Table 10. Summary table for multivariate analyses. In each case, the two significant predictors are considered in the model and we display the associated p-values. To give an idea of the degree of independence between predictors, we also provide a simple estimate of correlation via linear regression. We find that there is a strong correlation between age and gender in our dataset, and we do indeed lack older women.

ORGANS	**V1 NAME**	**V2 NAME**	**MODEL1** σ **= 1 + V1 + V2**		**MODEL2** **V1= 1 + V2**
			V1	V2	V2
			p-value		
Right Kidney	Age	FVF	0.014	0.027	0.640
Liver	FVF	Sex	0.004	<0.001	0.603
Pancreas	Age	Sex	0.340	0.676	0.003
Duodenum	BMI	Sex	0.031	<0.001	0.954
Heart	FVF	Sex	0.004	0.01	0.322
Aorta	Age	Sex	0.079	0.051	0.003

Figure 36. Linear regression fitting plots illustrating the correlation between σ_{EPT} and age/FVF/BMI/Sex, with a focus on cases exhibiting a statistically significant p-value (< 0.05).

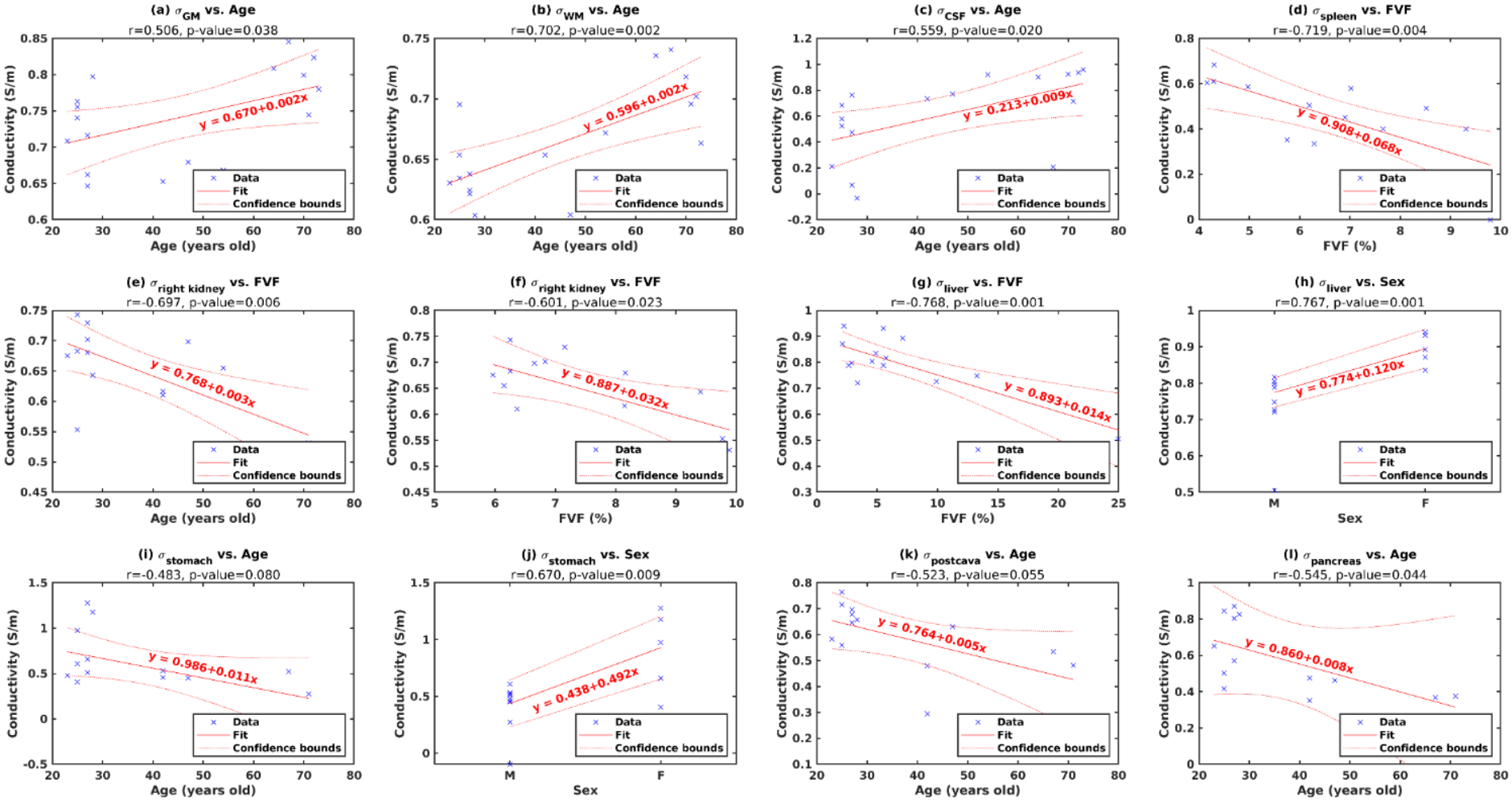

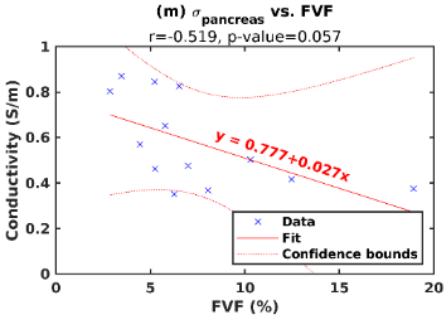
(m) σpancreas vs. FVF
r=-0.519, p-value=0.057
y = 0.777+0.027x
Data
Fit
Confidence bounds
Conductivity (S/m)
FVF (%)

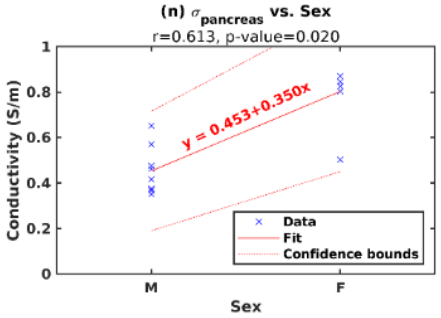
(n) σpancreas vs. Sex
r=0.613, p-value=0.020
y = 0.453+0.350x
Data
Fit
Confidence bounds
Conductivity (S/m)
Sex

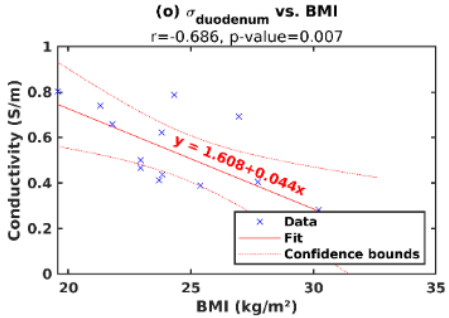
(o) σduodenum vs. BMI
r=-0.686, p-value=0.007
y = 1.608+0.044x
Data
Fit
Confidence bounds
Conductivity (S/m)
BMI (kg/m²)

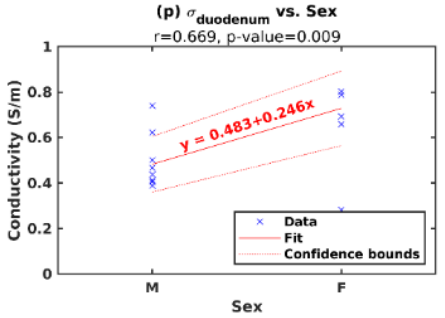
(p) σduodenum vs. Sex
r=0.669, p-value=0.009
y = 0.483+0.246x
Data
Fit
Confidence bounds
Conductivity (S/m)
Sex

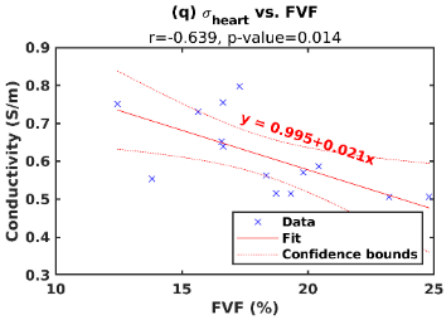
(q) σheart vs. FVF
r=-0.639, p-value=0.014
y = 0.995+0.021x
Data
Fit
Confidence bounds
Conductivity (S/m)
FVF (%)

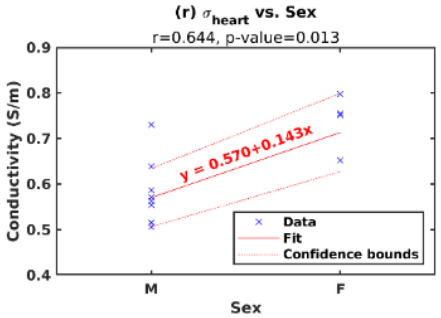
(r) σheart vs. Sex
r=0.644, p-value=0.013
y = 0.570+0.143x
Data
Fit
Confidence bounds
Conductivity (S/m)
Sex

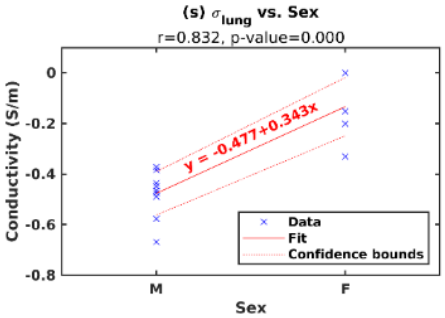
(s) σlung vs. Sex
r=0.832, p-value=0.000
y = -0.477+0.343x
Data
Fit
Confidence bounds
Conductivity (S/m)
Sex

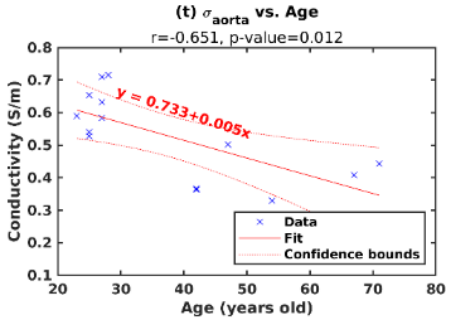
(t) σaorta vs. Age
r=-0.651, p-value=0.012
y = 0.733+0.005x
Data
Fit
Confidence bounds
Conductivity (S/m)
Age (years old)

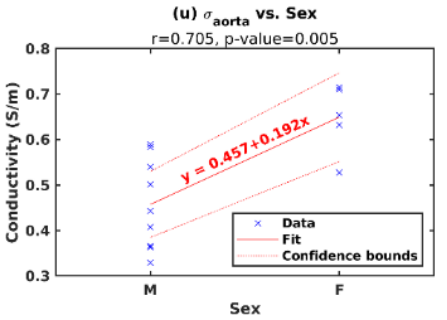
(u) σaorta vs. Sex
r=0.705, p-value=0.005
y = 0.457+0.192x
Data
Fit
Confidence bounds
Conductivity (S/m)
Sex

7.4. Discussion

This study provides new insights for tissue conductivity characterization with MRI, by focusing on macroscopic measurements and their dependence on general individual factors. It shows that it is possible to identify trends by looking at the macroscopic conductivity of each organ. We chose the median as a simple preferred metric as it seemed more robust than the classical mean, but a next step might be to look closer at the histograms within each ROI [66].The use of a single UTE sequence and the associated simple EPT formulation also makes post-processing easier, as well as its integration into a standard imaging protocol.

Regarding the reconstruction method used in this work [27], [53], the ZTE/UTE-based framework has the advantage of cleverly reducing the weight of certain assumptions made in the more conventional MR-EPT models. Firstly, it avoids the need for the so-called “transceive phase assumption” (TPA) as the total RF phase is used and not an estimate of the transmit phase which is not directly measurable [52], [69]. In theory, this means that the method can be used with any combination of transmit/receive antennas, provided that the combination is optimal and the SNR is sufficient [53], [128]. The TPA suffers especially from geometric asymmetries as it works best for cylindrically symmetrical setups, and becomes increasingly invalid as the tissue is further away from the magnet's center [82]. The use of formulations involving the product of RF fields, and not B_1^+ and/or phase alone, enables reconstructions that are more accurate because they better compensate for inhomogeneities between transmit and receive fields while reducing errors associated with model simplification in each case [53], [54]. In this study, the pipeline applied to the brain fulfilled these geometric conditions better than for the torso, where estimation deteriorated more markedly in the peripheral regions. This is also why small or tortuous structures, such as the esophagus or duodenum for which the SD is very large, are less amenable to this kind of analysis. Finally, unlike computationally intensive reconstruction schemes [44], [51], [145], [146], the implementation of our algorithm is fairly light: the calculation time for a brain volume, for example, is of the order of 5 min.

In addition, a recent study showed that the selected MR-EPT formulation provides satisfactory conductivity values compared with an external absolute probe reference in large homogeneous regions [85]. Its in vivo use requires proper boundary error control, which remain a serious issue for clinical applications [55], [147]. As for Laplacian estimation, the use of a second order Savitzky-Golay kernel has been shown theoretically to be the best linear method to avoid noise amplification [56].By constraining it to an anatomical prior, we artificially recreate the homogeneity criterion that "forces" the conditions of application of the model [37], [122]. The use of both a large selection window ([31 31 31]) and a restricted calculation window with a constant number of voxels (brain: $n=15^3$; torso: $n=23^3$), further limits potential differences between central and peripheral voxels within the same ROI. Our simulation study shows that this procedure works as long as the conductivity model is piecewise constant

and we might expect this not to be true of extended structures such as white matter or the liver. The piecewise-constant assumption is nevertheless a preliminary prerequisite for deriving consistent macroscopic values and taking a step towards standardization for more realistic EM models. The consistency of conductivity values in the WM across our population (0.66 +/- 0.04 S/m) is a valuable piece of evidence in the validation of in vivo conductivity measurements. One problem, however, lies in estimating and eliminating the contrast term I_0, which could temper the latter. Filtering strategies can be used at the cost of degraded resolution [54].

To calculate the SAR accurately, the permittivity must also be known. However, it can be estimated with a slight underestimation using conductivity alone and a theoretical permittivity model [39]. From a practical point of view, and even if we have not studied permittivity in this work, our pipeline makes it possible to consider its simultaneous reconstruction, as well as that of complex admittivity, which could also be a useful EM biomarker [54]. Extending the database will reduce the uncertainty regarding these quantities.

In terms of estimated values, we first observe that we tend to overestimate conductivity values in GM and WM compared to previous studies [82], [131], [139], [148], [149]. While GM conductivity is still greater than WM conductivity, it is about 0.3 S/m greater than the expected values and the gap between the two tissue types is reduced [130].These discrepancies could be explained by a systematic error propagated in our reconstruction pipeline : depending on whether the phase is used alone or not, many authors point to under- or over-estimates compared to reference values [126], [149]. In our case, the overestimation, already found in in reconstructions from ZTE images [53], could be related to Gibbs-ringing [150]. Future work will quantify this effect, by adjusting reconstruction matrix sizes. The low standard deviation for these two regions in our population nevertheless shows that these measurements are reliable and can be used to identify statistical trends. The values found for CSF, on the other hand, appear unreliable due to image edge effects and are probably subject to the pulsatile effect described previously [106]. Regarding values for the torso regions, we also note an overestimation of 0.3 S/m compared with previous published results for the largest ROIs, i.e. the liver [67] and visceral adipose tissue. A value close to the literature is found for the bulk heart [100], without differentiating between muscle tissue and blood. The low SNR of the UTE in the lung region results in negative conductivity values [151]. We are not aware of any in vivo reference values for the other tissues listed in our study and we observe that the conductivity values encountered tend to be lower than the ex vivo values in these regions. All values should be treated with caution, e.g. considering the number of voxels or the ROI-wise standard deviation as a surrogate confidence metric as we suggested, and will benefit from comparative studies with more advanced methods from different sequences and manufacturers. Finally, with regard to the trends observed, we emphasize the increase in conductivity in all cerebral compartments with age which is at odds with published work on animal excised pieces [152]. In our working frequency range, the body is usually considered a as mixture of particles in the aqueous

extracellular space which then reflects most of its EM behavior. Increased conductivity may then suggest an increase in ionic concentration, water content, fluid content [38] or even a change in the structure of the extracellular space over time.

While the biology of the aging brain is a complex process, some studies indicate an increase in brain water content, which is associated with neurodegenerative processes and cognitive decline [153], [154] while others suggest a decrease in an animal model [155].These variations are closely linked [38], [148] to global conductivity in gray or white matter, for example, which would then be added to the list of parameters of interest for quantitative MRI applied to longitudinal studies. Furthermore, and this is one of the limitations of our study, we need to be able to say whether the evolution of EPs over time, and therefore of their physiological bases, is linear or not. Furthermore, the decrease in EEG power with age could be another indication of the overall increase in cerebral conductivity, even at low frequencies, with the addition of concomitant shunting effects [156]. The drop in conductivity in one of the two kidneys could also reflect these changes in free water concentration associated with the dehydration more frequently encountered in the elderly while the drop for aortic blood could be related to augmented whole blood viscosity [157]. The decreases in conductivity in several organs with respect to the fat fraction are consistent with the low theoretical conductivity of fat, whose increased level lowers simultaneously water content and ionic mobility. Finally, gender seems to be a good predictor of a difference in conductivity for the liver in particular. If the difference is real, it is once again probably associated with ionic substrates, such as iron content, or physic-chemical substrates, such as fat content [158]. Multi-variate regression provides initial clues to the potential independence of certain predictors (Table 10), such as age and FVF for liver. In contrast, there is a strong correlation between gender and age for the pancreas and aorta estimates, partly because older women are under-represented in our small cohort.

7.5. Conclusion

In conclusion, the main aim of our study was to establish a reliable protocol for estimating in vivo conductivity in several organs, compare our population values with reference ex vivo values and identify trends in relation to their characteristics. Our cohort is small and the results are preliminary but they suggest that in vivo conductivity values may deviate from the ex vivo reference values, and that inter-individual variations (e.g. vs. age or sex) may not be negligible. Beyond statistical power, the limitations of our study include the use of a simple reconstruction method and the low SNR/contrast in certain organs (such as lung or CSF) with the UTE sequence which could lead to estimation bias. As the variability of in vivo EPs has not been addressed extensively by existing studies, there is still no ground truth available for absolute quantification of conductivity in vivo, so our results will have to be confirmed by larger studies using different methods and MRI scanners If these correlations prove significant in larger cohorts, they could provide a new tool for studying structural and functional

differences between individuals. Overall, we believe that electromagnetic models for SAR management and patient safety, as well as the addition of electromagnetic parameters to clinical studies, will benefit greatly from these in vivo studies.

Chapter 8. Application to Local SAR Estimation

8.1. Introduction

The management of Specific Absorption Rate (SAR) is a critical aspect of MRI safety, referring to the rate at which radiofrequency (RF) radiation energy is absorbed by the human body. In MRI systems, the RF field's wavelength in tissues is comparable to body dimensions, creating local hot spots and posing significant safety concerns. The importance of SAR management becomes more pronounced with increasing magnetic field strength, as the Larmor frequency of the RF field also increases. Therefore, respecting the global and local SAR limits is essential for MRI safety. For instance, it is crucial to ensure that the global SAR in the patient's head remains below 3.2 W/kg when averaged over 6 minutes and that the local SAR (over mass of 10g) stays below 10 W/kg in normal operating modes [159].

The spatial distribution of SAR depends on the RF coil design, the RF power delivered to the coil, and the body's electrical properties (EPs). Current SAR estimation practices involve electromagnetic field simulations incorporating the RF coil and standard numerical human body models. In these simulations, EPs are assigned to different tissues based on ex vivo databases. However, EP values are individual-dependent, depending on factors such as age, fat fraction, sex, and pathology, as shown in Chapter 7. Additionally, discrepancies between patient anatomy and virtual body models, positioning of the body with respect to the RF coil, and RF loading effects can further increase the unreliability of SAR estimation.

To improve local SAR accuracy, a personalized EPT-based local SAR calculation has been suggested using measured B_1^+-related data and reconstructed EP maps. This method, using quadrature excitation, was first studied at 1.5T [109] and later applied to the human brain [39]. The concept was extended to non-quadrature multi-transmit coil arrays (i.e., parallel transmission) by using absolute transmit phase from multi-channel data instead of half of the transceive phase, i.e., the transceive phase assumption (TPA) [160], [161]. This idea was similar to gradient EPT [51] mentioned in Section 2.3 and was further improved by absolute $|B_1^-|$ estimation, excluding proton density weighting [162].

In this chapter, we focus on EPT-based local SAR estimation in quadrature transmission, which is the current standard for 1.5T and 3T MRI systems. First, we validated the EPT-based SAR formulation in simulation and then compared to MRI measurements. Second, we aim to analyze the significant overestimation of conductivity observed between in vivo measurements by EPT and ex vivo databases [130], in particular in brain. This analysis involves comparing their differences in SAR modeling and determining which set of values in simulation aligns more closely with the MRI measurements in terms of complex B_1^+ data and SAR. This comparison also indirectly verifies the reliability of conductivity

reconstructed by EPT, thereby enhancing the accuracy and reliability of SAR estimations in MRI systems.

A part of this study resulted in a conference communication:

Paillart G, **He Z**, Soullié P, Romero G, Ferry P, Felblinger J, Odille F. Radiofrequency safety modeling in Magnetic Resonance Imaging (MRI): an experimental study of the impact of electrical properties. In: *Proceedings of European Society for Magnetic Resonance in Medicine and Biology (ESMRMB) 2024 Annual scientific meeting*. Barcelona, Spain; 2024 :397. (Poster)

8.2. Theory

The local SAR [23] is given by

$$SAR = \frac{\sigma|\mathbf{E}|^2}{2\rho_m} = \frac{\sigma}{2\rho_m|\mu_0\kappa|^2}|\nabla \times \mathbf{B}|^2 \tag{8.1}$$

where ρ_m is the tissue mass density (which could be approximated by the water density around 1000 kg/m^3 with only a 5% deviation from muscle and fat [23], [39]) and $\kappa = \sigma + i\omega\varepsilon_0\varepsilon_r$ is the admittivity (or EPs). The electrical field **E** can be further expressed via **B** using the Maxwell-Ampere's Law:

$$\mathbf{E} = \frac{1}{\mu_0\kappa}\nabla \times \mathbf{B} \tag{8.2}$$

where the magnetic field **B** can be further related via the circular field components $B_1^+ \overset{\text{def}}{=} \frac{1}{2}(B_x + iB_y)$ and $B_1^- \overset{\text{def}}{=} \frac{1}{2}(B_x - iB_y)$ of the transmit birdcage/quadrature coil [41]:

$$\mathbf{B} = \begin{bmatrix} B_x \\ B_y \\ B_z \end{bmatrix} = \begin{bmatrix} B_1^+ + B_1^- \\ -i(B_1^+ - B_1^-) \\ B_z \end{bmatrix} \tag{8.3}$$

Overall, three main challenges need to be addressed with such approaches [161]: first, determining all spatial magnetic field components (pure B_1^+, B_1^- and B_z) is required; second, the measured complex MR signal must be separated into transmission related and unrelated phase contributions (i.e., to obtain pure φ^+ or φ^-); and third, an accurate estimation of tissue EPs maps is required.

In practice, only the B_1^+ component can be measured in MRI. This is achieved through via the $|B_1^+|$ mapping technique for its magnitude and the TPA assumption or a multiple transmission system to access its phase φ^+. We will now show for the derivation of B_1^+-based SAR estimation in this study. Assuming $\nabla B_z = 0$, the curl of B can be expressed as follow:

$$\nabla \times \mathbf{B} = \begin{bmatrix} \frac{\partial B_z}{\partial y} - \frac{\partial B_y}{\partial z} \\ \frac{\partial B_x}{\partial z} - \frac{\partial B_z}{\partial x} \\ \frac{\partial B_y}{\partial x} - \frac{\partial B_x}{\partial y} \end{bmatrix} \approx \begin{bmatrix} -\frac{\partial B_y}{\partial z} \\ \frac{\partial B_x}{\partial z} \\ \frac{\partial B_y}{\partial x} - \frac{\partial B_x}{\partial y} \end{bmatrix} \tag{8.4}$$

The z-component (i.e. E_z) can be derived using Eq.(8.3):

$$\frac{\partial B_y}{\partial x} - \frac{\partial B_x}{\partial y} = -i\frac{\partial B_1^+}{\partial x} + i\frac{\partial B_1^-}{\partial x} - \frac{\partial B_1^+}{\partial y} - \frac{\partial B_1^-}{\partial y} \approx -2\left(i\frac{\partial B_1^+}{\partial x} + \frac{\partial B_1^+}{\partial y}\right) = -2i\left(\frac{\partial B_1^+}{\partial x} - i\frac{\partial B_1^+}{\partial y}\right) \tag{8.5}$$

assuming that $-i\frac{\partial B_1^+}{\partial x} \approx i\frac{\partial B_1^-}{\partial x}$ and $\frac{\partial B_1^+}{\partial y} \approx \frac{\partial B_1^-}{\partial y}$. This assumption is valid in a symmetric setup [160], [163] (e.g. a left/right symmetric object to be imaged and at the center of birdcage/quadrature coil) where:

$$|B_1^+(x,y,z)| \approx |B_1^-(-x,y,z)| \tag{8.6}$$

This means that the two contributions of B_1^+ and B_1^- are equal [161]. Therefore, the formulation for the B_1^+-based SAR estimation is given by:

$$SAR = \frac{\sigma}{2\rho_m|\mu_0\kappa|^2}|\nabla \times \mathbf{B}|^2 \approx \frac{\sigma}{2\rho_m|\mu_0\kappa|^2}\left(\underbrace{\left|\frac{\partial B_y}{\partial z}\right|^2 + \left|\frac{\partial B_x}{\partial z}\right|^2}_{=\left|2\frac{\partial B_1^+}{\partial z}\right|^2} + \left|2\left(\frac{\partial B_1^+}{\partial x} - i\frac{\partial B_1^+}{\partial y}\right)\right|^2\right)$$

$$= \frac{2\sigma}{\rho_m|\mu_0\kappa|^2}\left(\left|\frac{\partial B_1^+}{\partial z}\right|^2 + \left|\frac{\partial B_1^+}{\partial x} - i\frac{\partial B_1^+}{\partial y}\right|^2\right) \tag{8.7}$$

It has been demonstrated that Eq.(8.7) compared to its complete version (8.1) is only 25% lower in SAR estimation at 1.5T [39]. Eq.(8.7) can be further simplified to phase-only version assuming that $|B_1^+|$ and the permittivity ($\varepsilon_r = 80$) are a constant [39]. Additionally, some studies [23], [164] ignored the $\left|\frac{\partial B_1^+}{\partial z}\right|^2$ term for the central axial plane where the E_z term is the dominant component and E_x and E_y can be neglected:

$$SAR_{z-middlle} = \frac{2\sigma}{\rho_m|\mu_0\kappa|^2}\left(\left|\frac{\partial B_1^+}{\partial x} - i\frac{\partial B_1^+}{\partial y}\right|^2\right) \tag{8.8}$$

8.3. Methods

8.3.1. Phantom Experiments

A phantom consisting of a gelled-saline solution (~0.3% NaCl) was prepared with dimensions of 355 mm × 355 mm × 55 mm. Unfortunately, there were some air bubbles in the phantom. These air bubbles could potentially affect the uniformity and accuracy of the MRI measurements. The electrical properties (EPs) of the phantom were measured using an open-ended axial probe connected to a Vector Network Analyzer (VNA), yielding conductivity of 0.47 S/m and relative permittivity of 80.

The experimental B_1^+ maps were acquired on a 3 T Prisma Siemens scanner (Siemens Healthineers, Erlangen, Germany). The magnitude $|B_1^+|$ was obtained using 2D presaturation turbo flash (satTFL) sequence [80] with parameters: TE/TR=2 ms/30s, matrix slice 256×192×16, voxel size 1.5×1.5×5 mm^3, flip angle = 80° and a scan time of 86 s. The phase φ^+ was estimated as half the transceive phase (under the transceive phase assumption, TPA), measured using a UTE Spiral VIBE sequence [112] (TE/TR=0.05/4 ms, 384×384×80, voxel size 1×1×1 mm^3, flip angle = 3°, scan time 5 min).

Numerical modeling was performed using CST Studio Suite software (Dassault Systèmes). A previously validated model of our 3T MRI RF body coil, excited by two voltage sources (ports), was utilized. The phantom model, designed with a 1 mm isotropic voxel size, mirrored the geometry and electrical properties of the experimental phantom. The RF transmission power was set to 1 W in the simulation.

To evaluate the accuracy of B_1^+-based SAR (via Eq.(8.7)), we compared it to the ground truth SAR (via Eq.(8.1)) and the E_z-only-based SAR (via Eq.(8.8)) in the noiseless simulated phantom data. Subsequently, we compared the B_1^+ and local SAR on the phantom between MRI measurements and simulation.

8.3.2. In Vivo Experiments

A healthy volunteer brain was scanned with the same sequences used in the phantom experiments (ethics approval: ClinicalTrials ID NCT04645628). The parameters for the $|B_1^+|$ mapping sequence were adjusted to matrix size 224×224×29, voxel size 1.2×1.2×7.5 mm^3, with a scan time of 60 s) and for the φ^+ phase mapping UTE sequence was set to matrix size 224×224×160, voxel size 1.2×1.2×1.2 mm^3 with a scan time of 9min 1s.

The anatomical model used was the "Emma" model from the CST Family 2.0. Default EP values in the brain were similar to those in ex-vivo databases, with a brain conductivity of 0.44 S/m, encompassing white matter, grey matter and CSF. To assess the impact of using in-vivo measurements by MR-EPT in the brain (see Chapter 7), simulations were repeated with a conductivity of 0.68 S/m, representing an

average in-vivo value from 17 adult brains. The relative permittivity of brain was set at 68, corresponding to the average of ex-vivo brain values.

8.3.3. Local SAR Calculation

The measured $|B_1^+|$ map was derived from the flip angle map (α) obtained via the satTFL sequence, using the following conversion based on the hard pulse assumption:

$$|B_1^+|_{MRI} = \frac{\alpha}{\gamma\tau} \tag{8.9}$$

where $\tau = 60\mu s$ is the pulse duration. The averages of flip angle map and the resulting $|B_1^+|$ map for the phantom were approximately 80° and 9μT, respectively. Since the RF transmission power of the MRI is unknown, the simulated complex data ${B_1^+}_{simu}$ was rescaled to match the measured ${B_1^+}_{MRI}$ by the ratio of the center voxels of ${B_1^+}_{simu}$ and ${B_1^+}_{MRI}$:

$${B_1^+}_{simu}^{rescaled} = {B_1^+}_{simu} \frac{{B_1^+}_{MRI}(x_c, y_c, z_c)}{{B_1^+}_{simu}(x_c, y_c, z_c)} \tag{8.10}$$

where (x_c, y_c, z_c) is the center coordinate. All B_1^+ maps (from the simulation and experiments) were resampled to the DICOM coordinate system of the $|B_1^+|_{MRI}$ maps.

For the numerical computation of the first derivatives in Eq.(8.7), an adaptive Savitzky-Golay filtering (See Section 6.2.2) with a size of [11 11 7] was used on the measured complex ${B_1^+}_{MRI}$ data, while a central finite difference method was used on the noiseless simulated ${B_1^+}_{simu}$ data. The average conductivity values obtained by Image-based EPT in both the phantom and the volunteer's brain were very close to the setting simulated values: $\sigma_{phantom} = 0.46 \pm 0.18\, S/m$, $\sigma_{GM} = 0.71 \pm 0.84\, S/m$, $\sigma_{WM} = 0.62 \pm 0.28\, S/m$ and $\sigma_{CSF} = 0.76 \pm 2.71\, S/m$. Consequently, we used conductivity values (i.e., 0.47 S/m for the phantom and 0.68 S/m for the whole brain) for the measured local SAR calculation.

For MRI, the safety limits are expressed in terms of global SAR and the peak of 10g-averaged local SAR ($pSAR_{10g}$) according to the current international guideline (IEC 60601-2-33). Global SAR was quantified by calculating the mean of local SAR in the ROI:

$$Global\ SAR = \frac{1}{V}\int \underbrace{\frac{\sigma|\mathbf{E}|^2}{2\rho_m}}_{Local\ SAR} dV = mean(Local\ SAR) \tag{8.11}$$

where V is the volume of ROI. Moreover, the $pSAR_{10g}$ was obtained by averaging the local SAR over a cube containing 10 g of tissue (i.e., a volume of 10 cm^3) and then taking the maximum value.

8.4. Results

8.4.1. Validation of B_1^+-based SAR

Results from the simulated phantom data with an RF transmission power of 1W are shown in Figure 37. The E-based SAR, considered as the ground truth (GT), increases gradually form the center to the peripheries. The simplified versions, namely B_1^+-based SAR and E_z-only-based SAR, are both underestimated compared to the GT, with the E_z-only-based SAR showing the greatest underestimation. However, the SAR values from all three formulations are similar at the phantom center. The B_1^+-based SAR is the closest approximation to the GT, achieving a normalized root mean square error (NRMSE) of 0.23. Additionally, the relative errors for both global SAR and $pSAR_{10g}$ are kept under 10%, demonstrating the accuracy and reliability of the B_1^+-based SAR approach.

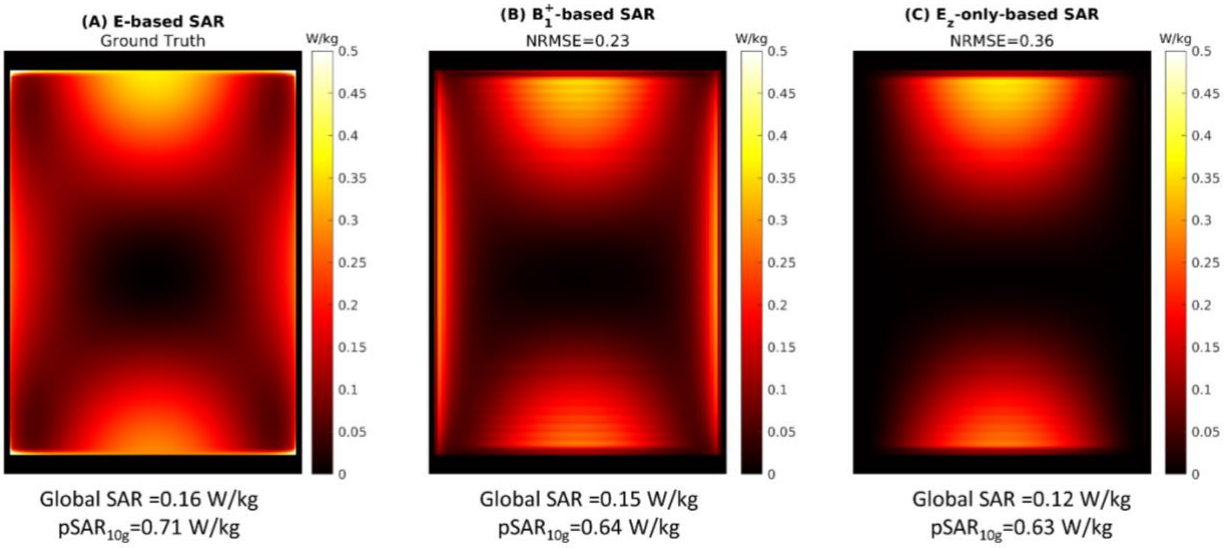

Figure 37. Local SAR (1g) maps on the simulated phantom data with an RF transmission power of 1W: (A) E-based SAR (exact reconstruction) via Eq.(8.1), (B) B_1^+-based SAR via Eq.(8.7) and (C) E_z-only-based SAR via Eq.(8.8). The NRMSEs of (B) and (C) compared to (A) as well as Global SAR and the peak of 10g-avereaged local SAR ($pSAR_{10g}$) for each case are also provided.

8.4.2. Phantom

Figure 38 shows the B_1^+ magnitude ($|B_1^+|$) and phase (φ^+) as well as local SAR on the phantom, comparing simulation and MRI measurements. In terms of magnitude, a good agreement was overserved between $|B_{1\,MRI}^+|$ and $|B_{1\,simu}^+|$, except for a higher variation in $|B_{1\,MRI}^+|$ at the coronal plane. In terms of phase, some air bubbles in the phantom can be observed in φ_{MRI}^+. The highest phase values of φ_{MRI}^+ are observed at the right-bottom, while those of φ_{simu}^+ are observed at the center. Additionally, the propagation of φ_{MRI}^+ in the sagittal plane is inverted compared to φ_{simu}^+, likely due to the effect caused by the transceive phase assumption (TPA).

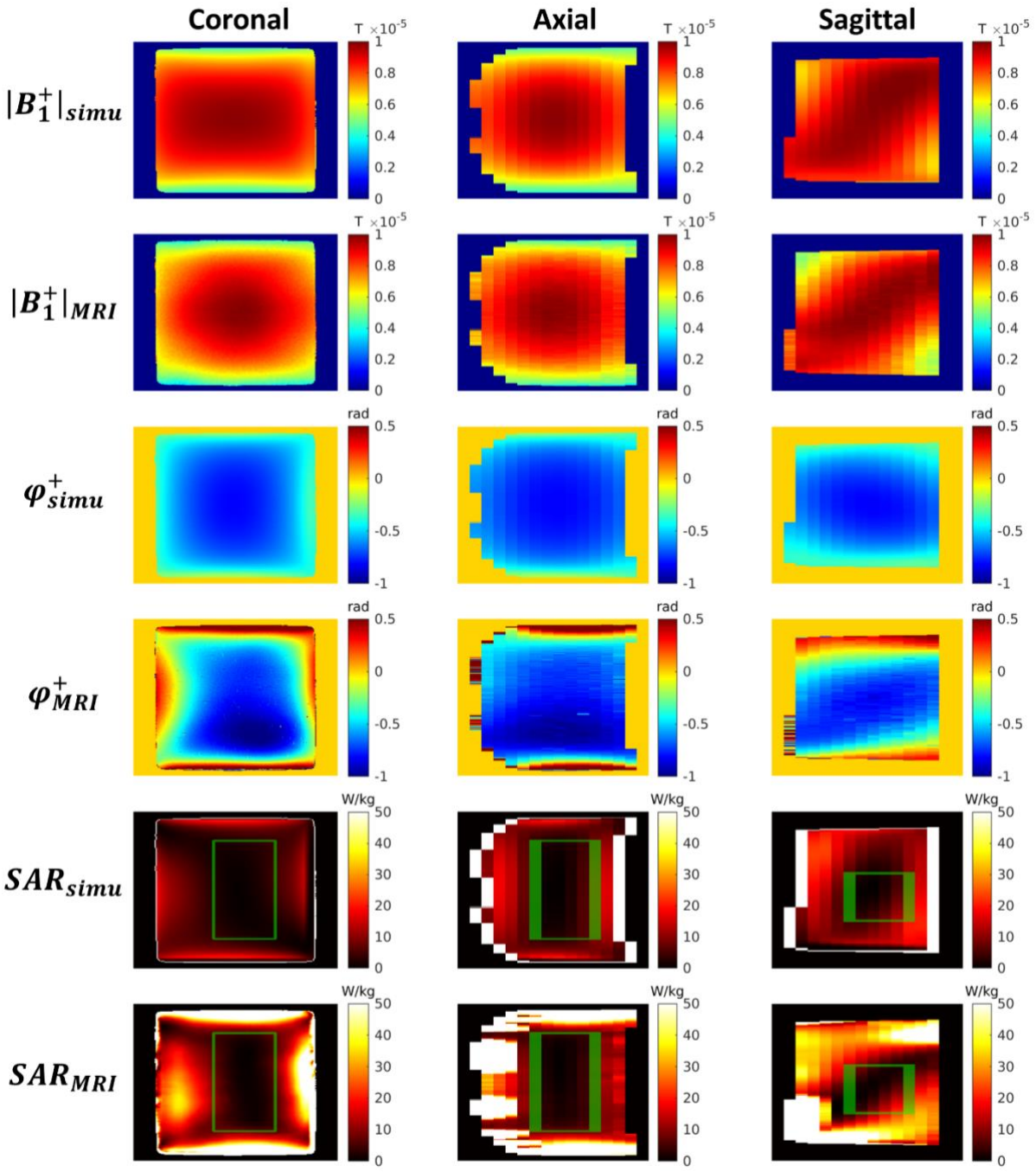

Figure 38. Comparison of B_1^+ magnitude ($|B_1^+|$) and phase (φ^+) as well as local SAR in the phantom between the simulation and MRI measurements. Some air bubbles in the phantom can be observed in φ^+_{MRI}. The ROIs depicted in green were used for Global SAR and the peak of 10g-averaged local SAR calculation (see Table 11).

The Local SAR distribution also show differences between the simulation and MRI measurements. Both SAR_{simu} and SAR_{MRI} exhibit boundary artifacts, with SAR_{MRI} showing more pronounced artifacts, likely due to its larger filter size compared to SAR_{simu}. In general, SAR_{MRI} provides higher values than SAR_{simu}, especially at the peripheries. However, a good agreement was observed in the center axial plane, which is free from the $\frac{\partial B_1^+}{\partial z}$ derivative. These differences between SAR_{MRI} and

SAR_{simu} may be attributed to the insufficient number of slices in the z-direction. This limited discretization resulted in significant derivative errors in the regions away from the center axial plane.

Focusing on the phantom center (i.e., the ROIs depicted in green in Figure 38), the quantified global SAR and the $pSAR_{10g}$ values are provided in Table 11. Both the measured global SAR is 23% higher, and $pSAR_{10g}$ is 48% higher, compared to the simulation values.

Table 11. Global SAR and the peak of 10g-averaged local SAR ($pSAR_{10g}$) values in the phantom and in vivo brain, comparing the simulation (noiseless) and MRI measurements. Notably, this SAR estimation corresponds to a duty cycle of 100% and a hard pulse.

		Global SAR (W/kg)	**$pSAR_{10g}$ (W/kg)**
Phantom σ**=0.47 S/m and** $\varepsilon_r = 80$	Simulation	4.95	17.36
	MRI measurements	6.08	25.76
In vivo brain $\varepsilon_r = 68$	Simulation σ = 0.44 S/m	11.21	25.90
	Simulation σ = 0.68 S/m	14.55	34.72
	MRI measurements σ = 0.68 S/m	16.13	34.72

8.4.3. In Vivo Brain

Figure 39 shows the B_1^+ magnitude ($|B_1^+|$) and phase (φ^+) as well as local SAR on the brain simulation model (with two sets of conductivity values) and MRI measurements. The difference between the two simulated $|B_{1\ simu}^+|$ maps is hardly noticeable, but the difference can be observed in the phase. This is due to the same permittivity but different conductivity values. Despite the volunteer's head being larger than the simulation model, the variations in $|B_{1\ MRI}^+|$ are greater than those in $|B_{1\ simu}^+|$. This suggests that the realistic relative permittivity is greater than the set value in simulation, i.e. $\varepsilon_r >$ 68. Additionally, φ_{simu}^+ and SAR_{simu} with $\sigma = 0.68$ S/m are closer to φ_{MRI}^+ and SAR_{MRI}, especially at the brain peripheries.

Excluding the local SAR values greater than 40 W/kg, the quantified global SAR and the $pSAR_{10g}$ values are provided in Table 11. Both the simulation values of global SAR and $pSAR_{10g}$ with $\sigma = 0.68$ S/m are closer to the MRI measurements, with both having the same $pSAR_{10g}$ values of 34.72 W/kg. The measured global SAR is 11% higher than the simulated value.

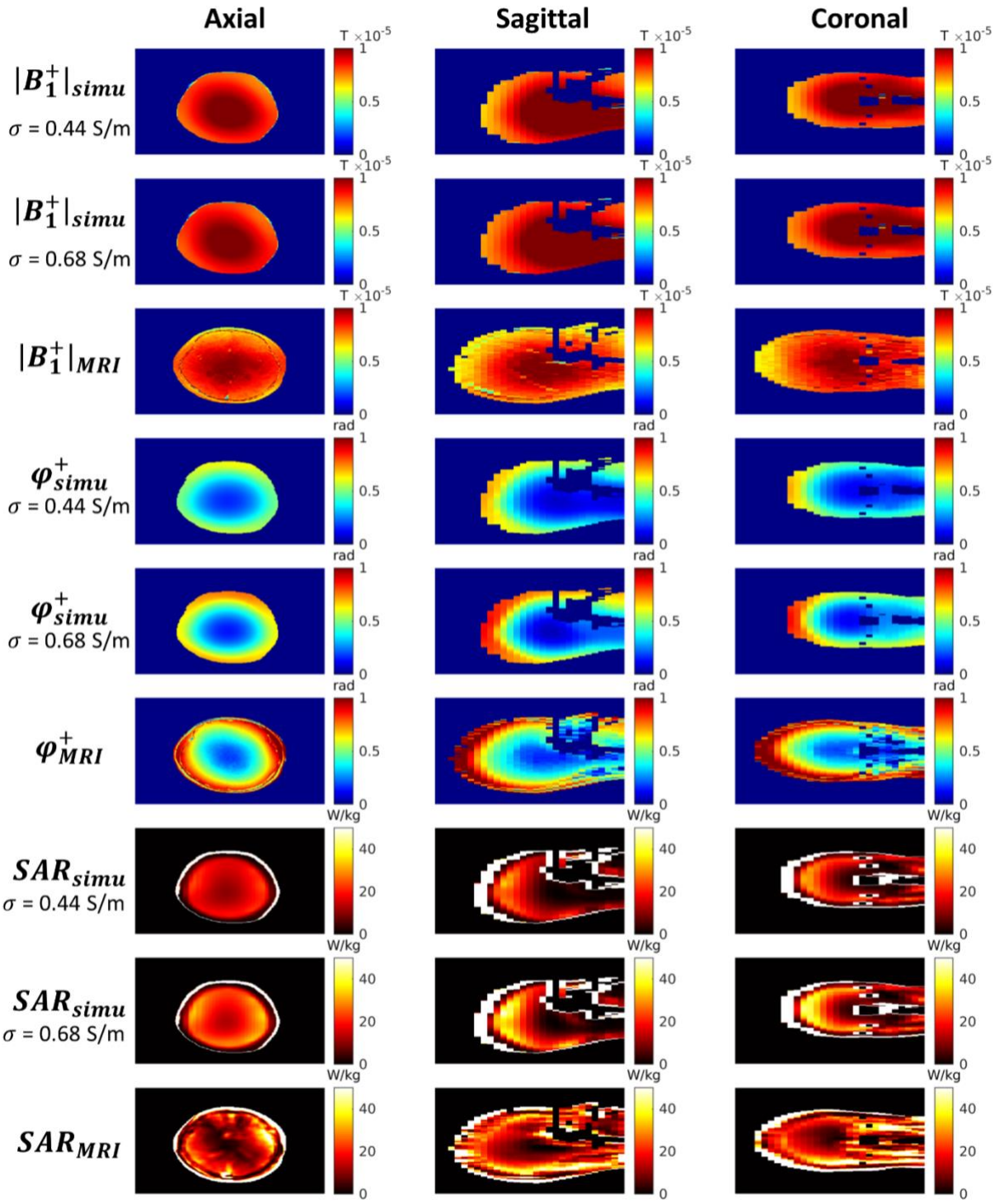

Figure 39. Comparison of B_1^+ magnitude ($|B_1^+|$) and phase (φ^+) as well as local SAR on the simulation model (Emma) with two sets of conductivity values and the volunteer brain. Excluding the local SAR values greater than 40 W/kg, the quantified global SAR and the $pSAR_{10g}$ values are provided in Table 11.

8.5. Discussion and Conclusion

In this study, we validated a local SAR estimation based on the complex B_1^+ data in simulation at 3T, achieving an NRMSE of 0.23 compared to the GT SAR. This B_1^+-based SAR approach was then compared between the simulations and MRI measurement on the phantom and in vivo brain. To align the simulation and MRI measurements, we used a complex scaling factor based on the ratio of the center voxels in the ${B_1^+}_{simu}$ data. The rescaled ${B_1^+}_{simu}$ data successfully matched the ${B_1^+}_{MRI}$ on the phantom and MRI measurements. However, it would be preferable to avoid this scaling factor if the RF transmission power in MRI was known.

The hot spots (i.e., areas with high local SAR values) were primarily located at the peripheries of the imaged object, such as regions near the skin. In the phantom results, the measured local SAR map at the axial center was the closest to the simulation, which is free from the $\frac{\partial B_1^+}{\partial z}$ derivative. This suggests that using a large number of z-slice and with smaller z-spacing or employing a 3D $|B_1^+|$ mapping sequence could improve the accuracy of measured SAR.

In the in vivo brain results, a $pSAR_{10g}$ value of 34.72 W/kg was found. This significant value is consistent with a previous study (Voigt el al., 2012 [160]), which reported a $pSAR_{10g}$ value of 45.9 W/kg at 3T. Additionally, our local SAR map is comparable with their findings. We also observed that the measured phase φ_{MRI}^+ and SAR_{MRI} were closer to φ_{simu}^+ and SAR_{simu} when the in vivo brain conductivity $\sigma = 0.68$ S/m was used. This suggests that using in vivo conductivity values rather than ex vivo values can improve SAR estimation accuracy and indirectly demonstrates the reliability of the EPT method.

However, the measured global SAR and $pSAR_{10g}$ in this study cannot be directly compared with the SAR safety limits. The SAR estimation in this study was performed under the hard pulse assumption and with a duty cycle of 100% and a flip angle of 80°. In practice, the local SAR values should be rescaled according to the specific flip angle, pulse shape, and sequence timing parameters. Nevertheless, the locations of the hot spots do not change, and the local SAR distribution is not distorted but only scaled globally [160].

We preliminarily tested only the average in vivo brain conductivity value from 17 adults as a constant in the whole brain, similar to current SAR modeling practices. In the future, investigating the local SAR differences using local EP maps derived from EPT, especially on higher field, will be important for improving SAR modelling efficiency. This approach could further enhance the accuracy and efficiency of SAR estimations in clinical settings, leading to better safety assessments and optimized MRI protocols.

Chapter 9. Conclusion

The main aim of this thesis is to establish a reliable protocol for estimating in vivo electrical properties (EPs) in various organs using Magnetic Resonance Electrical Properties Tomography (EPT), compare adult population values with reference ex vivo values, and identify trends related to their characteristics. After the various validations on phantoms with the ground truth Vector Network Analyzer (VNA) measurements, the Image-based EPT with the Ultra-short Echo Time (UTE) sequence was recommended in terms of accuracy and acquisition speed. Despite our small population and preliminary results, our findings suggest that in vivo conductivity values may deviate from ex vivo reference values, and inter-individual variations (e.g., age, sex and fat fraction) may be significant. This could have a significant impact on Specific Absorption Rate (SAR) studies for Radio Frequency (RF) safety investigations.

9.1. Contributions

In this thesis, various EPT methods have been explored and optimized to better understand their performance and applicability in clinical settings. Several key contributions have been made:

1. **Sequence Optimizations**: Different MR sequences were tested to acquire EPT data. The UTE sequence with a flip angle of 3° has been recommended for conductivity and permittivity reconstruction via the Image-based EPT, in terms of accuracy and time-saving.

2. **Phantom Validations**: Various phantoms were designed and used to validate the EPT methods compared to the ground truth VNA measurements. The Generalized-Image-based (GIB) method has been found to provide good accuracy (NRMSE < 0.35) for structures down to 5 mm. Structures below 5 mm may still be detected in the conductivity maps, but with significantly lower accuracy. These experiments have confirmed the accuracy of these techniques and provided a benchmark for in vivo studies.

3. **Adaptive Savitzky-Golay Kernel Design**: An adaptive Savitzky-Golay kernel has been proposed to account for arbitrary tissue shapes with anatomical prior knowledge for numerical differentiation. This approach improves the homogeneity of Helmholtz EPT formulations in large homogeneous regions and reduces noise effects and boundary artifacts. Additionally, the numerical calculation of surface-integral-based EPT in an adaptive scheme has been achieved, with better accuracy in simulation and phantom studies compared to the traditional Laplacian-based EPT.

4. **In Vivo Conductivity Change Study**: In vivo conductivity changes in the brain and torso have been investigated, finding correlations with age, fat fraction, and sex. These findings are crucial for accurate Specific Absorption Rate (SAR) modeling.

5. **Local SAR Applications**: In vivo conductivity values obtained by EPT have been applied to local SAR calculations based on the measured complex B_1^+ data and compared with those based on literature values. This comparison suggested the use of in vivo conductivity values and validated the reliability of EPT, emphasizing its importance in SAR modeling.

9.2. Future Work

Future directions for the development and research of EPT are suggested as follows:

1. **RF Phase Shimming:** Vendor-specific RF magnitude shimming in MRI scanners is inadequate for permittivity reconstruction [69]. Permittivity reconstruction could benefit from RF phase shimming ($\nabla\varphi^+ \approx 0$), provided that the resulting "inhomogeneous" $|B_1^+|$ does not create signal voids or significant deviations from constancy, i.e. $\nabla|B_1^+| \neq 0$. For example, in Image-based EPT, this RF phase shimming can be performed by adjusting the complex channel weights (c_n) using complex UTE maps measured from each channel. This involves coil combinations:

$$\{c_n\} = \arg\min_{c_n} \sum_{ROI} \sqrt{(\nabla_x \varphi_{comb})^2 + \left(\nabla_y \varphi_{comb}\right)^2 + (\nabla_z \varphi_{comb})^2} \tag{9.1}$$

with

$$\varphi_{comb} = angle(I_{comb}) = angle(c_1 I_1 + c_2 I_2 + \cdots c_n I_n)$$

where $|c_n| = 1$ and I_n is the complex UTE images at the channel *n*. This optimization aims to find the relative phases of different channels that minimize the sum of total phase variation of the combined image I_{comb}. These weights can be determined in a ROI of the phantom. However, this loss function may not provide the maximum magnitude of the combined image, resulting in relatively low SNR. Thus, a regularization term on the combined magnitude can be added into Eq.(9.1):

$$\{c_n\} = \arg\min_{c_n} \sum_{ROI} \left(\sqrt{(\nabla_x \varphi_{comb})^2 + \left(\nabla_y \varphi_{comb}\right)^2 + (\nabla_z \varphi_{comb})^2} - \lambda |I_{comb}| \right) \tag{9.2}$$

where λ is a regularization coefficient.

2. **Proton Density Mapping:** Due to the B_1^- maps typically being weighted by proton density, which cannot be removed in a straightforward way, the Image-based EPT assumes that the proton density is piecewise constant. However, this assumption is only valid in large homogenous region and results in reconstruction errors near tissue boundaries. This assumption

can be avoided with the quantitative proton density mapping technique [165], such as using the linear relationship between $\frac{1}{T_1}$ and $\frac{1}{\rho_0}$ for human brain [166]. Additionally, knowledge of B_1^- without proton density weighting can help determine B_x and B_y, allowing for more accurate local SAR estimation by only neglecting the unmeasurable B_z component.

3. **Regularization Strategy in Divergence-based EPT:** The divergence-based EPT [49] (i.e., the surface integral form of the cr-EPT family) converts the second-order to the first order derivatives of B_1^+, thereby improving the robustness against noise. However, the inverse problem is ill-posed and requires more boundary conditions than the cr-EPT family (in Laplacian form). To stabilize the solution, a regularization strategy such as adding a diffusion term or incorporating total variation of EPs can be tested.

4. **Physics-Informed Neural Network (PINNs)-based EPT:** Recently, a new approach based on the model-driven rather than data-driven deep learning method, PINNs-based EPT [167], was proposed and validated in simulation and practical phantom experiments. This approach uses the central physical equation of the cr-EPT as a loss function with multiple constraints, including similarity and gradient constraints of EPs. This method is promising due to its rapid reconstruction speed and robust generalization for any kind of tissue.

5. **Automated Selection of the Regularization Parameter and Filter Kernel Size:** Selecting the appropriate regularization parameters and filter kernel size is crucial for accurate reconstruction, as deviations from optimal values can lead to suboptimal results. Automating this selection process (such as by deep learning [48]) can streamline the workflow, eliminating the need for manual adjustments and reducing subjectivity in the final reconstructed images.

6. **Larger Population studies:** Conducting larger population studies to validate our findings and explore the variability of EPs in different groups (for example in a children population). These studies will help establish an in vivo EPs database, facilitating the development of more accurate SAR modeling.

References

[1] D. Miklavčič, N. Pavšelj, and F. X. Hart, "Electric Properties of Tissues," in *Wiley Encyclopedia of Biomedical Engineering*, 1st ed., M. Akay, Ed., Wiley, 2006. doi: 10.1002/9780471740360.ebs0403.

[2] Xiaotong Zhang, Jiaen Liu, and Bin He, "Magnetic-Resonance-Based Electrical Properties Tomography: A Review," *IEEE Rev. Biomed. Eng.*, vol. 7, pp. 87–96, 2014, doi: 10.1109/RBME.2013.2297206.

[3] Y. Li *et al.*, "A fast approach to determine excitation eigenfrequencies for TD-EIT and FD-EIT," *Meas. Sci. Technol.*, vol. 34, no. 10, p. 105501, Oct. 2023, doi: 10.1088/1361-6501/acdff3.

[4] J. K. Seo, E. J. Woo, U. Katscher, and Y. Wang, *Electro-magnetic tissue properties MRI*. in Modelling and simulation in medical imaging, no. vol. 1. London: Imperial College Press, 2014.

[5] R. Sadleir and A. S. Minhas, Eds., *Electrical Properties of Tissues: Quantitative Magnetic Resonance Mapping*, vol. 1380. in Advances in Experimental Medicine and Biology, vol. 1380. Cham: Springer International Publishing, 2022. doi: 10.1007/978-3-031-03873-0.

[6] S. Z. K. Sajib, O. I. Kwon, H. J. Kim, and E. J. Woo, "Electrodeless conductivity tensor imaging (CTI) using MRI: basic theory and animal experiments," *Biomed. Eng. Lett.*, vol. 8, no. 3, pp. 273–282, Aug. 2018, doi: 10.1007/s13534-018-0066-3.

[7] N. Katoch *et al.*, "Conductivity Tensor Imaging of *In Vivo* Human Brain and Experimental Validation Using Giant Vesicle Suspension," *IEEE Trans. Med. Imaging*, vol. 38, no. 7, pp. 1569–1577, Jul. 2019, doi: 10.1109/TMI.2018.2884440.

[8] S. Mandija, "Non-Invasive Characterization of Brain Tissue Electrical Properties with MRI," PhD Thesis, Utrecht University, 2018.

[9] Jin Keun Seo and Eung Je Woo, "Electrical Tissue Property Imaging at Low Frequency Using MREIT," *IEEE Trans. Biomed. Eng.*, vol. 61, no. 5, pp. 1390–1399, May 2014, doi: 10.1109/TBME.2014.2298859.

[10] A. Peyman, S. J. Holden, S. Watts, R. Perrott, and C. Gabriel, "Dielectric properties of porcine cerebrospinal tissues at microwave frequencies: *in vivo , in vitro* and systematic variation with age," *Phys. Med. Biol.*, vol. 52, no. 8, pp. 2229–2245, Apr. 2007, doi: 10.1088/0031-9155/52/8/013.

[11] C. Gabriel and A. Peyman, "Dielectric Properties of Biological Tissues; Variation With Age," in *Conn's Handbook of Models for Human Aging*, Elsevier, 2018, pp. 939–952. doi: 10.1016/B978-0-12-811353-0.00069-5.

[12] A. Peyman *et al.*, "Variation in dielectric properties due to pathological changes in human liver," *Bioelectromagnetics*, vol. 36, no. 8, pp. 603–612, Dec. 2015, doi: 10.1002/bem.21939.

[13] I. Hancu, J. C. Roberts, S. Bulumulla, and S.-K. Lee, "On conductivity, permittivity, apparent diffusion coefficient, and their usefulness as cancer markers at MRI frequencies: Conductivity, Permittivity, and Apparent Diffusion Coefficients as Cancer Markers," *Magn. Reson. Med.*, vol. 73, no. 5, pp. 2025–2029, May 2015, doi: 10.1002/mrm.25309.

[14] W. T. Joines, Y. Zhang, C. Li, and R. L. Jirtle, "The measured electrical properties of normal and malignant human tissues from 50 to 900 MHz," *Medical Physics*, vol. 21, no. 4, pp. 547–550, 1994, doi: https://doi.org/10.1118/1.597312.

[15] J. Shin *et al.*, "Initial study on in vivo conductivity mapping of breast cancer using MRI: In Vivo Conductivity Mapping of Breast Cancer," *J. Magn. Reson. Imaging*, vol. 42, no. 2, pp. 371–378, Aug. 2015, doi: 10.1002/jmri.24803.

[16] S.-Y. Kim *et al.*, "Correlation between conductivity and prognostic factors in invasive breast cancer using magnetic resonance electric properties tomography (MREPT)," *Eur Radiol*, vol. 26, no. 7, pp. 2317–2326, Jul. 2016, doi: 10.1007/s00330-015-4067-7.

[17] E. Balidemaj *et al.*, "*In vivo* electric conductivity of cervical cancer patients based on B1+ maps at 3T MRI," *Phys. Med. Biol.*, vol. 61, no. 4, pp. 1596–1607, Feb. 2016, doi: 10.1088/0031-9155/61/4/1596.

[18] C. Rossmanna and D. Haemmerich, "Review of Temperature Dependence of Thermal Properties, Dielectric Properties, and Perfusion of Biological Tissues at Hyperthermic and Ablation Temperatures," *Crit Rev Biomed Eng*, vol. 42, no. 6, pp. 467–492, 2014, doi: 10.1615/CritRevBiomedEng.2015012486.

[19] N. R. Datta *et al.*, “Local hyperthermia combined with radiotherapy and-/or chemotherapy: Recent advances and promises for the future,” *Cancer Treatment Reviews*, vol. 41, no. 9, pp. 742–753, Nov. 2015, doi: 10.1016/j.ctrv.2015.05.009.
[20] O. Bottauscio, M. Chiampi, L. Zilberti, and M. Zucca, “Evaluation of Electromagnetic Phenomena Induced by Transcranial Magnetic Stimulation,” *IEEE Trans. Magn.*, vol. 50, no. 2, pp. 1033–1036, Feb. 2014, doi: 10.1109/TMAG.2013.2281739.
[21] K. Wendel *et al.*, “EEG/MEG Source Imaging: Methods, Challenges, and Open Issues,” *Computational Intelligence and Neuroscience*, vol. 2009, pp. 1–12, 2009, doi: 10.1155/2009/656092.
[22] Zhongming Liu, Chenguang Liu, and Bin He, “Noninvasive reconstruction of three-dimensional ventricular activation sequence from the inverse solution of distributed equivalent current density,” *IEEE Trans. Med. Imaging*, vol. 25, no. 10, pp. 1307–1318, Oct. 2006, doi: 10.1109/TMI.2006.882140.
[23] J. Liu, Y. Wang, U. Katscher, and B. He, “Electrical Properties Tomography Based on $B_{{1}}$ Maps in MRI: Principles, Applications, and Challenges,” *IEEE Trans. Biomed. Eng.*, vol. 64, no. 11, pp. 2515–2530, Nov. 2017, doi: 10.1109/TBME.2017.2725140.
[24] A. La Gioia *et al.*, “Open-Ended Coaxial Probe Technique for Dielectric Measurement of Biological Tissues: Challenges and Common Practices,” *Diagnostics*, vol. 8, no. 2, p. 40, Jun. 2018, doi: 10.3390/diagnostics8020040.
[25] R. Harikumar, R. Prabu, and S. Raghavan, “Electrical Impedance Tomography (EIT) and Its Medical Applications: A Review,” vol. 3, no. 4, 2013.
[26] L. Ma and M. Soleimani, “Methods and Applications of Magnetic Induction Tomography: A review”.
[27] R. Leijsen, W. Brink, C. van den Berg, A. Webb, and R. Remis, “Electrical Properties Tomography: A Methodological Review,” *Diagnostics*, vol. 11, no. 2, p. 176, Jan. 2021, doi: 10.3390/diagnostics11020176.
[28] C. Gabriel, S. Gabriel, and E. Corthout, “The dielectric properties of biological tissues: I. Literature survey,” *Phys. Med. Biol.*, vol. 41, no. 11, pp. 2231–2249, Nov. 1996, doi: 10.1088/0031-9155/41/11/001.
[29] S. Gabriel, R. W. Lau, and C. Gabriel, “The dielectric properties of biological tissues: II. Measurements in the frequency range 10 Hz to 20 GHz,” *Phys. Med. Biol.*, vol. 41, no. 11, pp. 2251–2269, Nov. 1996, doi: 10.1088/0031-9155/41/11/002.
[30] S. Gabriel, R. W. Lau, and C. Gabriel, “The dielectric properties of biological tissues: III. Parametric models for the dielectric spectrum of tissues,” *Phys. Med. Biol.*, vol. 41, no. 11, pp. 2271–2293, Nov. 1996, doi: 10.1088/0031-9155/41/11/003.
[31] J. S. Bobowski and T. Johnson, “PERMITTIVITY MEASUREMENTS OF BIOLOGICAL SAMPLES BY AN OPEN-ENDED COAXIAL LINE,” *PIER B*, vol. 40, pp. 159–183, 2012, doi: 10.2528/PIERB12022906.
[32] E. J. Woo and J. K. Seo, “Magnetic resonance electrical impedance tomography (MREIT) for high-resolution conductivity imaging,” *Physiol. Meas.*, vol. 29, no. 10, pp. R1–R26, Oct. 2008, doi: 10.1088/0967-3334/29/10/R01.
[33] E. M. Haacke, L. S. Petropoulos, E. W. Nilges, and D. H. Wu, “Extraction of conductivity and permittivity using magnetic resonance imaging,” *Phys. Med. Biol.*, vol. 36, no. 6, pp. 723–734, Jun. 1991, doi: 10.1088/0031-9155/36/6/002.
[34] H. Wen, “Non-invasive Quantitative Mapping of Conductivity and Dielectric Distributions Using the RF Wave Propagation Effects in High Field MRI,” in *Medical Imaging 2003: Physics of Medical Imaging*, Bellingham, WA USA, 2003, pp. 471–477.
[35] J. Luo, J. Nassar, O. C. Kiersnowski, O. Arsenov, P. Fuchs, and K. Shmueli, “Preliminary Whole-Brain Functional Electrical Properties Tomography using Gradient-Echo Echo-Planar Imaging,” in *Proceedings of 31st annual Meeting of International Society of Magnetic Resonance in Medicine (ISMRM)*, Singapore, 2024, p. 3681.
[36] M. Helle and U. Katscher, “Electrical Properties Tomography based Functional Magnetic Resonance Imaging (EPT-fMRI),” in *Proceedings of 27th annual Meeting of International Society of Magnetic Resonance in Medicine (ISMRM)*, Honolulu, United States, 2019, p. 3759.

[37] Y. Liao, N. Lechea, A. W. Magill, W. A. Worthoff, V. Gras, and N. J. Shah, “Correlation of quantitative conductivity mapping and total tissue sodium concentration at 3T/4T,” *Magnetic Resonance in Med*, vol. 82, no. 4, pp. 1518–1526, Oct. 2019, doi: 10.1002/mrm.27787.
[38] E. Michel, D. Hernandez, and S. Y. Lee, “Electrical conductivity and permittivity maps of brain tissues derived from water content based on T $_1$ -weighted acquisition,” *Magnetic Resonance in Med*, vol. 77, no. 3, pp. 1094–1103, Mar. 2017, doi: 10.1002/mrm.26193.
[39] T. Voigt, H. Homann, U. Katscher, and O. Doessel, “Patient-individual local SAR determination: In vivo measurements and numerical validation,” *Magnetic Resonance in Medicine*, vol. 68, no. 4, pp. 1117–1126, Oct. 2012, doi: 10.1002/mrm.23322.
[40] M. V. Vaidya, C. M. Collins, D. K. Sodickson, R. Brown, G. C. Wiggins, and R. Lattanzi, “Dependence of and field patterns of surface coils on the electrical properties of the sample and the MR operating frequency,” *Concepts Magn Reson*, vol. 46, no. 1, pp. 25–40, Feb. 2016, doi: 10.1002/cmr.b.21319.
[41] D. I. Hoult, “The principle of reciprocity in signal strength calculations?A mathematical guide,” *Concepts Magn. Reson.*, vol. 12, no. 4, pp. 173–187, 2000, doi: 10.1002/1099-0534(2000)12:4<173::AID-CMR1>3.0.CO;2-Q.
[42] A. L. H. M. W. Van Lier *et al.*, “Electrical Properties Tomography in the Human Brain at 1.5, 3, and 7T: A Comparison Study,” *Magnetic Resonance in Med*, vol. 71, no. 1, pp. 354–363, Jan. 2014, doi: 10.1002/mrm.24637.
[43] K. Jung *et al.*, “Data-driven electrical conductivity brain imaging using 3 T MRI,” *Human Brain Mapping*, vol. 44, no. 15, pp. 4986–5001, Oct. 2023, doi: 10.1002/hbm.26421.
[44] E. Balidemaj *et al.*, “CSI-EPT: A Contrast Source Inversion Approach for Improved MRI-Based Electric Properties Tomography,” *IEEE Trans. Med. Imaging*, vol. 34, no. 9, pp. 1788–1796, Sep. 2015, doi: 10.1109/TMI.2015.2404944.
[45] R. Leijsen, P. Fuchs, W. Brink, A. Webb, and R. Remis, “Developments in Electrical-Property Tomography Based on the Contrast-Source Inversion Method,” *J. Imaging*, vol. 5, no. 2, p. 25, Feb. 2019, doi: 10.3390/jimaging5020025.
[46] N. Gurler and Y. Z. Ider, “Gradient-based electrical conductivity imaging using MR phase,” *Magn Reson Med*, vol. 77, no. 1, pp. 137–150, Jan. 2017, doi: 10.1002/mrm.26097.
[47] X. Sun, L. Lu, L. Qi, Y. Mei, X. Liu, and W. Chen, “MR-Based Electrical Conductivity Imaging Using Second-Order Total Generalized Variation Regularization,” *Applied Sciences*, vol. 10, no. 21, p. 7910, Nov. 2020, doi: 10.3390/app10217910.
[48] A. J. G. Inda, S. Y. Huang, N. İmamoğlu, and W. Yu, “Physics-Coupled Neural Network Magnetic Resonance Electrical Property Tomography (MREPT) for Conductivity Reconstruction,” *IEEE Trans. on Image Process.*, vol. 31, pp. 3463–3478, 2022, doi: 10.1109/TIP.2022.3172220.
[49] C. Liu *et al.*, “Divergence-Based Magnetic Resonance Electrical Properties Tomography,” *IEEE Trans. Biomed. Eng.*, vol. 68, no. 1, pp. 192–203, Jan. 2021, doi: 10.1109/TBME.2020.3003460.
[50] F. S. Hafalir, O. F. Oran, N. Gurler, and Y. Z. Ider, “Convection-Reaction Equation Based Magnetic Resonance Electrical Properties Tomography (cr-MREPT),” *IEEE Trans. Med. Imaging*, vol. 33, no. 3, pp. 777–793, Mar. 2014, doi: 10.1109/TMI.2013.2296715.
[51] J. Liu, X. Zhang, S. Schmitter, P.-F. Van de Moortele, and B. He, “Gradient-based electrical properties tomography (gEPT): A robust method for mapping electrical properties of biological tissues in vivo using magnetic resonance imaging,” *Magnetic Resonance in Medicine*, vol. 74, no. 3, pp. 634–646, 2015, doi: https://doi.org/10.1002/mrm.25434.
[52] T. Voigt, U. Katscher, and O. Doessel, “Quantitative conductivity and permittivity imaging of the human brain using electric properties tomography: In Vivo Electric Properties Tomography,” *Magn. Reson. Med.*, vol. 66, no. 2, pp. 456–466, Aug. 2011, doi: 10.1002/mrm.22832.
[53] S.-K. Lee, S. Bulumulla, F. Wiesinger, L. Sacolick, W. Sun, and I. Hancu, “Tissue Electrical Property Mapping from Zero Echo-Time Magnetic Resonance Imaging,” *IEEE Trans Med Imaging*, vol. 34, no. 2, pp. 541–550, Feb. 2015, doi: 10.1109/TMI.2014.2361810.
[54] P. Soullié, A. Missoffe, K. Ambarki, J. Felblinger, and F. Odille, “MR electrical properties imaging using a generalized image-based method,” *Magn. Reson. Med.*, vol. 85, no. 2, pp. 762–776, Feb. 2021, doi: 10.1002/mrm.28458.
[55] S. Mandija, A. Sbrizzi, U. Katscher, P. R. Luijten, and C. A. T. van den Berg, “Error analysis of helmholtz-based MR-electrical properties tomography: MR-Electrical Properties Tomography

Reconstruction Errors," *Magn. Reson. Med*, vol. 80, no. 1, pp. 90–100, Jul. 2018, doi: 10.1002/mrm.27004.
[56] S.-K. Lee, S. Bulumulla, and I. Hancu, "Theoretical Investigation of Random Noise-Limited Signal-to-Noise Ratio in MR-Based Electrical Properties Tomography," *IEEE Trans. Med. Imaging*, vol. 34, no. 11, pp. 2220–2232, Nov. 2015, doi: 10.1109/TMI.2015.2427236.
[57] J. P. Marques, D. K. Sodickson, O. Ipek, C. M. Collins, and R. Gruetter, "Single acquisition electrical property mapping based on relative coil sensitivities: A proof-of-concept demonstration: Single Acquisition Electrical Property Mapping," *Magn. Reson. Med.*, vol. 74, no. 1, pp. 185–195, Jul. 2015, doi: 10.1002/mrm.25399.
[58] G. Yildiz and Y. Z. Ider, "Use of dielectric padding to eliminate low convective field artifact in cr-MREPT conductivity images," *Magn Reson Med*, vol. 81, no. 5, pp. 3168–3184, May 2019, doi: 10.1002/mrm.27648.
[59] C. Li, W. Yu, and S. Y. Huang, "An MR-Based Viscosity-Type Regularization Method for Electrical Property Tomography," *Tomography*, vol. 3, no. 1, pp. 50–59, Mar. 2017, doi: 10.18383/j.tom.2016.00283.
[60] S. Ozdemir and Y. Z. Ider, "bSSFP phase correction and its use in magnetic resonance electrical properties tomography," *Magn Reson Med*, vol. 81, no. 2, pp. 934–946, Feb. 2019, doi: 10.1002/mrm.27446.
[61] Y. Wang, P.-F. Van De Moortele, and B. He, "Automated gradient-based electrical properties tomography in the human brain using 7 Tesla MRI," *Magnetic Resonance Imaging*, vol. 63, pp. 258–266, Nov. 2019, doi: 10.1016/j.mri.2019.08.003.
[62] Y. Wang, P.-F. Van De Moortele, and B. He, "CONtrast Conformed Electrical Properties Tomography (CONCEPT) Based on Multi- Channel Transmission and Alternating Direction Method of Multipliers," *IEEE Trans. Med. Imaging*, vol. 38, no. 2, pp. 349–359, Feb. 2019, doi: 10.1109/TMI.2018.2865121.
[63] Y. Wang *et al.*, "Mapping electrical properties heterogeneity of tumor using boundary informed electrical properties tomography (BIEPT) at 7T," *Magnetic Resonance in Med*, vol. 81, no. 1, pp. 393–409, Jan. 2019, doi: 10.1002/mrm.27414.
[64] J. Liu *et al.*, "In vivo imaging of electrical properties of an animal tumor model with an 8-channel transceiver array at 7 T using electrical properties tomography," *Magnetic Resonance in Med*, vol. 78, no. 6, pp. 2157–2169, Dec. 2017, doi: 10.1002/mrm.26609.
[65] U. Katscher and C. A. T. van den Berg, "Electric properties tomography: Biochemical, physical and technical background, evaluation and clinical applications," *NMR in Biomedicine*, vol. 30, no. 8, p. e3729, Aug. 2017, doi: 10.1002/nbm.3729.
[66] K. K. Tha *et al.*, "Noninvasive electrical conductivity measurement by MRI: a test of its validity and the electrical conductivity characteristics of glioma," *Eur Radiol*, vol. 28, no. 1, pp. 348–355, Jan. 2018, doi: 10.1007/s00330-017-4942-5.
[67] K. K. Tha, Y. Kikuchi, K. Ishizaka, T. Kamiyama, M. Yoneyama, and U. Katscher, "Higher Electrical Conductivity of Liver Parenchyma in Fibrotic Patients: Noninvasive Assessment by Electric Properties Tomography," *Magnetic Resonance Imaging*, vol. 54, no. 5, pp. 1689–1691, Nov. 2021, doi: 10.1002/jmri.27701.
[68] K. K. Tha, M. Kitagawa, D. Sakamoto, H. Hamaguchi, and U. Katscher, "Potential of phase-based electrical conductivity in evaluating lumbar intervertebral disc degeneration," in *Proceedings of 31st annual Meeting of International Society of Magnetic Resonance in Medicine (ISMRM)*, Singapore, 2024, p. 0189.
[69] U. Katscher, D.-H. Kim, and J. K. Seo, "Recent Progress and Future Challenges in MR Electric Properties Tomography," *Computational and Mathematical Methods in Medicine*, vol. 2013, pp. 1–11, 2013, doi: 10.1155/2013/546562.
[70] Y. Z. Ider and M. N. Akyer, "Properties and implementation issues of phase based cr-MRECT for conductivity imaging," in *Proceedings of the ISMRM & SMRT Virtual Conference & Exhibition*, Online, 2020, pp. 8–14.
[71] S. Mandija, "Brain Tissue Conductivity Measurements with MR-Electrical Properties Tomography: An In Vivo Study," *Brain Topography*, p. 8, 2021.
[72] A. Karsa and K. Shmueli, "New Approaches for Simultaneous Noise Suppression and Edge Preservation to Achieve Accurate Quantitative Conductivity Mapping in Noisy Images," in

Proceedings of 29th annual Meeting of International Society of Magnetic Resonance in Medicine (ISMRM), Online, 2021, p. 3774.
[73] S. B. Bulumulla, S.-K. Lee, and T. B. D. Yeo, "Calculation of Electrical Properties from B1+ Maps - A Comparison of Methods," in *Proceedings of the 20th Scientific Meeting of the International Society of Magnetic Resonance in Medicine (ISMRM)*, Melbourne, Australia, 2012.
[74] S.-M. Gho, J. Shin, M.-O. Kim, and D.-H. Kim, "Simultaneous quantitative mapping of conductivity and susceptibility using a double-echo ultrashort echo time sequence: Example using a hematoma evolution study: Simultaneous QCM and QSM," *Magn. Reson. Med.*, vol. 76, no. 1, pp. 214–221, Jul. 2016, doi: 10.1002/mrm.25869.
[75] C. Stehning, T. R. Voigt, and U. Katscher, "Real-Time Conductivity Mapping using Balanced SSFP and Phase-Based Reconstruction," in *Proceedings of the 19th Annual Meeting of the International Society of Magnetic Resonance in Medicine (ISMRM)*, Montreal,Canada, 2011, p. 128.
[76] R. Stollberger and P. Wach, "Imaging of the active B_1 field *in vivo*," *Magnetic Resonance in Med*, vol. 35, no. 2, pp. 246–251, Feb. 1996, doi: 10.1002/mrm.1910350217.
[77] K. Nehrke and P. Börnert, "DREAM-a novel approach for robust, ultrafast, multislice B_1 mapping: DREAM B_1 Mapping," *Magn Reson Med*, vol. 68, no. 5, pp. 1517–1526, Nov. 2012, doi: 10.1002/mrm.24158.
[78] L. I. Sacolick, F. Wiesinger, I. Hancu, and M. W. Vogel, "B1 mapping by Bloch-Siegert shift," *Magnetic Resonance in Medicine*, vol. 63, no. 5, pp. 1315–1322, 2010, doi: https://doi.org/10.1002/mrm.22357.
[79] V. L. Yarnykh, "Actual flip-angle imaging in the pulsed steady state: A method for rapid three-dimensional mapping of the transmitted radiofrequency field," *Magnetic Resonance in Medicine*, vol. 57, no. 1, pp. 192–200, 2007, doi: https://doi.org/10.1002/mrm.21120.
[80] S. Chung, D. Kim, E. Breton, and L. Axel, "Rapid B_1^+ mapping using a preconditioning RF pulse with TurboFLASH readout," *Magnetic Resonance in Med*, vol. 64, no. 2, pp. 439–446, Aug. 2010, doi: 10.1002/mrm.22423.
[81] J. L. Kent, I. Dragonu, L. Valkovič, and A. T. Hess, "Rapid 3D absolute B_1^+ mapping using a sandwiched train presaturated TurboFLASH sequence at 7 T for the brain and heart," *Magnetic Resonance in Med*, vol. 89, no. 3, pp. 964–976, Mar. 2023, doi: 10.1002/mrm.29497.
[82] A. L. H. M. W. Van Lier *et al.*, "*B* 1+ Phase mapping at 7 T and its application for in vivo electrical conductivity mapping: Electrical Conductivity Mapping," *Magn. Reson. Med.*, vol. 67, no. 2, pp. 552–561, Feb. 2012, doi: 10.1002/mrm.22995.
[83] N. Choi, M. Ghim, S. Yang, S.-Y. Zho, and D.-H. Kim, "In vivo conductivity mapping using double spin echo for flow effect removal," in *Proceedings of the 19th Annual Meeting of the ISMRM*, Concord, CA , USA, 2011, p. 4466.
[84] C. Lesbats *et al.*, "High-frequency electrical properties tomography at 9.4T as a novel contrast mechanism for brain tumors," *Magnetic Resonance in Medicine*, vol. 86, no. 1, pp. 382–392, 2021, doi: https://doi.org/10.1002/mrm.28685.
[85] Z. He *et al.*, "Phantom evaluation of electrical conductivity mapping by MRI: Comparison to vector network analyzer measurements and spatial resolution assessment," *Magnetic Resonance in Medicine*, Jan. 2024, doi: 10.1002/mrm.30009.
[86] M. A. Schofield and Y. Zhu, "Fast phase unwrapping algorithm for interferometric applications," *Opt. Lett.*, vol. 28, no. 14, p. 1194, Jul. 2003, doi: 10.1364/OL.28.001194.
[87] R. Cusack and N. Papadakis, "New Robust 3-D Phase Unwrapping Algorithms: Application to Magnetic Field Mapping and Undistorting Echoplanar Images," *NeuroImage*, vol. 16, no. 3, pp. 754–764, Jul. 2002, doi: 10.1006/nimg.2002.1092.
[88] B. Dymerska *et al.*, "Phase unwrapping with a rapid opensource minimum spanning tree algorithm (ROMEO)," *Magnetic Resonance in Med*, vol. 85, no. 4, pp. 2294–2308, Apr. 2021, doi: 10.1002/mrm.28563.
[89] QSM Consensus Organization Committee *et al.*, "Recommended implementation of quantitative susceptibility mapping for clinical research in the brain: A consensus of the ISMRM electro-magnetic tissue properties study group," *Magnetic Resonance in Med*, vol. 91, no. 5, pp. 1834–1862, May 2024, doi: 10.1002/mrm.30006.
[90] O. C. Kiersnowski *et al.*, "Rapid High Resolution Integrated Structural and Functional Susceptibility and Conductivity Mapping in the Human Brain," in *Proceedings of 31st annual*

Meeting of International Society of Magnetic Resonance in Medicine (ISMRM), Singapore, 2024, p. 0188.
[91] M. Kadbi *et al.*, "4D UTE flow: A phase-contrast MRI technique for assessment and visualization of stenotic flows," *Magnetic Resonance in Medicine*, vol. 73, no. 3, pp. 939–950, 2015, doi: https://doi.org/10.1002/mrm.25188.
[92] J. P. Mugler III, S. W. Fielden, C. H. Meyer, T. Altes, G. W. Miller, and A. Stemmer, "Breath-hold UTE lung imaging using a stack-of-spirals acquisition," in *Proc Intl Soc Mag Reson Med*, 2015, p. 1476.
[93] Y. Qian and F. E. Boada, "Acquisition-weighted stack of spirals for fast high-resolution three-dimensional ultra-short echo time MR imaging," *Magnetic Resonance in Medicine*, vol. 60, no. 1, pp. 135–145, 2008, doi: https://doi.org/10.1002/mrm.21620.
[94] V. Fauveau *et al.*, "Performance of spiral UTE-MRI of the lung in post-COVID patients," *Magnetic Resonance Imaging*, vol. 96, pp. 135–143, Feb. 2023, doi: 10.1016/j.mri.2022.12.002.
[95] K. Scheffler and S. Lehnhardt, "Principles and applications of balanced SSFP techniques," *Eur Radiol*, vol. 13, no. 11, pp. 2409–2418, Nov. 2003, doi: 10.1007/s00330-003-1957-x.
[96] O. Bieri, M. Markl, and K. Scheffler, "Analysis and compensation of eddy currents in balanced SSFP," *Magnetic Resonance in Med*, vol. 54, no. 1, pp. 129–137, Jul. 2005, doi: 10.1002/mrm.20527.
[97] S. Gavazzi *et al.*, "Transceive phase mapping using the PLANET method and its application for conductivity mapping in the brain," *Magn Reson Med*, vol. 83, no. 2, pp. 590–607, Feb. 2020, doi: 10.1002/mrm.27958.
[98] O. Bieri and K. Scheffler, "Flow compensation in balanced SSFP sequences," *Magnetic Resonance in Med*, vol. 54, no. 4, pp. 901–907, Oct. 2005, doi: 10.1002/mrm.20619.
[99] M. L. Lauzon and R. Frayne, "Analytical characterization of RF phase-cycled balanced steady-state free precession," *Concepts in Magnetic Resonance Part A*, vol. 34A, no. 3, pp. 133–143, 2009, doi: https://doi.org/10.1002/cmr.a.20138.
[100] U. Katscher and S. Weiss, "Mapping electric bulk conductivity in the human heart," *Magnetic Resonance in Med*, vol. 87, no. 3, pp. 1500–1506, Mar. 2022, doi: 10.1002/mrm.29067.
[101] H. M. Gach, A. N. Curcuru, S. Mutic, and T. Kim, "B_0 field homogeneity recommendations, specifications, and measurement units for MRI in radiation therapy," *Medical Physics*, vol. 47, no. 9, pp. 4101–4114, Sep. 2020, doi: 10.1002/mp.14306.
[102] S. Iyyakkunnel, J. Schäper, and O. Bieri, "Configuration-based electrical properties tomography," *Magn. Reson. Med.*, vol. 85, no. 4, pp. 1855–1864, Apr. 2021, doi: 10.1002/mrm.28542.
[103] Q.-S. Xiang and M. N. Hoff, "Banding artifact removal for bSSFP imaging with an elliptical signal model: Banding Artifact Removal for bSSFP Imaging," *Magn. Reson. Med*, vol. 71, no. 3, pp. 927–933, Mar. 2014, doi: 10.1002/mrm.25098.
[104] Y. Shcherbakova, C. A. T. van den Berg, C. T. W. Moonen, and L. W. Bartels, "PLANET: An ellipse fitting approach for simultaneous T_1 and T_2 mapping using phase-cycled balanced steady-state free precession: Ellipse Fitting Approach for T_1 and T_2 Mapping," *Magn. Reson. Med.*, vol. 79, no. 2, pp. 711–722, Feb. 2018, doi: 10.1002/mrm.26717.
[105] K. Keskin, U. Yilmaz, and T. Cukur, "Constrained Ellipse Fitting for Efficient Parameter Mapping With Phase-Cycled bSSFP MRI," *IEEE Trans. Med. Imaging*, vol. 41, no. 1, pp. 14–26, Jan. 2022, doi: 10.1109/TMI.2021.3102852.
[106] U. Katscher, C. Stehning, and K. K. Tha, "The impact of CSF pulsation on reconstructed brain conductivity," in *Proceedings of the ISMRM 26th Annual Meeting & Exhibition*, Paris, France, 2018, p. 0546.
[107] S. Gavazzi *et al.*, "Accuracy and precision of electrical permittivity mapping at 3T: the impact of three mapping techniques," *Magn Reson Med*, p. mrm.27675, Feb. 2019, doi: 10.1002/mrm.27675.
[108] Y. Ishimori, T. Shimanuki, T. Kobayashi, and M. Monma, "Fast B1 mapping based on double-angle method with T1 correction using standard pulse sequence," *J Med Phys*, vol. 47, no. 1, p. 93, 2022, doi: 10.4103/jmp.jmp_78_21.

[109] U. Katscher, T. Voigt, C. Findeklee, P. Vernickel, K. Nehrke, and O. Dossel, "Determination of Electric Conductivity and Local SAR Via B1 Mapping," *IEEE Trans. Med. Imaging*, vol. 28, no. 9, pp. 1365–1374, Sep. 2009, doi: 10.1109/TMI.2009.2015757.
[110] A. Stogryn, "Equations for Calculating the Dielectric Constant of Saline Water (Correspondence)," *IEEE Transactions on Microwave Theory and Techniques*, vol. 19, no. 8, pp. 733–736, 1971, doi: 10.1109/TMTT.1971.1127617.
[111] Jin Keun Seo *et al.*, "Error Analysis of Nonconstant Admittivity for MR-Based Electric Property Imaging," *IEEE Trans. Med. Imaging*, vol. 31, no. 2, pp. 430–437, Feb. 2012, doi: 10.1109/TMI.2011.2171000.
[112] J. P. Mugler *et al.*, "Breath-hold UTE lung imaging using a stack-of-spirals acquisition," in *23rd Annual Meeting International of the Society for Magnetic Resonance in Medicine*, Toronto, Canada, 2015, p. 1476.
[113] D. O. Walsh, A. F. Gmitro, and M. W. Marcellin, "Adaptive reconstruction of phased array MR imagery," *Magn. Reson. Med.*, vol. 43, no. 5, pp. 682–690, May 2000, doi: 10.1002/(SICI)1522-2594(200005)43:5<682::AID-MRM10>3.0.CO;2-G.
[114] A. Peyman, C. Gabriel, and E. H. Grant, "Complex permittivity of sodium chloride solutions at microwave frequencies," *Bioelectromagnetics*, vol. 28, no. 4, pp. 264–274, May 2007, doi: 10.1002/bem.20271.
[115] Abraham. Savitzky and M. J. E. Golay, "Smoothing and Differentiation of Data by Simplified Least Squares Procedures.," *Anal. Chem.*, vol. 36, no. 8, pp. 1627–1639, Jul. 1964, doi: 10.1021/ac60214a047.
[116] Y. Z. Ider and M. N. Akyer, "Properties and implementation issues of phase based cr-MRECT for conductivity imaging," in *Proceedings of 28th annual Meeting of International Society of Magnetic Resonance in Medicine (ISMRM)*, Online, 2020, p. 3190.
[117] A. L. H. M. W. van Lier *et al.*, "Electrical Properties Tomography in the Human Brain at 1.5, 3, and 7T: A Comparison Study: EPT at 1.5, 3, and 7T," *Magn. Reson. Med.*, vol. 71, no. 1, pp. 354–363, Jan. 2014, doi: 10.1002/mrm.24637.
[118] Z. He, B. Chen, P. M. Lefebvre, and F. Odille, "An Adaptative Savitzky-Golay Kernel for Laplacian Estimation in Magnetic Resonance Electrical Property Tomography," in *2023 45th Annual International Conference of the IEEE Engineering in Medicine & Biology Society (EMBC)*, Sydney, Australia, Jul. 2023, pp. 1–4. doi: 10.1109/EMBC40787.2023.10341200.
[119] A. J. Garcia, S. Huang, and W. Yu, "Region-specific regularization of convection-reaction Magnetic Resonance Electrical Property Tomography (MREPT) for improving the accuracy and noise-tolerance of EP reconstruction," in *Proceedings of 26th annual Meeting of International Society of Magnetic Resonance in Medicine (ISMRM)*, Paris, France, 2018, p. 2286.
[120] K. Jung *et al.*, "Improving phase-based conductivity reconstruction by means of deep learning–based denoising of phase data for 3T MRI," *Magn. Reson. Med.*, vol. 86, no. 4, pp. 2084–2094, Oct. 2021, doi: 10.1002/mrm.28826.
[121] E. Michel, D. Hernandez, M. H. Cho, and S. Y. Lee, "Denoising of B1+ field maps for noise-robust image reconstruction in electrical properties tomography: Denoising of B1+ field maps," *Med. Phys.*, vol. 41, no. 10, p. 102304, Sep. 2014, doi: 10.1118/1.4895987.
[122] U. Katscher *et al.*, "Estimation of Breast Tumor Conductivity Using Parabolic Phase Fitting," in *Proceedings of the ISMRM 20th Annual Meeting & Exhibition*, Melbourne, Australia, 2012, p. 3482.
[123] A. Karsa, P. Fuchs, and K. Shmueli, "Optimal Kernel Radii for Calculating the Derivatives of Noisy B1 Phase for Accurate Phase-Based Quantitative Conductivity Mapping," in *Proceedings of 29th annual Meeting of International Society of Magnetic Resonance in Medicine (ISMRM)*, 2021, p. 3775.
[124] D. Zhu and W. A. P. Smith, "Least Squares Surface Reconstruction on Arbitrary Domains," in *Computer Vision – ECCV 2020*, vol. 12367, A. Vedaldi, H. Bischof, T. Brox, and J.-M. Frahm, Eds., in Lecture Notes in Computer Science, vol. 12367. , Cham: Springer International Publishing, 2020, pp. 530–545. doi: 10.1007/978-3-030-58542-6_32.
[125] M. Schmid, D. Rath, and U. Diebold, "Why and How Savitzky–Golay Filters Should Be Replaced," *ACS Meas. Au*, vol. 2, no. 2, pp. 185–196, Apr. 2022, doi: 10.1021/acsmeasuresciau.1c00054.

[126] J. H. Lee *et al.*, "In vivo electrical conductivity measurement of muscle, cartilage, and peripheral nerve around knee joint using MR-electrical properties tomography," *Sci Rep*, vol. 12, no. 1, p. 73, Dec. 2022, doi: 10.1038/s41598-021-03928-y.

[127] A. Arduino, F. Pennecchi, U. Katscher, M. Cox, and L. Zilberti, "Repeatability and Reproducibility Uncertainty in Magnetic Resonance-Based Electric Properties Tomography of a Homogeneous Phantom," *Tomography*, vol. 9, no. 1, pp. 420–435, Feb. 2023, doi: 10.3390/tomography9010034.

[128] J. Lee, J. Shin, and D.-H. Kim, "MR-based conductivity imaging using multiple receiver coils: Multi-RX Conductivity MRI," *Magn. Reson. Med.*, vol. 76, no. 2, pp. 530–539, Aug. 2016, doi: 10.1002/mrm.25891.

[129] S. Mandija and C. Van Den Berg, "The first MR Electrical Properties Tomography (MR-EPT) reconstruction challenge," presented at the Joint Annual Meeting ISMRM-ESMRMB ISMRT 31st Annual Meeting, London, England, UK, 2022, p. 0704. doi: 10.58530/2022/0704.

[130] IT'IS Foundation, "Tissue Properties Database V4.1." IT'IS Foundation, 2022. doi: 10.13099/VIP21000-04-1.

[131] K. M. Ropella and D. C. Noll, "A regularized, model-based approach to phase-based conductivity mapping using MRI," *Magnetic Resonance in Medicine*, vol. 78, no. 5, pp. 2011–2021, 2017, doi: 10.1002/mrm.26590.

[132] H. McCann, "Correction to: Variation in Reported Human Head Tissue Electrical Conductivity Values," *Brain Topography*, p. 6, 2021.

[133] S. J. Malik, J. W. Hand, D. W. Carmichael, and J. V. Hajnal, "Evaluation of specific absorption rate and heating in children exposed to a 7T MRI head coil," *Magnetic Resonance in Med*, vol. 88, no. 3, pp. 1434–1449, Sep. 2022, doi: 10.1002/mrm.29283.

[134] F. Schweser, L. Huang, K.-H. Herrmann, M. Kramer, A. Deistung, and R. Reichenbach, "Conductivity mapping using ultrashort echo time (UTE) imaging," in *Proceedings of the 21st Annual Meeting of ISMRM, Salt Lake City, UT*, 2013, p. 4190.

[135] A. Grimm *et al.*, "Evaluation of 2-point, 3-point, and 6-point Dixon magnetic resonance imaging with flexible echo timing for muscle fat quantification," *European Journal of Radiology*, vol. 103, pp. 57–64, Jun. 2018, doi: 10.1016/j.ejrad.2018.04.011.

[136] I. Panagiotelis and M. Blasche, "TrueForm™Technology," *MAGNETOM Flash*, vol. 114, no. 1, 2009.

[137] D. O. Walsh, A. F. Gmitro, and M. W. Marcellin, "Adaptive reconstruction of phased array MR imagery," *Magnetic Resonance in Medicine*, vol. 43, no. 5, pp. 682–690, 2000, doi: 10.1002/(SICI)1522-2594(200005)43:5<682::AID-MRM10>3.0.CO;2-G.

[138] M. Lustig and J. M. Pauly, "SPIRiT: Iterative self-consistent parallel imaging reconstruction from arbitrary k-space," *Magn Reson Med*, vol. 64, no. 2, pp. 457–471, Aug. 2010, doi: 10.1002/mrm.22428.

[139] J. Cao, I. Ball, P. Humburg, S. Dokos, and C. Rae, "Repeatability of brain phase-based magnetic resonance electric properties tomography methods and effect of compressed SENSE and RF shimming," *Phys Eng Sci Med*, vol. 46, no. 2, pp. 753–766, Jun. 2023, doi: 10.1007/s13246-023-01248-1.

[140] V. Vishnevskiy, T. Gass, G. Szekely, C. Tanner, and O. Goksel, "Isotropic Total Variation Regularization of Displacements in Parametric Image Registration," *IEEE Transactions on Medical Imaging*, vol. 36, no. 2, pp. 385–395, Feb. 2017, doi: 10.1109/TMI.2016.2610583.

[141] F. Isensee, P. F. Jaeger, S. A. A. Kohl, J. Petersen, and K. H. Maier-Hein, "nnU-Net: a self-configuring method for deep learning-based biomedical image segmentation," *Nat Methods*, vol. 18, no. 2, Art. no. 2, Feb. 2021, doi: 10.1038/s41592-020-01008-z.

[142] J. YUANFENG, "Amos: A large-scale abdominal multi-organ benchmark for versatile medical image segmentation." Zenodo, Nov. 28, 2022. doi: 10.5281/zenodo.7155725.

[143] A. Paszke *et al.*, "PyTorch: An Imperative Style, High-Performance Deep Learning Library," in *Advances in Neural Information Processing Systems*, Curran Associates, Inc., 2019. Accessed: Feb. 06, 2024. [Online]. Available: https://papers.nips.cc/paper_files/paper/2019/hash/bdbca288fee7f92f2bfa9f7012727740-Abstract.html

[144] J. Egger *et al.*, "GBM Volumetry using the 3D Slicer Medical Image Computing Platform," *Sci Rep*, vol. 3, no. 1, Art. no. 1, Mar. 2013, doi: 10.1038/srep01364.
[145] J. E. C. Serralles *et al.*, "Noninvasive Estimation of Electrical Properties From Magnetic Resonance Measurements via Global Maxwell Tomography and Match Regularization," *IEEE Trans. Biomed. Eng.*, vol. 67, no. 1, pp. 3–15, Jan. 2020, doi: 10.1109/TBME.2019.2907442.
[146] S. Mandija, E. F. Meliadò, N. R. F. Huttinga, P. R. Luijten, and C. A. T. Van Den Berg, "Opening a new window on MR-based Electrical Properties Tomography with deep learning," *Sci Rep*, vol. 9, no. 1, p. 8895, Jun. 2019, doi: 10.1038/s41598-019-45382-x.
[147] S. Duan, C. Xu, G. Deng, J. Wang, F. Liu, and S. X. Xin, "Quantitative analysis of the reconstruction errors of the currently popular algorithm of magnetic resonance electrical property tomography at the interfaces of adjacent tissues: Error Analysis of Mrept Algorithm at Tissue Interfaces," *NMR Biomed.*, vol. 29, no. 6, pp. 744–750, Jun. 2016, doi: 10.1002/nbm.3522.
[148] Y. Liao, N. Lechea, A. W. Magill, W. A. Worthoff, V. Gras, and N. J. Shah, "Correlation of quantitative conductivity mapping and total tissue sodium concentration at 3T/4T," *Magnetic Resonance in Medicine*, vol. 82, no. 4, pp. 1518–1526, 2019, doi: 10.1002/mrm.27787.
[149] T. Voigt, U. Katscher, and O. Doessel, "Quantitative conductivity and permittivity imaging of the human brain using electric properties tomography," *Magnetic Resonance in Medicine*, vol. 66, no. 2, pp. 456–466, 2011, doi: 10.1002/mrm.22832.
[150] E. Balidemaj, A. L. H. M. W. van Lier, A. J. Nederveen, J. Crezee, and C. van den Berg, "Feasibility of EPT in the Human Pelvis at 3T," *Proc. 20th Sci. Meet. Int. Soc. Magn. Reson. Med.*, Singapore, p. 3468, 2012.
[151] U. Katscher and P. Börnert, "Imaging of Lung Conductivity Using Ultrashort Echo-Time Imaging," in *Proceedings of the ISMRM 24th Annual Meeting & Exhibition*, Singapore, 2016, p. 2923.
[152] C. Gabriel, "Dielectric properties of biological tissue: Variation with age," *Bioelectromagnetics*, vol. 26, no. S7, pp. S12–S18, 2005, doi: 10.1002/bem.20147.
[153] J. M. Gullett *et al.*, "The association of white matter free water with cognition in older adults," *NeuroImage*, vol. 219, p. 117040, Oct. 2020, doi: 10.1016/j.neuroimage.2020.117040.
[154] S. Filo *et al.*, "Disentangling molecular alterations from water-content changes in the aging human brain using quantitative MRI," *Nat Commun*, vol. 10, no. 1, p. 3403, Jul. 2019, doi: 10.1038/s41467-019-11319-1.
[155] A. Gottschalk, S. Scafidi, and T. J. K. Toung, "Brain water as a function of age and weight in normal rats," *PLoS ONE*, vol. 16, no. 9, p. e0249384, Sep. 2021, doi: 10.1371/journal.pone.0249384.
[156] M. He, F. Liu, A. Nummenmaa, M. Hämäläinen, B. C. Dickerson, and P. L. Purdon, "Age-Related EEG Power Reductions Cannot Be Explained by Changes of the Conductivity Distribution in the Head Due to Brain Atrophy," *Front. Aging Neurosci.*, vol. 13, p. 632310, Feb. 2021, doi: 10.3389/fnagi.2021.632310.
[157] M. J. Simmonds, H. J. Meiselman, and O. K. Baskurt, "Blood rheology and aging," *Journal of Geriatric Cardiology : JGC*, vol. 10, no. 3, p. 291, Sep. 2013, doi: 10.3969/j.issn.1671-5411.2013.03.010.
[158] Y. X. J. Wáng, "Gender-specific liver aging and magnetic resonance imaging," *Quantitative Imaging in Medicine and Surgery*, vol. 11, no. 7, p. 2893, Jul. 2021, doi: 10.21037/qims-21-227.
[159] M. N. Hoff *et al.*, "Safety Considerations of 7-T MRI in Clinical Practice," *Radiology*, vol. 292, no. 3, pp. 509–518, Sep. 2019, doi: 10.1148/radiol.2019182742.
[160] U. Katscher, C. Findeklee, and T. Voigt, "B_1-based specific energy absorption rate determination for nonquadrature radiofrequency excitation," *Magnetic Resonance in Med*, vol. 68, no. 6, pp. 1911–1918, Dec. 2012, doi: 10.1002/mrm.24215.
[161] S. Buchenau, M. Haas, D. N. Splitthoff, J. Hennig, and M. Zaitsev, "Iterative separation of transmit and receive phase contributions and B 1 + -based estimation of the specific absorption rate for transmit arrays," *Magn Reson Mater Phy*, vol. 26, no. 5, pp. 463–476, Oct. 2013, doi: 10.1007/s10334-013-0367-6.
[162] X. Zhang, P.-F. V. de Moortele, S. Schmitter, and B. He, "Complex B_1 mapping and electrical properties imaging of the human brain using a 16-channel transceiver coil at 7T," *Magn Reson Med*, vol. 69, no. 5, pp. 1285–1296, May 2013, doi: 10.1002/mrm.24358.

[163] S. Buchenau, M. Haas, J. Hennig, and M. Zaitsev, “Quality assessment of B1-based local SAR estimation as a function of position within a parallel transmit coil at 3T,” in *Proc. Intl. Soc. Mag. Reson. Med. 19*, Montréal, Canada, 2011, p. 0493.

[164] Xiaotong Zhang, S. Schmitter, P. Van De Moortele, Jiaen Liu, and Bin He, “From Complex ${\rm B}_{1}$ Mapping to Local SAR Estimation for Human Brain MR Imaging Using Multi-Channel Transceiver Coil at 7T,” *IEEE Trans. Med. Imaging*, vol. 32, no. 6, pp. 1058–1067, Jun. 2013, doi: 10.1109/TMI.2013.2251653.

[165] A. Mezer, A. Rokem, S. Berman, T. Hastie, and B. A. Wandell, “Evaluating quantitative proton-density-mapping methods,” *Human Brain Mapping*, vol. 37, no. 10, pp. 3623–3635, Oct. 2016, doi: 10.1002/hbm.23264.

[166] S. Volz, U. Nöth, A. Jurcoane, U. Ziemann, E. Hattingen, and R. Deichmann, “Quantitative proton density mapping: correcting the receiver sensitivity bias via pseudo proton densities,” *NeuroImage*, vol. 63, no. 1, pp. 540–552, Oct. 2012, doi: 10.1016/j.neuroimage.2012.06.076.

[167] G. Ruan *et al.*, “Magnetic Resonance Electrical Properties Tomography Based on Modified Physics-Informed Neural Network and Multiconstraints,” *IEEE Trans. Med. Imaging*, pp. 1–1, 2024, doi: 10.1109/TMI.2024.3391651.

RÉSUMÉ

Les propriétés électriques des tissus (EPs), qui comprenne la conductivité et la permittivité, définissent le flux de courant dans le corps en réponse aux champs électromagnétiques. Influencées par la composition des tissus, la structure, le vieillissement, la teneur en eau, la concentration en ions et le milieu (intra- ou extracellulaire), les EPs varient selon les tissus et les conditions pathologiques, ce qui en fait des biomarqueurs potentiels pour des applications cliniques telles que le diagnostic du cancer et le suivi thérapeutique. Comprendre les EPs est crucial pour calculer la distribution des champs électromagnétiques et évaluer le débit d'absorption spécifique (DAS) personnalisé dans les systèmes d'IRM pour assurer la sécurité des radiofréquences (RF). La tomographie des propriétés électriques par résonance magnétique (EPT) est une technologie non invasive et à haute résolution qui reconstruit les EPs à partir des variations du champ B_1 en IRM. Cette thèse évalue et optimise les méthodes EPT et explore la variabilité des EPs pour améliorer la modélisation du DAS. La thèse passe en revue les méthodes EPT, en se concentrant sur la précision et les limites de résolution à l'aide de fantômes de conductivité. L'EPT basée sur l'image avec la séquence Ultra-short Echo Time (UTE) a été identifiée comme la plus prometteuse. La précision de la reconstruction de la permittivité a été améliorée avec un angle de bascule optimal. Un noyau adaptatif de Savitzky-Golay a été proposé pour l'EPT de Helmholtz homogène, et une méthode EPT par intégrale de surface a réduit le bruit. Des études in vivo sur la conductivité du cerveau et du torse en relation avec l'âge, la fraction de graisse et le sexe ont informé une modélisation précise du DAS. Les calculs de DAS basés sur l'EPT ont validé la fiabilité et l'importance de l'EPT.

Mots-clés : IRM, EPT, propriété électriques, conductivité, permittivité, DAS, UTE, Savitzky-Golay, âge, électromagnétisme, RF

ABSTRACT

Tissue electrical properties (EPs), including conductivity and permittivity, define current flow in the body in response to electromagnetic fields. Influenced by tissue composition, structure, aging, water content, ion concentration, and medium (intra- or extracellular), EPs vary across tissues and pathological conditions, making them potential biomarkers for clinical applications such as cancer diagnosis and therapy monitoring. Understanding EPs is crucial for calculating EM field distribution and assessing personalized specific absorption rate (SAR) in MRI systems for RF safety. Magnetic Resonance Electrical Properties Tomography (EPT) is a non-invasive, high-resolution technology that reconstructs EPs from B1 field variations in MRI. This thesis evaluates and optimizes EPT methods and explores EP variability to improve SAR modeling. The thesis reviews EPT methods, focusing on accuracy and resolution limits using conductivity phantoms. Image-based EPT with Ultra-short Echo Time (UTE) sequence was identified as the most promising. Permittivity reconstruction accuracy was enhanced with an optimal flip angle. An adaptive Savitzky-Golay kernel was proposed for homogeneous Helmholtz EPT, and a surface integral EPT method reduced noise. In vivo studies on brain and torso conductivity related to age, fat fraction, and sex informed accurate SAR modeling. EPT-based SAR calculations validated EPT's reliability and importance.

Keywords : MRI, EPT, electrical properties, conductivity, permittivity, SAR, UTE, Savitzky-Golay, age, electromagnetism, RF